PALACKÝ UNIVERSITY OLOMOUC

FACULTY OF MEDICINE AND DENTISTRY

DEPARTMENT OF NEUROLOGY

Faculty of Medicine and Dentistry

Palacký University Olomouc

TRACT-SPECIFIC DIFFUSION MRI IN DEGENERATIVE CERVICAL SPINAL CORD COMPRESSION

Dissertation thesis in the field of Neurosciences

Ing. Jan Valošek

Olomouc 2022

This page is intentionally left blank

TRACT-SPECIFIC DIFFUSION MRI IN DEGENERATIVE CERVICAL SPINAL CORD COMPRESSION

Ing. Jan Valošek

Advisor: prof. MUDr. Ing. Petr Hluštík, Ph.D.

Consultant: MUDr. Alena Svátková, Ph.D.

Institution: Department of Neurology

Faculty of Medicine and Dentistry

Palacký University Olomouc

University Hospital Olomouc

E-mail: jan.valosek@upol.cz

ABSTRACT

The aim of this PhD thesis is to advance the diffusion magnetic resonance imaging (MRI) in different stages of degenerative spinal cord compression. We strive to optimize both the acquisition protocol as well as the processing analysis pipeline to provide markers sensitive to microstructural damage in patients with non-myelopathic degenerative cervical spinal cord compression (NMDC), a condition that precedes the degenerative cervical myelopathy (DCM), which is the most common cause of non-traumatic spinal cord dysfunction.

First, the thesis describes basic principles of MRI as well as diffusion MRI, introduces spinal cord anatomy and degenerative spinal cord compression, defines the current challenges of spinal cord MRI and details their potential solutions. Next, clinical and electrophysiological assessments of spinal cord compression are discussed and predictors of progression from non-myelopathic compression to symptomatic degenerative cervical myelopathy are reviewed. After this introduction, aims of the thesis are stated, including the studies addressing them.

Second, materials and methods together with results of two original research articles are described in detail. In the first article, optimized multi-shell diffusion protocol based on reduced field-of-view technique was proposed and its reproducibility and clinical useability in both healthy controls as well as NMDC patients was examined. In the second manuscript, we employed tract-specific analysis of microstructural metrics derived from conventional DTI and multi-compartment ball-and-sticks diffusion models on a large cohort of NMDC and DCM patients relative to healthy controls. We detected changes in diffusion markers in the dorsal and lateral tracts as well as the gray matter at the level of compression and rostrally pointing to demyelination, trans-synaptic degeneration and Wallerian degeneration. The depicted changes were more severe in symptomatic DCM patients than in NMDC patients and were mirrored by abnormalities in clinical scale and electrophysiological measures. Importantly, we demonstrated, for the first time, the utility of multi-compartment ball-and-sticks model in spinal cord imaging.

Lastly, the discussion elaborates on contribution of the above-mentioned findings as well as the findings published within several other related manuscripts to the current scientific knowledge, discuss the limitations and outline future directions of our research.

In conclusion, this PhD thesis demonstrated that high-resolution tract-specific dMRI is a sensitive microstructural marker of SC alterations and offers new opportunities for longitudinal trials aiming to provide early predictors of progression from NMDC to symptomatic DCM.

DECLARATION OF AUTORSHIP

I, Jan Valošek hereby declare that the work presented in this dissertation thesis is my own and that I have not used sources other than those listed in the bibliography and identified as references.

……. …….

Place and date Signature of the author

ACKNOWLEDGMENTS

First and foremost, I am thankful to my PhD advisor, prof. MUDr. Ing. Petr Hluštík, Ph.D., for his excellent supervision and continuous support during the past five years. He has been mentoring and supporting me throughout my entire doctorate study and I would not be here without him. I would also like to express my deepest gratitude to my PhD consultant MUDr. Alena Svátková, Ph.D., and informal co-advisor Ing. René Labounek, Ph.D., for their guidance and valuable advice. I appreciate the opportunity which all three gave me to join them and to start with the amazing journey in magnetic resonance imaging research.

I am thankful to prof. MUDr. Josef Bednařík, CSc., from University Hospital Brno who was the principal investigator of the project that I have built my PhD thesis on. Also, I would like to thank everyone who was involved in the project presented in this thesis, namely, MUDr. Petr Bednařík, Ph.D., MUDr. Tomáš Horák, MUDr. Magda Horáková, Ing. Lubomír Vojtíšek, Ph.D., doc. MUDr. Miloš Keřkovský, Ph.D., doc. MUDr. Eva Vlčková, Ph.D., MUDr. Jan Kočica, MUDr. Tomáš Rohan, Ing. Marek Dostál, Ph.D., Ing. Petr Kudlička, Associate Professor Christophe Lenglet and Assistant Professor Igor Nestrašil.

My sincere thanks belong also to Associate Professor Julien Cohen-Adad from Polytechnique Montreal for his invaluable advice and feedback on my work.

I am grateful to prof. MUDr. Petr Kaňovský, CSc., head of the Department of Neurology, University Hospital Olomouc and Palacký University Olomouc for supporting me and providing me with valuable advice.

I am thankful for the support of my colleagues from fMRI laboratory Olomouc, Palacký University Olomouc as well as all members of the Department of Biomedical Engineering, University Hospital Olomouc, who are not only my colleagues in performance of clinical duties but also my friends.

Last but not least, I would like to thank my fiancée and my future wife Natalie as well as my mum, dad, brother and grandparents for their constant support and great deal of understanding.

FUNDING

The experimental part of this work was supported by the Czech Health Research Council (AZV), grant number NV18-04-00159, and by Ministry of Health of the Czech Republic projects for conceptual development of research organizations, project numbers 65269705 (University Hospital Brno) and 00098892 (University Hospital Olomouc, Czech Republic).

I acknowledge the core facility of the Multimodal and Functional Imaging Laboratory, Masaryk University, CEITEC, supported by Ministry of Education, Youth and Sport of the Czech Republic (LM2018129 Czech-BioImaging). Access to computational resources and storage facilities supplied by the project “e-Infrastruktura CZ” (e-INFRA LM2018140) provided within the program Projects of Large Research, Development and Innovations Infrastructures is also greatly appreciated.

The international scholarship during my doctoral study (“Aktion Österreich-Tschechien, AÖCZ-Semesterstipendien" scholarship MPC-2020-00013) was supported by the Austrian Agency for International Cooperation in Education and Research (OeAD-GmbH), Mobility Programmes, Bilateral and Multilateral Cooperation (MPC) financed by Federal Ministry of Education, Science and Research (BMBWF) of Austria.

CONTENTS

1 INTRODUCTION 10

1.1 Magnetic resonance imaging 10

1.1.1 Quantitative MRI 13

1.1.2 Diffusion MRI 13

1.1.3 Diffusion tensor imaging 15

1.1.4 Higher-order diffusion models 17

1.2 Spinal cord anatomy 18

1.3 Degenerative spinal cord compression 19

1.4 Clinical and electrophysiological assessment of spinal cord compression 22

1.5 MRI in the spinal cord compression 22

1.5.1 Acquisition of spinal cord MRI data 23

1.5.2 Processing of spinal cord diffusion MRI data 26

1.5.3 Conventional MRI in the spinal cord compression 29

1.5.4 Diffusion MRI in the spinal cord compression 31

1.5.5 Other quantitative MRI methods in the spinal cord compression 33

1.6 Predictors of progression from non-myelopathic compression 34

2 AIMS OF THE THESIS 36

3 MATERIALS AND METHODS 37

3.1 Study design 37

3.2 Participants 37

3.3 Radiological evaluation 37

3.4 Clinical evaluation 38

3.4.1 DCM symptoms 38

3.4.2 DCM signs 38

3.5 Electrophysiological measures 38

3.5.1 Somatosensory evoked potentials 39

3.5.2 Motor evoked potentials 39

3.5.3 Electromyography 39

3.6 3T MRI acquisition protocol 40

3.7 3T MRI data analysis 43
3.7.1 Processing of anatomical data (same for both studies) 43
3.7.2 Study I (dMRI methodology) 44
3.7.3 Study II (Prospective dMRI study) 48
4 RESULTS 51
4.1 Participant characteristics 51
4.1.1 Study I (dMRI methodology) 51
4.1.2 Study II (Prospective dMRI study) 51
4.2 Imaging results 54
4.2.1 Study I (dMRI methodology) 54
4.2.2 Study II (Prospective dMRI study) 60
5 DISCUSSION 70
5.1 Study I (dMRI methodology) 70
5.2 Study II (Prospective dMRI study) 71
5.2.1 dMRI changes at maximally compressed level 71
5.2.2 Rostral alterations above the compression level 72
5.2.3 Relationship between dMRI metrics, mJOA scale and electrophysiological measures 73
5.3 Limitations 74
5.3.1 Study I (dMRI methodology) 74
5.3.2 Study II (Prospective dMRI study) 75
5.4 General considerations about used spinal cord MRI protocol 75
5.5 Future directions 76
6 Summary and conclusions 78
6.1 Key findings 78
6.2 General conclusions 80
7 REFERENCES 81
8 LIST OF ABBREVIATIONS 100
9 LIST OF FIGURES 102
10 LIST OF TABLES 104
11 LIST OF PUBLICATIONS 105

11.1 Published research papers directly related to the topic of the thesis 105

11.2 Published research papers from broader area of quantitative spinal cord MRI 106

11.3 Other published original research papers using MRI methodology 108

11.4 Author record 109

12 ANNEXES 110

12.1 Annex 1 – Study I (dMRI methodology) 110

12.2 Annex 2 – Study II (Prospective dMRI study) 129

12.3 Annex 3 – Narrative Review 143

1 INTRODUCTION

The central nervous system, which comprises the brain and the spinal cord (SC) can be affected by many different disorders and pathological conditions resulting in diseases significantly reducing patient's quality of life. Degenerative cervical SC compression is one of these conditions, which affects primary the SC, but secondary remote changes can be also observed in the brain. Initially mild and, in many cases, asymptomatic SC compression progresses over time into more severe and often irreversible SC damage, if not diagnosed and treated in time. Magnetic resonance imaging (MRI) is an integral part of both clinical diagnosis as well as scientific research of the central nervous system and provides quantitative biomarkers sensitive to underlying microstructural tissue changes. Such biomarkers might provide in-vivo insight into pathophysiology and extent our understanding of degenerative SC compression.

This section introduces basic principles of MRI as well as diffusion MRI, describes SC anatomy and degenerative SC compression, and discuss clinical and electrophysiological assessment of the SC compression. Next, MRI is put into context of degenerative SC compression and both MRI data acquisition and processing are elaborated on.

1.1 Magnetic resonance imaging

MRI utilizes interaction of atomic nuclei with non-zero magnetic moment and strong external magnetic field. Generally, magnetic moment can be observed in atoms with odd number of protons or neutrons such as ^{1}H, ^{13}C, ^{23}NA, ^{31}P (Lipton, 2008). For the sake of simplicity, and fact that water molecules containing hydrogen atoms (^{1}H) are most abundant in the human body, following paragraphs cover ^{1}H imaging.

Typical clinical MRI scanners have magnetic field strength between 1.5T to 3T, and recently even 7T MRI scanners were approved for clinical use. After inserting a tissue sample into the MRI scanner, individual atomic nuclei align parallelly and anti-parallelly with this external magnetic field and start to perform move called precession, which is similar to rotative movement of a spinning top or a gyroscope (Figure 1). Parallelly and anti-parallelly aligned atomic nuclei can cancel each other's forces out, but since there are more nuclei aligned parallelly (i.e., on lower energy level) the tissue sample forms a magnetization vector parallel to the external magnetic field. Precession frequency of a nucleus is proportional to the strength

of the magnetic field (B_0) and gyromagnetic ratio (γ), which is a constant reflecting size, mass and spin and is specific for each atom, and is described by Larmor equation (Equation (1)):

$$\omega_0 = \gamma B_0 \tag{1}$$

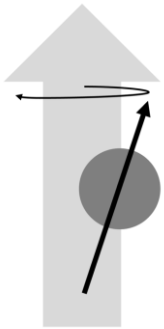

Figure 1 – Illustration of the precession movement. Precession is a result of an interaction of atomic nuclei and external magnetic field. Adapted from (Lipton, 2008).

At this moment, if radiofrequency (RF) pulse with the frequency defined by the Larmor equation is applied to the tissue sample, a resonance phenomenon occurs causing two effects (Figure 2A). First, some atomic nuclei pick up the energy from the RF wave and go from a lower to a higher energy level resulting in a decrease of longitudinal magnetization. Second, individual atomic nuclei start to precess in a same phase establishing a new transversal magnetization, which is perpendicular to the external magnetic field (Figure 2B).

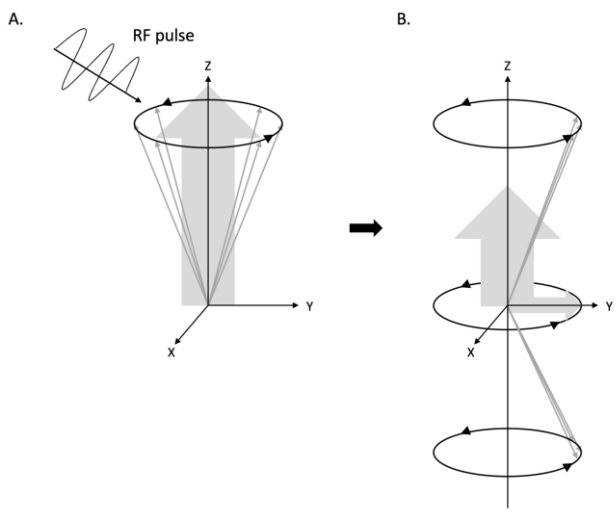

Figure 2 – Resonance phenomenon. Radiofrequency (RF) pulse with the Larmor frequency applied to the tissue sample has two effects; (A) decrease of longitudinal magnetization and (B) increase of transverse magnetization. Adapted from (Schild, 1990).

Once the RF pulse is turned off, longitudinal magnetization starts to increase again, and transverse magnetization starts to decrease resulting in measurable signal. The former is described by the T_1 time constant (longitudinal relaxation time), while the latter is characterized by the T_2 time constant (transverse relaxation time). Longitudinal and transversal relaxations are independent of each other, where T_1 mirrors a return to energy equilibrium and T_2 reflects dephasing of atomic nuclei. Distinct tissues have different intrinsic properties such as amount of water, degree of myelination, or fat content leading to tissue specific T_1 and T_2 time constant. Thus, adjusting of parameters like repetition time (TR) or echo time (TE) of MRI pulse sequence produces images with different degree of so-called T_1- or T_2-weigting. With a short TR and short TE, we get a T_1-weighted image, whereas with long TR and long TE we obtain a T_2-weighted image. A sequence with short TE and long TR then results in so-called proton density (PD) weighted image, which is neither T_1- nor T_2-weighted but proportion to the density of atomic nuclei.

Since B_0 field is not absolutely homogenous, due to subtle variation in the magnetic susceptibility of different tissues, the adjacent atomic nuclei precess on slightly different frequencies, which in turn cause loss of phase coherence and greater decline of transversal magnetization. This mechanism is described by T_2* effect. The spin echo method is used for compensation of transversal magnetization loss due to T_2* effect and consist of series of 180° RF pulses, which refocus the dephasing atomic nuclei (Figure 3).

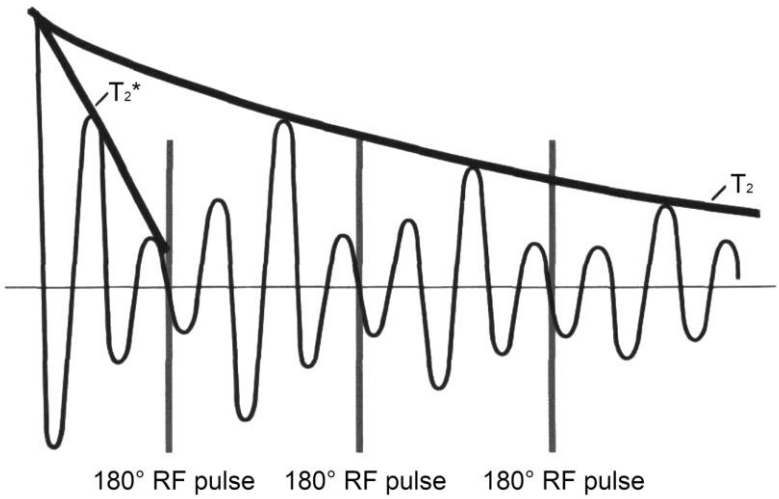

Figure 3 – Visualization of T2* effect. 180° RF pulses are used to refocus the dephasing atomic nuclei and thus minimize the T2* effect. Adapted from (Schild, 1990).

To spatially distinguish between signals emitted from different locations of the tissue after the RF pulse turn off, additional gradient magnetic fields are applied to linearly modify B_0 to slightly shift Larmor frequency across the tissue sample. Then, since atomic nuclei along the gradient fields are exposed to slightly different magnetic field strengths, they have different precession frequencies and phases. The signal produced by the tissue sample is consequently measured by an antenna, denoted as a receive coils, and gradually sampled into so-called k-space. Once the k-space is filled with measured signals from different locations of the tissue, an inverse Fourier transform is applied to reconstruct the final image.

1.1.1 Quantitative MRI

Standard clinical SC protocols contain images with T_1-, T_2-weighting, and/or images with suppressed fat. Although these images provide contrast between different tissues such SC and cerebrospinal fluid (CSF), and white (WM)/gray matter (GM) based on difference in their T_1 and T_2 time constants, such information reflects only gross SC anatomy and does not provide insight into microstructural tissue properties.

Conversely, quantitative MRI (qMRI) represents a group of techniques, which aim to reveal information about microstructural, functional and metabolic tissues properties. Most commonly used qMRI methods used in the SC research are diffusion MRI sensitive to microstructural tissue damage, magnetization transfer imaging mirroring level of myelination, functional MRI measuring neuronal activity and magnetic resonance spectroscopy quantifying neurochemical profile of metabolites (Cohen-Adad and Wheeler-Kingshott, 2014).

1.1.2 Diffusion MRI

Diffusion magnetic resonance imaging (dMRI, or diffusion-weighted imaging, DWI) is a qMRI technique sensitive to random water molecule movement within the tissue (Johansen-Berg and Behrens, 2013). Basic concept of dMRI sequence is based on application of pair of diffusion encoding gradients (Figure 4). The first, so-called dephasing, gradient results in slight modification of B_0 field along the gradient direction, which in turn causes that atomic nuclei start to resonate at different frequencies depending on their location (Mori and Tournier, 2014). After the end of the first gradient application, atomic nuclei return to their original resonance frequency, but their phases are no longer same leading to loss of overall signal. The second, so-called rephasing, gradient has exactly same strength and length but opposite

polarity causing that atomic nuclei regain their original phase. Since the water molecules perform constant movement (i.e., diffusion), which is moreover restricted by the tissue architecture such as level of myelination and axonal configuration, measurable signal attenuation can be detected after the end of the second gradient (Mori and Tournier, 2014). The signal attenuation along the certain diffusion gradient can be used together with reference image without the diffusion weighting to compute a diffusion constant *D*:

$$S_i = S_0 e^{-bD} \rightarrow D = \frac{\ln(S_i/S_0)}{-b} \tag{2}$$

Where S_i is diffusion weighted signal along certain diffusion gradient, S_0 denotes the signal without diffusion weighting (i.e., without application of the gradient pair), and *b* is a b-value expressed as:

$$b = \gamma^2 G^2 \delta^2 (\Delta - \delta/3) \tag{3}$$

The b-value is a parameter that characterizes the pair of diffusion gradient, namely, *G* is the strength of the gradients, δ denotes the duration of the gradients, Δ characterizes the time between the gradients and γ is a gyromagnetic ratio (Figure 4).

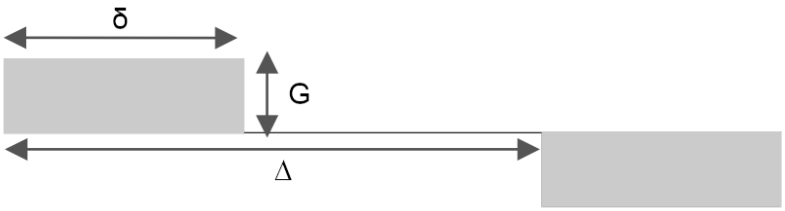

Figure 4 – Illustration of basic concept of the diffusion-weighted experiment. The pair of dephasings and rephasing gradients is applied to produce diffusion-weighted signal. G, strength of the gradients; δ, duration of the gradients, Δ, time between the gradients. Adapted from (Mori and Tournier, 2014).

Higher b-value means that the image has more diffusion-weighted contrast and is thus more sensitive to the underlying processes mirrored by the diffusion, yet also decrease the amplitude of measurable signal, which in turn decrease the signal-to-noise ratio (SNR). Thus, a trade-off must be found between amount of diffusion weighting (i.e., b-value) and sufficient SNR.

Whereas in the clinical routine, dMRI has been used for quantification of diffusion restriction or apparent diffusion coefficient in stroke or tumors, the research applications usually rely on mathematically reconstruction of diffusion directionality (so-called diffusion models fitting) (Johansen-Berg and Behrens, 2013). The most commonly used diffusion model in the SC research is diffusion tensor imaging model (David et al., 2019; Martin et al., 2016; Mori and Tournier, 2014).

1.1.3 Diffusion tensor imaging

Diffusion tensor imaging (DTI) model characterizes the diffusion directionally by 3D ellipsoid, which takes shape of sphere for unrestricted diffusion (i.e., isotropic diffusion) in mediums without any barriers like CSF, and shape of tensor for restricted diffusion (i.e., anisotropic diffusion) in tissues with ordered structures such as axonal tracts (Figure 5a) (Mori and Tournier, 2014).

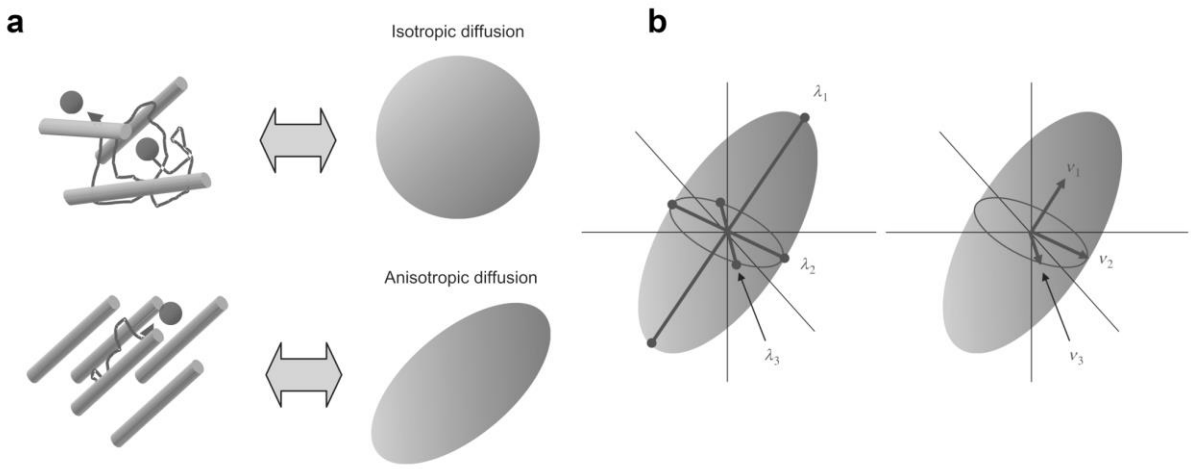

Figure 5 – Isotropic and anisotropic diffusion and diffusion tensor. (a) Visualization of isotropic and anisotropic diffusion, (b) 3 eigenvalues (λ_1, λ_2, λ_3) representing lengths of the tensor's axis and 3 eigenvectors (v_1, v_2, v_3) describing directions of these axis. Adapted from (Mori and Tournier, 2014).

Diffusion tensor is described by 3×3 symmetric matrix. Elements in the matrix represent individual diffusion constants *D* (Equation (2)) along certain diffusion gradient directions, and since the matrix is symmetric, 6 unique diffusion constants are required. Matrix decomposition can be then used to determine 3 eigenvalues (λ_1, λ_2, λ_3) representing lengths of the tensor's axis and 3 eigenvectors (v_1, v_2, v_3) describing directions of these axis (Figure 5b) (Mori and Tournier, 2014):

$$\begin{array}{l} D_{xx} = \dfrac{\ln(S_x/S_0)}{-b} \\ D_{yy} = \dfrac{\ln(S_y/S_0)}{-b} \\ \vdots \end{array} \quad \bar{\bar{D}} = \begin{bmatrix} D_{xx} & D_{xy} & D_{xz} \\ D_{yx} & D_{yy} & D_{yz} \\ D_{zx} & D_{zy} & D_{zz} \end{bmatrix} \xrightarrow{\text{decomposition}} \lambda_1, \lambda_2, \lambda_3, \boldsymbol{v}_1, \boldsymbol{v}_2, \boldsymbol{v}_3$$

(4)

The eigenvalues can be consequently used to derive several DTI parameters (or metrics) such as fractional anisotropy (FA) (Equation (5)) referring to the directional preference of diffusion affected by the degree of myelination, axonal packing, axon size, and/or coherence and co-linearity of fiber organization (Johansen-Berg and Behrens, 2013). Whereas FA ranges from values close to 0 in the tissues with no boundaries for water movement (e.g., CSF) to values around 1 in highly anisotropic tissues with parallel and highly organized fiber structure, mean diffusivity (MD) (Equation (6)) measures the overall molecular diffusion rate. Axial (AD) (Equation (7)) and radial diffusivity (RD) (Equation (8)) then provide diffusion rates in the main and transverse axes of the tensor, referring to the degree of tissue edema, axonal damage, and demyelination, respectively (Cohen-Adad, 2018; Johansen-Berg and Behrens, 2013).

$$FA = \sqrt{\frac{1}{2}} \frac{\sqrt{((\lambda_1 - \lambda_2)^2 + (\lambda_2 - \lambda_3)^2 + (\lambda_3 - \lambda_1)^2)}}{\sqrt{\lambda_1^2 + \lambda_2^2 + \lambda_3^2}}$$

(5)

$$MD = \frac{(\lambda_1 + \lambda_2 + \lambda_3)}{3}$$

(6)

$$AD = \lambda_1$$

(7)

$$RD = \frac{(\lambda_2 + \lambda_3)}{2}$$

(8)

However, DTI model allows to reconstruct just a single primary diffusion direction (so-called single-compartment model), and thus provides only a gross over-simplification of the actual anatomy (Mori and Tournier, 2014). Higher-order diffusion models such as ball-and-sticks (Behrens et al., 2003), composite hindered and restricted model of diffusion (CHARMED) (Assaf

et al., 2004), diffusion kurtosis imaging (DKI) (Jensen et al., 2005), neurite orientation dispersion and density imaging (NODDI) (Zhang et al., 2012), Q-space imaging (QSI) (Assaf et al., 2000) or q-ball imaging (Tuch, 2004) overcome the DTI's limitation by modeling several tissue compartments and provide a more precise depiction of tissue microstructure.

1.1.4 Higher-order diffusion models

Whereas DTI model can be robustly estimated from dMRI data with 30 diffusion encoding directions (Jones, 2004), higher-order diffusion models usually require high angular resolution diffusion imaging (HARDI) (Tuch et al., 2002) and sequences utilizing two or more b-values (i.e., multi-shell sequences) (Caruyer et al., 2013) that rely on optimized acquisition protocols and processing tools (see Chapter 1.5).

Multi-compartment ball-and-sticks model (Behrens et al., 2003) describes diffusion by an optional number of crossing fiber bundles with their partial volume fractions (*fk*) and single mean diffusivity (*d*) representing isotropic compartment (Jbabdi et al., 2012):

$$\frac{S_i}{S_0} = (1 - \sum_k f_k)^{-b_i d} + \sum_k f_k^{-b_i d (g_i^T x_k)^2} \tag{9}$$

Where S_i is diffusion weighted signal along certain diffusion gradient with vector g_i and b-value b_i. S_0 denotes the signal without diffusion weighting. Each anisotropic compartment *fk* is modeled using a stick tensor (i.e., cylinder with zero radius) oriented along x_k, and *d* represents the isotropic compartment.

Another multi-compartment approach such as CHARMED (Assaf et al., 2004) models the diffusion-weighted signal by extra-cellular tensor compartment and several cylindrical components. Unlike ball-and-sticks model, CHARMED requires relative long multi-shell acquisition to obtain enough information for the model fit, though, which is limitation for patients studies (Mori and Tournier, 2014).

Expansion of the Equation (2) by the non-Gaussian diffusion effect between measured signal and b-value, which is observable at higher b-values, is the basis of DKI model, which provides mean kurtosis, DKI fractional anisotropy (DKI-FA), DKI mean diffusivity (DKI-MD) metrics (Jensen et al., 2005):

$$S_i = S_0 e^{-bD+\frac{b^2D^2K}{6}}$$

(10)

Where S_i is diffusion weighted signal along certain diffusion gradient, S_0 denotes the signal without diffusion weighting, b is a b-value, D represents the diffusion constant, and K is the diffusional kurtosis.

Finally, a three-compartment NODDI technique (Zhang et al., 2012) separates measured diffusion signal into intracellular volume fraction, isotropic CSF volume fraction, and orientation dispersion index. Advantage of NODDI over DTI should be its ability to separate WM components confounded in FA (Cohen-Adad and Wheeler-Kingshott, 2014). Although NODDI does not require as much b-values as CHARMED model, it still demands HARDI sampling with at least one b-value ≥ 2000 s.mm^{-2} (Li et al., 2020; Zhang et al., 2012), which can be constrain for SC imaging on clinical scanners due to low SNR.

1.2 Spinal cord anatomy

The spinal cord (SC) is the second major part of the central nervous system conducting electrical signals from the brain to periphery and vice versa. The SC is 40 to 50 cm long with 1 to 1.5 cm transversal diameter and in the superior-inferior direction is divided into cervical, thoracic, lumbar and sacral regions. In transverse section, the SC shows an outer layer of white matter (WM) consisting of ascending and descending nerve fibers (i.e., tracts), an inner core of gray matter (GM) containing cell bodies, and a small central canal filled with cerebrospinal fluid (CSF) at the center (Standring, 2020). The SC WM is divided into the dorsal (or posterior) columns, lateral columns and ventral (or anterior) columns, each of which contains a number of specific tract (Standring, 2020). The major descending tracts that carry electrical signals from the motor cortex to muscles are lateral and ventral corticospinal tracts, while major ascending tracts conducting sensory information from the periphery to the somatosensory cortex are spinothalamic tracts, fasciculus cuneatus and fasciculus gracilis (Standring, 2020). The SC GM consists of dendrites and is divided into dorsal horns comprised of sensory nuclei, ventral horns consisting of motor neurons, and dorsal and ventral grey commissures surrounding the central canal (Standring, 2020). Blood supply of the SC is provided by three major longitudinal arteries, namely, a single anterior spinal artery and two posterior spinal arteries, and several segmental arteries (Standring, 2020).

1.3 Degenerative spinal cord compression

Degenerative SC compression frequently occurs in the elderly due to pathological changes such as intervertebral disc bulging, herniation or osteophyte formation (Adamova et al., 2015; Badhiwala et al., 2020; Kovalova et al., 2016; Smith et al., 2021). Relative resilience of the cervical SC to incipient compressive changes often leads to asymptomatic or non-myelopathic degenerative cervical spinal cord compression (NMDC) (Bednarik et al., 2008, 2004; Fehlings et al., 2017), a condition that precedes the clinically manifest degenerative cervical myelopathy (DCM), which is the most common cause of SC dysfunction (Badhiwala et al., 2020; Fehlings et al., 2017). Although, NMDC studies have suffered from a lack of nomenclature and inclusion criteria consistency that differs between regions and countries (Table 1), the recent systematic review (Smith et al., 2021) showed that the prevalence of NMDC in the Caucasian population over 60 years is up to 39.7% and increases with age (Kovalova et al., 2016; Smith et al., 2021; Witiw et al., 2018). NMDC patients may exhibit cervical axial pain and/or signs or symptoms of radiculopathy, although they usually do not show any signs or symptoms of clinical manifest myelopathy such as upper motor neuron signs in the upper and/or lower limbs (e.g., hyperreflexia, clonus, a positive Hoffman sign, a positive Trömner sign, an upgoing plantar response and lower limb spasticity), gait disturbance, clumsy hand syndrome, Lhermitte's sign (Badhiwala et al., 2020; Bednarik et al., 2008). Despite limited clinical symptomatology in the beginning, up to 23% of NMDC patients progress into symptomatic DCM during a follow-up of 44 months (Wilson et al., 2013). The current clinical guidelines (Fehlings et al., 2017) and Recommendations of World Federation of Neurosurgical Societies Spine Committee (WFNS, 2019) imply conservative clinical treatment in NMDC patients without symptoms of radiculopathy, whereas guidelines recommend a consideration of surgical intervention in NMDC patients with clinical and/or electrophysiological evidence of radiculopathy. Since the surgery is associated with risks of neurological deterioration in 7–11% of patients (Badhiwala et al., 2020), the population worldwide is aging, and fact that DCM substantially reduced quality of life (Badhiwala et al., 2020; Oh et al., 2017), there is an urgent need to reliable identify NMDC patients with a higher risk of progression to irreversible DCM (WFNS, 2019).

The cervical SC compression occurs predominantly between C4/5 and C6/7 cervical levels (Kovalova et al., 2016) and histopathological reports demonstrated that primary damage at the level of compression arises from malperfusion throughout the territory of compressed anterior

spinal artery with restrained blood supplies in the lateral columns, anterior part of dorsal columns and ventral GM horns but not in ventral columns (Figure 6a) (Badhiwala et al., 2020; Mair and Druckman, 1953). Figure 6b shows secondary changes such as axonal degeneration and demyelination that propagate remotely in both superior and inferior directions affecting WM and GM above (David et al., 2022; Grabher et al., 2017, 2016; Horak et al., 2021; Vallotton et al., 2021; Valošek et al., 2021, 2020) and below (David et al., 2022), and causing changes even in the brain areas (Bernabéu-Sanz et al., 2020; David et al., 2019; Kowalczyk et al., 2012). Affected tracts are motor lateral corticospinal tracts and sensory dorsal columns (i.e., fasciculus gracilis and fasciculus cuneatus) and spinothalamic tracts (David et al., 2019). The SC gray matter horns then undergo trans-synaptic degeneration (David et al., 2019).

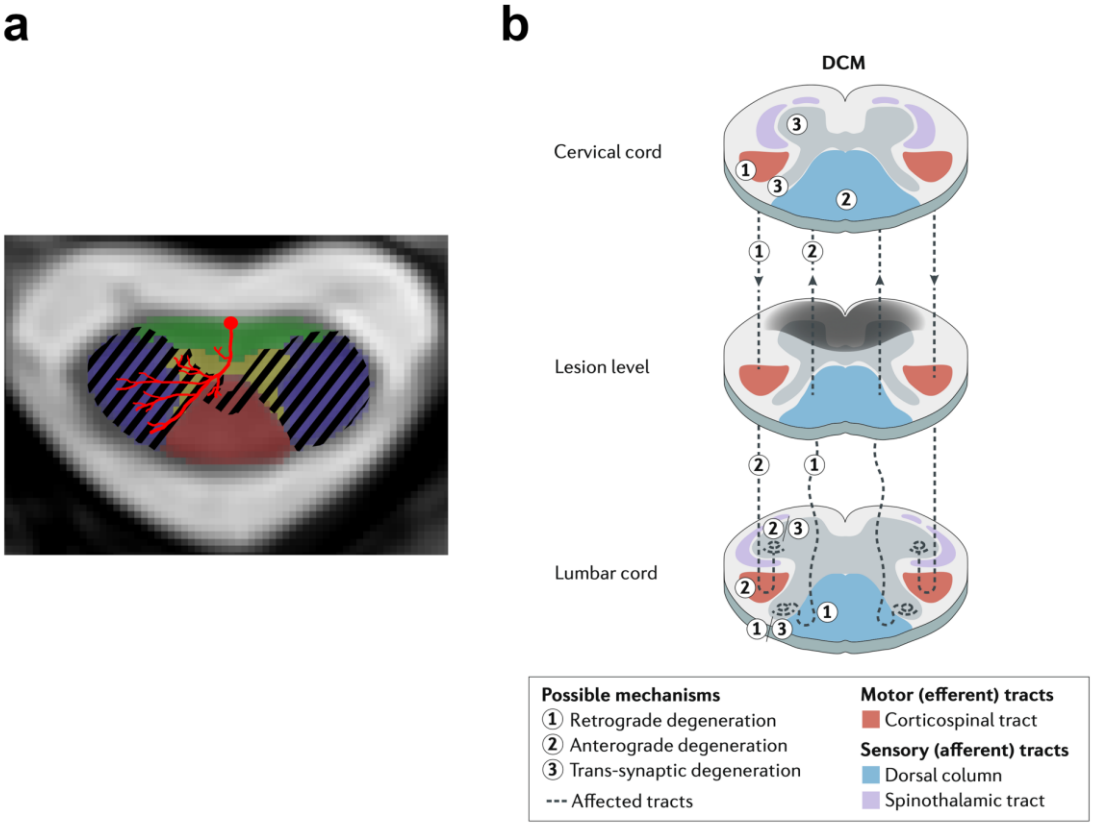

Figure 6 – Primary and secondary changes caused by the compression. (a) Lesion distribution caused by compressed anterior spinal artery. Filled areas are affected by the compression, that is, lateral columns, anterior part of dorsal columns and ventral GM horns. Adapted from (Mair and Druckman, 1953) and (Valošek et al., 2021). (b) Illustration of primary and secondary damage in degenerative cervical myelopathy caused by degenerative spinal cord compression. Primary changes at level of compression affect lateral columns, anterior part of dorsal columns and ventral GM horns. Secondary changes propagate rostrally and caudally resulting in retrograde and anterograde degeneration of white matter tracts and trans-synaptic degeneration of gray matter horns. Adapted from (David et al., 2019).

Table 1 - Nomenclature and definitions of non-myelopathic spinal cord compression across studies. Adapted from (Valošek et al., 2022).

Study	Nomenclature	Definition
	Original articles	
(Bednarik et al., 2004), (Bednarik et al., 2008)	Pre-symptomatic spondylotic cervical cord compression (P-SCCC)	MR signs of spondylotic or discogenic SC compression and axial cervical pain or clinical signs and/or symptoms of radiculopathy but no clinical signs of myelopathy (mJOA ≥ 16, note – mJOA decrease due to radiculopathy)
(Kerkovský et al., 2012)	Asymptomatic spondylotic cervical cord encroachment (SCCE)	MR signs of spondylotic cervical SC compression and cervical pain and/or symptoms/signs of cervical radiculopathy, but without symptoms/signs of cervical spondylotic myelopathy (mJOA = 18)
(Adamova et al., 2015)	Asymptomatic spondylotic cervical cord compression (ASCCC)	No detailed description (study focused on prevalence of ASCCC in patients with clinically symptomatic lumbar spinal stenosis) (mJOA not reported)
(Kovalova et al., 2016)	Nonmyelopathic spondylotic cervical cord compression (NMSCCC)	MR signs of SC compression and possible presence of radiculopathy but no myelopathic signs (mJOA not reported)
(Keřkovský et al., 2017)	Asymptomatic degenerative cervical cord compression (ADCCC)	MR finding of SC compression and various clinical signs of cervical spine degenerative disease (cervical pain, radiculopathy) but no signs or symptoms of DCM (mJOA = 18)
(Ellingson et al., 2018)	Asymptomatic cervical stenosis patients	No neurological symptomatology (mJOA = 18) but complaints of neck pain
(Martin et al., 2018a)	Asymptomatic spinal cord compression (ASCC)	MR finding of cervical SC compression but an absence of any neurological symptoms and signs; neck pain was not considered a neurological symptom (mJOA = 18)
(Kadanka et al., 2017), (Labounek et al., 2020)	Nonmyelopathic degenerative cervical cord compression (NMDCCC)	MR signs of SC compression but an absence of any myelopathic signs or possible presence of axial pain and/or symptoms or signs of upper extremity monoradiculopathy or completely asymptomatic individuals (mJOA not reported)
(Kadanka et al., 2021)	Non-myelopathic degenerative cervical cord compression (NMDCC)	MR signs of cervical SC compression and presence of maximally one clinical myelopathic symptom but no clinical myelopathic signs (mJOA ≥ 17)
(Valošek et al., 2021), (Horak et al., 2021), (Horáková et al., 2022)	Non-myelopathic degenerative cervical spinal cord compression (NMDC)	MR signs of cervical SC compression with or without radiculopathy and electrophysiological changes but without myelopathic symptoms/signs (mJOA = 18)
	Reviews	
(Wilson et al., 2013)	Nonmyelopathic patients with cervical stenosis	review – no single definition
(Witiw et al., 2018)	Asymptomatic cervical spinal cord compression (CSCC)	review – no single definition
(Smith et al., 2021)	Asymptomatic spinal cord compression (ASCC)	review – no single definition
(Badhiwala et al., 2020)	Cervical spinal cord compression without myelopathy	review – MR signs of cervical SC compression, absence of any myelopathic signs and clinical radiculopathy with or without electrophysiological changes or no signs of symptoms of radiculopathy (mJOA = 18)

1.4 Clinical and electrophysiological assessment of spinal cord compression

Impairment in symptomatic DCM patients can be assessed by clinical scores such as modified Japanese Orthopaedic Association (mJOA) scale (Tetreault et al., 2017) or Nurick classification system (Nurick, 1972). The mJOA scale is currently the most widely accepted outcome measure for DCM patients (Badhiwala et al., 2020), which utilizes 18-point scale and assess separately upper limb motor function, lower limb motor function, upper limb sensation and sphincter function. The mJOA scale classifies the DCM severity as mild (mJOA scale 15-17), moderate (mJOA scale 12-14) or severe (mJOA score ≤11) (Tetreault et al., 2017). The Nurick classification system assesses the functional status using 6-point scale, from grade 0 with signs or symptoms of root involvement, but without evidence of spinal cord disease to grade 5 where is patient chair- bound or bedridden (Badhiwala et al., 2020; Nurick, 1972).

Electrophysiological measurements including somatosensory-evoked potentials (SEP) and motor-evoked potentials (MEP) asses functional changes of sensory and motor SC tracts, and were reported to be sensitive to subclinical functional changes, which are otherwise “clinically silent” (Bednarik et al., 2008; Bednařík et al., 1998). Both SEP and MEP reflect central conduction abnormality attributed to possible cervical SC lesion based on abnormalities in the appearance, latency, and amplitude of evoked potentials (Bednařík et al., 1998).

Electromyography (EMG) performed with needle electrodes is a highly sensitive technique for the detection of anterior horn cells damage, or compression of nerve roots that occurs in DCM as a result of compression (Dvorak et al., 2003). EMG examinates segmentally affected muscles and assesses spontaneous activity, motor unit action potential (MUP/MUAP) parameters, and interference patters (Bednarik et al., 2008).

Recently, contact heat evoked potentials demonstrated high sensitivity in DCM patients (Jutzeler et al., 2017) and might be promising in future longitudinal studies besides currently used methods.

1.5 MRI in the spinal cord compression

In this chapter, the conventional and diffusion MRI is put into context of degenerative SC compression. Challenges of SC MRI acquisition and data processing are elaborated on, and possible workarounds are considered. Next, studies utilizing structural MRI to assess compression severity and to validate SC atrophy are discussed. Finally, contemporary dMRI

studies on NMDC and DCM patients are reviewed. For the context, concise overview of other quantitate MRI techniques used in patients with SC compression is provided as well.

1.5.1 Acquisition of spinal cord MRI data

In-vivo SC MRI is challenging due to its small cross-sectional area, physiological motion artifacts caused by breathing and cardiac pulsation, and presence of tissues with distinct magnetic susceptibility characteristics such as WM and GM, CSF, bony vertebrae and air in the lungs and trachea that results in image distortions, especially in dMRI (Cohen-Adad and Wheeler-Kingshott, 2014).

1.5.1.1 Small spinal cord cross-sectional area

Since the SC is curved-shaped structure with a relatively small anteroposterior and transverse diameters at C2 level of 8.8 and 12.4 mm, respectively (Sherman et al., 1990), optimized acquisition protocols with sufficient SNR are needed. Relatively homogenous structure of the SC in the superior-inferior direction allow the usage of anisotropic resolution on the order of 1×1×5 mm to increase the SNR and to preserve high in-plane resolution (Cohen-Adad et al., 2021b; Cohen-Adad and Wheeler-Kingshott, 2014).

1.5.1.2 Physiological motion

Close proximity of lungs and heart to the SC introduces respiratory-related dynamic distortions of the B_0 magnetic field along the phase-encoding direction and periodic SC motion (Samson et al., 2016; Verma and Cohen-Adad, 2014). While the cardiac or respiratory triggering significantly reduces motion artifacts, it also results in prolonged acquisition time, which can cause additional movement particularly in older patients with the SC compression. Although the comparison of SC DTI with and without cardiac triggering showed no significant differences for fractional anisotropy (Martin et al., 2017a), the recent multi-center study recommends to acquire dMRI data during the quiescent phase of the cardiac cycle utilizing pulse oximeter to minimize cardiac-related SC motion (Cohen-Adad et al., 2021b).

1.5.1.3 Susceptibility artifacts

Differences in magnetic susceptibility between various tissues introduce geometrical distortions, especially in fast acquisition techniques utilizing echo planar imaging (EPI) (Cohen-Adad and Wheeler-Kingshott, 2014) (Figure 7). EPI sequences are commonly used for DWI,

because they are rapid, and provide high SNR efficiency (i.e., SNR per square root of the acquisition time) (Samson et al., 2016).

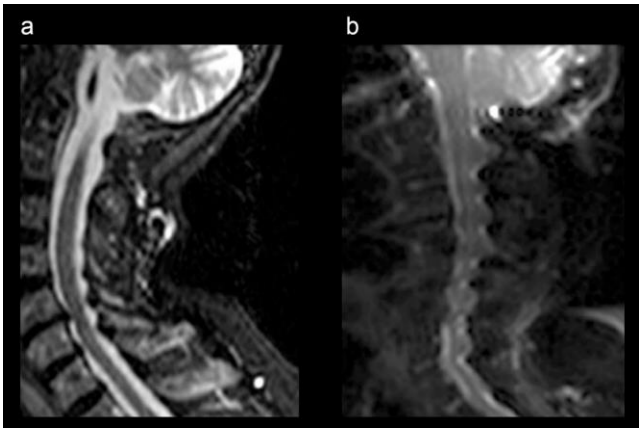

Figure 7 – Illustration susceptibility-induced distortions. (a) T2-w structural image, (b) single-shot echo planar imaging (EPI) image demonstrating susceptibility-induced distortions along the spinal cord. Adapted from (Cohen-Adad and Wheeler-Kingshott, 2014).

The susceptibility-induced voxel displacement along the phase-encoding direction in the EPI image can be expressed as (Cohen-Adad and Wheeler-Kingshott, 2014):

$$d_{PE}(r) = \frac{\Delta f(r)\, T_{ESP}\, FOV_{PE}}{N_{int}\, R} \tag{11}$$

Where $d_{PE}(r)$ is the location displacement of a voxel in the phase-encoding direction by a distance r, $\Delta f(r)$ denotes off-resonance effect in Hz (i.e., field inhomogeneity) at position r, T_{ESP} is the echo spacing (i.e., time interval between two adjacent echoes during an EPI readout), FOV_{PE} represents the field-of-view in the phase-encoding direction, N_{int} is the number of interleaves in the EPI (e.g., N_{int} = 1 for single-shot EPI), and R denotes the acceleration factor for parallel imaging (e.g., R = 1 for no acceleration) (Cohen-Adad and Wheeler-Kingshott, 2014).

As expressed in Equation (11), susceptibility induced distortions can be decreased by acceleration of k-scape filling, which in turn reduces the off-resonance effect $\Delta f(r)$. Thus, several techniques were proposed to accelerate the filling of the k-scape such as reduced field-of-view (FOV) methods (Samson et al., 2016) or techniques utilizing readout-segmented EPI (Cohen-Adad, 2012) (Figure 8).

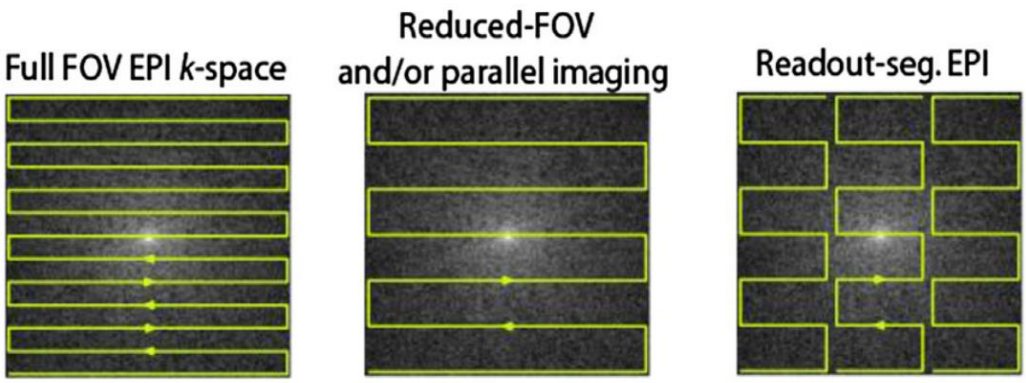

Figure 8 – MRI sequences used to accelerate k-space filling to reduce susceptibility induced distortions in echo planar imaging (EPI). From left – sequence without acceleration, reduced field-of-view (FOV) technique, readout-segmented EPI method. Adapted from (Cohen-Adad and Wheeler-Kingshott, 2014).

1.5.1.4 Reduced field-of-view techniques

The reduced FOV technique has several implementations; some based on inner volume excitation using 2D or cross-sectional excitation pulses (Finsterbusch, 2009; Wheeler-Kingshott et al., 2002) and others based on outer volume suppression using saturation bands (Samson et al., 2016; Wilm et al., 2007) (Figure 9). The reduced FOV methods utilizing inner volume excitation are available on scanners of all three major MRI vendors (i.e., ZOOMit for Siemens, FOCUS for GE and Zoom DWI for Philips) and are preferred over the outer volume suppression approach, which produces more distorted images (Cohen-Adad et al., 2021b; Samson et al., 2016).

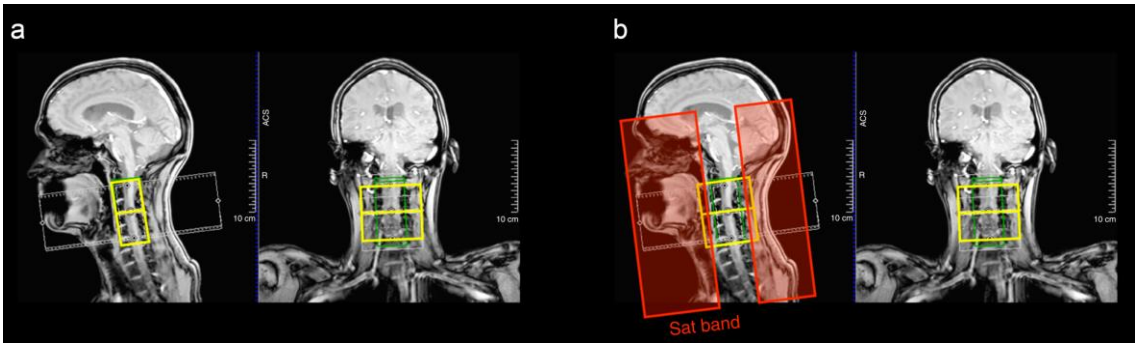

Figure 9 – Reduced field-of-view (FOV) techniques. (a) Inner volume excitation approach, (b) outer volume suppression implementation utilizing saturation bands (red boxes). Adapted from (Cohen-Adad et al., 2021b).

1.5.1.5 Readout-segmented echo planar imaging technique

The readout-segmented EPI technique utilizes series of consecutive segments along the readout direction to fill the k-space (Figure 8) resulting in reduction in the length of the EPI readouts, which in turn reduce the level of susceptibility-induced distortion (Cohen-Adad,

2012). At the same time, the approach is less sensitive to motion artifacts (Cohen-Adad and Wheeler-Kingshott, 2014). Siemens implementation of the readout-segmented EPI technique has the trade name RESOLVE (Readout Segmentation Of Long Variable Echo-trains) (Cohen-Adad, 2012).

1.5.1.6 Angular resolution

Angular resolution is characterized by the strength of diffusion gradient (i.e., b-value) and by the number of diffusion encoding directions (Cohen-Adad and Wheeler-Kingshott, 2014). As described in Chapter 1.1.2, the b-value is the parameter that sets the amplitude of the diffusion weighting. Although higher b-values provide higher diffusion-based contrast (i.e., more diffusion weighting), the measured signal is, at the same time, more attenuated, which in turn results in lower SNR. Whereas higher diffusion weighting is desired for estimation of multi-compartment diffusion models and to detect complex fiber geometry, the tradeoff must be found between acquisition time, SNR and number of diffusion-encoding directions. Monte Carlo simulations utilizing b-value = 1000 $s.mm^{-2}$ showed that at least 20 unique diffusion encoding directions are necessary for a robust estimation of DTI's FA, while at least 30 unique diffusion encoding directions are required for a robust estimation of DTI's MD (Jones, 2004).

An increased SNR of the 3T DWI sequences relative to 1.5T allows the acquisition of multi-shell diffusion data with higher b-values, which is crucial for fitting of multi-compartment diffusion models such as NODDI, ball-and-sticks, or DKI (Cohen-Adad et al., 2021b). Usually, HARDI (Tuch et al., 2002) sequences utilizing diffusion gradient sampling on several spheres in the q-space (i.e., multi-shell) (Caruyer et al., 2013) are employed. HARDI protocols aim to distribute diffusion encoding directions uniformly on the entire sphere(s) in order to increase so-called angular resolution, which in turn improve the reconstruction of multiple fibers per voxel (Caruyer et al., 2013).

1.5.2 Processing of spinal cord diffusion MRI data

This chapter describes typical processing steps and artifacts correction methods during SC dMRI data analysis.

1.5.2.1 Artifacts correction

Variation in magnetic susceptibility between different tissues induces image distortions, and breathing with cardiac cycle generates motion artifacts. Moreover, rapid diffusion gradient switching during the dMRI acquisition induces eddy currents producing additional image distortions, which manifest as translation, scaling and shearing (Andersson and Sotiropoulos, 2016; Mori and Tournier, 2014). Acquisition of pair of dMRI sequences with opposite phase-encoding directions (e.g., anterior-posterior and posterior-anterior) and usage of dedicated post-processing tools for correction of motion artifacts, eddy currents distortions and susceptibility-induced distortions (Andersson et al., 2003; Andersson and Sotiropoulos, 2016) are commonly used across SC studies, even though these tools are primarily designed for the brain and their usage for the SC is the subject of ongoing debate (https://forum.spinalcordmri.org/t/how-to-correct-for-distortions-in-spinal-cord-diffusion-mri-data/326, Accessed January 15, 2022).

Last but not least, dMRI dataset consist of a collection of multiple 3D volumes, each acquired along certain diffusion gradient resulting in acquisition time on order of several minutes. Subject movement during the acquisition can thus introduce additional motion artifacts propagated as a shift between individual 3D volumes. Dedicated methods tailored for the SC were proposed based on an iterative 2D translations to correct this type of motion artifacts (De Leener et al., 2017; Xu et al., 2013).

1.5.2.2 Steps of spinal cord MRI data analysis

Common tasks included in the SC MRI data processing are segmentations of SC and WM/GM, vertebral levels identification, multi-modal registrations, registration to template and quantitative analysis using the SC atlas. Tools for dealing with all these challenges are implemented in the open-source software package Spinal Cord Toolbox (SCT) (De Leener et al., 2017). Alternative packages such as FMRIB Software Library (FSL) (Jenkinson et al., 2012), Statistical Parametric Mapping (SPM) software package (Penny et al., 2007) or JIM (http://www.xinapse.com, Accessed January 15, 2022) designed for brain analysis, can also be used for SC data processing. Usually, a combination of tools is used to facilitate multimodal qMRI analysis; for example, SCT is utilized for automatic SC and GM segmentations, morphometric metrics extraction, and registration of PAM50 atlas, and is supplemented by

other tools, which provide frameworks for estimation of higher-order diffusion models. Overview of individual processing steps is illustrated in Figure 10.

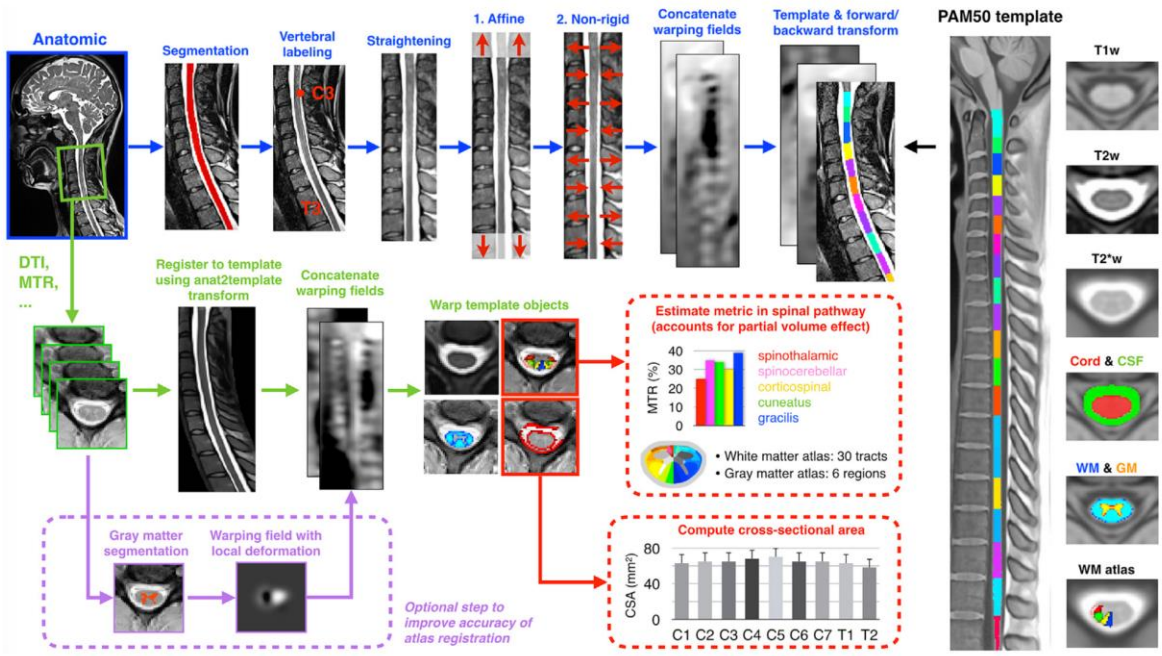

Figure 10 – Overview of common processing steps included in spinal cord atlas-based dMRI analysis. Spinal cord is segmented, and individual vertebral levels are identified from anatomical image to allow consequent registration to the spinal cord template. Transformation from this registration is then used for registration of the template to the dMRI data. Finally, probabilistic spinal cord atlas is warped to the dMRI space to extract diffusion metrics from individual white matter tracts and gray matter areas. Reproduced from (Cohen-Adad, 2018).

Since dMRI data are usually acquired with anisotropic resolution and covers only several vertebral segments (e.g., from C2 to C5) (Cohen-Adad et al., 2021b), additional structural high-resolution T_1-w and/or T_2-w images with larger spatial coverage are required for reliable dMRI analysis and accurate template registration (Cohen-Adad, 2018; De Leener et al., 2017). A template is an image that has been averaged across multiple individuals (population-derived or obtained within specific study) to provide standard reference space for group analyses and atlas-based approach (Cohen-Adad, 2018). The template included in the SCT is called PAM50 and covers full SC and the brainstem (De Leener et al., 2018).

Typically, the SC analysis starts with the SC segmentation of T_1-w or T_2-w images to obtain binary mask of the SC, followed by identification of individual vertebral levels (i.e., vertebral labeling) to allow registration to the template (De Leener et al., 2017). The registration to the template consists of SC straightening to match the shape of the template, followed by multi-step nonlinear registrations (Figure 10) (De Leener et al., 2017). Once the registration of

structural image to template is done, transformation produced by this registration (so-called warping field) can be used for registration of the template to dMRI data. To achieve maximal robustness (e.g., in subjects with compressed SC), it is recommended to provide also binary masks of the SC (i.e., SC segmentations) to the registration algorithm (De Leener et al., 2017). The atlas-based analysis can be then performed to extract dMRI-derived metrics such as FA or MD within specific WM tracts and GM regions (Cohen-Adad, 2018). Considering small size of some WM tracts (e.g., spinocerebellar tract has < 1mm size), partial volume correction is crucial step to eliminate potential contamination from surrounding tissues such as CSF (Lévy et al., 2015). Several methods for partial volume correction are available starting from basic approach based on averaging the dMRI data within the thresholded binary mask to more advanced ones built on gaussian mixture model assuming that the signal in each voxel is a linear combination of signals from adjacent regions (Lévy et al., 2015).

Alternative approaches to the dMRI atlas-based analysis are tractography (Budzik et al., 2011; Cui et al., 2015; McLachlin et al., 2021), utilizing of manually drawn ROIs (Maki et al., 2018, 2016; Wang et al., 2017), or usage of tract-based spatial statistics approach (Dostál et al., 2020). However, tractography can suffer from inaccuracies caused by severe compression and manually defined ROIs are prone to user bias and take time to draw; thus atlas-based approach is currently preferred (Cohen-Adad, 2018; Cohen-Adad and Wheeler-Kingshott, 2014).

1.5.2.3 Between-subject variation

Since SC shape and length is variable between subjects due to anatomical and biological factors such as age, sex, height or weight, qMRI and morphometric metrics might suffer from inter-subject variability related to these factors (Bédard and Cohen-Adad, 2021; Kovalova et al., 2016; Martin et al., 2017a; Papinutto et al., 2020). Thus, normalization of extracted qMRI metrics (including dMRI) or statistical models adjusted for anatomical and biological factors are commonly employed (Bédard and Cohen-Adad, 2021; Kovalova et al., 2016; Martin et al., 2018a, 2017a).

1.5.3 Conventional MRI in the spinal cord compression

Conventional, also referred as a structural, MRI includes T_1-w, T_2-w, T_2*-w images and is used in clinical routine to depict macrostructural information about the SC structure and to assess the severity of compression and SC atrophy.

Conventional clinical MRI sequences acquired in sagittal orientation are primarily used to evaluate signal abnormalities of SC, such as the presence of T_2-w hyperintensities and T_1-w hypointensities (Nouri et al., 2017). Although the subjectively-evaluated presence of T2-w hyperintensities does not necessarily correspond with the clinical DCM signs and symptoms, it is still considered an important factor influencing decision-making for decompressive surgery (Wilson et al., 2013). Intramedullary T_2-w hyperintensities have, indeed, been reported in 58-85% of patients with clinically manifest DCM (Nouri et al., 2016), whereas in wide range of NMDC patients (2.3%–24.6%) (Bednarik et al., 2008; Kadanka et al., 2017; Kato et al., 2012; Kovalova et al., 2016). T_1-w hypointensities are associated with permanent SC injury (Nouri et al., 2017) and are relatively rare, occurring in 19-30 % of DCM patients (Martin et al., 2022); thus they predictive value in NMDC patients is limited.

In addition to the conventional clinical description of signal changes, T_1-w, T_2-w and T_2*-w images with sufficient axial in-plane resolution (usually 3D isotropic or 2D axial sequences) and good contrast between SC and cerebrospinal fluid (CSF) are used for computation of morphometric metrics reflecting the compression severity. The degree of SC compression at maximally compressed level (MCL) can be assessed by the cross-sectional area (CSA) (i.e., area of the SC in axial plane) and the compression ratio (CR) (i.e., ratio between the anteroposterior diameter and the transverse diameter) (Figure 11), which were reported as potential predictors of DCM development (Badhiwala et al., 2020; Bednarik et al., 2008; Kadanka et al., 2017; Kovalova et al., 2016). Radiological severity of the compression can be then established and compression can be classified as mild (i.e., compression ratio ≥0.4 or CSA ≥70.1 mm^2) or severe (i.e., compression ratio <0.4 and CSA <70.1 mm^2) (Kadanka et al., 2017).

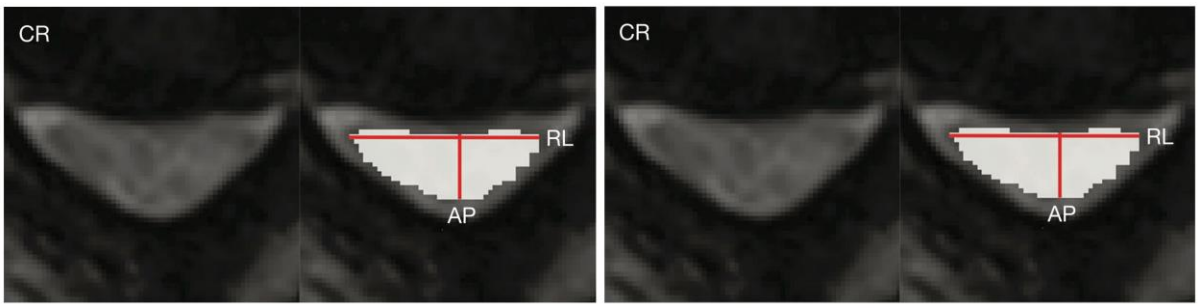

Figure 11 – Morphometric metrics assessing compression severity. The left panel depicts compression ratio (CR) calculated as a ratio between anteroposterior (AP) and transverse (RL) diameters, and the right panel illustrates cross-sectional area (CSA) calculated as an area of the spinal cord in axial plane. Adapted from (Horáková et al., 2022).

As opposed to CR and CSA assessing the compression severity in the single axial slice, volumetry analysis covering whole vertebral levels can be employed. Volumetry analysis is usually performed above the compression levels (e.g., levels C2 and/or C3). To date, studies reported gradual reduction of SC, WM and GM volumes at C2/3 above the compression level in DCM patients relative to HC (David et al., 2022; Grabher et al., 2017, 2016; Horak et al., 2021; Vallotton et al., 2021) and similar changes were reported in DCM patients also caudally at T11-L1 level (David et al., 2022).

1.5.4 Diffusion MRI in the spinal cord compression

This chapter is partly based on the narrative review (Valošek et al., 2022) and discusses current dMRI studies comprising patients in different stages of SC compression (i.e., both NMDC and DCM patients).

1.5.4.1 Diffusion tensor imaging model

Generally, the most commonly used diffusion model in the SC research is the DTI model (David et al., 2019; Martin et al., 2016; Mori and Tournier, 2014). Multiple studies (Banaszek et al., 2014; Budzik et al., 2011; Cui et al., 2015; Ellingson et al., 2014; Guan et al., 2015; Jones et al., 2013; Kerkovský et al., 2012; Keřkovský et al., 2017; Lee et al., 2011; Maki et al., 2016, 2018; Mamata et al., 2005; Martin et al., 2018b; Nouri et al., 2016; Okita et al., 2018; Rajasekaran et al., 2014; Rao et al., 2018; Seif et al., 2020; Uda et al., 2013; Vallotton et al., 2021; Wang et al., 2017; Wen et al., 2014b, 2014a; Zhang et al., 2022) and reviews (Ellingson et al., 2015b; Guan et al., 2015) covered DTI in symptomatic DCM patients, whereas a limited number of works comprised also NMDC patients (Ellingson et al., 2018; Kadanka et al., 2017; Kerkovský et al., 2012; Keřkovský et al., 2017; Martin et al., 2018a). As outlined in Chapter 1.3 and Table 1, DTI studies in NMDC patients have also suffered from a lack of nomenclature and inclusion criteria. Some studies indeed included only NMDC subjects without any symptoms (Martin et al., 2018a), while others also incorporated those with radiculopathy (Kerkovský et al., 2012; Keřkovský et al., 2017). One of the first 1.5T studies in NMDC patients compared DTI metrics from a single region of interest (ROI) from the entire axial SC of 13 HC with 20 DCM patients (mJOA < 18) and 32 NMDC patients with cervical pain and/or radiculopathy without symptoms/signs of myelopathy (mJOA = 18) and detected lower FA and higher MD at MCL in DCM patients compared to NMDC patients, with lower FA and no significant MD deficits

between NMDC patients and HC (Kerkovský et al., 2012). Conclusions between NMDC and DCM patients were confirmed in a second study (Keřkovský et al., 2017) on a group of 37 DCM patients, 93 NMDC patients and 71 HC with the same inclusion/exclusion criteria, although no comparison between NMDC patients and HC was provided. In fact, a single ROI that covers the SC confounds WM and GM, and it is thus unclear whether was decreased FA caused by a higher proportion of GM with naturally lower FA compared to WM or by actual WM damage. The first 3T DTI study (Martin et al., 2018a) on 20 HC and 20 NMDC patients without any neurological symptoms and signs (mJOA = 18) excluded also those with radiculopathy, detected lower FA in the entire axial SC at MCL in NMDC patients relative to HC, and corroborated the 1.5T study (Kerkovský et al., 2012), while it utilized slightly distinct inclusion criteria than the Czech studies (Kerkovský et al., 2012; Keřkovský et al., 2017). A potential bias from WM and GM mixing was further mitigated by additional column-specific analysis that detected decreased FA in the ventral columns of NMDC patients (Martin et al., 2018a). Lower FA and higher RD at MCL in lateral corticospinal tracts were also found in 16 DCM patients with clinical DCM symptoms without evidence of SC damage on T_2-w images compared to 20 controls at 1.5T (Lindberg et al., 2016), while no changes were demonstrated in the remaining medial SC part confirming post-mortem studies (Badhiwala et al., 2020; Mair and Druckman, 1953) when delineated demyelination in dorsal and lateral WM tracts.

1.5.4.2 Higher-order models

So far, degenerative cervical SC compression studies utilizing higher-order diffusion models have comprised mainly DCM patients (Hori et al., 2018, 2014, 2012; Iwama et al., 2020; Okita et al., 2018; Zhang et al., 2022) and only two recent works from our group utilizing multi-compartment ball-and-sticks model also included NMDC patients (Labounek et al., 2020; Valošek et al., 2021). These two works are detailly elaborated on in further parts of the thesis.

Three-compartment NODDI model was utilized alongside DTI in two retrospective studies (Iwama et al., 2020; Okita et al., 2018) to monitor surgical outcome in DCM patients and showed increased FA at MCL two weeks after surgery and increased intracellular volume fraction at MCL six months after surgery (Iwama et al., 2020; Okita et al., 2018). Authors concluded that findings indicate that neurite density damage in DCM patients might not be irreversible (Iwama et al., 2020). Other studies utilized DKI and QSI in DCM patients (Hori et al., 2014, 2012), and a concurrent DTI, NODDI and DKI study showed lower FA and DKI-FA, and

higher DKI-MD, isotropic CSF volume fraction, and orientation dispersion index from the entire axial SC ROI at MCL in 48 DCM patients (mJOA < 18) relative to 36 HC (Zhang et al., 2022).

1.5.5 Other quantitative MRI methods in the spinal cord compression

This chapter briefly discusses another quantitative MRI methods used for imaging of patients with degenerative cervical SC compression. Complete comprehensive overview is provided in the narrative review (Valošek et al., 2022).

Magnetization transfer (MT) imaging is based on the exchange of magnetization between protons associated with free water and those linked with immobile macromolecules such as proteins and lipids, which in turn causes measurable MRI signal attenuation and provides MT ratio (MTR) and MT saturation markers (Cohen-Adad and Wheeler-Kingshott, 2014; Helms et al., 2008). The study from (Martin et al., 2018a) reported decreased MTR extracted from the entire axial SC ROI in 20 NMDC subjects compared to 20 HC above the compression (C1-C3) but not at MCL; and additional column-specific analysis corroborated demonstrated decreased MTR in ventral columns of NMDC subjects relative to HC (Martin et al., 2018a). A combination of MT imaging and dMRI was used to calculate myelin water fraction, and axon volume fraction in 24 DCM patients compared to 5 HC and reported changes in axon volume fraction between groups in fasciculus gracilis, fasciculus cuneatus, and lateral corticospinal tract (Hori et al., 2018). The MTR together with FA, CSA, and T2* WM/GM ratio were reported as useful measures within a composite score and identified worsening in 11 of 26 DCM patients (Martin et al., 2018b). Another work then showed the predictive value of a combination of the preoperative magnetization transfer ratio and shape SC analysis for surgery response and recovery in DCM patients (Paliwal et al., 2020)

Single voxel proton magnetic resonance spectroscopy (^{1}H-MRS) quantifies the neurochemical profile within the spectroscopic volume of interest and provides information about neurochemical composition of the neural tissue otherwise inaccessible with conventional imaging methods (Öz et al., 2014). Studies in DCM exploring above the compression level reported increased levels of total creatine (tCr)/total N-acetylaspartate (tNAA) (Aleksanderek et al., 2017a, 2017b; Ellingson et al., 2015a; Holly et al., 2017) and total choline (tCho)/tNAA (Ellingson et al., 2015a; Holly et al., 2017; Salamon et al., 2013). Recent ^{1}H-MRS study from our group in 60 NMDC patients with or without electrophysiological changes and radiculopathy

but without myelopathic symptoms (mJOA scale =18) showed, for the first time, increased tCr/tNAA and myo-inositol/tNAA ratios above the stenosis level in NMDC relative to HC pointing to neurochemical changes detectable in clinically silent subjects (Horak et al., 2021).

T1 relaxometry, sensitive to myelination (Cohen-Adad, 2018), provided, so far, contradictory outcomes when 1.5T study detected lower T1 times in 31 DCM patients at compression levels compared to non-stenotic levels above and below (Maier et al., 2020), but 3T study showed higher T1 times at compression levels in 22 DCM patients compared to 10 HC (Baucher et al., 2021). These opposite trends must be further explored with a need for harmonization of field strengths, imaging protocols, and inclusion criteria. Recently, the multicomponent driven equilibrium steady-state observation of T1 and T2 approach utilizing three sequences for estimation of both T1 and T2 times and myelin water fraction was applied in 28 HC to provide myelin imaging atlas and framework for future studies (Dvorak et al., 2021).

To date, functional MRI measuring oscillations in neuronal activity revealed mainly secondary cortical changes in DCM patients (Bernabéu-Sanz et al., 2020; Cronin et al., 2021; Duggal et al., 2010; Tan et al., 2015), and only single SC fMRI report showed neuronal activity changes in GM horns in 18 DCM patients relative to 25 HC and association of severity of myelopathy with neuronal activity response (Liu et al., 2016).

Finally, a 3T study employing perfusion weighted imaging in 22 patients with cervical spondylosis with or without myelopathy identified a relationship between perfusion markers and anteroposterior SC diameter and mJOA scale and suggested that the degree of ischemia and hypoxia correlates with compression severity and clinical status, respectively (Ellingson et al., 2019).

1.6 Predictors of progression from non-myelopathic compression

Although DCM studies consistently reported correlations between functional impairment assessed by clinical scores such as mJOA scale and markers derived from dMRI (Ellingson et al., 2018; Maki et al., 2016; Zhang et al., 2022) and MRS (Holly et al., 2017; Horak et al., 2021; Salamon et al., 2013), the usage of these scores in NMDC patients is limited since NMDC patients are usually asymptomatic and thus without clinical deficits (Table 1).

The presence of electrophysiological abnormalities together with clinical signs of cervical radiculopathy were reported as predictors of early progression of NMDC to DCM (Bednarik et

al., 2008) and are reflected in the current clinical guidelines on practical management of NMDC patients (Fehlings et al., 2017). Indeed, prolonged SEP and MEP were present in a higher percentage of NMDC patients with radiculopathy who developed myelopathy (43.8% and 37.5%, respectively) than those who did not (16.4% and 16.9%, respectively) (Fehlings et al., 2017).

Although diffusion MRI proved its sensibility to microstructural changes across various diseases (see for example comprehensive review from (Martin et al., 2016)) as well as in DCM patients (Ellingson et al., 2015b; Guan et al., 2015), there are only sparse reports, which were exploring the potential of dMRI to mirror electrophysiological findings. One of the first study focused on relationship between dMRI-derived metrics and electrophysiological abnormalities, however, did not found significant differences in FA and MD DTI metrics for subsets of compressed patients with and without electrophysiological abnormality (Kerkovský et al., 2012). The longitudinal study from (Kadanka et al., 2017) in 112 NMDC patients then did not show any predictive power of DTI metrics (i.e., did not detect any significant difference in FA and MD metrics between NMDC patients with and without electrophysiological abnormality). Importantly to note, both studies utilized 1.5T scanners, single shell diffusion protocols and extracted dMRI metrics from entire axial SC ROI, which is tissue non-specific, and thus subtle changes at the level of individual WM tracts could have been confounded. Indeed, a few recent tract-specific reports found relationship between qMRI metrics from dorsal columns and SEP abnormalities (Liu et al., 2017; Wen et al., 2014b).

In summary, despite the extensive methodological work in recent years, progress in dMRI acquisitions and advent of spinal cord template and probabilistic atlas that provide an opportunity for reliable tract-specific analysis, to date, dMRI studies are not consistent in conclusions regarding the relationship between electrophysiological measures and dMRI-derived metrics, and no work has confirmed dMRI as a predictor of DCM development.

2 AIMS OF THE THESIS

The aim of this PhD thesis was to evaluate if combination of high-resolution multi-shell dMRI and tract-specific atlas-based analysis is sensitive to microstructural alternations in different stages of degenerative spinal cord compression and thus if dMRI-derived biomarkers could serve as potential predictor of NMDC patients with a higher risk of progression to irreversible DCM. To this end, the following objectives of the thesis were formulated:

1. Study I (dMRI methodology)
   - To investigate if optimized multi-shell diffusion protocol with reduced field-of-view utilizing inner volume excitation is clinically applicable, not affected by imaging artifacts, and able to provide dMRI-derived metrics sensitive to early microstructural changes in NMDC patients.
   - To explore if multi-shell diffusion data together with multi-compartment ball-and-sticks model can reveal crossing white matter fibers.
2. Study II (Prospective dMRI study)
   - To utilize the state-of-the-art SC MRI data acquisition and data processing including spatially selective (i.e., tract-specific) analysis to detect dMRI-derived microstructural changes on a large cohort of NMDC and DCM patients relative to healthy controls.
   - To explore if degenerative SC compression causes also secondary changes such as Wallerian degeneration, trans-synaptic degeneration and atrophy rostrally to the compression levels.
   - To study the relationship between functional impairments measured by electrophysiological measures (i.e., MEP, SEP and EMG) and microstructural changes revealed by dMRI from corresponding tracts.

3 MATERIALS AND METHODS

3.1 Study design

Studies conducted within this thesis are either a methodological or a prospective cohort study in a group of NMDC patients, DCM patients and healthy volunteers with the aim to disclose pathophysiology and improve diagnosis and clinical management of degenerative cervical SC compression utilizing advanced magnetic resonance techniques. Studies were carried out in accordance with World Medical Association Declaring of Helsinki and all participants signed an informed consent approved by local ethics committee of *University Hospital Brno (Brno, Czech Republic)* number EKV-2017-055 prior to their inclusion in the study.

3.2 Participants

The study participants were NMDC, and DCM patients recruited from the database of a spinal center of a tertiary university hospital (University Hospital Brno, Brno, Czech Republic). Healthy controls (HC) were required to frequency match the age and sex of participants with compression and had to be physically healthy with no history of any neurological or other somatic disorder. Additionally, in the Study I, young healthy volunteers were required to participate in between-session (test-retest) reproducibility of dMRI protocols.

3.3 Radiological evaluation

NMDC and DCM patients, and age-comparable HC underwent routine clinical MRI examination on a 1.5 T Philips Ingenia scanner (Philips, Best, The Netherlands) to evaluate radiological signs of degenerative compression and estimate MCL, CSA, and CR. Possible radiological signs of myelopathy (i.e., T_2-w hyperintensity) were evaluated in DCM patients. Two experienced radiologists performed analysis of the clinical MRI data. The imaging criteria for SC compression were defined as a change in SC contour or shape at the intervertebral disc level on axial MRI scan compared to the midpoint level of neighboring vertebrae (Bednarik et al., 2008; Kadanka et al., 2017). The SC contour was manually segmented in IntelliSpace Portal Concerto v10.1 software (Philips, Best, The Netherlands), and CSA and CR were calculated. In patients with multilevel compression, the MCL corresponded to the compressed level with the lowest CR. Subgroups of patients with mild and severe compression were defined based on the previous

work as (Kadanka et al., 2017): mild compression (CR ≥ 0.4 or CSA ≥ 70.1 mm^2), severe compression (CR < 0.4 and CSA < 70.1 mm^2).

3.4 Clinical evaluation

A detailed clinical examination was carried out at the beginning of the study and performed by a neurologist highly experienced in the diagnosis and the practical management of myelopathic cases. Diagnosis of DCM was based on the presence of at least one symptom and one sign of DCM (in addition to MRI signs of cervical cord compression) specified in the following paragraphs (Bednarik et al., 2008). The degree of disability and functional impairment was scored on the mJOA scale (3–18 points) (Tetreault et al., 2017).

3.4.1 DCM symptoms

The following symptoms were considered for DCM diagnosis: gait disturbance, numb and/or clumsy hands, Lhermitte's phenomenon, bilateral arm paresthesia, weakness of lower or upper extremities, urinary urgency, frequency, or incontinence.

3.4.2 DCM signs

The following signs were considered for DCM diagnosis: corticospinal tract signs, hyperreflexia/clonus, spasticity, pyramidal signs (Babinski's or Hoffman's sign), spastic paresis of any of the extremities (most frequently lower spastic paraparesis), flaccid paresis of one or two upper extremities in plurisegmental, distribution, atrophy of hand muscles, sensory involvement of various distributions in upper or lower extremities, (always plurisegmental), gait ataxia with positive Romberg sign.

3.5 Electrophysiological measures

Further, to reveal functional abnormalities, NMDC and DCM patients underwent electrophysiological examination, performed by a neurology specialist, to detect abnormalities of dorsal columns and/or dorsal gray matter (GM) horns (i.e., somatosensory evoked potentials, SEP), dysfunction in lateral columns (i.e., motor evoked potentials, MEP) and lesions of ventral GM horns (i.e., electromyography, EMG) as described previously in (Bednarik et al., 2008; Bednařík et al., 1998). For the assessment of SEP, MEP and EMG recording, normal data obtained by examination of the control group were used (Bednařík et al., 1999).

3.5.1 Somatosensory evoked potentials

Short-latency SEP from the median (SEP MED) and the tibial nerves (SEP TIB) were elicited by electrical stimulation of the mixed nerves at the wrist and the ankle, respectively, and recorded using a four-channel Nicolet Natus electrodiagnostic unit (Natus Medical Inc., San Carlos, CA). Central conduction abnormality attributed to possible cervical SC lesion was defined as follows. SEP MED: absent N13, P14, and/or N20 waves, and/or abnormal N13-N20 interpeak latency, and/or abnormal P9/N13 amplitude ratio, all with normal N9 wave. SEP TIB: absent P40 wave, and/or abnormal N22-P40 interpeak latency, all with normal N22. SEP abnormality was then defined as a presence of any abnormality in SEP MED and/or SEP TIB.

3.5.2 Motor evoked potentials

MEPs were elicited by means of transcranial and root magnetic stimulation (Magstim 200 magnetic stimulator, Magstim Company Ltd., Spring Gardens, Wales, UK and a circular, 90 mm (Type 9784) stimulating coil with a peak magnetic field strength of 2.0 T) and recorded using a Keypoint electromyograph (Dantec, Skovlunde, Denmark) from the abductor digiti minimi (UMEP) and abductor hallucis muscles (LMEP) on both sides, with surface electrodes placed on the belly and the tendon of the muscles. Central conduction abnormality attributed to possible cervical SC lesion was defined as an abnormal central motor conduction time (CMCT) and/or abnormal MEP/CMAP (compound muscle action potential) amplitude ratio and was considered as a MEP abnormality.

3.5.3 Electromyography

EMG examination was performed using a Keypoint electromyograph (Dantec, Skovlunde, Denmark). Motor and sensory conduction measures were performed on six motor nerves (median, ulnar, and tibial nerves bilaterally) and four sensory nerves (ulnar and sural bilaterally). Needle EMG from four muscle bilaterally (deltoid, biceps brachii, triceps brachii, and first dorsal interosseous) was performed, with particular attention to spontaneous activity, motor unit action potential (MUP/MUAP) parameters, and interference patters. EMG signs of acute motor axonal neuropathy in one myotome (C5-Th1) corresponding with radicular signs and symptoms were classified as radicular. EMG signs of acute, subacute, or chronic motor axonal neuropathy confirmed in more than one myotome (C5-Th1) unilaterally or bilaterally

were classifies as sings of anterior horn cell lesion resulting from DCM and were considered as an EMG abnormality.

3.6 3T MRI acquisition protocol

All participants were scanned on a 3 T Siemens Prisma scanner (Siemens Healthcare, Erlangen, Germany) using 64-channel head/neck and 32-channel coils between October 2017 and August 2020. Seven young healthy volunteers enrolled in the Study I were scanned twice with a mean ± SD inter-scan interval 7 ± 11 weeks in order to evaluate between-session (test-retest) reproducibility of dMRI protocols. Lordosis, which could introduce a partial volume effect from the surrounding CSF and negatively influence field homogeneity, was minimized by keeping the SC as straight as possible. The acquisition protocol was partly inspired by the *spine generic* consensus acquisition protocol (Cohen-Adad et al., 2021b), which however was not finalized at the time of beginning of this study. The final protocol contained high resolution structural turbo spin echo (TSE) T_1-w axial, TSE T_2-w sagittal, multi-echo gradient echo (ME-GRE) T_2*-w axial images, and multi-shell diffusion protocol with reduced field of view (so-called HARDI-ZOOMit) with a voxel size 0.65 × 0.65 × 3 mm^3 after interpolation in Fourier domain. Additionally, in the Study I, non-interpolated version of the HARDI-ZOOMit protocol (with voxel size 1.3 × 1.3 × 3 mm^3), and clinically used single-shell readout-segmented diffusion protocol (so-called DTI-RESOLVE) were acquired for a comparison with the interpolated HARDI-ZOOMit protocol. Detailed parameters for all sequences are listed in the Table 2.

Table 2 – Detailed sequence parameters and their intended purpose.

Sequence	Parameters	Purpose
T_1-weighted (axial)	Turbo spin echo 42 contiguous slices TR = 763.0ms TE = 9.7ms FOV = 180 × 180 mm matrix size = 256 × 256 (interpolated: 512 × 512) voxel = 0.70 × 0.70 × 2.5 mm^3 (interpolated: 0.35 × 0.35 × 2.5 mm^3) TA = 8:28	High WM/GM contrast suitable for GM segmentation High in-plane resolution and good SC/CSF contrast suitable for SC segmentation and volumetry analysis
T_2-weighted (sagittal)	Turbo spin echo 30 contiguous slices TR = 8640.0ms TE = 98.0ms FOV = 250 × 250 mm matrix size = 448 × 448 (interpolated: 896 × 896) voxel = 0.56 × 0.56 × 1.3 mm^3 (0.28 × 0.28 × 1.3 mm^3) TA = 8:49	High spatial resolution and large spatial coverage in sagittal plane suitable for spinal cord labeling and template registration
T_2*-weighted (axial)	Multi-echo gradient echo (Siemens's MEDIC) 42 contiguous slices TR = 778.0ms TE = 17.0ms (4 echoes) 2 averages FOV = 180 × 180 mm matrix size = 256 × 256 (interpolated: 512 × 512) voxel = 0.70 × 0.70 × 2.5 mm^3 (interpolated: 0.35 × 0.35 × 2.5 mm^3) TA = 7:51	High WM/GM contrast suitable for GM segmentation High in-plane resolution and good SC/CSF contrast suitable for SC segmentation and volumetry analysis
HARDI-ZOOMit	Reduced field-of-view (Siemens ZOOMit) 35 contiguous slices Anterior-posterior phase encoding: 42 b-values = 1000 $s.mm^{-2}$, 24 b-values = 550 $s.mm^{-2}$, 7 b_0 Posterior-anterior phase encoding: 5 b_0 TR = 6700ms TE = 73ms FOV = 44 × 129 mm matrix size = 34 × 100 (interpolated: 68 × 200) voxel = 1.3 × 1.3 × 3.0 mm^3 (interpolated: 0.65 × 0.65 × 3.0 mm^3) Total TA = 12:46	Sensitivity to microstructural changes such as demyelination or axonal degeneration
DTI-RESOLVE	Readout-segmented EPI (Siemens RESOLVE) 30 contiguous slices Anterior-posterior phase encoding: 30 b-values = 650 $s.mm^{-2}$, 5 b_0 Posterior-anterior phase encoding: 30 b-values = 650 $s.mm^{-2}$, 5 b_0 TR = 4500ms TE1 = 50ms TE2 = 77ms FOV = 74 × 132 mm Matrix size = 66 × 118 Voxel = 1.1 × 1.1 × 3.3 mm^3 Total TA = 16:16	Sensitivity to microstructural changes such as demyelination or axonal degeneration

Structural T_1-w axial and ME-GRE T2*-w axial images were acquired to cover the C3-C7 vertebral levels with 42 contiguous slices with slice thickness 2.5 mm. Both sequences had a voxel size 0.35 × 0.35 × 2.5 mm^3 after interpolation in Fourier domain. Structural T_2-w sagittal image covered the whole cervical SC and part of the thoracic SC (i.e., from C1 to Th1-Th3 based on subject proportion).

Both interpolated and non-interpolated HARDI-ZOOMit protocols were acquired to cover C3-C7 vertebral levels. Sixty-three diffusion-weighted images were acquired with anterior-posterior (AP) phase encoding on two b-values (forty two gradient directions with b-value = 1000 $s.mm^{-2}$ and twenty four gradient directions with b-value = 550 $s.mm^{-2}$, Figure 12) together with seven images with b-value = 0 $s.mm^{-2}$ (so-called b_0 images). Additionally, five images with opposite phase encoding, i.e., posterior-anterior (PA), with b-value = 0 $s.mm^{-2}$ were collected. Single-shell DTI-RESOLVE protocol covered the same C3-C7 vertebral levels area and consisted of two identical sequences with opposite phase encodings (AP and PA). For each phase encoding, thirty diffusion-weighted images with b-value = 650 $s.mm^{-2}$ and five images with b-value = 0 $s.mm^{-2}$ were collected.

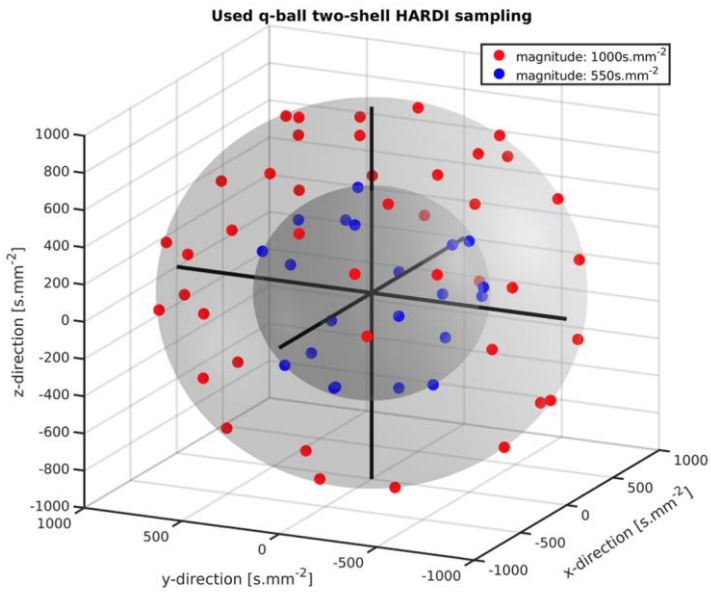

Figure 12 – Visualization of HARDI-ZOOMit sampling scheme. Sixty-three unique diffusion gradients are uniformly sampled over two spherical shells with b-values = 550 $s.mm^{-2}$ and 1000 $s.mm^{-2}$. Adapted from (Labounek et al., 2020).

3.7 3T MRI data analysis

The acquired 3.0 T MRI data were processed by the same processing tools for Study I and Study II. Specifically, using Spinal Cord Toolbox (SCT) v3.2.3 (De Leener et al., 2017), Advanced Normalization Tools (ANTs) v2.1.0 (Avants et al., 2011), FMRIB Software Library (FSL) v5.0.10 (Jenkinson et al., 2012), and in-house made scripts written in bash and MATLAB (MathWorks, Natick, USA).

Preprocessing of the anatomical images was same for both studies and a common processing pipeline is thus described in the following paragraph. Considering a different character of studies, when Study I focused on comparison of three different dMRI protocols, while Study II covered tissue-specific analysis of dMRI metrics on a larger cohort, diffusion preprocessing is described for each study separately.

3.7.1 Processing of anatomical data (same for both studies)

T_2-w sagittal and T_2*-w axial images were thresholded to remove areas outside the body and N4 bias-field correction (Tustison et al., 2011) was performed for both scans. T_2*-w axial data acquired in inter-leaved mode was slice-by-slice corrected with in-house script utilizing affine registration and additive fusion (Jan, 2005) for even and odd slices. T_2-w sagittal image was resampled to voxel size 0.28 × 0.35 × 0.28 mm^3 (to match in-plane resolution of T_2*-w axial image), cropped to cover only a cervical SC area, the SC was segmented using *sct_deepseg_sc* algorithm based on convolution neural network (Gros et al., 2019), and SC vertebral labeling was performed by *sct_label_vertebrae* function (De Leener et al., 2015) with manual initialization of C2/3 vertebral disc. Then, T_2-w sagittal image was co-registered to the T_2*-w axial image using a series of ANTs registration algorithms implemented in *sct_register_multimodal* function (De Leener et al., 2015) to warp the SC segmentation and vertebral labeling into T_2*-w axial space. Finally, the SC was segmented for T_2*-w axial image, vertebral labeling was performed with initialization using warped T_2-w sagittal labeling, GM segmentation was utilized by *sct_deepseg_gm* function (Perone et al., 2018), and WM area was obtained by subtraction of the SC and WM segmentations. Segmentations and vertebral labeling were visually inspected and corrected if necessary.

Additionally, for the Study II, mean cross-sectional area (CSA) at the C3 level was calculated to quantify atrophy above the compression level from T_2*-w images using *sct_process_segmentation* function (De Leener et al., 2017).

3.7.2 Study I (dMRI methodology)

3.7.2.1 Processing of diffusion data

For the dMRI data, each diffusion protocol was processed separately, utilizing the same pipeline, as follows: susceptibility, motion and eddy currents artifacts were corrected by FSL's *topup* (Andersson et al., 2003) and *eddy* (Andersson and Sotiropoulos, 2016) functions, and DTI (Basser et al., 1994) and ball-and-sticks (Behrens et al., 2003) models were estimated using FSL. Next, fractional anisotropy (FA) and mean diffusivity (MD) maps, and two crossing fiber bundles with their partial volume fractions (f1, f2) along with single mean diffusivity values (d) maps were derived for DTI and ball-and-sticks model, respectively.

Corrected dMRI data (output from *eddy* function) were split into b_0 and DWI images (i.e., images with b-values > 0 $s.mm^{-2}$) to calculate mean b_0 and mean DWI images. Next, SC was automatically segmented using *sct_deepseg_sc* algorithm from the mean DWI image. Single-subject mean b_0 image was co-registered to the T_2*-w axial image utilizing the SC segmentations as masks to achieve maximum robustness (De Leener et al., 2015). Estimated warping field was consequently used for geometrical transformation of dMRI-derived metrics from diffusion space of each protocol into the T_2*-w axial space. Finally, two regions of interest (ROIs) covering WM and GM from C3-6 levels were defined to compare dMRI metrics among 4 subjects' groups (i.e., NMDC patients, DCM patients, HC and young healthy volunteers) and over 3 dMRI protocols.

3.7.2.2 dMRI protocol's signal-to-noise ratio estimation

For each of the three dMRI protocols (i.e., interpolated HARDI-ZOOMit, non-interpolated HARDI-ZOOMit and DTI-RESOLVE), SNR was estimated separately as follows. First, original 4D dMRI data without any preprocessing were split into DWI images and b_0 images, and mean DWI and b_0 images were calculated. The SC was automatically segmented using *sct_deepseg_sc* algorithm (Gros et al., 2019) from the mean DWI image. The first four and last four slices for each dMRI protocol were excluded due to potentially low signal at the borders of field-of-view. For multi-shell protocols (interpolated HARDI-ZOOMit and non-interpolated

HARDI-ZOOMit), DWI images for individual b-values (i.e., 550 s.mm^{-2} and 1000 s.mm^{-2}) were identified and mean signal inside the SC (I_{SC}) was calculated for each b-value. Tissue structures were thresholded out from the mean b_0 image for each dMRI protocol and noise standard deviation from the air (σ_{air}) was computed. The SNR was estimated by method optimized for two different ROIs (Dietrich et al., 2007):

$$SNR = \frac{I_{SC}}{\sqrt{\frac{2}{4-\pi}}\sigma_{air}} \tag{12}$$

Where I_{SC} stands for the mean signal inside the SC, σ_{air} denotes noise standard deviation from the air and the fraction in denominator represents Rayleigh distribution of background noise (Dietrich et al., 2007). Finally, group SNR medians, means and SDs were computed to evaluate the level of the noise of each b-value and each protocol.

3.7.2.3 Mutual information between dMRI metric and WM/GM

The T_2*-w axial image with high WM/GM contrast was semi-binarized in order to compute a mutual information (MI) with dMRI-derived metrics. The MI is a similarity criterion detecting increased magnitude for similar images with both linear and non-linear contrast transform functions (Jan, 2005; Maes et al., 1997). Considering a non-linear transform function between dMRI-derived maps (i.e., FA, f1, MD and d) and WM/GM structures in semi-binarized T_2*-w (background = 0, GM = 1 and WM = 2), non-normalized MI inside C3-6 area was calculated according to Equation (13) (Jan, 2005):

$$MI = E_a + E_b - E_{ab} = -\sum_{m=1}^{q} s(a_m)\log\big(s(a_m)\big) - \sum_{n=1}^{r} u(b_n)\log\big(u(b_n)\big) + \sum_{m=1}^{q}\sum_{n=1}^{r} v(a_m, b_n)\log(v((a_m, b_n)) \tag{13}$$

Where *a* denotes individual dMRI-derived maps, *b* individual structures of semi-binarized T_2*-w axial image, E_a the entropy of the image *a*, E_b the entropy of the image *b*, and E_{ab} the joint entropy between images *a* and *b*. Function *s(a)* is the histogram of image *a* with intensity indexes from 1 to *q*, function *u(b)* is the histogram of the image *b* with intensity indexes from 1 to *r*, and function *v(a,b)* is the joint histogram between images *a* and *b*.

3.7.2.4 Statistical analysis

Statistical testing was performed by SPSS v23 (IBM, Armonk, New York) and MATLAB (MathWorks, Natick, USA).

For each subject and each dMRI-derived metric, mean, median, SD, skewness and kurtosis were evaluated within WM and GM from the C3-6 area, together with gradient between WM and GM (i.e., differences between means and medians in the WM and GM) resulting in overall 48 descriptive statistics parameters for each dMRI protocol.

Due to non-Gaussian distribution of many dMRI-derived metrics, smooth probability density function was fitted using MATLAB's *fitdist* function and mean probability density functions with Q1 – Q3 confidence intervals (Q – quartile) were computed for each group and each dMRI protocol. Then, a heuristic parameter (H) which may distinguish NMDC patients and HC were proposed as Equation (14):

$$H_x = \int_{x_1}^{x_2} g(x)dx \tag{14}$$

Where H is the heuristic parameter, and x_1 and x_2 are marginal values of a dMRI-derived metric (x).

For each dMRI protocol separately, Wilcoxon rank-sum tests with Bonferroni correction were used for between-group comparison of the 48 descriptive statistics parameters as well as the heuristic parameters. To minimize the effect of age, post-hoc analysis of covariance (ANCOVA) was used as an additional test between HC and NMDC patients with age as a covariate. Effect of radiculopathy was evaluated by post-hoc Wilcoxon rank-sum test between NMDC patients with and without radiculopathy. Significance level for post-hoc analysis was set to $p < .05$.

Linear dependency between dMRI-derived metrics, which demonstrated significant between-group differences, was evaluated by cross-subject Pearson correlation coefficients. Unique dMRI-derived metrics that maximize difference between HC and NMDC patients were identified using stepwise linear regression as Equation (15):

$$Y = \beta_0 + X\beta + \epsilon \tag{15}$$

Where *Y* is a vector equal to 0.5 for HC and -0.5 for NMDC patients, *X* is a model matrix containing dMRI-derived metrics, which demonstrated significant between-group differences, and age. Pearson correlation coefficient (r) between Y and predicted signal ($Y_p = X\beta$) were then computed for best model fit for each dMRI protocol.

Finally, the significant dMRI-derived metrics from stepwise linear regression were used as an input feature matrix into k-means clustering, which automatically assigned dMRI metrics into 2 classes (i.e., HC and NMDC patients). Sensitivity and specificity of each dMRI protocol was then evaluated by comparison of the k-means clustering output with classification performed by experienced radiologist and neurologist.

3.7.2.5 Level of susceptibility artifacts

To evaluate the level of susceptibility distortions caused by spin-echo EPI among individual dMRI protocols, single-subject mean, median, and SD of absolute off-resonance fields (output of FSL's *topup* function (Andersson et al., 2003)) were estimated. Three different ROIs were defined based on the SC segmentation and vertebral labeling, namely: C3-6 area, C3 area characterizing cervical SC region without compression, and C5-6 area characterizing region with compression in NMDC patients. Between-group differences were tested by Wilcoxon rank-sum test. Correlation with dMRI-derived metrics, which demonstrated significant between-group differences, was evaluated using cross-subject Pearson correlation to examine the effect of susceptibility distortions on dMRI-derived metrics.

3.7.2.6 Reproducibility of dMRI protocols

Between-session reproducibility was tested in a group of seven young healthy volunteers who were scanned twice. Mean coefficients of variation (CoV) were calculated for dMRI metrics' means and medians from the WM and GM from C3-6 area. For dMRI-derived metrics, which demonstrated significant between-group differences, absolute differences between consecutive measurements (i.e., test-retest) were calculated. Finally, normalization to range 0–1 was utilized on variable's differences and Wilcoxon signed-ranks tests with Bonferroni correction were used for a dMRI protocol comparison.

3.7.3 Study II (Prospective dMRI study)

3.7.3.1 Processing of diffusion data

Interpolated HARDI-ZOOMit protocol was corrected for susceptibility, motion and eddy current artifacts using FSL's *topup* (Andersson et al., 2003) and *eddy* (Andersson and Sotiropoulos, 2016) functions. Corrected dMRI data were split into b_0 and DWI images, and mean DWI image was calculated to automatically segment SC using *sct_deepseg_sc* algorithm. Next, the PAM50 SC template (De Leener et al., 2018) was registered to DWI mean image using the initial transformation from the T_2*-w axial image and employing the SC segmentations to achieve maximal robustness in subjects with compression (De Leener et al., 2017). Finally, the probabilistic WM and GM atlas (Lévy et al., 2015) was warped into the diffusion space to allow tract-specific analysis.

DTI (Basser et al., 1994) and ball-and-sticks (Behrens et al., 2003) models were estimated using FSL to provide six diffusion metrics, namely, fractional anisotropy (FA), mean diffusivity (MD), axial diffusivity (AD) and radial diffusivity (RD) for the DTI model, and primary partial volume fraction (f1) along with single mean diffusivity (d) for the ball-and-sticks model.

3.7.3.2 Diffusion metric extraction

Diffusion metrics were extracted for each subject for several ROIs utilizing *sct_extract_metric* function (De Leener et al., 2017) with use of the *maximum a posteriori* method (De Leener et al., 2017; Lévy et al., 2015) to eliminate partial volume effect and variability in tract size. ROIs included ventral columns, lateral columns, dorsal columns, fasciculus gracilis, fasciculus cuneatus, lateral corticospinal tracts, spinal lemniscus (i.e., spinothalamic and spinoreticular tracts), the whole GM, dorsal GM horns and ventral GM horns (Figure 13a). Diffusion metrics for individual ROIs were averaged from the whole C3-6 area and from C3 above the compression vertebral level (Figure 13b).

3.7.3.3 Statistical analysis

Statistical analysis was performed by SPSS v25 (IBM, Armonk, New York), MATLAB 2019b (MathWorks, Natick, USA) and Python 3.7.

Data normality was examined using the Shapiro-Wilk test. Between-group comparison of age, height, weight, body mass index (BMI), and CSA at C3 level were performed using the Kruskal-Wallis H test, and sex by the Fisher's exact test.

Diffusion-derived metrics from the C3-6 area and the C3 above the compression level (Figure 13b) were compared between groups per individual tracts and GM regions using ANCOVA with age and BMI as covariates using Tukey-Kramer post-hoc tests and Holm-Bonferroni multiple comparison correction.

Associations between dMRI-derived metrics from the C3-6 area and participants characteristics (i.e., age and BMI) in 60 HC were examined using the Spearman correlation. Associations between compression measures (i.e., CSA at MCL and CR at MCL) and dMRI-derived metrics from the C3-6 area and C3 level in NMDC and DCM patients together with the relationship between the degree of myelopathy (i.e., mJOA scale) and dMRI metrics in DCM patients were examined using the Spearman correlation.

3.7.3.4 Relationship between dMRI metrics and electrophysiological measures

Relationships between electrophysiological measures, reported as categorical variables (i.e., 0 – normal findings, 1 – abnormal findings) and dMRI-derived metrics, were quantified in NMDC and DCM patients by the Mann-Whitney rank tests with Holm-Bonferroni correction. MEPs were correlated to dMRI metrics from motor tracts, that is, lateral columns and lateral corticospinal tracts. SEPs were related with dMRI metrics from sensory tracts, that is, the dorsal column, fasciculus cuneatus, fasciculus gracilis, and dorsal GM horns. EMG was correlated with dMRI metrics from GM and ventral GM horns (Figure 13c).

Additionally, post-hoc correlation analysis between quantitative electrophysiological parameters and dMRI metrics was performed using Spearman correlation with Holm-Bonferroni correction in NMDC and DCM patients. Namely, between central sensory conduction times (CSCT), N20 wave and P40 wave obtained from median and tibial SEPs and dMRI metrics from dorsal columns. And similarly, between CMCT and cortical latencies obtained from upper and lower extremity MEP and dMRI metrics from lateral corticospinal tracts (both sides merged).

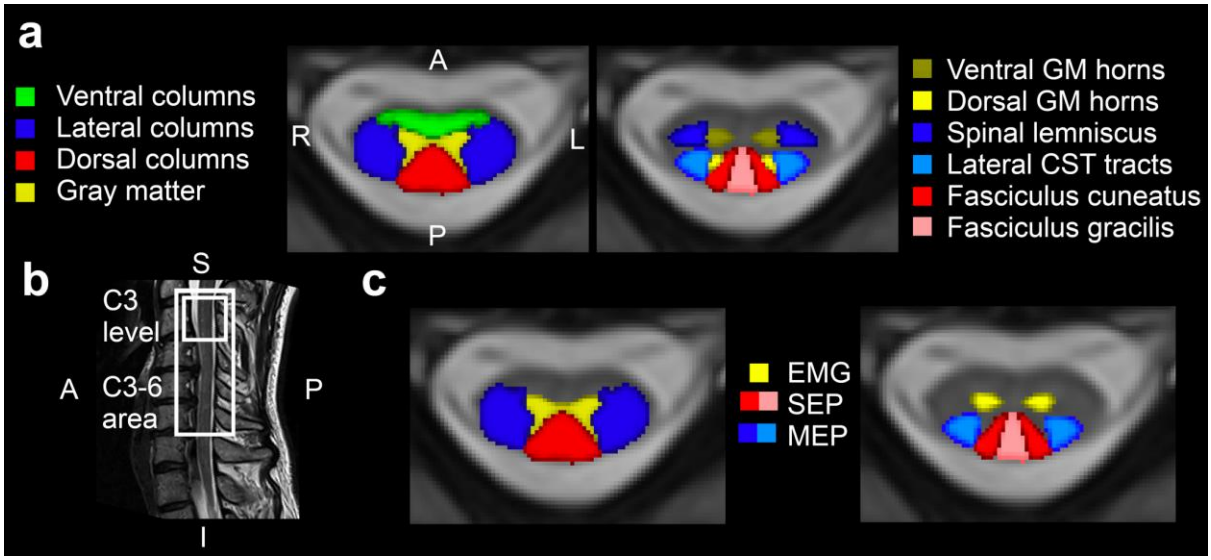

Figure 13 – Visualization of individual regions of interest (ROIs). (a) ROIs defined based on probabilistic PAM50 atlas used for extraction of diffusion metrics, (b) two analyzed areas – C3-6 area and the C3 above the compression level, (c) individual ROIs related to corresponding electrophysiological measures. EMG, electromyography; SEP, somatosensory evoked potentials; MEP, motor evoked potentials. Adapted from (Valošek et al., 2021).

4 RESULTS

4.1 Participant characteristics

4.1.1 Study I (dMRI methodology)

Thirty-three NMDC patients (14 females, 19 males, mean ± standard deviation (SD) age 56.7 ± 6.4 years), thirteen age-comparable healthy controls (9 females, 4 males, age 51.9 ± 9.4 years) and seven young healthy volunteers (3 females, 4 males, age 27.4 ± 1.7 year) were enrolled in the Study I. The radiological evaluation sub-divided NMDC patients into 18 patients with mild compression (7 females, 11 males, age 55.6 ± 6.1 years) and 15 patients with severe compression (7 females, 8 males, age 58.1 ± 6.8 years). Neurological examination confirmed no DCM symptoms in NMDC patients. A 13 from 33 NMDC patients showed clinical symptoms and/or signs of cervical monoradiculopathy manifesting mostly as a radicular pain, less frequently as a motor deficit in a corresponding myotome. Since two-sample t-test identified the probability of age difference between HC and NMDC patients at $p = 0.052$, and mild NMDC patients at $p = 0.195$, and severe NMDC patients at $p = 0.056$, the age and the effect of radiculopathy were considered in between-group comparison (details in Chapter 3.7.2.4).

4.1.2 Study II (Prospective dMRI study)

A total of 116 NMDC patients, 31 DCM patients and 64 HC were enrolled in the Study II (Figure 14). Thirteen NMDC, ten DCM and four HC were initially excluded due to the presence of motion artifacts, low contrast between SC and cerebrospinal fluid in T_2*-w axial images limiting proper SC segmentation, sub-optimal fat saturation, and/or dMRI signal dropouts caused by excessive cardiac pulsation. The final cohort consisted of 103 NMDC patients (59 females, 44 males, age 56.5 ± 9.8 years), 21 DCM patients (12 females, 9 males, age 58.2 ± 10.8 years) and 60 HC (38 females, 22 males, age 53.7 ± 8.7 years). Three DCM and thirteen NMDC patients from the final cohort did not agree with the electrophysiological examination.

Even though there were no statistically significant differences between groups in participants characteristics (i.e., age, height, weight, BMI and sex) (Table 3), correlation analysis revealed significant decrease of *f1*, FA, *d* and AD and increase of RD from the C3-6 area with age. Significant negative correlations were also found between BMI and FA, MD, AD and *d* diffusion

metrics. Thus, age and BMI were used as covariates to rule out their possible effects on dMRI metrics (details in Chapter 3.7.3.3).

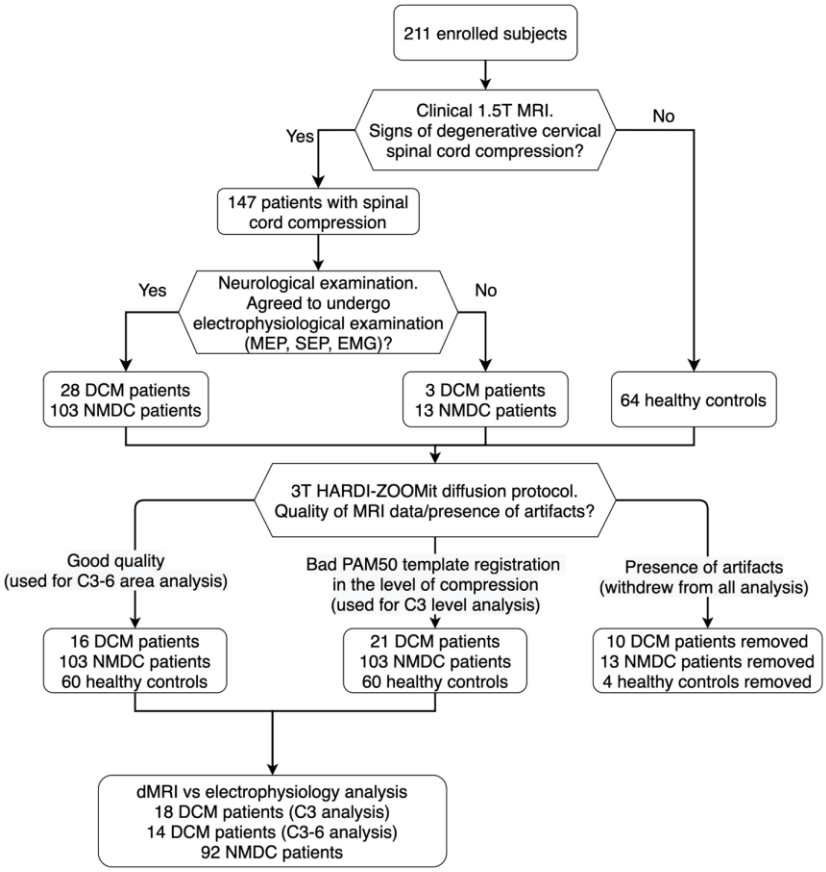

Figure 14 – Flowchart of participant's requirement for the Study II. Adapted from (Valošek et al., 2021).

Radiological examination showed no MR signs of degenerative cervical SC compression in HC, while all NMDC and DCM patients exhibited MR signs of compression varying from local impingement to flat compression with partially preserved or lost subarachnoid space (Bednarik et al., 2008; Kadanka et al., 2017). Since 93.6% of NMDC and DCM patients had MCL at C4/5 level and/or lower (Table 3), the C3 level was considered as a reference level above the compression to evaluate rostral remote changes. NMDC patients showed no radiological signs or neurological signs/symptoms of DCM and had mJOA scale = 18. Twelve DCM patients showed T_2-w hyperintensity in one cervical level and two DCM patients showed T_2-w hyperintensity in two cervical levels. The mean mJOA scale in DCM patients was 14.5. Five out of 21 DCM patients were used only in the analysis of the C3 above the compression level due to imperfect PAM50 template and atlas registration caused by severe compression.

Table 3 – Characteristics of participants included in the Study II. Asterisk (*) indicates significance ($p < 0.05$). Abbreviations: DCM, degenerative cervical myelopathy; EMG, electromyography; MEP, motor evoked potentials; mJOA, modified Japanese Orthopaedic Association; NMDC, non-myelopathic degenerative cervical spinal cord compression; SEP, somatosensory evoked potentials. Adapted from (Valošek et al., 2021).

Characteristic	Healthy controls (n = 60)	NMDC patients (n = 103)	DCM patients (n = 21)	p-value
Age [y.o.]	53.7 ± 8.7	56.5 ± 9.8	58.2 ± 10.8	.084
Sex [females/males]	38/22	59/44	12/9	.711
Height [cm]	172.4 ± 9.8	170.0 ± 8.7	167.0 ± 10.5	.227
Weight [kg]	78.9 ± 16.5	81.2 ± 16.7	81.7 ± 13.3	.880
Body mass index (BMI)	26.5 ± 4.8	28.0 ± 4.6	28.8 ± 4.1	0.073
Cross sectional area (CSA) at C3 level [mm^2]	69.7 ± 7.6	66.0 ± 7.4	56.7 ± 7.1	<.001*
mJOA	18.0 ± 0.0	18 ± 0.0	14.5 ± 2.6	
Maximally compressed level (MCL)				
C3/4	-	5 (4.8%)	3 (14.3%)	
C4/5	-	28 (27.2%)	4 (19.0%)	
C5/6	-	49 (47.6%)	14 (66.7%)	
C6/7	-	21 (20.4%)	-	
Compression ratio (CR) at MCL	-	0.41 ± 0.07	0.35 ± 0.08	
Cross-sectional area (CSA) at MCL	-	60.71 ± 11.3	52.14 ± 13.84	
Number of stenotic levels				
1 compression	-	39 (37.9%)	6 (28.6%)	
2 compressions	-	33 (32.0%)	8 (38.1%)	
3 compressions	-	25 (24.3%)	4 (19.0%)	
4 compressions	-	6 (5.8%)	3 (14.3%)	
Electrophysiological measurements				
Abnormal MEP	-	11 patients from 87 (12.6%)	12 patients from 18 (66.7%)	
Abnormal SEP	-	28 patients from 87 (32.2%)	13 patients from 18 (72.2%)	
Abnormal EMG	-	24 patients from 92 (26.1%)	11 patients from 17 (64.7%)	

4.2 Imaging results

4.2.1 Study I (dMRI methodology)

Figure 15 shows T_2-w sagittal image, ME-GRE T_2*-w axial image with segmented WM/GM and vertebral labeling, and images acquired by 3 dMRI protocols. Both HARDI-ZOOMit protocols (i.e., interpolated and non-interpolated) were about 3 min 30 s faster compared to DTI-RESOLVE protocol.

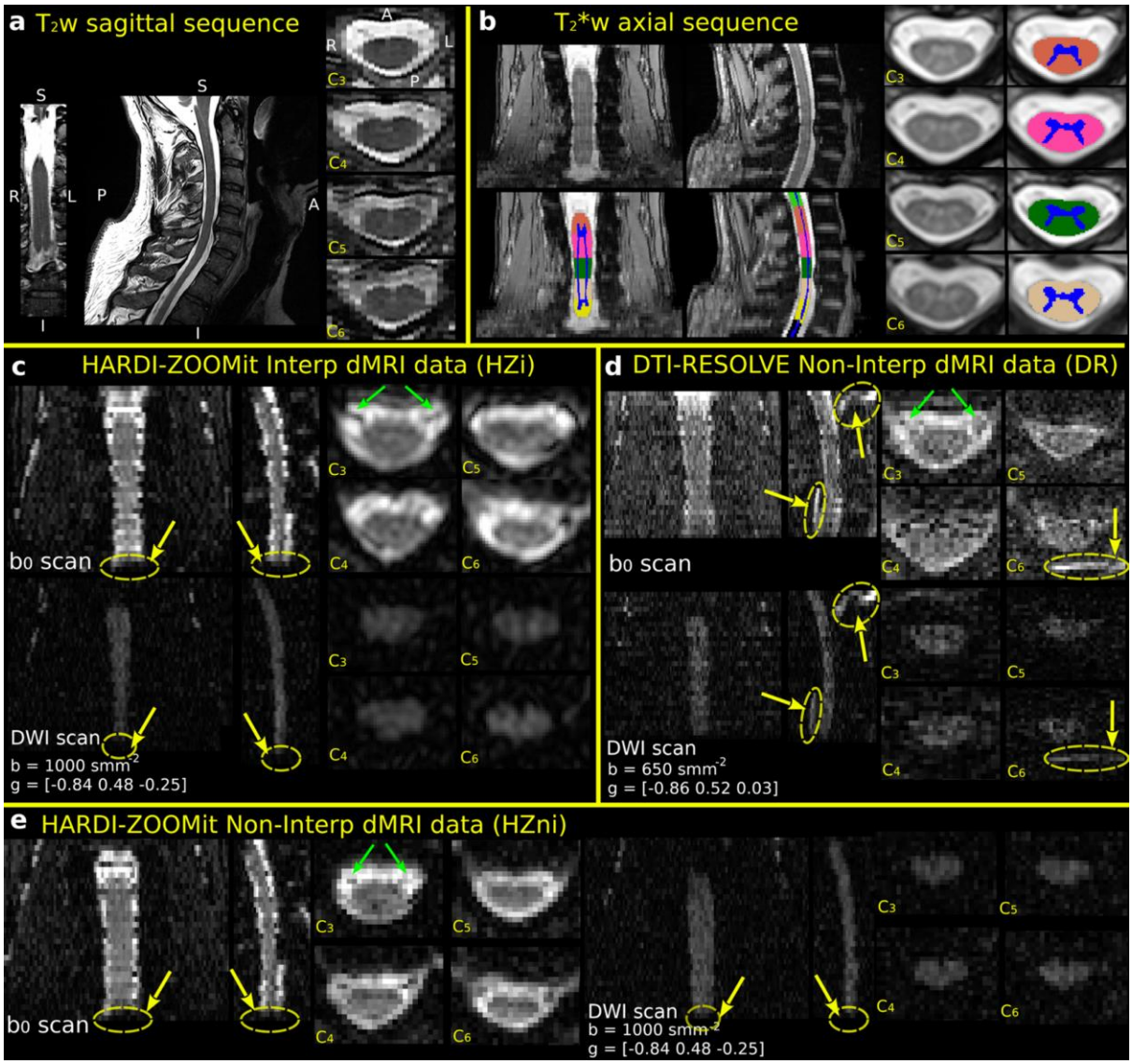

Figure 15 – Illustrative data visualization. (a) T_2-w sagittal image, (b) multi-echo gradient echo (ME-GRE) T_2*-w axial image with segmented WM/GM and vertebral labeling, (c) Interpolated HARDI-ZOOMit protocol, (d) DTI-RESOLVE protocol, (e) Non-interpolated HARDI-ZOOMit protocol. b_0 stand for images with b-value = 0 s.mm^{-2} (i.e., without diffusion weighting). Vectors *g* stand for direction of a gradient vector. Yellow arrows indicated areas with signal loss. Green arrows indicated nerve roots. C3, C4, C5, C6 denote individual vertebral levels. Adapted from (Labounek et al., 2020).

4.2.1.1 *dMRI protocol's signal-to-noise ratio and mutual information between WM/GM*

As anticipated, signal-to-noise ratio (SNR) for DTI-RESOLVE protocol with b-value = 650 s.m^{-2} was lower (SNR 5.1 ± 1.3) than for HARDI-ZOOMit b-value = 550 s.mm^{-2} (SNR interpolated protocol 6.2 ± 1.2, SNR non-interpolated protocol 5.7 ± 1.1) and higher than HARDI-ZOOMit b-value = 1000 s.mm^{-2} (SNR interpolated protocol 4.5 ± 0.9, SNR non-interpolated protocol 4.7 ± 0.9). For all protocols, SNR was lower for NMDC patients relative to HC (Figure 16). Lower SNR was also observed in the caudal part of C7 vertebral level for both interpolated and non-interpolated HARDI-ZOOMit protocols (Figure 15c, e) and may be caused by increased level of susceptibility artifacts originating from the lungs. From this reason, only area covering C3-6 was used in analysis of dMRI-derived microstructural metrics.

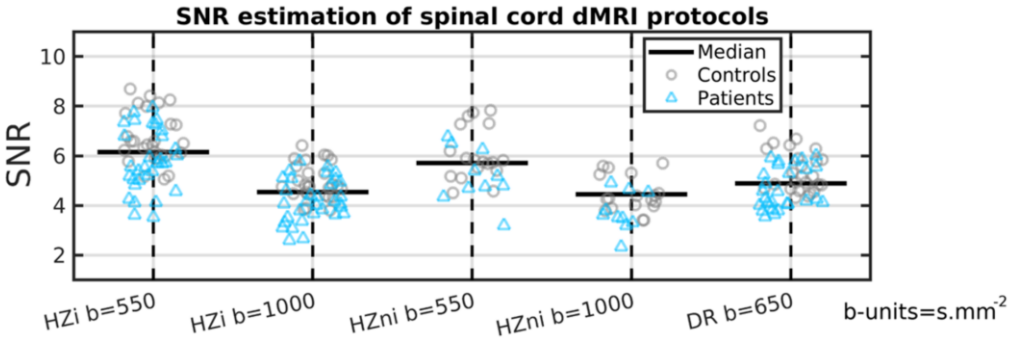

Figure 16 – Signal-to-noise ratio across individual diffusion protocols and their b-values. SNR, signal-to-noise ratio; HZi, interpolated HARDI-ZOOMit; HZni, non-interpolated HARDI-ZOOMit; DR, DTI-RESOLVE. Adapted from (Labounek et al., 2020).

Across all dMRI-derived metrics from both DTI and ball-and-sticks models, HARDI-ZOOMit protocols demonstrated higher mutual information than DTI-RESOLVE protocol (Figure 17).

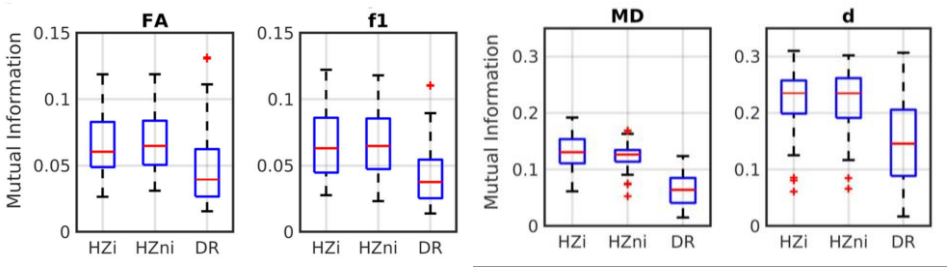

Figure 17 – Visualization of mutual information between dMRI-derived maps (i.e., FA, f1, MD and d) and WM/GM structures in semi-binarized T_2*-w axial image (background = 0, GM = 1 and WM = 2) from C3-6 area. FA, fractional anisotropy estimated from DTI model; f1, primary partial volume fraction estimated from ball-and-sticks model; MD, mean diffusivity estimated from DTI model; d, diffusivity estimated from ball-and-sticks model; HZi, interpolated HARDI-ZOOMit; HZni, non-interpolated HARDI-ZOOMit; DR, DTI-RESOLVE. Adapted from (Labounek et al., 2020).

4.2.1.2 *Microstructural dMRI metrics*

HARDI-ZOOMit protocols demonstrated better visual contrast between WM and GM for all dMRI-derived metrics (i.e., lower values in GM and higher values in WM) than DTI-RESOLVE protocol (Figure 18). Also, HARDI-ZOOMit protocols showed higher mean and median values of FA and *f1* metrics and lower MD and *d* mean and median values in both WM and GM compared to DTI-RESOLVE protocol. Across all dMRI protocols, DTI model estimated lower MD values than ball-and-sticks model for *d* metric (Figure 18).

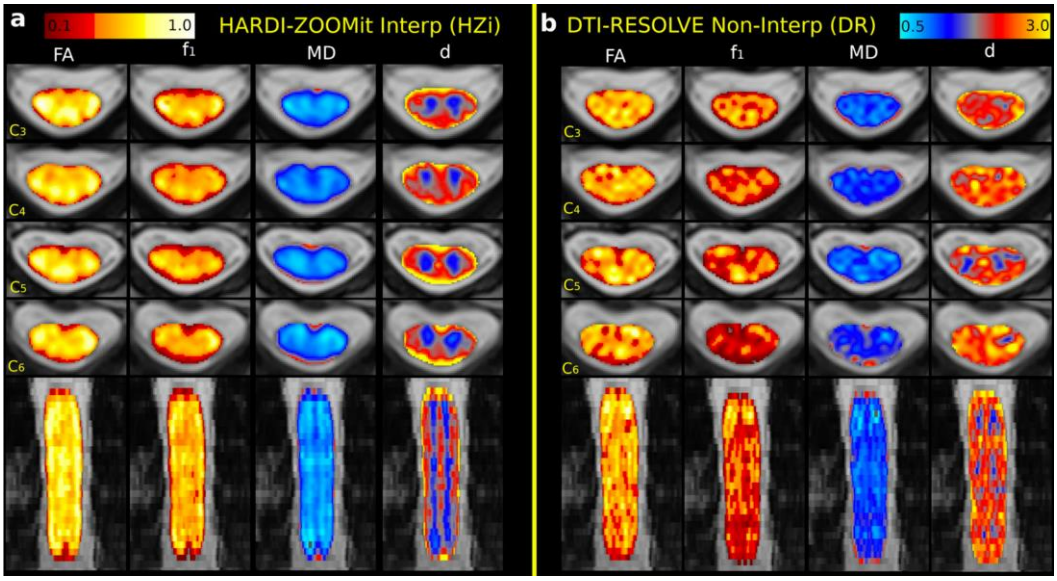

Figure 18 – Single-subject dMRI-derived metrics for (a) interpolated HARDI-ZOOMit protocol and (b) DTI-RESOLVE protocol. FA, fractional anisotropy estimated from DTI model; f1, primary partial volume fraction estimated from ball-and-sticks model; MD, mean diffusivity estimated from DTI model; d, diffusivity estimated from ball-and-sticks model. Adapted from (Labounek et al., 2020).

Group-averaged distributions of dMRI-derived metrics from C3-6 region demonstrated distinctions between NMDC patients and HC with higher discrimination for dMRI metrics extracted from WM than GM (Figure 19). Several heuristic parameters (H) for both WM and GM were proposed based on disjunctive probability density functions of the dMRI-derived group-averaged distributions:

$$H_{FA} = \int_{0.47}^{0.67} g(FA)dFA \tag{16}$$

$$H_{f_1} = \int_{0.30}^{0.55} g(f_1)df_1 \tag{17}$$

$$H_{MD} = \int_{0.84}^{1.26} g(MD)dMD$$

(18)

For ball-and-sticks *d* metric, separate heuristic parameters were established for WM and GM:

$$H_{d_{WM}} = \int_{1.70}^{2.20} g(d)dd$$

(19)

$$H_{d_{GM}} = \int_{1.00}^{1.48} g(d)dd$$

(20)

All heuristic parameters for WM and H_{MD} and H_d in GM demonstrated significant differences between HC and NMDC patients for interpolated HARDI-ZOOMit protocol. DTI-RESOLVE showed significant between-group differences for H_{MD} in GM. Post-hoc ANCOVA with age as a covariate rejected H_d in WM for interpolated HARDI-ZOOMit protocol and H_{MD} in GM for DTI-RESOLVE protocol but revealed significance for the H_d in GM for DTI-RESOLVE protocol.

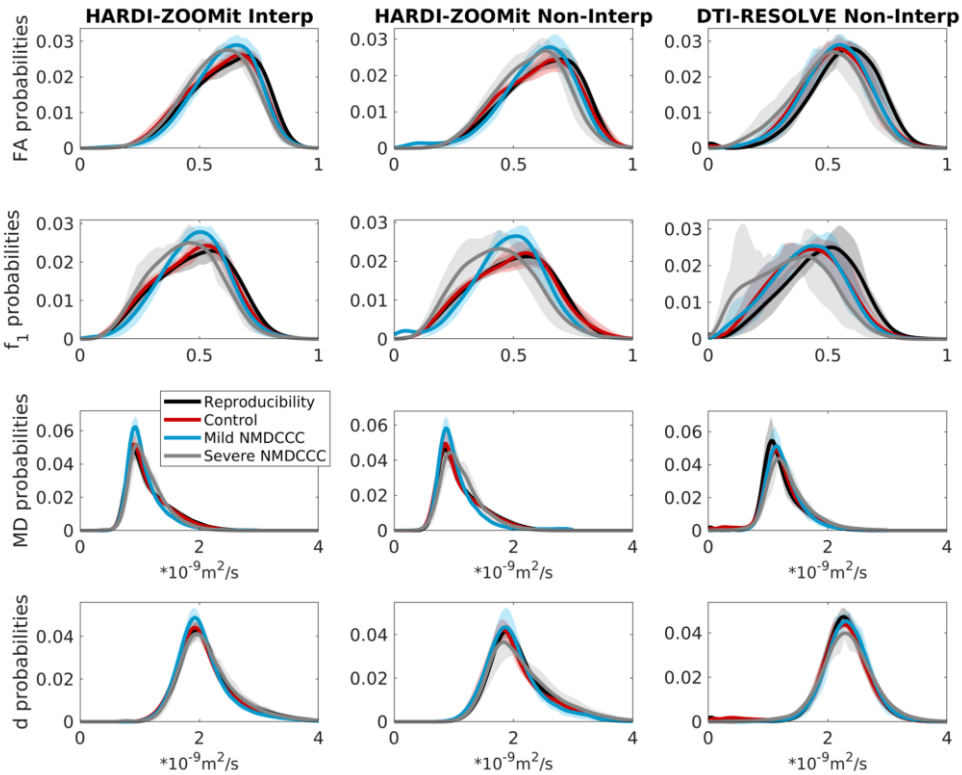

Figure 19 – Group-averaged distributions for fractional anisotropy (FA), primary partial volume fraction (f1), mean diffusivity (MD) and diffusivity estimated from ball-and-sticks model (d) from C3-6 white matter. Semi-transparent colors represent Q1-Q3 confidence intervals. Adapted from (Labounek et al., 2020).

The ball-and-sticks model identified crossing WM fiber bundles (i.e., the second significant fully anisotropic component, f2) for all dMRI protocols. The HARDI-ZOOMit protocol detected larger number of crossing fibers (5–15% of voxels) with physiologically plausible orientations compared to DTI-RESOLVE protocol (0–8% of voxels). These fibers were especially detected in areas of dorsal GM horns and anterior WM commissure (Figure 20).

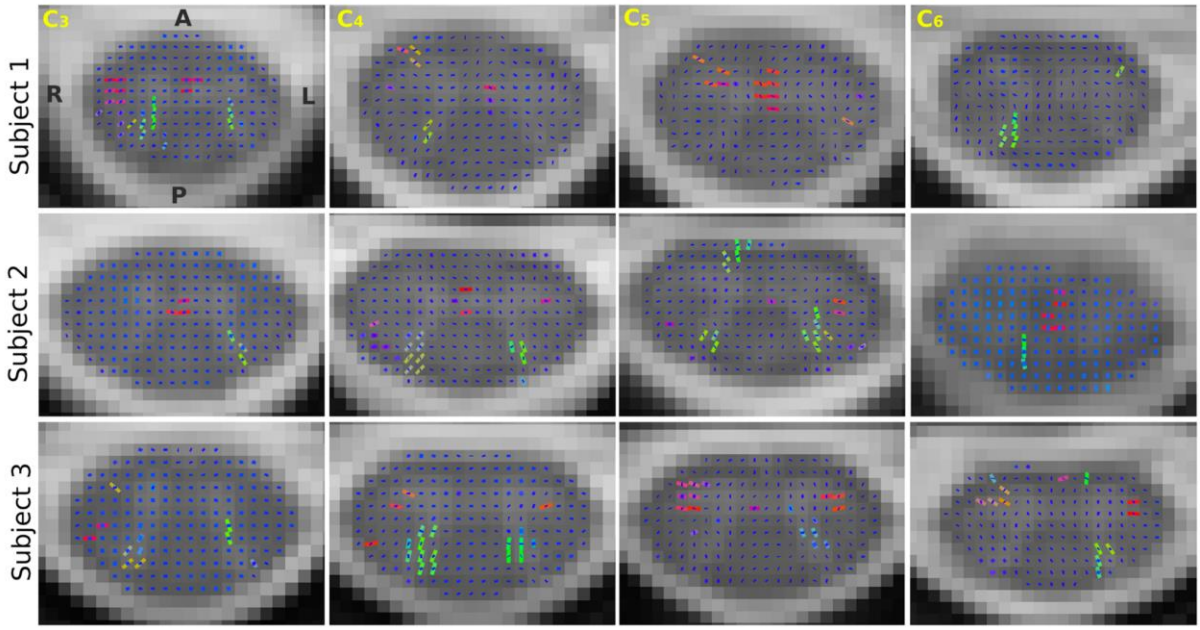

Figure 20 – Visualization of the crossing fibers for three participants across individual vertebral levels for interpolated HARDI-ZOOMit protocol. The orientation of the second fiber bundles (i.e., the second significant fully anisotropic component, f2 estimated using ball-and-sticks model) is visualized as red in right-left direction and as green in anterior-posterior direction. The dark-blue dots denote the primary fiber bundles (i.e., f1 estimated using ball-and-sticks model) passing in superior-inferior direction. Voxels where projections of two lines are present, represent crossing fibers. C3, C4, C5, C6 denote individual vertebral levels. Adapted from (Labounek et al., 2020).

4.2.1.3 Between-group differences in dMRI metrics

Wilcoxon rank-sum tests with Bonferroni correction revealed significant ($p_{FWE} < 0.05$) differences between HC and NMDC patients in seventeen descriptive statistics parameters for interpolated HARDI-ZOOMit protocol and in eight descriptive statistics parameters for DTI-RESOLVE protocol. Post-hoc ANCOVA with age as a covariate showed similar differences between HC and NMDC patients, specifically, 14 significant descriptive statistics parameters for interpolated HARDI-ZOOMit protocol and 9 significant descriptive statistics parameters for DTI-RESOLVE protocol. Non-interpolated HARDI-ZOOMit protocol demonstrated similar results but with fewer significant differences between groups. Post-hoc Wilcoxon rank-sum tests between NMDC patients with and without radiculopathy showed not significant differences.

4.2.1.4 *Cross-correlation, stepwise-linear regression, k-means clustering*

Cross-subject Pearson correlations between dMRI-derived metrics, which demonstrated significant between-group differences, identified linear dependency between several pair of dMRI metrics. Namely, ball-and-sticks *f1* demonstrated complementarity with DTI FA, and similarly, ball-and-sticks *d* showed similarity with DTI MD.

Stepwise linear regression identified unique dMRI-derived metrics that maximize the difference between HC and NMDC patients for each dMRI protocol. Specifically, two dMRI-derived metrics were identified for interpolated HARDI-ZOOMit protocol with r = 0.733; four dMRI-derived metrics were found significant for non-interpolated HARDI-ZOOMit protocol with r = 0.892; and three dMRI-derived metrics were identified for DTI-RESOLVE protocol with r = 0.670. None of the models found age as a model-significant variable.

K-means clustering of significant dMRI metrics identified by stepwise linear regression is shown in Figure 21. Sensitivity (SE) and specificity (SP) for individual dMRI protocols were SE = 87.88%, SP = 92.31% for interpolated HARDI-ZOOMit protocol; SE = 90.91%, SP = 100.00% for non-interpolated HARDI-ZOOMit protocol; and SE = 87.88%, SP = 76.92% for DTI-RESOLVE protocol.

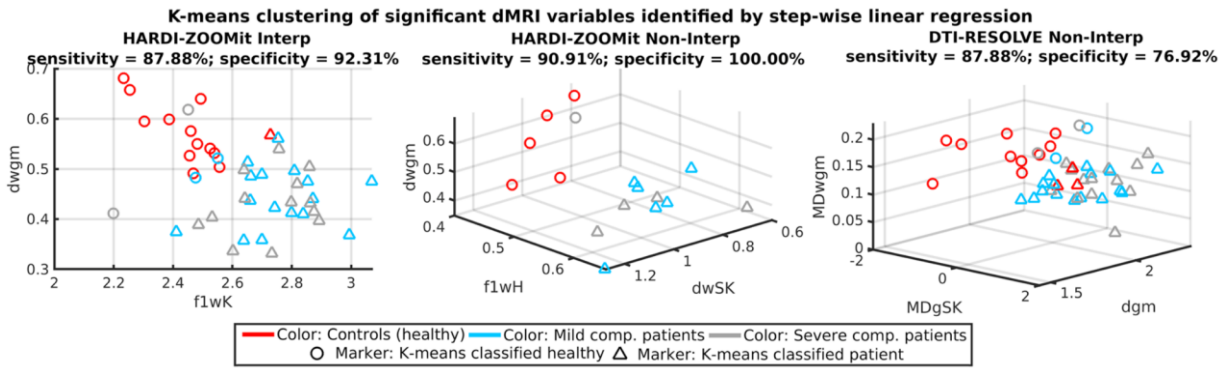

Figure 21 – Visualization of k-means clustering. dwgm, WM-GM gradient of d means; f1wK, WM kurtosis of f1; f1wH, heuristic parameter of f1 in WM; dwSK, WM skewness of d; MDwgm, WM-GM gradient of MD means; MDgSK, GM skewness of MD; dgm, GM mean of d. Adapted from (Labounek et al., 2020).

4.2.1.5 *Level of susceptibility artifacts and reproducibility of dMRI protocols*

Level of susceptibility distortions characterized by off-resonance effects showed no significant differences between NMDC patients and HC for any ROI and any dMRI protocol. At the same time, off-resonance effects were not significantly correlated with dMRI-derived metrics for any

dMRI protocol. HARDI-ZOOMit protocols showed smaller off-resonance effects than DTI-RESOLVE protocol.

Overall, the reproducibility of both interpolated and non-interpolated HARDI-ZOOMit protocols was comparable or higher relative to DTI-RESOLVE protocol.

4.2.2 Study II (Prospective dMRI study)

Figure 22 shows ME-GRE T_2*-w axial image with SC segmentation, FA map estimated from interpolated HARDI-ZOOMit protocol, and PAM50 atlas registered into diffusion space for NMDC and DCM patients from the level with compression.

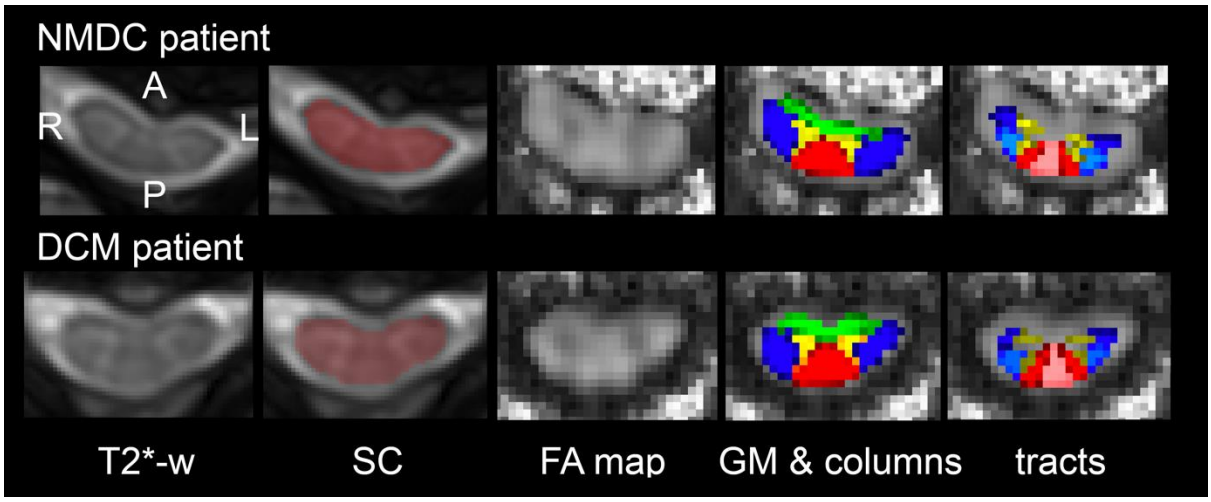

Figure 22 – Representative data from the C4/5 disc for NMDC and DCM patients. From the left: ME-GRE T_2*-w axial image, spinal cord (SC) segmentation used for PAM50 registration, fractional anisotropy (FA) map, white matter columns, gray matter (GM) and individual tracts from PAM50 atlas in diffusion space. Color coding of individual PAM50 regions of interests is same as in Figure 13a. Adapted from (Valošek et al., 2021).

4.2.2.1 Relationship between dMRI metrics and compression measures

Significant negative correlation was observed between CSA at MCL and MD, AD, RD and *d* diffusion metrics from the C3-6 area in dorsal and lateral tracts and dorsal and ventral GM horns. Positive correlation was found between CSA at MCL and Ball-and-sticks *f1* in fasciculus cuneatus. CR at MCL positively correlated with *f1* and FA diffusion metrics from the C3-6 area in lateral corticospinal tracts, spinal lemniscus, and ventral columns and MD from all analyzed ROIs except spinal lemniscus. CR at MCL also positively correlated with AD in fasciculus cuneatus, ventral columns, and ventral and dorsal GM horns, and RD in lateral and ventral columns, fasciculus gracilis, lateral corticospinal tracts, and spinal lemniscus. Finally,

Ball-and-sticks *d* from the C3-6 area in dorsal, lateral and ventral columns, fasciculus gracilis, fasciculus cuneatus and ventral and dorsal GM horns correlated with CR at MCL.

Positive associations between CSA at MCL and FA and *f1* diffusion metrics at C3 above the compression level were identified in fasciculus cuneatus and dorsal GM horns. Negative correlations with CSA at MCL were found in MD at C3 level in fasciculus gracilis and ventral and dorsal GM horns, AD and *d* in fasciculus gracilis and ventral GM horns, and RD in fasciculus cuneatus and dorsal GM horns. Positive correlations between CR at MCL and FA and *f1* in lateral corticospinal tracts as well as *f1* in fasciculus cuneatus above the compression level. Inverse relationships were identified between CR at MCL and MD in fasciculus cuneatus and lateral corticospinal tracts, AD in ventral GM horns, RD in lateral corticospinal tracts, and *d* in fasciculus cuneatus and ventral GM horns. Figure 23 shows an illustrative correlations between dMRI-derived metrics and CSA and CR; figures for all dMRI-derived metrics can be found in supplementary material of (Valošek et al., 2021).

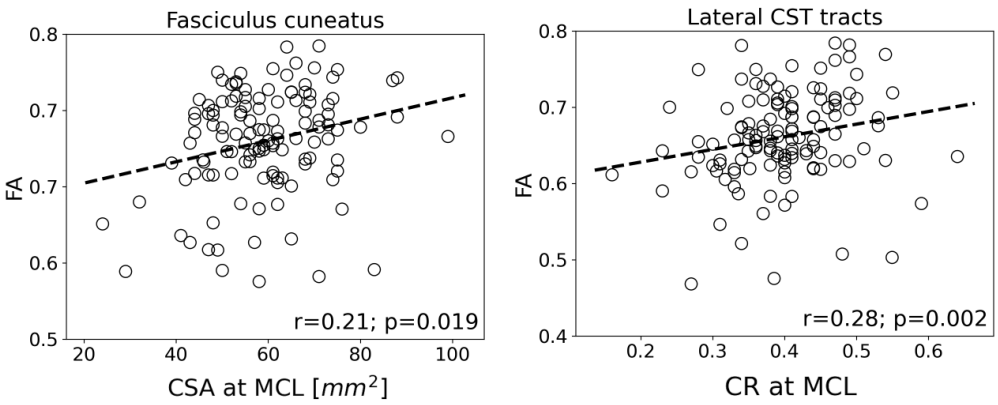

Figure 23 – Illustrative visualization of significant correlation between fractional anisotropy (FA) at the above the compression level C3 and cross-sectional area (CSA) and compression ratio (CR) at maximally compressed level (MCL). Adapted from (Valošek et al., 2021).

4.2.2.2 Cross-sectional area at the C3 above the compression level

As illustrated in Figure 24, the Kruskal-Wallis H test and consequent Dunn's post-hoc tests revealed significant CSA reduction at C3 above the compression level between HC and NMDC patients (-5.0%, $p = 0.007$), HC and DCM patients (-18.4%, $p < 0.0001$) and NMDC and DCM patients (-14.1%, $p < 0.0001$).

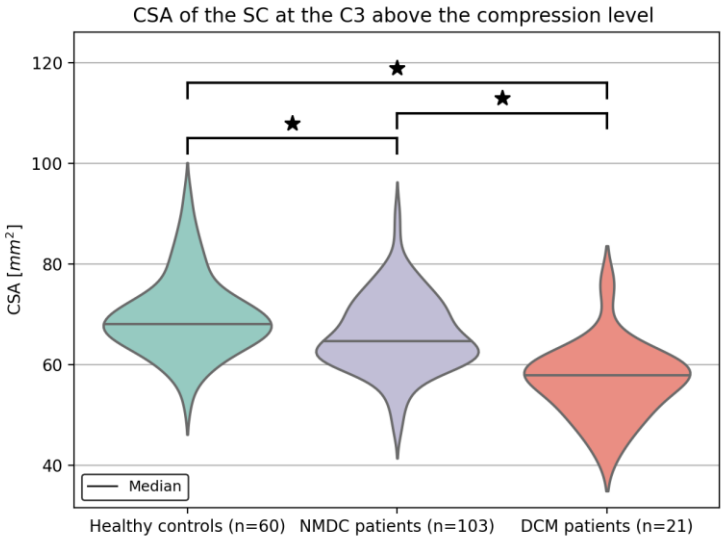

Figure 24 – Between-group differences in cross-sectional area (CSA) at C3 above the compression level. Asterisk symbols (*) indicate significance ($p_{FWEcorr}$<.05). Obtained from supplementary material of (Valošek et al., 2021).

4.2.2.3 Differences in dMRI metrics between HC and NMDC patients

NMDC patients exhibited significantly lower *f1* and FA ($p_{FWEcorr} < 0.05$) in the C3-6 area relative to HC in dorsal and lateral tracts, specifically in the fasciculus gracilis, fasciculus cuneatus, lateral corticospinal tracts and spinal lemniscus. Higher d, MD, AD and RD in NMDC patients compared to HC were observed in dorsal and lateral tracts and GM horns. Alterations in ventral columns were only revealed by the ball-and-sticks model and showed higher *d* in NMDC patients in comparison to HC.

Lower *f1* values at C3 above the compression level were found in NMDC patients relative to HC in lateral columns, namely in the spinal lemniscus (Figure 25 and Figure 26).

4.2.2.4 Differences in dMRI metrics between HC and DCM patients

Comparison of DCM patients and HC revealed significantly lower *f1* and FA ($p_{FWEcorr} < 0.05$) in the C3-6 area compared to HC in dorsal and lateral tracts, that is, fasciculus cuneatus, fasciculus gracilis, lateral corticospinal tracts and spinal lemniscus. The ball-and-sticks model showed lower *f1* values in DCM patients relative to HC in ventral columns and ventral and dorsal GM horns. Higher MD and RD values in DCM patients in comparison to HC were detected in dorsal and lateral tracts, whilst higher RD in DCM patients was also observed in ventral columns. In contrast, higher *d* and AD in DCM patients were solely revealed in dorsal tracts. Ventral and dorsal GM horns exhibited higher d, MD, AD and RD in DCM patients compared to HC.

The C3 above the compression level showed lower *f1* in DCM patients relative to HC in dorsal and lateral tracts, namely in the fasciculus cuneatus, fasciculus gracilis, lateral corticospinal tracts, spinal lemniscus and dorsal GM horns, while lower FA was detected in identical areas but spared the dorsal GM. DCM patients also showed higher MD and RD in dorsal and lateral columns and GM, and higher *d* and AD in ventral GM horns and the GM compared to HC. No differences were detected in dMRI metrics between DCM patients and HC at the C3 level in ventral columns (Figure 25 and Figure 26).

4.2.2.5 Differences in dMRI metrics between NMDC and DCM patients

DCM patients showed significantly lower *f1* and FA ($p_{FWEcorr} < 0.05$) in the C3-6 area relative to NMDC patients in dorsal and lateral tracts, namely in fasciculus cuneatus, fasciculus gracilis, lateral corticospinal tracts and spinal lemniscus, and lower *f1* values also in the dorsal GM horns. Higher MD and RD were observed in the dorsal and lateral tracts as well as ventral and dorsal GM horns with higher *d* and AD in GM horns in DCM patients compared to NMDC patients.

At C3 above the compression level, lower *f1* and FA and higher MD and RD were observed in the fasciculus cuneatus, fasciculus gracilis, lateral corticospinal tracts and spinal lemniscus, and the dorsal GM horns in DCM patients relative to NMDC patients. Higher *d* and AD were detected in GM, specifically in ventral GM horns in DCM patients in comparison to NMDC patients (Figure 25 and Figure 26).

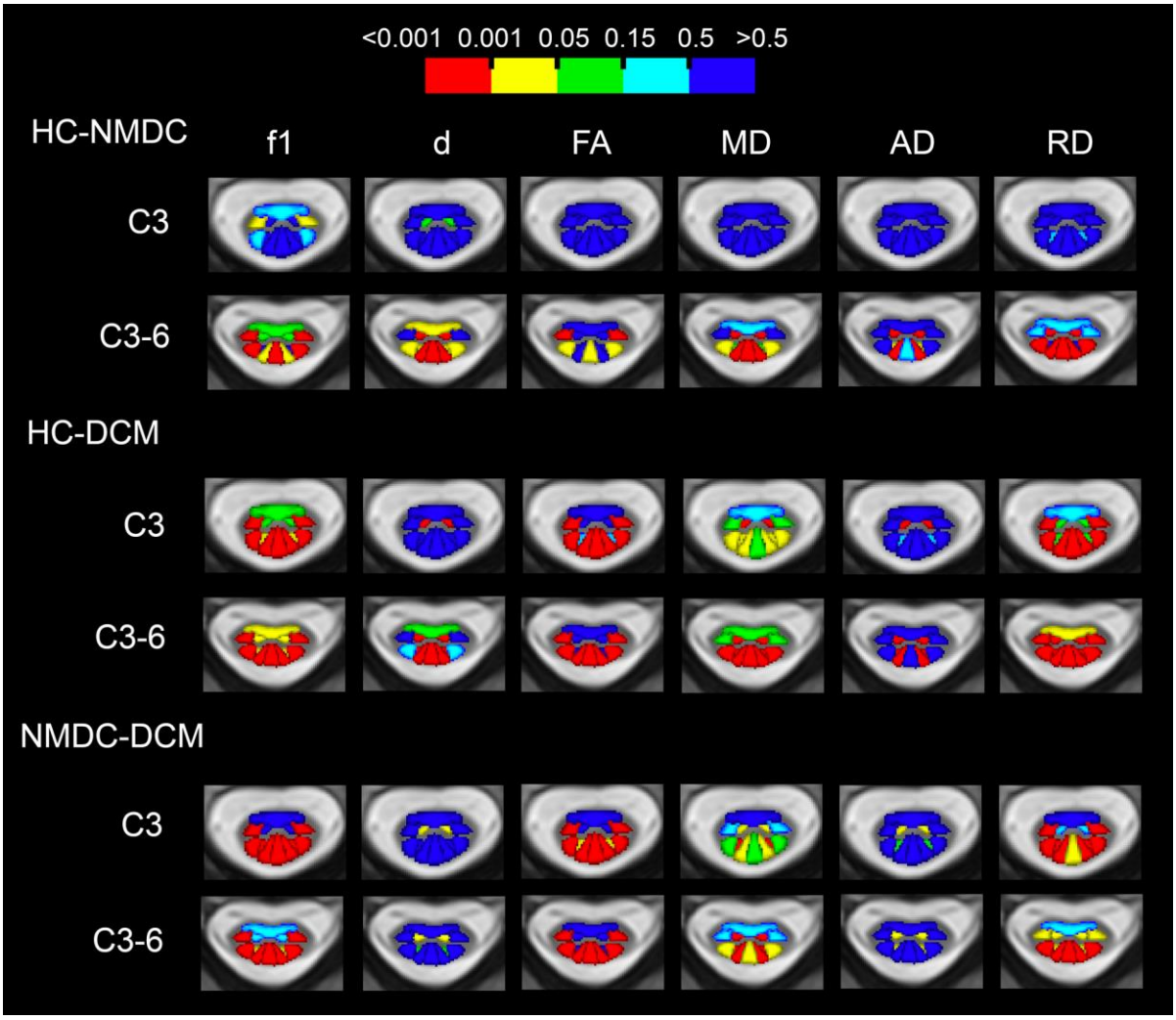

Figure 25 – Between-group differences in dMRI-derived metrics for individual regions of interest comprising white matter tracts and gray matter areas from C3 above the compression level and C3-6 area. Colors represent p-values gained using ANCOVA ($p_{FWEcorr}$<.05). Abbreviations: HC, healthy controls; DCM, degenerative cervical myelopathy; NMDC, non-myelopathic degenerative cervical spinal cord compression. Obtained from (Valošek et al., 2021).

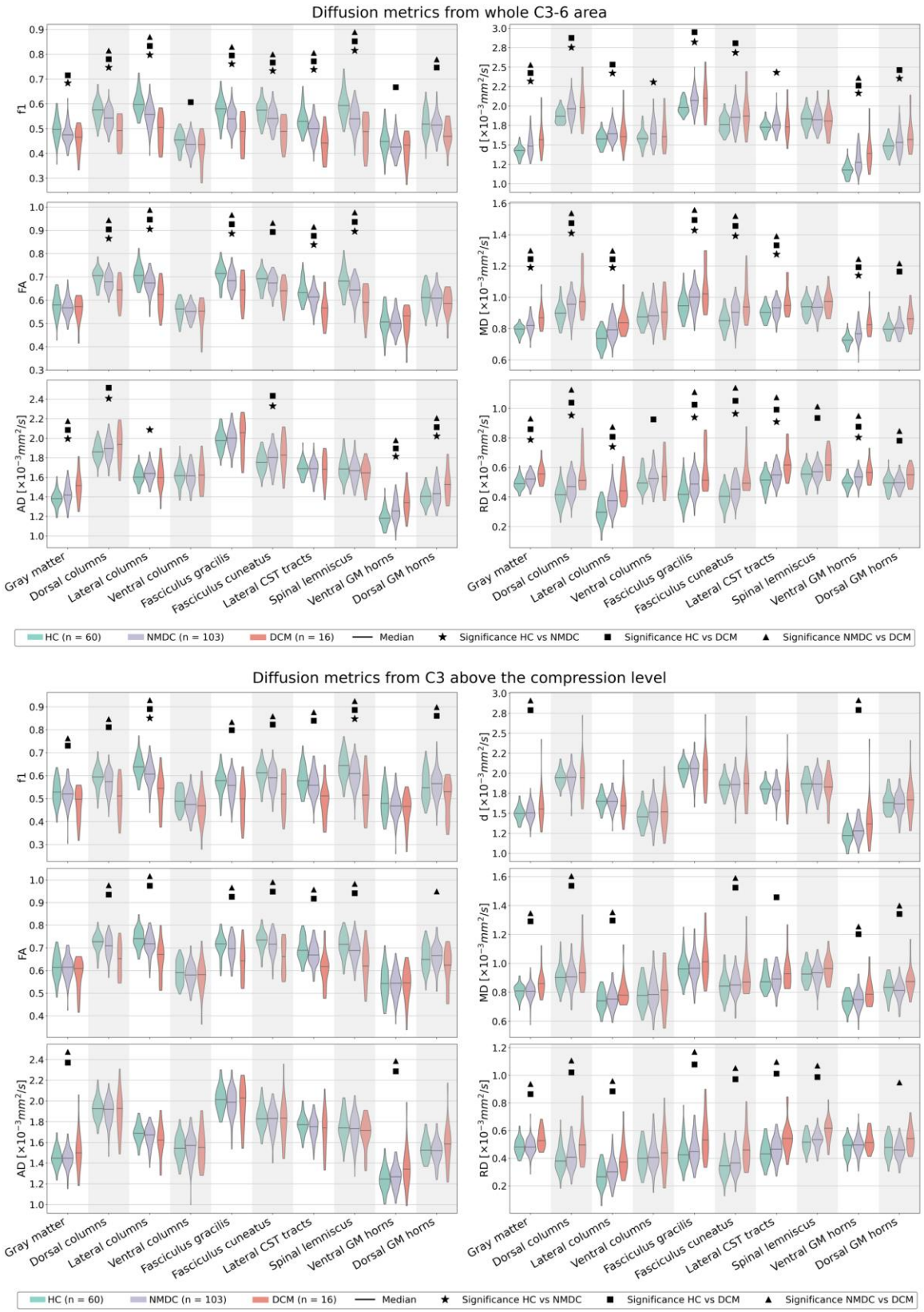

Figure 26 – Violin plots showing between-group differences in dMRI-derived metrics for individual regions of interest from C3 above the compression level and C3-6 area. Markers indicate $p_{FWEcorr}$<.05 gained using ANCOVA. Abbreviations: HC, healthy controls; DCM, degenerative cervical myelopathy; NMDC, non-myelopathic degenerative cervical spinal cord compression. Obtained from (Valošek et al., 2021).

4.2.2.6 Relationship between dMRI metrics and electrophysiological measures

Patients with abnormal electrophysiological measures showed significantly lower *f1*, FA, *d* and AD values, and higher RD values, in corresponding anatomical areas in comparison to patients with normal electrophysiological findings at both C3-6 area and C3 above the compression level. A detailed description follows.

First, a comparison of dMRI-dervied metrics from the C3-6 area revealed significantly lower *f1* and FA ($p_{FWEcorr} < 0.05$) in lateral columns and lateral corticospinal tracts and lower AD in lateral columns in patients with abnormal MEP findings relative to patients with normal MEP findings. Similarly, patients with altered SEPs demonstrated significantly lower FA in the dorsal columns, fasciculus gracilis, fasciculus cuneatus and dorsal GM horns compared to unaffected patients. Abnormal EMG was reflected by higher RD in GM and ventral GM horns comparing patients with abnormal and normal EMG (Figure 27).

Next, a comparison of dMRI-derived metrics at C3 above the compression level showed significantly lower ($p_{FWEcorr} < 0.05$) f1 and FA and higher RD in the lateral columns and lateral corticospinal tracts in patients with abnormal MEP relative to these with normal MEP. Also, lower *d* and AD were detected in the lateral columns in patients with abnormal MEP. Altered SEP measurements were associated with lower *f1* and FA in dorsal columns, fasciculus gracilis and fasciculus cuneatus, as well as lower FA and *d* in dorsal GM horns compared to patients with normal SEP. Lower *f1*, FA and RD were detected in the GM in patients with abnormal EMG compared to individuals with unaffected EMG (Figure 27).

Similarly, post-hoc analysis between quantitative MEP parameters and dMRI-derived metrics from lateral corticospinal tracts from C3-6 area showed significant ($p_{FWEcorr} < 0.05$) negative correlations for *f1* and FA and UMEP and LMEP cortical latencies and LMEP CMCT. Positive correlations were detected for RD and UMEP and LMEP cortical latencies. Similarly, post-hoc analysis between quantitative SEP parameters and dMRI-derived metrics from dorsal columns from C3-6 area revealed significant ($p_{FWEcorr} < 0.05$) negative correlations for *f1* and P40 wave; FA and N20 wave, P40 wave and CSCT from tibial nerve; and AD and N20 wave, P40 wave and CSCT from median nerve.

Post-hoc analysis between quantitative MEP parameters and dMRI-derived metrics from lateral corticospinal tracts at C3 above the compression level demonstrated significant

($p_{FWEcorr} < 0.05$) negative correlations for FA and UMEP and LMEP cortical latencies and both UMEP and LMEP CMCT. Positive correlation was detected for RD and LMEP CMCT. Post-hoc analysis between quantitative SEP parameters and dMRI-derived metrics from dorsal columns at C3 above the compression level revealed significant ($p_{FWEcorr} < 0.05$) negative correlations for *f1* and FA and P40 wave and CSCT from tibial nerve; and AD and N20 wave and P40 wave.

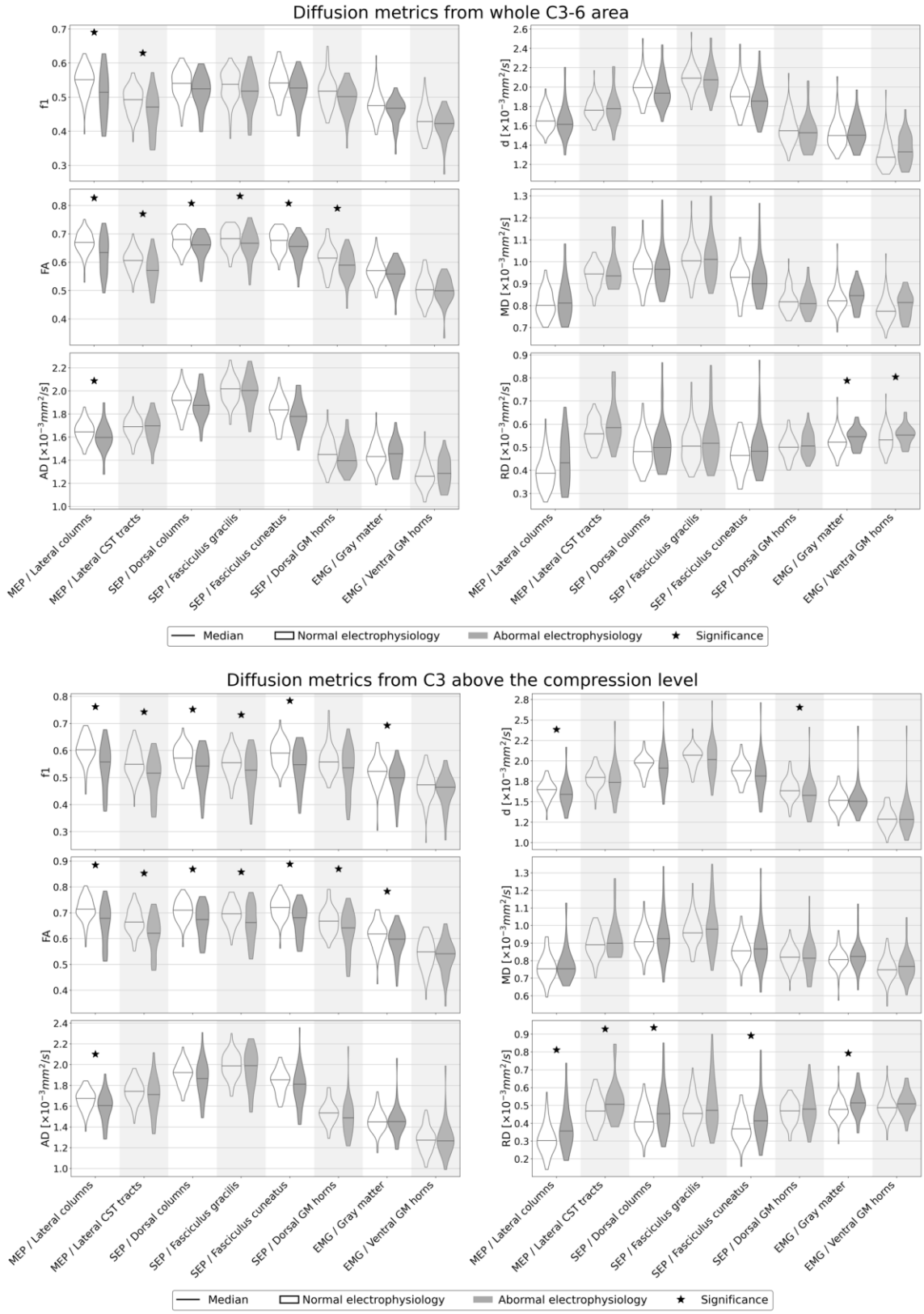

Figure 27 – Violin plots showing relationship between electrophysiological measures and dMRI-derived metrics from corresponding regions of interest from C3 above the compression level and C3-6 area. Asterisks (*) indicate $p_{FWEcorr}$<.05. Abbreviations: MEP, motor evoked potentials; SEP, somatosensory evoked potentials; EMG, electromyography; GM, gray matter. Obtained from (Valošek et al., 2021).

4.2.2.7 *Relationship between dMRI metrics and mJOA scale*

Exploratory correlation analysis in patients with decreased mJOA scale (i.e., DCM patients) revealed significant positive correlation of mJOA scale with *f1*, FA, *d* and AD in lateral columns, FA, AD and *d* in spinal lemniscus and FA in ventral columns at C3 above the compression level. A negative correlation between mJOA scale and RD in lateral columns at C3 above the compression level was also identified (Figure 28).

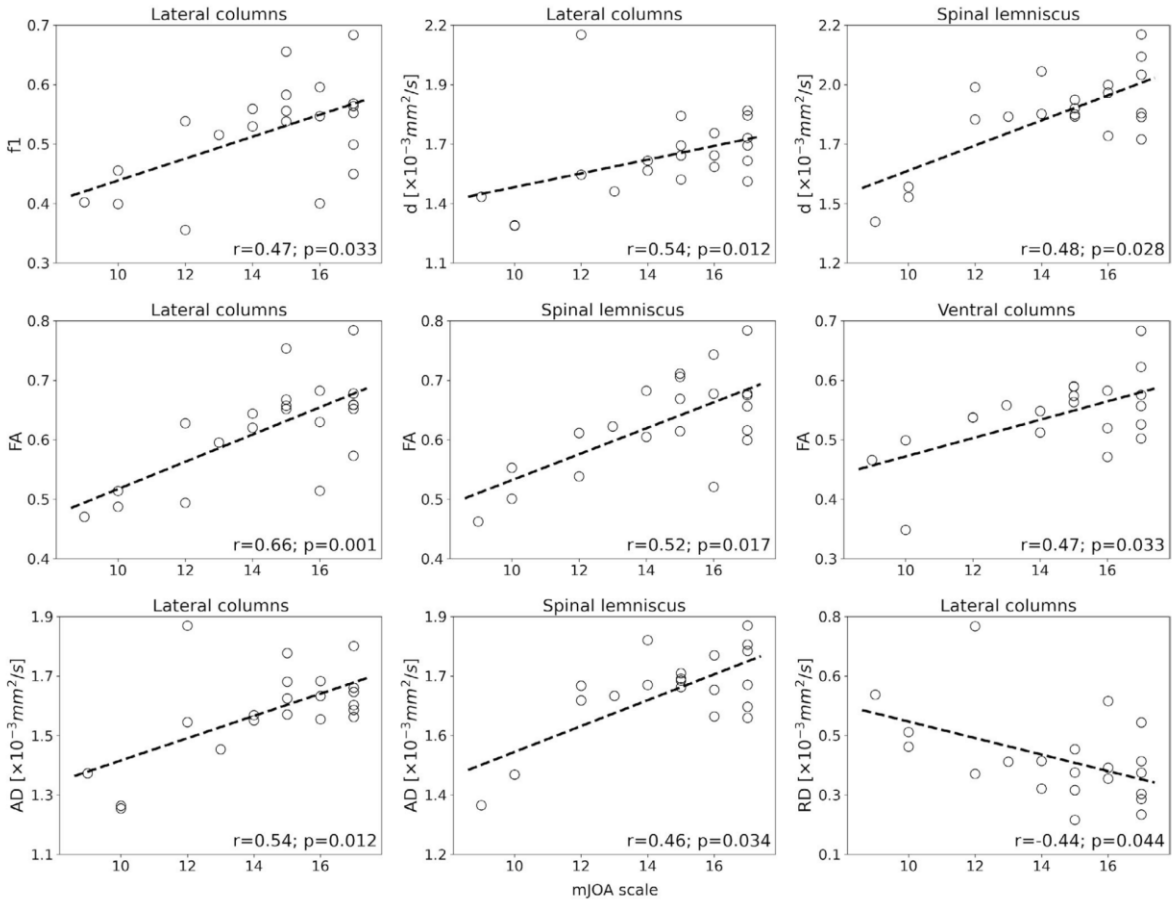

Figure 28 - Spearman correlations between dMRI-derived metric from C3 above the compression level and modified Japanese Orthopaedic Association (mJOA) scale in DCM patients. Obtained from (Valošek et al., 2021).

5 DISCUSSION

In this section, methodological advantages of optimized multi-shell HARDI-ZOOMit protocol are summarized (Study I) and tract-based analysis of a large cohort of NMDC and DCM patients is discussed (Study II). Next, limitations of both studies are elaborated on. Finally, employed MRI protocol and tract-based analysis are put into context of the current state-of-the art knowledge and future directions are outlined.

5.1 Study I (dMRI methodology)

Both multi-shell HARDI-ZOOMit and single-shell DTI-RESOLVE protocols depicted microstructural differences between NMDC patients and HC in dMRI-derived metrics from C3-6 region estimated using DTI and ball-and-sticks models. Findings corroborated outcomes from another quantitative MRI methods such as magnetization transfer imaging and T_2*-w WM/GM ratio (Martin et al., 2017a). Detection of microstructural dMRI changes may help to identify asymptomatic NMDC patients with higher risk of progression into symptomatic and potentially irreversible DCM, in addition to already descripted predictors such as electrophysiological abnormalities and radiculopathy (Bednarik et al., 2008; Kadanka et al., 2017).

The HARDI-ZOOMit protocol utilized multi-shell gradient sampling (i.e., two b-values) over whole spheres of the q-space (Figure 12) (Caruyer et al., 2013) leading to higher angular resolution compared to DTI-RESOLVE protocol, which is based on single-shell gradient sampling (i.e., single b-value) and covered only the half of the q-space's sphere. The increased angular resolution of the multi-shell HARDI-ZOOMit protocol allowed detection of higher number of crossing fibers relative to the single-shell DTI-RESOLVE protocol. At the same time, higher mean and median values of FA and *f1* metrics derived from DTI and ball-and-sticks models, respectively, provided by HARDI-ZOOMit protocols suggest lower level of noise compared to DTI-RESOLVE protocol. Generally, HARDI-ZOOMit protocols outperformed DTI-RESOLVE protocol when provided about 3 min 30 s shorter acquisition time, revealed between-group differences in more dMRI-derived metrics, showed higher specificity, detected more second fiber bundles and increased mutual information between dMRI-derived maps and WM/GM structures.

Newly proposed heuristic parameters and usage of skewness and kurtosis revealed additional differences between NMDC patients and HC in addition to conventionally used mean and median values. Finally, the multi-compartment ball-and-sticks model, which was so far applied only in brain studies, allowed estimation of multiple fiber bundles in each voxel (i.e., crossing fibers), particularly in areas of dorsal horns and anterior white matter commissure.

5.2 Study II (Prospective dMRI study)

The combination of multi-shell HARDI-ZOOMit protocol and tract-specific atlas-based analysis detected significant distinctions in dMRI-derived metric between asymptomatic NMDC and symptomatic DCM patients relative to HC in dorsal columns (i.e., fasciculus cuneatus and fasciculus gracilis), lateral columns (i.e., lateral corticospinal tracts and spinal lemniscus) and GM. Alterations in dMRI-derived metrics were found in C3-6 area as well as C3 above the compression level, and were accompanied by reduced cross-sectional area at the C3 level in both NMDC and DCM patients relative to HC. Importantly, tract-specific changes in dMRI-derived metrics were reflected by electrophysiological abnormalities in corresponding SC regions and correlated with clinical mJOA scale, implying the importance of tract-specific analysis.

5.2.1 dMRI changes at maximally compressed level

Differences in dMRI-derived metrics in the C3-6 area in NMDC patients relative to HC confirmed incipient SC microstructural damage in the early stages of degenerative SC compression in dorsal and lateral tracts. The findings are consistent with post-mortem histopathological studies, in which chronic SC compression led to damage of the lateral pial plexus resulting in hypoperfusion and axonal degeneration of lateral corticospinal tracts and dorsal areas (Badhiwala et al., 2020). Malperfusion through the compressed anterior spinal artery initially affects GM, lateral columns and the anterior part of the dorsal columns (Figure 6a) and can ultimately result in progressive demyelination (Badhiwala et al., 2020; Mair and Druckman, 1953). Indeed, lower values of *f1* and FA and higher values of diffusivity metrics in the lateral and dorsal tracts and GM observed in the study in both NMDC and DCM patients relative to HC suggest ongoing demyelination (David et al., 2019). While changes in ventral columns were detected only sparsely, alterations in ball-and-sticks *f1* in the lateral and dorsal tracts distinguished DCM patients from NMDC patients and showed more profound deficits in

DCM than NMDC. Thus, changes in dMRI-derived metrics corroborate post-mortem reports (Mair and Druckman, 1953), which reported lesions of the anterior GM horns, the lateral columns and the anterior part of the dorsal columns in the early stages of degenerative SC compression (David et al., 2019). Direct comparison of NMDC and DCM patients demonstrated alterations in dorsal and lateral columns as well as GM that further confirmed the influence of gradual changes of arterial flow on the compression-related deficits and myelopathy (Badhiwala et al., 2020; Baptiste and Fehlings, 2006). While lower FA corroborates DTI studies in DCM patients (Lee et al., 2011; Lindberg et al., 2016; Martin et al., 2017b; Seif et al., 2020; Wen et al., 2014a), NMDC patients (Martin et al., 2018a) and patients with slowly progressing SC compression (Facon et al., 2005), to date no study showed tract-specific changes in a large cohort of both DCM and NMDC patients.

5.2.2 Rostral alterations above the compression level

Our results also showed secondary effects of the compression on microstructural SC integrity above the compression level at the C3 level. Alterations at the C3 level in NMDC patients were limited to the spinal lemniscus (i.e., spinothalamic and spinoreticular tracts) and were depicted solely by ball-and-sticks *f1* metric pointing to incipient remote degeneration rostrally in NMDC patients in the early stages of degenerative SC compression. The ball-and-sticks model thus demonstrated higher discrimination than DTI model when detected changes in spinal lemniscus in *f1* metric that were not observed by complementary FA estimated by DTI model. As the compression progressed to symptomatic DCM, additional *f1*, FA and RD changes in dorsal and lateral columns occurred. Significantly lower *f1* and FA at C3 above the compression level in DCM patients relative to HC point to progressive anterograde and retrograde axonal degeneration of dorsal sensory tracts (i.e., fasciculus gracilis, fasciculus cuneatus and spinal lemniscus) as well as motor tracts (i.e., lateral corticospinal tracts), respectively (Figure 6b) (Badhiwala et al., 2020; David et al., 2019; Seif et al., 2020). Changes of FA at the C3 level are in agreement with a recent study (Seif et al., 2020), which demonstrated a remote FA decrease in the lateral corticospinal and spinothalamic tracts at the C2/3 level in DCM patients and patients with traumatic spinal cord injury relative to HC. Alterations in GM together with cross-sectional area reduction at above the compression level in DCM patients compared to NMDC patients and HC point to trans-synaptic degeneration and GM atrophy above the stenosis level in myelopathic patients (David et al., 2019). Direct comparison of symptomatic

DCM and asymptomatic NMDC patients revealed more severe deficits in DCM patients in the dorsal and lateral columns, as well as in the ventral and dorsal GM horns. While remote neurodegeneration in DCM patients compared to HC corroborates previous studies (Budzik et al., 2011; David et al., 2019; Grabher et al., 2016; Seif et al., 2020; Wen et al., 2014a), the used tract-specific approach also delineated gradual changes between DCM and NMDC patients. Rostral alterations above the compression level further endorse brain studies (Bernabéu-Sanz et al., 2020; Kowalczyk et al., 2012; Zhou et al., 2015) that reported changes in motor and somatosensory cortex in DCM patients with degenerative SC compression. A decrease of SC cross-sectional area at the C3 level in DCM patients relative to HC corresponds with previous reports (David et al., 2019; Grabher et al., 2016; Martin et al., 2017b; Seif et al., 2020) and further points to Wallerian neurodegeneration and atrophy rostrally to the compression. A smaller yet significant cross-sectional area reduction was also found in NMDC patients, suggesting more profound changes in DCM patients than in NMDC patients compared to HC.

5.2.3 Relationship between dMRI metrics, mJOA scale and electrophysiological measures

Tract-specific analysis also disclosed a relationship between the clinical status assessed by mJOA scale and dMRI-derived metrics in lateral columns and spinal lemniscus in DCM patients. Lower mJOA scale (i.e., worse DCM disability) was associated with a decrease of *f1*, FA and AD and an increase of RD in DCM patients pointing to more severe demyelination and axonal damage in DCM patients with profound motor and sensory disability.

Importantly, statistically significant changes in dMRI-derived metrics between patient with and without electrophysiological deficits point to a crucial relationship between functional impairments and microstructural degeneration. Patients with abnormal electrophysiological findings demonstrated lower *f1*, FA, *d* and AD metrics and higher RD and MD compared to patients with normal electrophysiological findings. Changes detected by dMRI in sensory and motor tracts were related to SEP and MEP, respectively, and dMRI alteration in GM were related to EMG abnormalities. While previous studies also examined the relationship between dMRI and electrophysiological measures, they failed to detect dMRI differences between patients with and without electrophysiological deficits (Kadanka et al., 2017; Kerkovský et al., 2012), or detected FA alterations in DCM patients with normal SEP (Wen et al., 2014a). Whereas electrophysiological measures serve as predictors of DCM development (Bednarik et al., 2008; Kadanka et al., 2017), optimized tract-specific dMRI analysis overcomes previous

spatially unselective analyses of the whole axial SC area. Thus, the observed relationship between electrophysiology and tract-based dMRI-derived metrics suggests that tract-specific approach might provide an objective tool to examine the relationship between diffusion-informed microstructural changes and functional electrophysiological impairments. Since dMRI is a non-invasive technique that is easier to perform than electrophysiological measures, tract-specific dMRI should be explored as a potential predictor of DCM development in future longitudinal studies.

5.3 Limitations

5.3.1 Study I (dMRI methodology)

Setting of DTI-RESOLVE protocol to exactly same b-values and diffusion gradient sampling scheme would be optimal for dMRI protocol comparison, yet it would lead to increase of DTI-RESOLVE's acquisition time, which was already longer relative to HARDI-ZOOMit protocols. Moreover, the goal of the work was to compare current clinically available dMRI protocol (i.e., RESOLVE) relative to optimized HARDI-ZOOMit protocols.

Although WM and GM ROIs provided higher spatial distinctions than usage of single ROI covering whole axial SC area, the template registration and utilizing of SC atlas (Lévy et al., 2015) could ensure even more spatially selective analysis. Indeed, tract-specific analysis demonstrated tissue specific changes in DCM (Wang et al., 2017) and ALS (Pisharady et al., 2020) patients and has been utilized in the Study II.

The signal dropouts in inferior parts (i.e., part of C7 and Th1 vertebral levels) of HARDI-ZOOMit's FOV limited its usage in caudal SC regions. The signal loss was probably caused by presence of air in the lungs and suppression of such artifacts will be the topic of future research.

Since changes in dMRI-derived metrics have been already reported also in symptomatic DCM patients (Kerkovský et al., 2012; Martin et al., 2018b), extension of our cohort was planned and has been done in the Study II.

Finally, the used stepwise linear regression and k-means clustering were used in relatively simple context and were limited by small cohort. More advanced algorithms may improve the classification results and yield to increase sensitivity.

5.3.2 Study II (Prospective dMRI study)

As described in the previous chapter, the study exanimated only C3-6 region due to spatial coverage of the HARDI-ZOOMit protocol. The analysis pipeline was semi-automatic and required time-consuming manual corrections of segmentations, mainly in patients with severe compressions. Severe compression further limited proper registration of SC template and atlas in five DCM patients. Although atlas-based approach allowed tract-specific analysis complemented by partial volume correction (Lévy et al., 2015), future studies may benefit from subject-specific tractography, which are not yet fully optimized for SC and are more sensitive to susceptibility induced distortions (Cohen-Adad and Wheeler-Kingshott, 2014), though.

The number of DCM patients was lower than number of NMDC patients, mainly due to lower prevalence of DCM relative to NMDC (Kovalova et al., 2016) and difficulty to require DCM patients since urgent surgery often takes priority.

5.4 General considerations about used spinal cord MRI protocol

The acquisition protocol discussed in this thesis was partly overlapping with multi-center *spine generic* consensus acquisition protocol (Cohen-Adad et al., 2021b), which however was not finalized at the time of beginning of this study. Nevertheless, I had been actively participating on prospective harmonization of the *spine generic* protocol (Cohen-Adad et al., 2021b) as well as on collecting of multi-subject dataset acquired across 42 centers worldwide (Cohen-Adad et al., 2021a).

Optimized HARDI-ZOOMit protocol is based on reduced field-of-view technique, which may not be available on all scanners, MR console software versions, or may be available within paid license. Despite the fact that optimized HARDI-ZOOMit protocol was tested only on Siemens scanners, potential translation to other vendors should be possible since both GE and Philips scanners also offer diffusion protocols built upon reduced field-of-view technique as well as possibility to manually import your own diffusion schemes (Cohen-Adad et al., 2021b). Entire acquisition protocol is freely available and can be easily imported to the scanner console.

Our group was also actively involved in international effort focused on visualization of spinal cord gray matter (Cohen-Adad et al., 2022). Our T_2*-w ME-GRE images submitted to this challenge (which were also used only with slight modification in the Study I and Study II) demonstrated excellent signal-to-noise and contrast-to-noise ratios comparable with

submitted protocols from other research centers (Cohen-Adad et al., 2022). Last but not least, the T_2*-w ME-GRE images were used in another parallel study from our group for computation of advanced morphometric metrics reflecting SC flattening, indentation and torsion and semi-automatically detected SC compression with better inter-trial variability compared to manual raters (Horáková et al., 2022).

It is also important to point out that our acquisition protocol contains turbo spin echo T_1-w axial image with high in-plane resolution and good WM/GM contrast; yet its usage is so far limited since current methods for GM segmentations based on convolution neural networks are trained solely on ME-GRE (i.e., T_2*-w) images (Perone et al., 2018).

5.5 Future directions

To our best knowledge, the multi-compartment ball-and-sticks model, which incorporates intra-axonal restriction and better characterizes dMRI data than DTI model (Panagiotaki et al., 2012), has not been utilized in the SC imaging on a large cohort of NMDC and DCM patients yet. Indeed, the ball-and-sticks *f1* metric revealed additional between-group differences that were not observed by complementary DTI FA metric, and allowed detection of second fiber bundles (i.e., *f2* metric) in areas of dorsal GM horns and anterior WM commissure (Figure 20). Further optimization of HARDI-ZOOMit protocol and utilizing of b-values > 1000 $s.mm^{-2}$ would allow estimation of other microstructural diffusion models, which were successfully translated from the brain to SC imaging but require higher b-values, such as NODDI (Grussu et al., 2015), CHARMED (Duval et al., 2017) or AxCaliber (Duval et al., 2018).

Since degenerative changes progress throughout aging, and the between-group age differences can be found in the literature (Kovalova et al., 2016; Martin et al., 2017a), we employed age as a covariate to our analyses to rule out its potential effect on the dMRI-derived metrics despite the fact that there were no significant age differences between groups in Study I nor Study II. To further mitigate potential bias from inter-subject variability, we also employed body mass index reflecting both participant's weight and height into between-group comparison in Study II. The investigation of potential relationship between the participants characteristics and dMRI-derived metrics is currently in the progress on the large multi-center dataset of >250 healthy participants (Cohen-Adad et al., 2021a).

We realize that future longitudinal trials are necessary and will be crucial for further understanding of underlying mechanisms in degenerative cervical SC compression and to validate prognostic value of proposed methodology. Indeed, we will continue in this effort in following years.

Regarding the broader context of rostral alterations detected by dMRI and volumetry in Study II pointing to Wallerian degeneration and atrophy, our other parallel study employing ^{1}H-MRS detected also neurochemical changes above the compression level (Horak et al., 2021). Thus, altogether, rostral changes were mirrored by three independent MR techniques: dMRI, volumetry and ^{1}H-MRS. Further investigation of the relationship between these techniques will be object of our future research.

Finally, we have been reformatting the dataset to facilitate the *Brain Imaging Data Structure* (BIDS) convention (Gorgolewski et al., 2016) to allow its release as an open-access dataset, similarly to the recently published dataset of healthy young volunteers (Cohen-Adad et al., 2021a). Such release is in line with current effort to make the MRI SC research more reproducible and will allow development of new processing methods and tools, for instance, GM segmentation algorithm for T_1-w axial images.

6 Summary and conclusions

6.1 Key findings

I studied in detail the potential of optimized multi-shell diffusion protocol to provide dMRI data suitable for fitting of the conventional DTI model as well as a multi-compartment ball-and-sticks model and its practical application in different stages of degenerative cervical spinal cord compression to serve as potential predictive marker of progression from NMDC to symptomatic DCM.

Our key findings are:

1. Optimized multi-shell dMRI protocol with reduced field-of-view (i.e., HARDI-ZOOMit) provided diffusion data with exceptional spatial and angular resolution in clinically feasible time without significant influence by image artifacts and outperformed a clinically used single-shell protocol based on readout-segmented EPI technique (i.e., DTI-RESOLVE).
2. Acquired multi-shell dMRI data were suitable for fitting of the conventional DTI model as well as multi-compartment ball-and-sticks model, which was so far applied only in brain imaging. The ball-and-sticks model detected crossing white matter fibers and revealed microstructural changes which were not detected by the conventional DTI model.
3. dMRI-derived microstructural metrics from both DTI and ball-and-sticks models demonstrated differences between NMDC and DCM patients relative to healthy controls with more progressive changes in DCM than NDMC patients.
4. Tissue-selective analysis revealed tract-specific alterations predominantly in dorsal and lateral columns and gray matter of the cervical spinal cord, congruent with previous histopathological studies and suggest demyelination and axonal degeneration as primary mechanisms of tissue degeneration.
5. Compression caused changes no only at the stenosis levels but also rostrally, pointing to Wallerian degeneration, trans-synaptic degeneration and atrophy rostrally to the compression levels.

6. Alterations detected by dMRI were reflected in clinical deficits assessed by mJOA scale and abnormal electrophysiology in relevant anatomical tracts pointing to crucial relationship between microstructural dMRI degeneration and functional impairments.

6.2 General conclusions

In conclusion, this PhD thesis clearly demonstrated that high-resolution multi-shell HARDI-ZOOMit protocol accompanied by optimized postprocessing and tract-specific analysis depicted spatially selective dMRI changes in different stages of degenerative spinal cord compression. The multi-shell HARDI-ZOOMit protocol provided dMRI data with high spatial and angular resolution suitable for estimation of diffusion models beyond the DTI model, i.e., the ball-and-sticks model. dMRI-derived alterations were predominantly detected in dorsal and lateral WM tracts and GM at the level of compression as well as rostrally at the level C3 pointing to demyelination, axonal degeneration and atrophy. Degenerative changes progressed from mild NMDC to more severe and symptomatic DCM and correlated with clinical deficits and abnormal electrophysiology in relevant anatomical tracts.

Thus, my work demonstrated that high-resolution tract-specific dMRI provides sensitive microstructural markers of SC alterations and offers new opportunities for longitudinal trials aiming to provide early predictors of progression into symptomatic myelopathy.

7 REFERENCES

Adamova, B., Bednarik, J., Andrasinova, T., Kovalova, I., Kopacik, R., Jabornik, M., Kerkovsky, M., Jakubcova, B., Jarkovsky, J., 2015. Does lumbar spinal stenosis increase the risk of spondylotic cervical spinal cord compression? Eur. Spine J. 24, 2946–2953. https://doi.org/10.1007/s00586-015-4049-0

Aleksanderek, I., McGregor, S.M.K., Stevens, T.K., Goncalves, S., Bartha, R., Duggal, N., 2017a. Cervical spondylotic myelopathy: Metabolite changes in the primary motor cortex after surgery. Radiology 282, 817–825. https://doi.org/10.1148/radiol.2016152083

Aleksanderek, I., Stevens, T.K., Goncalves, S., Bartha, R., Duggal, N., 2017b. Metabolite and functional profile of patients with cervical spondylotic myelopathy. J. Neurosurg. Spine 26, 547–553. https://doi.org/10.3171/2016.9.SPINE151507

Andersson, J.L.R., Skare, S., Ashburner, J., 2003. How to correct susceptibility distortions in spin-echo echo-planar images: application to diffusion tensor imaging. Neuroimage 20, 870–888. https://doi.org/10.1016/S1053-8119(03)00336-7

Andersson, J.L.R., Sotiropoulos, S.N., 2016. An integrated approach to correction for off-resonance effects and subject movement in diffusion MR imaging. Neuroimage 125, 1063–1078. https://doi.org/10.1016/j.neuroimage.2015.10.019

Assaf, Y., Freidlin, R.Z., Rohde, G.K., Basser, P.J., 2004. New modeling and experimental framework to characterize hindered and restricted water diffusion in brain white matter. Magn. Reson. Med. 52, 965–978. https://doi.org/10.1002/mrm.20274

Assaf, Y., Mayk, A., Cohen, Y., 2000. Displacement imaging of spinal cord using q-space diffusion-weighted MRI. Magn. Reson. Med. 44, 713–722. https://doi.org/10.1002/1522-2594(200011)44:5<713::AID-MRM9>3.0.CO;2-6

Avants, B.B., Tustison, N., Song, G., 2011. Advanced Normalization Tools (ANTS) 1–35.

Badhiwala, J.H., Ahuja, C.S., Akbar, M.A., Witiw, C.D., Nassiri, F., Furlan, J.C., Curt, A., Wilson, J.R., Fehlings, M.G., 2020. Degenerative cervical myelopathy — update and future directions. Nat. Rev. Neurol. 16, 108–124. https://doi.org/10.1038/s41582-019-0303-0

Banaszek, A., Bladowska, J., Szewczyk, P., Podgórski, P., Sąsiadek, M., 2014. Usefulness of

diffusion tensor MR imaging in the assessment of intramedullary changes of the cervical spinal cord in different stages of degenerative spine disease. Eur. Spine J. 23, 1523–1530. https://doi.org/10.1007/s00586-014-3323-x

Baptiste, D.C., Fehlings, M.G., 2006. Pathophysiology of cervical myelopathy. Spine J. 6, 190–197. https://doi.org/10.1016/j.spinee.2006.04.024

Basser, P.J., Mattiello, J., LeBihan, D., 1994. MR diffusion tensor spectroscopy and imaging. Biophys. J. 66, 259–267. https://doi.org/10.1016/S0006-3495(94)80775-1

Baucher, G., Rasoanandrianina, H., Levy, S., Pini, L., Troude, L., Roche, P.-H., Callot, V., 2021. T1 Mapping for Microstructural Assessment of the Cervical Spinal Cord in the Evaluation of Patients with Degenerative Cervical Myelopathy. Am. J. Neuroradiol. 42, 1348–1357. https://doi.org/10.3174/ajnr.A7157

Bédard, S., Cohen-Adad, J., 2021. Normalizing automatic spinal cord cross-sectional area measures. bioRxiv. https://doi.org/10.1101/2021.09.30.462636

Bednarik, J., Kadanka, Z., Dusek, L., Kerkovsky, M., Vohanka, S., Novotny, O., Urbanek, I., Kratochvilova, D., 2008. Presymptomatic spondylotic cervical myelopathy: An updated predictive model. Eur. Spine J. 17, 421–431. https://doi.org/10.1007/s00586-008-0585-1

Bednarik, J., Kadanka, Z., Dusek, L., Novotny, O., Surelova, D., Urbanek, I., Prokes, B., 2004. Presymptomatic spondylotic cervical cord compression. Spine (Phila. Pa. 1976). 29, 2260–2269. https://doi.org/10.1097/01.brs.0000142434.02579.84

Bednařík, J., Kadaňka, Z., Voháňka, S., Novotný, O., Šurelová, D., Filipovičová, D., Prokeš, B., 1998. The value of somatosensory and motor evoked potentials in pre-clinical spondylotic cervical cord compression. Eur. Spine J. 7, 493–500. https://doi.org/10.1007/s005860050113

Bednařík, J., Kadaňka, Z., Voháňka, S., Stejskal, L., Vlach, O., Schröder, R., 1999. The value of somatosensory- and motor-evoked potentials in predicting and monitoring the effect of therapy in spondylotic cervical myelopathy: Prospective randomized study. Spine (Phila. Pa. 1976). 24, 1593–1598. https://doi.org/10.1097/00007632-199908010-00014

Behrens, T.E.J., Woolrich, M.W., Jenkinson, M., Johansen-Berg, H., Nunes, R.G., Clare, S., Matthews, P.M., Brady, J.M., Smith, S.M., 2003. Characterization and Propagation of

Uncertainty in Diffusion-Weighted MR Imaging. Magn. Reson. Med. 50, 1077–1088. https://doi.org/10.1002/mrm.10609

Bernabéu-Sanz, Á., Mollá-Torró, J.V., López-Celada, S., Moreno López, P., Fernández-Jover, E., 2020. MRI evidence of brain atrophy, white matter damage, and functional adaptive changes in patients with cervical spondylosis and prolonged spinal cord compression. Eur. Radiol. 30, 357–369. https://doi.org/10.1007/s00330-019-06352-z

Budzik, J.F., Balbi, V., Le Thuc, V., Duhamel, A., Assaker, R., Cotten, A., 2011. Diffusion tensor imaging and fibre tracking in cervical spondylotic myelopathy. Eur. Radiol. 21, 426–433. https://doi.org/10.1007/s00330-010-1927-z

Caruyer, E., Lenglet, C., Sapiro, G., Deriche, R., 2013. Design of multishell sampling schemes with uniform coverage in diffusion MRI. Magn. Reson. Med. 69, 1534–1540. https://doi.org/10.1002/mrm.24736

Cohen-Adad, J., 2018. Microstructural imaging in the spinal cord and validation strategies. Neuroimage 182, 169–183. https://doi.org/10.1016/j.neuroimage.2018.04.009

Cohen-Adad, J., 2012. High-Resolution DWI in Brain and Spinal Cord with syngo RESOLVE. MAGNETOM Flash 2.

Cohen-Adad, J., Alonso-Ortiz, E., Abramovic, M., Arneitz, C., Atcheson, N., Barlow, L., Barry, R.L., Barth, M., Battiston, M., Büchel, C., Budde, M., Callot, V., Combes, A.J.E., De Leener, B., Descoteaux, M., de Sousa, P.L., Dostál, M., Doyon, J., Dvorak, A., Eippert, F., Epperson, K.R., Epperson, K.S., Freund, P., Finsterbusch, J., Foias, A., Fratini, M., Fukunaga, I., Gandini Wheeler-Kingshott, C.A.M., Germani, G., Gilbert, G., Giove, F., Gros, C., Grussu, F., Hagiwara, A., Henry, P.-G., Horák, T., Hori, M., Joers, J., Kamiya, K., Karbasforoushan, H., Keřkovský, M., Khatibi, A., Kim, J.-W., Kinany, N., Kitzler, H.H., Kolind, S., Kong, Y., Kudlička, P., Kuntke, P., Kurniawan, N.D., Kusmia, S., Labounek, R., Laganà, M.M., Laule, C., Law, C.S., Lenglet, C., Leutritz, T., Liu, Y., Llufriu, S., Mackey, S., Martinez-Heras, E., Mattera, L., Nestrasil, I., O'Grady, K.P., Papinutto, N., Papp, D., Pareto, D., Parrish, T.B., Pichiecchio, A., Prados, F., Rovira, À., Ruitenberg, M.J., Samson, R.S., Savini, G., Seif, M., Seifert, A.C., Smith, A.K., Smith, S.A., Smith, Z.A., Solana, E., Suzuki, Y., Tackley, G., Tinnermann, A., Valošek, J., Van De Ville, D., Yiannakas, M.C., Weber II, K.A., Weiskopf, N., Wise, R.G., Wyss, P.O., Xu, J., 2021a. Open-access quantitative MRI data of the spinal cord and

reproducibility across participants, sites and manufacturers. Sci. Data 8, 219. https://doi.org/10.1038/s41597-021-00941-8

Cohen-Adad, J., Alonso-Ortiz, E., Abramovic, M., Arneitz, C., Atcheson, N., Barlow, L., Barry, R.L., Barth, M., Battiston, M., Büchel, C., Budde, M., Callot, V., Combes, A.J.E., De Leener, B., Descoteaux, M., de Sousa, P.L., Dostál, M., Doyon, J., Dvorak, A., Eippert, F., Epperson, K.R., Epperson, K.S., Freund, P., Finsterbusch, J., Foias, A., Fratini, M., Fukunaga, I., Wheeler-Kingshott, C.A.M.G., Germani, G., Gilbert, G., Giove, F., Gros, C., Grussu, F., Hagiwara, A., Henry, P.-G., Horák, T., Hori, M., Joers, J., Kamiya, K., Karbasforoushan, H., Keřkovský, M., Khatibi, A., Kim, J.-W., Kinany, N., Kitzler, H., Kolind, S., Kong, Y., Kudlička, P., Kuntke, P., Kurniawan, N.D., Kusmia, S., Labounek, R., Laganà, M.M., Laule, C., Law, C.S., Lenglet, C., Leutritz, T., Liu, Y., Llufriu, S., Mackey, S., Martinez-Heras, E., Mattera, L., Nestrasil, I., O'Grady, K.P., Papinutto, N., Papp, D., Pareto, D., Parrish, T.B., Pichiecchio, A., Prados, F., Rovira, À., Ruitenberg, M.J., Samson, R.S., Savini, G., Seif, M., Seifert, A.C., Smith, A.K., Smith, S.A., Smith, Z.A., Solana, E., Suzuki, Y., Tackley, G., Tinnermann, A., Valošek, J., Van De Ville, D., Yiannakas, M.C., Weber, K.A., Weiskopf, N., Wise, R.G., Wyss, P.O., Xu, J., 2021b. Generic acquisition protocol for quantitative MRI of the spinal cord. Nat. Protoc. 16, 4611–4632. https://doi.org/10.1038/s41596-021-00588-0

Cohen-Adad, J., Wheeler-Kingshott, C., 2014. Quantitative MRI of the Spinal Cord, Quantitative MRI of the Spinal Cord. Elsevier. https://doi.org/10.1016/C2011-0-07594-4

Cohen-Adad, J., Alonso-Ortiz, E., Alley, S., Lagana, M.M., Baglio, F., Vannesjo, S.J., Karbasforoushan, H., Seif, M., Seifert, A.C., Xu, J., Kim, J.-W., Labounek, R., Vojtíšek, L., Dostal, M., Valošek, J., Samson, R.S., Grussu, F., Battiston, M., Wheeler-Kingshott, C.A.M., Yiannakas, M.C., Gilbert, G., Schneider, T., Johnson, B., Prados, F., 2022. Comparison of multi-center MRI protocols for visualizing the spinal cord gray matter. Magn. Reson. Med. under revi.

Cronin, A.E., Detombe, S.A., Duggal, C.A., Duggal, N., Bartha, R., 2021. Spinal cord compression is associated with brain plasticity in degenerative cervical myelopathy. Brain Commun. 3, 1–12. https://doi.org/10.1093/braincomms/fcab131

Cui, J.L., Li, X., Chan, T.Y., Mak, K.C., Luk, K.D.K., Hu, Y., 2015. Quantitative assessment of column-specific degeneration in cervical spondylotic myelopathy based on diffusion

tensor tractography. Eur. Spine J. 24, 41–47. https://doi.org/10.1007/s00586-014-3522-5

David, G., Mohammadi, S., Martin, A.R., Cohen-Adad, J., Weiskopf, N., Thompson, A., Freund, P., 2019. Traumatic and nontraumatic spinal cord injury: pathological insights from neuroimaging. Nat. Rev. Neurol. 15, 718–731. https://doi.org/10.1038/s41582-019-0270-5

David, G., Vallotton, K., Hupp, M., Curt, A., Freund, P., Seif, M., 2022. Extent of Cord Pathology in the Lumbosacral Enlargement in Non-Traumatic versus Traumatic Spinal Cord Injury. J. Neurotrauma. https://doi.org/10.1089/neu.2021.0389

De Leener, B., Cohen-Adad, J., Kadoury, S., 2015. Automatic Segmentation of the Spinal Cord and Spinal Canal Coupled with Vertebral Labeling. IEEE Trans. Med. Imaging. https://doi.org/10.1109/TMI.2015.2437192

De Leener, B., Fonov, V.S., Collins, D.L., Callot, V., Stikov, N., Cohen-Adad, J., 2018. PAM50: Unbiased multimodal template of the brainstem and spinal cord aligned with the ICBM152 space. Neuroimage 165, 170–179. https://doi.org/10.1016/j.neuroimage.2017.10.041

De Leener, B., Lévy, S., Dupont, S.M., Fonov, V.S., Stikov, N., Louis Collins, D., Callot, V., Cohen-Adad, J., 2017. SCT: Spinal Cord Toolbox, an open-source software for processing spinal cord MRI data. Neuroimage 145, 24–43. https://doi.org/10.1016/j.neuroimage.2016.10.009

Dietrich, O., Raya, J.G., Reeder, S.B., Reiser, M.F., Schoenberg, S.O., 2007. Measurement of signal-to-noise ratios in MR images: Influence of multichannel coils, parallel imaging, and reconstruction filters. J. Magn. Reson. Imaging 26, 375–385. https://doi.org/10.1002/jmri.20969

Dostál, M., Keřkovský, M., Staffa, E., Bednařík, J., Šprláková-Puková, A., Mechl, M., 2020. Voxelwise analysis of diffusion MRI of cervical spinal cord using tract-based spatial statistics. Magn. Reson. Imaging 73, 23–30. https://doi.org/10.1016/j.mri.2020.07.008

Duggal, N., Rabin, D., Bartha, R., Barry, R.L., Gati, J.S., Kowalczyk, I., Fink, M., 2010. Brain reorganization in patients with spinal cord compression evaluated using fMRI. Neurology

74, 1048–1054. https://doi.org/10.1212/WNL.0b013e3181d6b0ea

Duval, T., Lévy, S., Stikov, N., Campbell, J., Mezer, A., Witzel, T., Keil, B., Smith, V., Wald, L.L., Klawiter, E., Cohen-Adad, J., 2017. g-Ratio weighted imaging of the human spinal cord in vivo. Neuroimage 145, 11–23. https://doi.org/10.1016/j.neuroimage.2016.09.018

Duval, T., Smith, V., Stikov, N., Klawiter, E.C., Cohen-Adad, J., 2018. Scan–rescan of axcaliber, macromolecular tissue volume, and g-ratio in the spinal cord. Magn. Reson. Med. 79, 2759–2765. https://doi.org/10.1002/mrm.26945

Dvorak, J., Sutter, M., Herdmann, J., 2003. Cervical myelopathy: clinical and neurophysiological evaluation. Eur. Spine J. 12, S181–S187. https://doi.org/10.1007/s00586-003-0631-y

Dvorak, A. V., Ljungberg, E., Vavasour, I.M., Lee, L.E., Abel, S., Li, D.K.B., Traboulsee, A., MacKay, A.L., Kolind, S.H., 2021. Comparison of multi echo T2 relaxation and steady state approaches for myelin imaging in the central nervous system. Sci. Rep. 11, 1369. https://doi.org/10.1038/s41598-020-80585-7

Ellingson, B.M., Salamon, N., Grinstead, J.W., Holly, L.T., 2014. Diffusion tensor imaging predicts functional impairment in mild-to-moderate cervical spondylotic myelopathy. Spine J. 14, 2589–2597. https://doi.org/10.1016/j.spinee.2014.02.027

Ellingson, B.M., Salamon, N., Hardy, A.J., Holly, L.T., 2015a. Prediction of neurological impairment in cervical spondylotic myelopathy using a combination of diffusion mri and proton mr spectroscopy. PLoS One 10, e0139451. https://doi.org/10.1371/journal.pone.0139451

Ellingson, B.M., Salamon, N., Holly, L.T., 2015b. Advances in MR imaging for cervical spondylotic myelopathy. Eur. Spine J. 24, 197–208. https://doi.org/10.1007/s00586-013-2915-1

Ellingson, B.M., Salamon, N., Woodworth, D.C., Yokota, H., Holly, L.T., 2018. Reproducibility, temporal stability, and functional correlation of diffusion MR measurements within the spinal cord in patients with asymptomatic cervical stenosis or cervical myelopathy. J. Neurosurg. Spine 28, 472–480. https://doi.org/10.3171/2017.7.SPINE176

Ellingson, B.M., Woodworth, D.C., Leu, K., Salamon, N., Holly, L.T., 2019. Spinal Cord Perfusion MR Imaging Implicates Both Ischemia and Hypoxia in the Pathogenesis of Cervical Spondylosis. World Neurosurg. 128, e773–e781.

https://doi.org/10.1016/j.wneu.2019.04.253

Facon, D., Ozanne, A., Fillard, P., Tournoux-facon, C., Ducreux, D., 2005. MR diffusion tensor imaging and fiber tracking in spinal cord compression. AJNR Am J Neuroradiol 26, 1587–1594. https://doi.org/10.1016/j.jns.2013.07.1941

Fehlings, M.G., Tetreault, L.A., Riew, K.D., Middleton, J.W., Aarabi, B., Arnold, P.M., Brodke, D.S., Burns, A.S., Carette, S., Chen, R., Chiba, K., Dettori, J.R., Furlan, J.C., Harrop, J.S., Holly, L.T., Kalsi-Ryan, S., Kotter, M., Kwon, B.K., Martin, A.R., Milligan, J., Nakashima, H., Nagoshi, N., Rhee, J., Singh, A., Skelly, A.C., Sodhi, S., Wilson, J.R., Yee, A., Wang, J.C., 2017. A Clinical Practice Guideline for the Management of Patients With Degenerative Cervical Myelopathy: Recommendations for Patients With Mild, Moderate, and Severe Disease and Nonmyelopathic Patients With Evidence of Cord Compression. Glob. Spine J. 7, 70S-83S. https://doi.org/10.1177/2192568217701914

Finsterbusch, J., 2009. High-resolution diffusion tensor imaging with inner field-of-view EPI. J. Magn. Reson. Imaging 29, 987–993. https://doi.org/10.1002/jmri.21717

Gorgolewski, K.J., Auer, T., Calhoun, V.D., Craddock, R.C., Das, S., Duff, E.P., Flandin, G., Ghosh, S.S., Glatard, T., Halchenko, Y.O., Handwerker, D.A., Hanke, M., Keator, D., Li, X., Michael, Z., Maumet, C., Nichols, B.N., Nichols, T.E., Pellman, J., Poline, J.-B., Rokem, A., Schaefer, G., Sochat, V., Triplett, W., Turner, J.A., Varoquaux, G., Poldrack, R.A., 2016. The brain imaging data structure, a format for organizing and describing outputs of neuroimaging experiments. Sci. Data 3, 160044. https://doi.org/10.1038/sdata.2016.44

Grabher, P., Mohammadi, S., David, G., Freund, P., 2017. Neurodegeneration in the Spinal Ventral Horn Prior to Motor Impairment in Cervical Spondylotic Myelopathy. J. Neurotrauma 34, 2329–2334. https://doi.org/10.1089/neu.2017.4980

Grabher, P., Mohammadi, S., Trachsler, A., Friedl, S., David, G., Sutter, R., Weiskopf, N., Thompson, A.J., Curt, A., Freund, P., 2016. Voxel-based analysis of grey and white matter degeneration in cervical spondylotic myelopathy. Sci. Rep. 6, 24636. https://doi.org/10.1038/srep24636

Gros, C., De Leener, B., Badji, A., Maranzano, J., Eden, D., Dupont, S.M., Talbott, J., Zhuoquiong, R., Liu, Y., Granberg, T., Ouellette, R., Tachibana, Y., Hori, M., Kamiya, K., Chougar, L.,

Stawiarz, L., Hillert, J., Bannier, E., Kerbrat, A., Edan, G., Labauge, P., Callot, V., Pelletier, J., Audoin, B., Rasoanandrianina, H., Brisset, J.-C., Valsasina, P., Rocca, M.A., Filippi, M., Bakshi, R., Tauhid, S., Prados, F., Yiannakas, M., Kearney, H., Ciccarelli, O., Smith, S., Treaba, C.A., Mainero, C., Lefeuvre, J., Reich, D.S., Nair, G., Auclair, V., McLaren, D.G., Martin, A.R., Fehlings, M.G., Vahdat, S., Khatibi, A., Doyon, J., Shepherd, T., Charlson, E., Narayanan, S., Cohen-Adad, J., 2019. Automatic segmentation of the spinal cord and intramedullary multiple sclerosis lesions with convolutional neural networks. Neuroimage 184, 901–915. https://doi.org/10.1016/j.neuroimage.2018.09.081

Grussu, F., Schneider, T., Zhang, H., Alexander, D.C., Wheeler-Kingshott, C.A.M., 2015. Neurite orientation dispersion and density imaging of the healthy cervical spinal cord in vivo. Neuroimage 111, 590–601. https://doi.org/10.1016/j.neuroimage.2015.01.045

Guan, X., Fan, G., Wu, X., Gu, G., Gu, X., Zhang, H., He, S., 2015. Diffusion Tensor Imaging Studies of Cervical Spondylotic Myelopathy: A Systemic Review and Meta-Analysis. PLoS One 10, e0117707. https://doi.org/10.1371/journal.pone.0117707

Helms, G., Dathe, H., Kallenberg, K., Dechent, P., 2008. High-resolution maps of magnetization transfer with inherent correction for RF inhomogeneity and T1 relaxation obtained from 3D FLASH MRI. Magn. Reson. Med. 60, 1396–1407. https://doi.org/10.1002/mrm.21732

Holly, L.T., Ellingson, B.M., Salamon, N., 2017. Metabolic imaging using proton magnetic spectroscopy as a predictor of outcome after surgery for cervical spondylotic myelopathy. Clin. Spine Surg. 30, E615–E619. https://doi.org/10.1097/BSD.0000000000000248

Horak, T., Horakova, M., Svatkova, A., Kadanka, Z., Kudlicka, P., Valosek, J., Rohan, T., Kerkovsky, M., Vlckova, E., Kadanka, Z., Deelchand, D.K., Henry, P.-G., Bednarik, J., Bednarik, P., 2021. In vivo Molecular Signatures of Cervical Spinal Cord Pathology in Degenerative Compression. J. Neurotrauma 38, 2999–3010. https://doi.org/10.1089/neu.2021.0151

Horáková, M., Horák, T., Valošek, J., Rohan, T., Koriťáková, E., Dostál, M., Kočica, J., Skutil, T., Keřkovský, M., Kadaňka Jr, Z., Bednařík, P., Svátková, A., Hluštík, P., Bednařík, J., 2022. Semi-automated detection of cervical spinal cord compression with the Spinal Cord Toolbox. Quant. Imaging Med. Surg. 12, 2261–2279. https://doi.org/10.21037/qims-21-782

Hori, M., Fukunaga, I., Masutani, Y., Nakanishi, A., Shimoji, K., Kamagata, K., Asahi, K., Hamasaki, N., Suzuki, Y., Aoki, S., 2012. New diffusion metrics for spondylotic myelopathy at an early clinical stage. Eur. Radiol. 22, 1797–1802. https://doi.org/10.1007/s00330-012-2410-9

Hori, M., Hagiwara, A., Fukunaga, I., Ueda, R., Kamiya, K., Suzuki, Y., Liu, W., Murata, K., Takamura, T., Hamasaki, N., Irie, R., Kamagata, K., Kumamaru, K.K., Suzuki, M., Aoki, S., 2018. Application of Quantitative Microstructural MR Imaging with Atlas-based Analysis for the Spinal Cord in Cervical Spondylotic Myelopathy. Sci. Rep. 8, 5213. https://doi.org/10.1038/s41598-018-23527-8

Hori, M., Tsutsumi, S., Yasumoto, Y., Ito, M., Suzuki, M., Tanaka, F.S., Kyogoku, S., Nakamura, M., Tabuchi, T., Fukunaga, I., Suzuki, Y., Kamagata, K., Masutani, Y., Aoki, S., 2014. Cervical spondylosis: Evaluation of microstructural changes in spinal cord white matter and gray matter by diffusional kurtosis imaging. Magn. Reson. Imaging 32, 428–432. https://doi.org/10.1016/j.mri.2014.01.018

Iwama, T., Ohba, T., Okita, G., Ebata, S., Ueda, R., Motosugi, U., Onishi, H., Haro, H., Hori, M., 2020. Utility and validity of neurite orientation dispersion and density imaging with diffusion tensor imaging to quantify the severity of cervical spondylotic myelopathy and assess postoperative neurological recovery. Spine J. 20, 417–425. https://doi.org/10.1016/j.spinee.2019.10.019

Jan, J., 2005. Medical Image Processing, Reconstruction and Restoration: Concepts and Methods. CRC, Taylor & Francis, Boca Raton.

Jbabdi, S., Sotiropoulos, S.N., Savio, A.M., Graña, M., Behrens, T.E., 2012. Model-based analysis of multishell diffusion MR data for tractography: How to get over fitting problems. Magn. Reson. Med. 68, 1846–1855. https://doi.org/10.1002/mrm.24204

Jenkinson, M., Beckmann, C.F., Behrens, T.E.J., Woolrich, M.W., Smith, S.M., 2012. FSL. Neuroimage 62, 782–790. https://doi.org/10.1016/j.neuroimage.2011.09.015

Jensen, J.H., Helpern, J.A., Ramani, A., Lu, H., Kaczynski, K., 2005. Diffusional kurtosis imaging: The quantification of non-Gaussian water diffusion by means of magnetic resonance imaging. Magn. Reson. Med. 53, 1432–1440. https://doi.org/10.1002/mrm.20508

Johansen-Berg, H., Behrens, T.E.J., 2013. Diffusion MRI: From Quantitative Measurement to In

vivo Neuroanatomy: Second Edition, Diffusion MRI: From Quantitative Measurement to In vivo Neuroanatomy: Second Edition. Elsevier Science. https://doi.org/10.1016/C2011-0-07047-3

Jones, D.K., 2004. The effect of gradient sampling schemes on measures derived from diffusion tensor MRI: A Monte Carlo study. Magn. Reson. Med. 51, 807–815. https://doi.org/10.1002/mrm.20033

Jones, J.G.A., Cen, S.Y., Lebel, R.M., Hsieh, P.C., Law, M., 2013. Diffusion tensor imaging correlates with the clinical assessment of disease severity in cervical spondylotic myelopathy and predicts outcome following surgery. Am. J. Neuroradiol. 34, 471–478. https://doi.org/10.3174/ajnr.A3199

Jutzeler, C.R., Ulrich, A., Huber, B., Rosner, J., Kramer, J.L.K., Curt, A., 2017. Improved Diagnosis of Cervical Spondylotic Myelopathy with Contact Heat Evoked Potentials. J. Neurotrauma 34, 2045–2053. https://doi.org/10.1089/neu.2016.4891

Kadanka, Z., Adamova, B., Kerkovsky, M., Kadanka, Z., Dusek, L., Jurova, B., Vlckova, E., Bednarik, J., 2017. Predictors of symptomatic myelopathy in degenerative cervical spinal cord compression. Brain Behav. 7, e00797. https://doi.org/10.1002/brb3.797

Kadanka, Z., Kadanka, Z., Skutil, T., Vlckova, E., Bednarik, J., 2021. Walk and Run Test in Patients with Degenerative Compression of the Cervical Spinal Cord. J. Clin. Med. 10, 927. https://doi.org/10.3390/jcm10050927

Kato, F., Yukawa, Y., Suda, K., Yamagata, M., Ueta, T., 2012. Normal morphology, age-related changes and abnormal findings of the cervical spine. Part II: Magnetic resonance imaging of over 1,200 asymptomatic subjects. Eur. Spine J. 21, 1499–1507. https://doi.org/10.1007/s00586-012-2176-4

Kerkovský, M., Bednarík, J., Dušek, L., Šprláková-Puková, A., Urbánek, I., Mechl, M., Válek, V., Kadanka, Z., 2012. Magnetic Resonance Diffusion Tensor Imaging in Patients With Cervical Spondylotic Spinal Cord Compression. Spine (Phila. Pa. 1976). 37, 48–56. https://doi.org/10.1097/BRS.0b013e31820e6c35

Keřkovský, M., Bednařík, J., Jurová, B., Dušek, L., Kadaňka, Z., Kadaňka, Z., Němec, M., Kovaľová, I., Šprláková-Puková, A., Mechl, M., 2017. Spinal Cord MR Diffusion Properties in Patients

with Degenerative Cervical Cord Compression. J. Neuroimaging 27, 149–157. https://doi.org/10.1111/jon.12372

Kovalova, I., Kerkovsky, M., Kadanka, Z., Kadanka, Z., Nemec, M., Jurova, B., Dusek, L., Jarkovsky, J., Bednarik, J., 2016. Prevalence and imaging characteristics of nonmyelopathic and myelopathic spondylotic cervical cord compression. Spine (Phila. Pa. 1976). 41, 1908–1916. https://doi.org/10.1097/BRS.0000000000001842

Kowalczyk, I., Duggal, N., Bartha, R., 2012. Proton magnetic resonance spectroscopy of the motor cortex in cervical myelopathy. Brain 135, 461–468. https://doi.org/10.1093/brain/awr328

Labounek, R., Valošek, J., Horák, T., Svátková, A., Bednařík, P., Vojtíšek, L., Horáková, M., Nestrašil, I., Lenglet, C., Cohen-Adad, J., Bednařík, J., Hluštík, P., 2020. HARDI-ZOOMit protocol improves specificity to microstructural changes in presymptomatic myelopathy. Sci. Rep. 10, 17529. https://doi.org/10.1038/s41598-020-70297-3

Lee, J.W., Kim, J.H., Park, J. Bin, Park, K.W., Yeom, J.S., Lee, G.Y., Kang, H.S., 2011. Diffusion tensor imaging and fiber tractography in cervical compressive myelopathy: Preliminary results. Skeletal Radiol. 40, 1543–1551. https://doi.org/10.1007/s00256-011-1161-z

Lévy, S., Benhamou, M., Naaman, C., Rainville, P., Callot, V., Cohen-Adad, J., 2015. White matter atlas of the human spinal cord with estimation of partial volume effect. Neuroimage 119, 262–271. https://doi.org/10.1016/j.neuroimage.2015.06.040

Li, C.X., Patel, S., Zhang, X., 2020. Evaluation of multi-shell diffusion MRI acquisition strategy on quantitative analysis using multi-compartment models. Quant. Imaging Med. Surg. 10, 824–834. https://doi.org/10.21037/QIMS.2020.03.11

Lindberg, P.G., Sanchez, K., Ozcan, F., Rannou, F., Poiraudeau, S., Feydy, A., Maier, M.A., 2016. Correlation of force control with regional spinal DTI in patients with cervical spondylosis without signs of spinal cord injury on conventional MRI. Eur. Radiol. 26, 733–742. https://doi.org/10.1007/s00330-015-3876-z

Lipton, M.L., 2008. Totally Accessible MRI: A User's Guide to Principles, Technology, and Applications, 1st ed. Springer Science & Business Media, New York, NY.

Liu, H., MacMillian, E.L., Jutzeler, C.R., Ljungberg, E., MacKay, A.L., Kolind, S.H., Mädler, B., Li,

D.K.B., Dvorak, M.F., Curt, A., Laule, C., Kramer, J.L.K., 2017. Assessing structure and function of myelin in cervical spondylotic myelopathy. Neurology 89, 602–610. https://doi.org/10.1212/WNL.0000000000004197

Liu, X., Qian, W., Jin, R., Li, X., Luk, K.D., Wu, E.X., Hu, Y., 2016. Amplitude of Low Frequency Fluctuation (ALFF) in the Cervical Spinal Cord with Stenosis: A Resting State fMRI Study. PLoS One 11, e0167279. https://doi.org/10.1371/journal.pone.0167279

Maes, F., Collignon, A., Vandermeulen, D., Marchal, G., Suetens, P., 1997. Multimodality image registration by maximization of mutual information. IEEE Trans. Med. Imaging 16, 187–198.

Maier, I.L., Hofer, S., Eggert, E., Schregel, K., Psychogios, M.-N., Frahm, J., Bähr, M., Liman, J., 2020. T1 Mapping Quantifies Spinal Cord Compression in Patients With Various Degrees of Cervical Spinal Canal Stenosis. Front. Neurol. 11, 1–8. https://doi.org/10.3389/fneur.2020.574604

Mair, W.G.P., Druckman, R., 1953. The pathology of spinal cord lesions and their relation to the clinical features in protrusion of cervical intervertebral discs (a report of four cases). Brain 76, 70–91. https://doi.org/10.1093/brain/76.1.70

Maki, S., Koda, M., Ota, M., Oikawa, Y., Kamiya, K., Inada, T., Furuya, T., Takahashi, K., Masuda, Y., Matsumoto, K., Kojima, M., Obata, T., Yamazaki, M., 2018. Reduced Field-of-View Diffusion Tensor Imaging of the Spinal Cord Shows Motor Dysfunction of the Lower Extremities in Patients With Cervical Compression Myelopathy. Spine (Phila. Pa. 1976). 43, 89–96. https://doi.org/10.1097/BRS.0000000000001123

Maki, S., Koda, M., Saito, J., Takahashi, S., Inada, T., Kamiya, K., Ota, M., Iijima, Y., Masuda, Y., Matsumoto, K., Kojima, M., Takahashi, K., Obata, T., Yamazaki, M., Furuya, T., 2016. Tract-Specific Diffusion Tensor Imaging Reveals Laterality of Neurological Symptoms in Patients with Cervical Compression Myelopathy. World Neurosurg. 96, 184–190. https://doi.org/10.1016/j.wneu.2016.08.129

Mamata, H., Jolesz, F.A., Maier, S.E., 2005. Apparent diffusion coefficient and fractional anisotropy in spinal cord: Age and cervical spondylosis-related changes. J. Magn. Reson. Imaging 22, 38–43. https://doi.org/10.1002/jmri.20357

Martin, A.R., Aleksanderek, I., Cohen-Adad, J., Tarmohamed, Z., Tetreault, L., Smith, N., Cadotte, D.W., Crawley, A., Ginsberg, H., Mikulis, D.J., Fehlings, M.G., 2016. Translating state-of-the-art spinal cord MRI techniques to clinical use: A systematic review of clinical studies utilizing DTI, MT, MWF, MRS, and fMRI. NeuroImage Clin. 10, 192–238. https://doi.org/10.1016/j.nicl.2015.11.019

Martin, A.R., De Leener, B., Cohen-Adad, J., Cadotte, D.W., Kalsi-Ryan, S., Lange, S.F., Tetreault, L., Nouri, A., Crawley, A., Mikulis, D.J., Ginsberg, H., Fehlings, M.G., 2017a. Clinically Feasible Microstructural MRI to Quantify Cervical Spinal Cord Tissue Injury Using DTI, MT, and T2*-Weighted Imaging: Assessment of Normative Data and Reliability. AJNR. Am. J. Neuroradiol. 38, 1257–1265. https://doi.org/10.3174/ajnr.A5163

Martin, A.R., De Leener, B., Cohen-Adad, J., Cadotte, D.W., Kalsi-Ryan, S., Lange, S.F., Tetreault, L., Nouri, A., Crawley, A., Mikulis, D.J., Ginsberg, H., Fehlings, M.G., 2017b. A novel MRI biomarker of spinal cord white matter injury: T2∗-weighted white matter to gray matter signal intensity ratio. Am. J. Neuroradiol. 38, 1266–1273. https://doi.org/10.3174/ajnr.A5162

Martin, A.R., De Leener, B., Cohen-Adad, J., Cadotte, D.W., Nouri, A., Wilson, J.R., Tetreault, L., Crawley, A.P., Mikulis, D.J., Ginsberg, H., Fehlings, M.G., 2018a. Can microstructural MRI detect subclinical tissue injury in subjects with asymptomatic cervical spinal cord compression? A prospective cohort study. BMJ Open 8, e019809. https://doi.org/10.1136/bmjopen-2017-019809

Martin, A.R., De Leener, B., Cohen-Adad, J., Kalsi-Ryan, S., Cadotte, D.W., Wilson, J.R., Tetreault, L., Nouri, A., Crawley, A., Mikulis, D.J., Ginsberg, H., Massicotte, E.M., Fehlings, M.G., 2018b. Monitoring for myelopathic progression with multiparametric quantitative MRI. PLoS One 13, e0195733. https://doi.org/10.1371/journal.pone.0195733

Martin, A.R., Tetreault, L., Nouri, A., Curt, A., Freund, P., Rahimi-Movaghar, V., Wilson, J.R., Fehlings, M.G., Kwon, B.K., Harrop, J.S., Davies, B.M., Kotter, M.R.N., Guest, J.D., Aarabi, B., Kurpad, S.N., 2022. Imaging and Electrophysiology for Degenerative Cervical Myelopathy [AO Spine RECODE-DCM Research Priority Number 9]. Glob. Spine J. 12, 130S-146S. https://doi.org/10.1177/21925682211057484

McLachlin, S., Leung, J., Sivan, V., Quirion, P., Wilkie, P., Cohen-Adad, J., Whyne, C.M., Hardisty,

M.R., 2021. Spatial correspondence of spinal cord white matter tracts using diffusion tensor imaging, fibre tractography, and atlas-based segmentation. Neuroradiology 63, 373–380. https://doi.org/10.1007/s00234-021-02635-9

Mori, S., Tournier, J.-D., 2014. Introduction to Diffusion Tensor Imaging: And Higher Order Models, 2 edition. ed. Academic Press, Amsterdam.

Nouri, A., Martin, A.R., Kato, S., Reihani-Kermani, H., Riehm, L.E., Fehlings, M.G., 2017. The Relationship between MRI Signal Intensity Changes, Clinical Presentation, and Surgical Outcome in Degenerative Cervical Myelopathy. Spine (Phila. Pa. 1976). 42, 1851–1858. https://doi.org/10.1097/BRS.0000000000002234

Nouri, A., Martin, A.R., Mikulis, D., Fehlings, M.G., 2016. Magnetic resonance imaging assessment of degenerative cervical myelopathy: A review of structural changes and measurement techniques. Neurosurg. Focus 40, E5. https://doi.org/10.3171/2016.3.FOCUS1667

Nurick, S., 1972. The pathogenesis of the spinal cord disorder associated with cervical spondylosis. Brain 95, 87–100. https://doi.org/10.1093/brain/95.1.87

Oh, T., Lafage, R., Lafage, V., Protopsaltis, T., Challier, V., Shaffrey, C., Kim, H.J., Arnold, P., Chapman, J., Schwab, F., Massicotte, E., Yoon, T., Bess, S., Fehlings, M., Smith, J., Ames, C., 2017. Comparing Quality of Life in Cervical Spondylotic Myelopathy with Other Chronic Debilitating Diseases Using the Short Form Survey 36-Health Survey. World Neurosurg. 106, 699–706. https://doi.org/10.1016/j.wneu.2016.12.124

Okita, G., Ohba, T., Takamura, T., Ebata, S., Ueda, R., Onishi, H., Haro, H., Hori, M., 2018. Application of neurite orientation dispersion and density imaging or diffusion tensor imaging to quantify the severity of cervical spondylotic myelopathy and to assess postoperative neurologic recovery. Spine J. 18, 268–275. https://doi.org/10.1016/j.spinee.2017.07.007

Öz, G., Alger, J.R., Barker, P.B., Bartha, R., Bizzi, A., Boesch, C., Bolan, P.J., Brindle, K.M., Cudalbu, C., Dinçer, A., Dydak, U., Emir, U.E., Frahm, J., González, R.G., Gruber, S., Gruetter, R., Gupta, R.K., Heerschap, A., Henning, A., Hetherington, H.P., Howe, F.A., Hüppi, P.S., Hurd, R.E., Kantarci, K., Klomp, D.W.J., Kreis, R., Kruiskamp, M.J., Leach, M.O.,

Lin, A.P., Luijten, P.R., Marjańska, M., Maudsley, A.A., Meyerhoff, D.J., Mountford, C.E., Nelson, S.J., Pamir, M.N., Pan, J.W., Peet, A.C., Poptani, H., Posse, S., Pouwels, P.J.W., Ratai, E.-M., Ross, B.D., Scheenen, T.W.J., Schuster, C., Smith, I.C.P., Soher, B.J., Tkáč, I., Vigneron, D.B., Kauppinen, R.A., 2014. Clinical Proton MR Spectroscopy in Central Nervous System Disorders. Radiology 270, 658–679. https://doi.org/10.1148/radiol.13130531

Paliwal, M., Weber, K.A., Hopkins, B.S., Cantrell, D.R., Hoggarth, M.A., Elliott, J.M., Dahdaleh, N.S., Mackey, S., Parrish, T.D., Dhaher, Y., Smith, Z.A., 2020. Magnetization Transfer Ratio and Morphometrics of the Spinal Cord Associates with Surgical Recovery in Patients with Degenerative Cervical Myelopathy. World Neurosurg. 144, e939–e947. https://doi.org/10.1016/j.wneu.2020.09.148

Panagiotaki, E., Schneider, T., Siow, B., Hall, M.G., Lythgoe, M.F., Alexander, D.C., 2012. Compartment models of the diffusion MR signal in brain white matter: A taxonomy and comparison. Neuroimage 59, 2241–2254. https://doi.org/10.1016/j.neuroimage.2011.09.081

Papinutto, N., Asteggiano, C., Bischof, A., Gundel, T.J., Caverzasi, E., Stern, W.A., Bastianello, S., Hauser, S.L., Henry, R.G., 2020. Intersubject Variability and Normalization Strategies for Spinal Cord Total Cross-Sectional and Gray Matter Areas. J. Neuroimaging 30, 110–118. https://doi.org/10.1111/jon.12666

Penny, W., Friston, K., Ashburner, J., Kiebel, S., Nichols, T., 2007. Statistical Parametric Mapping, Statistical Parametric Mapping: The Analysis of Functional Brain Images. Elsevier. https://doi.org/10.1016/B978-0-12-372560-8.X5000-1

Perone, C.S., Calabrese, E., Cohen-Adad, J., 2018. Spinal cord gray matter segmentation using deep dilated convolutions. Sci. Rep. 8, 5966. https://doi.org/10.1038/s41598-018-24304-3

Pisharady, P.K., Eberly, L.E., Cheong, I., Manousakis, G., Guliani, G., Clark, H.B., Bathe, M., Walk, D., Lenglet, C., 2020. Tract-specific analysis improves sensitivity of spinal cord diffusion MRI to cross-sectional and longitudinal changes in amyotrophic lateral sclerosis. Commun. Biol. 3, 370. https://doi.org/10.1038/s42003-020-1093-z

Rajasekaran, S., Yerramshetty, J.S., Chittode, V.S., Kanna, R.M., Balamurali, G., Shetty, A.P.,

2014. The Assessment of Neuronal Status in Normal and Cervical Spondylotic Myelopathy Using Diffusion Tensor Imaging. Spine (Phila. Pa. 1976). 39, 1183–1189. https://doi.org/10.1097/BRS.0000000000000369

Rao, A., Soliman, H., Kaushal, M., Motovylyak, O., Vedantam, A., Budde, M.D., Schmit, B., Wang, M., Kurpad, S.N., 2018. Diffusion Tensor Imaging in a Large Longitudinal Series of Patients With Cervical Spondylotic Myelopathy Correlated With Long-Term Functional Outcome. Neurosurgery 83, 753–760. https://doi.org/10.1093/neuros/nyx558

Salamon, N., Ellingson, B.M., Nagarajan, R., Gebara, N., Thomas, A., Holly, L.T., 2013. Proton magnetic resonance spectroscopy of human cervical spondylosis at 3T. Spinal Cord 51, 558–563. https://doi.org/10.1038/sc.2013.31

Samson, R.S., Lévy, S., Schneider, T., Smith, A.K., Smith, S.A., Cohen-Adad, J., Gandini Wheeler-Kingshott, C.A.M., 2016. ZOOM or Non-ZOOM? Assessing Spinal Cord Diffusion Tensor Imaging Protocols for Multi-Centre Studies. PLoS One 11, e0155557. https://doi.org/10.1371/journal.pone.0155557

Schild, H.H., 1990. MRI made easy. Schering AG, Berlin.

Seif, M., David, G., Huber, E., Vallotton, K., Curt, A., Freund, P., 2020. Cervical Cord Neurodegeneration in Traumatic and Non-Traumatic Spinal Cord Injury. J. Neurotrauma 37, 860–867. https://doi.org/10.1089/neu.2019.6694

Sherman, J.L., Nassaux, P.Y., Citrin, C.M., 1990. Measurements of the normal cervical spinal cord on MR imaging. Am. J. Neuroradiol. 11, 369–372.

Smith, S.S., Stewart, M.E., Davies, B.M., Kotter, M.R.N., 2021. The Prevalence of Asymptomatic and Symptomatic Spinal Cord Compression on Magnetic Resonance Imaging: A Systematic Review and Meta-analysis. Glob. Spine J. 11, 597–607. https://doi.org/10.1177/2192568220934496

Standring, S., 2020. Gray's Anatomy, 42nd ed, Gray's Anatomy. Elsevier.

Tan, Y., Zhou, F., Wu, L., Liu, Z., Zeng, X., Gong, H., He, L., 2015. Alteration of Regional Homogeneity within the Sensorimotor Network after Spinal Cord Decompression in Cervical Spondylotic Myelopathy: A Resting-State fMRI Study. Biomed Res. Int. 2015, 1–6. https://doi.org/10.1155/2015/647958

Tetreault, L., Kopjar, B., Nouri, A., Arnold, P., Barbagallo, G., Bartels, R., Qiang, Z., Singh, A., Zileli, M., Vaccaro, A., Fehlings, M.G., 2017. The modified Japanese Orthopaedic Association scale: establishing criteria for mild, moderate and severe impairment in patients with degenerative cervical myelopathy. Eur. Spine J. 26, 78–84. https://doi.org/10.1007/s00586-016-4660-8

Tuch, D.S., 2004. Q-ball imaging. Magn. Reson. Med. 52, 1358–1372. https://doi.org/10.1002/mrm.20279

Tuch, D.S., Reese, T.G., Wiegell, M.R., Makris, N., Belliveau, J.W., Van Wedeen, J., 2002. High angular resolution diffusion imaging reveals intravoxel white matter fiber heterogeneity. Magn. Reson. Med. 48, 577–582. https://doi.org/10.1002/mrm.10268

Tustison, N.J., Cook, P.A., Gee, J.C., 2011. N4ITK: improved N3 bias correction. IEEE Trans. Med. Imaging 29, 1310–1320. https://doi.org/10.1109/TMI.2010.2046908.N4ITK

Uda, T., Takami, T., Tsuyuguchi, N., Sakamoto, S., Yamagata, T., Ikeda, H., Nagata, T., Ohata, K., 2013. Assessment of cervical spondylotic myelopathy using diffusion tensor magnetic resonance imaging parameter at 3.0 tesla. Spine (Phila. Pa. 1976). 38, 407–414. https://doi.org/10.1097/BRS.0b013e31826f25a3

Vallotton, K., David, G., Hupp, M., Pfender, N., Cohen-Adad, J., Fehlings, M.G., Samson, R.S., Wheeler-Kingshott, C.A.M.G., Curt, A., Freund, P., Seif, M., 2021. Tracking White and Gray Matter Degeneration along the Spinal Cord Axis in Degenerative Cervical Myelopathy. J. Neurotrauma 38, 2978–2987. https://doi.org/10.1089/neu.2021.0148

Valošek, J., Bednařík, P., Horák, T., Horáková, M., Svátková, A., Labounek, R., Hluštík, P., Bednařík, J., 2020. Cervical Spinal Cord Atrophy Above Level of Asymptomatic Degenerative Cervical Cord Compression, in: 26th Annual Meeting of the Organization for Human Brain Mapping. Virtual, p. 3136.

Valošek, J., Bednařík, P., Keřkovský, M., Hluštík, P., Bednařík, J., Svátková, A., 2022. Quantitative MR Markers in Non-Myelopathic Spinal Cord Compression: A Narrative Review. J. Clin. Med. (accepted). https://doi.org/10.20944/preprints202202.0355

Valošek, J., Labounek, R., Horák, T., Horáková, M., Bednařík, P., Keřkovský, M., Kočica, J., Rohan, T., Lenglet, C., Cohen-Adad, J., Hluštík, P., Vlčková, E., Kadaňka, Z., Bednařík, J., Svatkova,

A., 2021. Diffusion magnetic resonance imaging reveals tract-specific microstructural correlates of electrophysiological impairments in non-myelopathic and myelopathic spinal cord compression. Eur. J. Neurol. 28, 3784–3797. https://doi.org/10.1111/ene.15027

Verma, T., Cohen-Adad, J., 2014. Effect of respiration on the B0 field in the human spinal cord at 3T. Magn. Reson. Med. 72, 1629–1636. https://doi.org/10.1002/mrm.25075

Wang, K.Y., Idowu, O., Thompson, C.B., Orman, G., Myers, C., Riley, L.H., Carrino, J.A., Flammang, A., Gilson, W., Sadowsky, C.L., Izbudak, I., 2017. Tract-Specific Diffusion Tensor Imaging in Cervical Spondylotic Myelopathy Before and After Decompressive Spinal Surgery: Preliminary Results. Clin. Neuroradiol. 27, 61–69. https://doi.org/10.1007/s00062-015-0418-7

Wen, C.Y., Cui, J.L., Liu, H.S., Mak, K.C., Cheung, W.Y., Luk, K.D.K., Hu, Y., 2014a. Is diffusion anisotropy a biomarker for disease severity and surgical prognosis of cervical spondylotic myelopathy. Radiology 270, 197–204. https://doi.org/10.1148/radiol.13121885

Wen, C.Y., Cui, J.L., Mak, K.C., Luk, K.D.K., Hu, Y., 2014b. Diffusion tensor imaging of somatosensory tract in cervical spondylotic myelopathy and its link with electrophysiological evaluation. Spine J. 14, 1493–1500. https://doi.org/10.1016/j.spinee.2013.08.052

WFNS, 2019. Cervical Spondylotic Myelopathy [WWW Document]. Recomm. WFNS Spine Comm. URL http://wfns-spine.org/recom-cervical-spondylotic-myelopathy-1 (accessed 5.15.22).

Wheeler-Kingshott, C.A.M., Hickman, S.J., Parker, G.J.M., Ciccarelli, O., Symms, M.R., Miller, D.H., Barker, G.J., 2002. Investigating cervical spinal cord structure using axial diffusion tensor imaging. Neuroimage 16, 93–102. https://doi.org/10.1006/nimg.2001.1022

Wilm, B.J., Svensson, J., Henning, A., Pruessmann, K.P., Boesiger, P., Kollias, S.S., 2007. Reduced field-of-view MRI using outer volume suppression for spinal cord diffusion imaging. Magn. Reson. Med. 57, 625–630. https://doi.org/10.1002/mrm.21167

Wilson, J.R., Barry, S., Fischer, D.J., Skelly, A.C., Arnold, P.M., Riew, K.D., Shaffrey, C.I., Traynelis, V.C., Fehlings, M.G., 2013. Frequency, Timing, and Predictors of Neurological Dysfunction

in the Nonmyelopathic Patient With Cervical Spinal Cord Compression, Canal Stenosis, and/or Ossification of the Posterior Longitudinal Ligament. Spine (Phila. Pa. 1976). 38, S37–S54. https://doi.org/10.1097/BRS.0b013e3182a7f2e7

Witiw, C.D., Mathieu, F., Nouri, A., Fehlings, M.G., 2018. Clinico-Radiographic Discordance: An Evidence-Based Commentary on the Management of Degenerative Cervical Spinal Cord Compression in the Absence of Symptoms or With Only Mild Symptoms of Myelopathy. Glob. Spine J. 8, 527–534. https://doi.org/10.1177/2192568217745519

Xu, J., Shimony, J.S., Klawiter, E.C., Snyder, A.Z., Trinkaus, K., Naismith, R.T., Benzinger, T.L.S., Cross, A.H., Song, S.-K., 2013. Improved in vivo diffusion tensor imaging of human cervical spinal cord. Neuroimage 6711. https://doi.org/10.1016/j.neuroimage.2012.11.014

Zhang, H., Schneider, T., Wheeler-Kingshott, C.A., Alexander, D.C., 2012. NODDI: Practical in vivo neurite orientation dispersion and density imaging of the human brain. Neuroimage 61, 1000–1016. https://doi.org/10.1016/j.neuroimage.2012.03.072

Zhang, M., Ou-Yang, H., Liu, J., Jin, D., Wang, C., Zhang, X., Zhao, Q., Liu, X., Liu, Z., Lang, N., Jiang, L., Yuan, H., 2022. Utility of Advanced DWI in the Detection of Spinal Cord Microstructural Alterations and Assessment of Neurologic Function in Cervical Spondylotic Myelopathy Patients. J. Magn. Reson. Imaging 55, 930–940. https://doi.org/10.1002/jmri.27894

Zhou, F.Q., Tan, Y.M., Wu, L., Zhuang, Y., He, L.C., Gong, H.H., 2015. Intrinsic functional plasticity of the sensory-motor network in patients with cervical spondylotic myelopathy. Sci. Rep. 5. https://doi.org/10.1038/srep09975

8 LIST OF ABBREVIATIONS

AD	axial diffusivity estimated by DTI model
ANCOVA	analysis of covariance
CR	compression ratio
CSA	cross-sectional area
CSF	cerebrospinal fluid
d	single mean diffusivity estimated by Ball-and-sticks model
DCM	degenerative cervical myelopathy
dMRI	diffusion MRI (equivalent to DWI)
DKI	diffusion kurtosis imaging
DTI	diffusion tensor imaging
DWI	diffusion-weighted imaging (equivalent to dMRI)
EPI	echo planar imaging
EMG	electromyography
f1	primary partial volume fraction estimated by ball-and-sticks model
FA	fractional anisotropy estimated by DTI model
FOV	field-of-view
GM	gray matter
HARDI	high angular resolution diffusion imaging
MCL	maximally compressed level
MD	mean diffusivity estimated by DTI model
MEP	motor-evoked potentials
mJOA scale	modified Japanese Orthopedic Association scale
MRI	magnetic resonance imaging

NMDC	non-myelopathic cervical spinal cord compression
NODDI	neurite orientation dispersion and density imaging
qMRI	quantitative magnetic resonance imaging
RD	radial diffusivity estimated by DTI model
ROI	region of interest
SC	spinal cord
SCT	Spinal Cord Toolbox
SEP	somatosensory-evoked potentials
WM	white matter
WoS	Web of Science

9 LIST OF FIGURES

Figure 1 – Illustration of the precession movement. 11

Figure 2 – Resonance phenomenon. 11

Figure 3 – Visualization of T2* effect. 12

Figure 4 – Illustration of basic concept of the diffusion-weighted experiment. 14

Figure 5 – Isotropic and anisotropic diffusion and diffusion tensor. 15

Figure 6 – Primary and secondary changes caused by the compression. 20

Figure 7 – Illustration susceptibility-induced distortions. 24

Figure 8 – MRI sequences used to accelerate k-space filling 25

Figure 9 – Reduced field-of-view (FOV) techniques. 25

Figure 10 – Overview of common processing steps included in spinal cord atlas-based dMRI analysis. 28

Figure 11 – Morphometric metrics assessing compression severity. 30

Figure 12 – Visualization of HARDI-ZOOMit sampling scheme. 42

Figure 13 – Visualization of individual regions of interest (ROIs). 50

Figure 14 – Flowchart of participant's requirement for the Study II. 52

Figure 15 – Illustrative data visualization. 54

Figure 16 – Signal-to-noise ratio across individual diffusion protocols and their b-values. 55

Figure 17 – Visualization of mutual information 55

Figure 18 – Single-subject dMRI-derived metrics 56

Figure 19 – Group-averaged distributions 57

Figure 20 – Visualization of the crossing fibers 58

Figure 21 – Visualization of k-means clustering. 59

Figure 22 – Representative data from the C4/5 disc for NMDC and DCM patients. 60

Figure 23 – Illustrative visualization of significant correlation between fractional anisotropy (FA) at the above the compression level C3 and cross-sectional area (CSA) 61

Figure 24 – Between-group differences in cross-sectional area (CSA) at C3 above the compression level. 62

Figure 25 – Between-group differences in dMRI-derived metrics 64

Figure 26 – Violin plots showing between-group differences in dMRI-derived metrics 65

Figure 27 – Violin plots showing relationship between electrophysiological measures and dMRI-derived metrics 68

Figure 28 - Spearman correlations between dMRI-derived metric from C3 above the compression level and modified Japanese Orthopaedic Association (mJOA) scale 69

10 LIST OF TABLES

Table 1 - Nomenclature and definitions of non-myelopathic spinal cord compression across studies.....21

Table 2 – Detailed sequence parameters and their intended purpose. 41

Table 3 – Characteristics of participants included in the Study II.....53

11 LIST OF PUBLICATIONS

Besides studies directly related to the topic of the thesis listed in Chapter 11.1, I further collaborated on five other research papers from broader area of the thesis (Chapter 11.2). Specifically, we detected neurochemical changes at above the compression level in NMDC and DCM patients relative to HC using ^{1}H-MRS (Horak et al., 2021); and we demonstrated that morphometric metrics computed from structural scans semi-automatically detected SC compression with lower variability than manual raters (Horáková et al., 2022). Next, we proposed prospectively harmonized SC qMRI protocol (so-called *spine generic*) for three major MRI scanner vendors (Cohen-Adad et al., 2021b) and acquired qMRI dataset of >250 healthy volunteers across 42 centers worldwide. The dataset was published online as an open-access dataset (Cohen-Adad et al., 2021a). Finally, we compared MRI protocols from 1.5 T, 3 T and 7 T scanners for visualization of the spinal cord gray matter (Cohen-Adad et al., 2022).

Works published during the doctoral study from September 2017 to March 2022:

11.1 Published research papers directly related to the topic of the thesis

1. Labounek R, **Valošek J**, Horák T, Svátková A, Bednařík P, Vojtíšek L, Horáková M, Nestrašil I, Lenglet C, Cohen-Adad J, Bednařík J, Hluštík P. HARDI-ZOOMit protocol improves specificity to microstructural changes in presymptomatic myelopathy. Sci Rep. 2020 Oct 16;10(1):17529. doi: 10.1038/s41598-020-70297-3

   WoS 2020: IF 4.380, Rank: 17/72, Times cited: 6

   Author contribution: J. Valošek significantly contributed to the design of processing pipeline, implemented final algorithms and functions, analyzed single-subject data, performed visual inspection of analyzed results, participated on group-level statistical analysis and co-wrote the manuscript draft.

2. **Valošek J**, Labounek R, Horák T, Horáková M, Bednařík P, Keřkovský M, Kočica J, Rohan T, Lenglet C, Cohen-Adad J, Hluštík P, Vlčková E, Kadaňka Z Jr, Bednařík J, Svatkova A. Diffusion magnetic resonance imaging reveals tract-specific microstructural correlates of electrophysiological impairments in non-myelopathic and myelopathic spinal cord compression. Eur J Neurol. 2021 Nov;28(11):3784-3797. doi: 10.1111/ene.15027

   WoS 2020: IF 6.089, Rank: 35/255, Times cited: 3

Author contribution: J. Valošek substantially contributed to conceptualization of the study design, implemented processing pipeline, analyzed single-subject data, performed visual inspection and manual corrections of analyzed results, performed group-level statistical analysis, created figures, and wrote and revised the manuscript.

3. **Valošek J**, Bednařík P, Keřkovský M, Hluštík P, Bednařík J, Svátková A. Quantitative MR Markers in Non-Myelopathic Spinal Cord Compression: A Narrative Review. Journal of Clinical Medicine. 2022 April (accepted). doi: 10.20944/preprints202202.0355

   WoS 2020: IF 4.242, Rank: 39/167, Times cited: 0

   Author contribution: J. Valošek significantly contributed to the literature review, prepared figures, and wrote and revised the manuscript.

11.2 Published research papers from broader area of quantitative spinal cord MRI

1. Horak T, Horakova M, Svatkova A, Kadanka Z, Kudlicka P, **Valosek J**, Rohan T, Kerkovsky M, Vlckova E, Kadanka Z, Deelchand DK, Henry PG, Bednarik J, Bednarik P. In vivo Molecular Signatures of Cervical Spinal Cord Pathology in Degenerative Compression. J Neurotrauma. 2021 Nov 1;38(21):2999-3010. doi: 10.1089/neu.2021.0151. PMID: 34428934.
2. Horáková M, Horák T, **Valošek J**, Rohan T, Koriťáková E, Dostál M, Kočica J, Skutil T, Keřkovský M, Kadaňka Jr Z, Bednařík P, Svátková A, Hluštík P, Bednařík J. Semi-automated detection of cervical spinal cord compression with the Spinal Cord Toolbox. Quantitative Imaging in Medicine and Surgery. 2022 April;12(4):2261-2279. doi: 10.21037/qims-21-782
3. Cohen-Adad J, Alonso-Ortiz E, Abramovic M, Arneitz C, Atcheson N, Barlow L, Barry RL, Barth M, Battiston M, Büchel C, Budde M, Callot V, Combes AJE, De Leener B, Descoteaux M, de Sousa PL, Dostál M, Doyon J, Dvorak A, Eippert F, Epperson KR, Epperson KS, Freund P, Finsterbusch J, Foias A, Fratini M, Fukunaga I, Wheeler-Kingshott CAMG, Germani G, Gilbert G, Giove F, Gros C, Grussu F, Hagiwara A, Henry PG, Horák T, Hori M, Joers J, Kamiya K, Karbasforoushan H, Keřkovský M, Khatibi A, Kim JW, Kinany N, Kitzler H, Kolind S, Kong Y, Kudlička P, Kuntke P, Kurniawan ND, Kusmia S, Labounek R, Laganà MM, Laule C, Law CS, Lenglet C, Leutritz T, Liu Y, Llufriu S, Mackey S, Martinez-Heras E, Mattera L, Nestrasil I, O'Grady KP, Papinutto N, Papp D, Pareto D,

Parrish TB, Pichiecchio A, Prados F, Rovira À, Ruitenberg MJ, Samson RS, Savini G, Seif M, Seifert AC, Smith AK, Smith SA, Smith ZA, Solana E, Suzuki Y, Tackley G, Tinnermann A, **Valošek J**, Van De Ville D, Yiannakas MC, Weber KA 2nd, Weiskopf N, Wise RG, Wyss PO, Xu J. Generic acquisition protocol for quantitative MRI of the spinal cord. Nat Protoc. 2021 Oct;16(10):4611-4632. doi: 10.1038/s41596-021-00588-0

4. Cohen-Adad J, Alonso-Ortiz E, Abramovic M, Arneitz C, Atcheson N, Barlow L, Barry RL, Barth M, Battiston M, Büchel C, Budde M, Callot V, Combes AJE, De Leener B, Descoteaux M, de Sousa PL, Dostál M, Doyon J, Dvorak A, Eippert F, Epperson KR, Epperson KS, Freund P, Finsterbusch J, Foias A, Fratini M, Fukunaga I, Gandini Wheeler-Kingshott CAM, Germani G, Gilbert G, Giove F, Gros C, Grussu F, Hagiwara A, Henry PG, Horák T, Hori M, Joers J, Kamiya K, Karbasforoushan H, Keřkovský M, Khatibi A, Kim JW, Kinany N, Kitzler HH, Kolind S, Kong Y, Kudlička P, Kuntke P, Kurniawan ND, Kusmia S, Labounek R, Laganà MM, Laule C, Law CS, Lenglet C, Leutritz T, Liu Y, Llufriu S, Mackey S, Martinez-Heras E, Mattera L, Nestrasil I, O'Grady KP, Papinutto N, Papp D, Pareto D, Parrish TB, Pichiecchio A, Prados F, Rovira À, Ruitenberg MJ, Samson RS, Savini G, Seif M, Seifert AC, Smith AK, Smith SA, Smith ZA, Solana E, Suzuki Y, Tackley G, Tinnermann A, **Valošek J**, Van De Ville D, Yiannakas MC, Weber Ii KA, Weiskopf N, Wise RG, Wyss PO, Xu J. Open-access quantitative MRI data of the spinal cord and reproducibility across participants, sites and manufacturers. Sci Data. 2021 Aug 16;8(1):219. doi: 10.1038/s41597-021-00941-8.
5. Cohen-Adad J, Alonso-Ortiz E, Alley S, Lagana MM, Baglio F, Vannesjo SJ, Karbasforoushan H, Seif M, Seifert AC, Xu J, Kim J-W, Labounek R, Vojtíšek L, Dostal M, **Valošek J**, Samson RS, Grussu F, Battiston M, Wheeler-Kingshott CAM, Yiannakas Marios C, Gilbert G, Schneider T, Johnson B, Prados F. Comparison of multi-center MRI protocols for visualizing the spinal cord gray matter. Magn. Reson. Med. 2022 April 05. doi: 10.1002/mrm.29249.

11.3 Other published original research papers using MRI methodology

1. Vastik M, Hok P, **Valosek J**, Hlustik P, Mensikova K, Kanovsky P. Freezing of gait is associated with cortical thinning in mesial frontal cortex. Biomed Pap Med Fac Univ Palacky Olomouc Czech Repub. 2017 Dec;161(4):389-396. doi: 10.5507/bp.2017.035. Epub 2017 Sep 13. PMID: 28928491.
2. Krahulík D, Nevrlý M, Otruba P, Bardoň J, Hrabálek L, Pohlodek D, Kaňovský P, **Valošek J**. O-Arm Navigated Frameless and Fiducial-Less Deep Brain Stimulation. Brain Sci. 2020 Sep 27;10(10):683. doi: 10.3390/brainsci10100683. PMID: 32992610; PMCID: PMC7600133.
3. Arkhipova A, Hok P, **Valošek J**, Trnečková M, Všetičková G, Coufalová G, Synek J, Zouhar V, Hluštík P. Changes in Brain Responses to Music and Non-music Sounds Following Creativity Training Within the "Different Hearing" Program. Front Neurosci. 2021 Oct 1;15:703620. doi: 10.3389/fnins.2021.703620.

11.4 Author record

Number of publications (Web of Science, WoS):	21
Original research papers (WoS):	12
Sum of Times Cited (WoS):	36
h-index:	4
Web of Science ResearcherID	X-5305-2018
ORCID iD	0000-0002-7398-4990

12 ANNEXES

12.1 Annex 1 – Study I (dMRI methodology)

www.nature.com/scientificreports

SCIENTIFIC REPORTS
natureresearch

Check for updates

OPEN

HARDI-ZOOMit protocol improves specificity to microstructural changes in presymptomatic myelopathy

René Labounek[1,2,3], Jan Valošek[1,2], Tomáš Horák[4,5,6], Alena Svátková[4,7,8], Petr Bednařík[4,9], Lubomír Vojtíšek[4], Magda Horáková[4,5,6], Igor Nestrašil[3,10], Christophe Lenglet[10], Julien Cohen-Adad[11], Josef Bednařík[4,5,6] & Petr Hluštík[2,12]✉

Diffusion magnetic resonance imaging (dMRI) proved promising in patients with non-myelopathic degenerative cervical cord compression (NMDCCC), i.e., without clinically manifested myelopathy. Aim of the study is to present a fast multi-shell HARDI-ZOOMit dMRI protocol and validate its usability to detect microstructural myelopathy in NMDCCC patients. In 7 young healthy volunteers, 13 age-comparable healthy controls, 18 patients with mild NMDCCC and 15 patients with severe NMDCCC, the protocol provided higher signal-to-noise ratio, enhanced visualization of white/gray matter structures in microstructural maps, improved dMRI metric reproducibility, preserved sensitivity (SE = 87.88%) and increased specificity (SP = 92.31%) of control-patient group differences when compared to DTI-RESOLVE protocol (SE = 87.88%, SP = 76.92%). Of the 56 tested microstructural parameters, HARDI-ZOOMit yielded significant patient-control differences in 19 parameters, whereas in DTI-RESOLVE data, differences were observed in 10 parameters, with mostly lower robustness. Novel marker the white-gray matter diffusivity gradient demonstrated the highest separation. HARDI-ZOOMit protocol detected larger number of crossing fibers (5–15% of voxels) with physiologically plausible orientations than DTI-RESOLVE protocol (0–8% of voxels). Crossings were detected in areas of dorsal horns and anterior white commissure. HARDI-ZOOMit protocol proved to be a sensitive and practical tool for clinical quantitative spinal cord imaging.

After the Stejskal and Tanner 1965 experiment[1], it took almost 3 decades until the diffusion magnetic resonance imaging (dMRI) was first applied to human brain imaging, utilizing estimation of the diffusion tensor imaging (DTI) model[2,3]. Since 2000 DTI has been used in the spinal cord (SC) imaging[4] and become considered for clinical applications[5,6], such as SC injury[7,8], multiple sclerosis[4], amyotrophic lateral sclerosis (ALS)[9], Walerian degeneration[10], adrenoleukodystrophy[11] and degenerative cervical myelopathy (DCM)[12–18]. Recently, DTI detected microstructural SC injury[19], and microstructural abnormality in patients with non-myelopathic degenerative cervical cord compression (NMDCCC) prior to development of subsequently expected neurological myelopathic symptoms and signs, i.e. DCM manifestation[20]. NMDCCC is a condition that is more frequent than

[1]Department of Biomedical Engineering, University Hospital Olomouc, 779 00 Olomouc, Czech Republic. [2]Department of Neurology, Palacký University, 779 00 Olomouc, Czech Republic. [3]Division of Clinical Behavioral Neuroscience, Department of Pediatrics, University of Minnesota, Minneapolis, MN 55414, USA. [4]Central European Institute of Technology, Masaryk University, 625 00 Brno, Czech Republic. [5]Department of Neurology, University Hospital Brno, 625 00 Brno, Czech Republic. [6]Faculty of Medicine, Masaryk University, 625 00 Brno, Czech Republic. [7]Department of Medicine III, Clinical Division of Endocrinology and Metabolism, Medical University of Vienna, 1090 Vienna, Austria. [8]Department of Imaging Methods, Faculty of Medicine, University of Ostrava, 701 03 Ostrava, Czech Republic. [9]High Field MR Centre, Medical University of Vienna, Vienna, Austria. [10]Center for Magnetic Resonance Research, Department of Radiology, University of Minnesota, Minneapolis, MN 55414, USA. [11]Institute of Biomedical Engineering, Polytechnique Montreal, Montreal, Canada. [12]Department of Neurology, University Hospital Olomouc, 779 00 Olomouc, Czech Republic. ✉email: phlustik@upol.cz

previously estimated[20,21]. The SC compression at this stage may become an important target in the prediction and/or prevention of significant myelopathic clinical symptoms and signs mostly leading to disabling DCM[22]. The dMRI derived parameters (e.g. FA or MD) have distinguished healthy controls from patients with advanced DCM[12–14], correlated with clinical disability in DCM patients[23], and been able to detect signs of microstructural SC injury in NMDCCC patients in an exploratory study[20]. There is an urgent need to confirm the previous findings but also to develop and validate a dMRI protocol that is fast, reliable, clinically feasible, and yet possesses the ability to detect microstructural cervical cord injury in the NMDCCC stage with high sensitivity (SE) and specificity (SP).

Clinical dMRI protocols for the SC aim to acquire high spatial resolution data with good quality (SNR) over a clinically acceptable time period. Spatial resolution is often less than $1.25 \times 1.25 \times 5\,mm^3$ and short single-shell diffusion weighted protocols with 20–30 directions are almost exclusively employed[19]. Within each voxel, DTI fits a *seven* (6 parameters for the tensor + 1 parameter for signal intensity without diffusion weighting) *parameter single-compartment model* corresponding to an ellipsoid tensor oriented in one dominant direction. For the SC tissue, this tensor characterizes the average fiber bundle orientation within the voxel[3].

One major limitation of such data is the inability to model complex intra-voxel fiber configurations (e.g. crossing fibers) due to a low angular resolution[24]. Yet, crossing fibers are known to be present in several areas of the SC at the histological level, e.g., the dorsal horns and the anterior commissure, where nerve fibers are oriented transversally, in contrast to the longitudinal organization of most of SC pathways. In dMRI data, crossing fibers are defined as multiple fiber bundles with different orientations within a single voxel, and have already been detected in the SC in animal models[25,26] or humans[7,27,28]. Importantly, in a human study of injured SC the analysis of crossing fibers provided an increased specificity for various sub-types of white matter pathology[7]. Unfortunately, increasing angular resolution within current protocols would make them too long for clinical scanning.

The advanced clinical SC dMRI protocol should thus be fast, provide high angular resolution within acceptable scanning time and be complemented with an advanced crossing fiber model. For the first requirement, we have employed a reduced field-of-view (FOV) EPI sequence, e.g. syngo ZOOMit (*Siemens Medical, Erlangen, Germany*), which decreases the acquisition time without compromising dMRI data quality[29]. To achieve high angular resolution, we have designed a novel two-shell HARDI-ZOOMit[24,28,29] protocol (high angular resolution diffusion imaging) covering the C3–C7 SC levels. Finally, to permit crossing fiber modeling, we have utilized the *three-compartment* "Ball and Stick and Stick model" that fits *eight parameters*[30] and better characterizes dMRI data than the single-compartment DTI model[31].

We have compared our new HARDI-ZOOMit protocol and model to a current standard clinical RESOLVE (REadout Segmentation Of Long Variable Echo trains) sequence[32] that is being used and considered to provide high signal-to-noise ratio (SNR)[33] in the evaluation of SC.

Multiple microstructural parameters were compared within SC regions of interest (ROIs), not only with single-subject mean/median and SD of dMRI metrics, but also advanced metrics such as skewness, kurtosis and several novel heuristic parameters. The sets of significant dMRI parameters and protocols' SEs/SPs were evaluated with Wilcoxon rank-sum tests, analyses of covariance (ANCOVA), step-wise linear regressions and K-means clusterings. Moreover, SNR, mutual information between dMRI metric maps and SC anatomy, off-resonance susceptibility artifact effect and test–retest reproducibility were evaluated for each investigated dMRI protocol.

Results

Subject characteristics. The study sample consisted of a cohort of 33 NMDCCC patients (14 females, 56.7 ± 6.4 year), 13 age-comparable healthy controls (9 females, age 51.9 ± 9.4 year), and seven young healthy volunteers (3 females, age 27.4 ± 1.7 year; acquired twice for reproducibility evaluations). The radiological measurements, i.e. cross-sectional area (CSA) and compression ratio (CR), sub-divided the cohort of 33 NMDCCC patients to sub-group of 18 patients with mild NMDCCC (7 females, age 55.6 ± 6.1 year) and sub-group of 15 patients with severe NMDCCC (7 females, 58.1 ± 6.8 year). The neurological examination confirmed no DCM symptom presence for NMDCCC patients. A smaller proportion of NMDCCC cohort (13 out of 33 patients) displayed clinical symptoms and/or signs of cervical monoradiculopathy (mostly a radicular pain, less frequently a motor deficit in a corresponding myotome). Two-sample t-test identified the probability of age difference between age-comparable healthy controls and NMDCCC patients at $p = 0.052$, and mild NMDCCC patients at $p = 0.195$, and severe NMDCCC patients at $p = 0.056$. To avoid the potential age or radiculopathy effects post-hoc ANCOVA or Wilcoxon rank-sum tests were performed for each presented significant between-group difference below.

Acquisition protocols. A visualization of acquired MRI data with segmented and labeled white (WM) and gray (GM) matter in T_2^*-w axial space (i.e. T2TRA space) is presented in Fig. 1a–e. T_2^*-w axial scans provided a superior WM/GM contrast that was ideally suited for WM/GM segmentation (Fig. 1b). Both HARDI-ZOOMit protocols, interpolated and non-interpolated (Fig. 1c,e), were about 3 min 30 s faster when compared to the DTI-RESOLVE non-interpolated protocol (Fig. 1d). In comparison to DTI-RESOLVE protocol with b-value $650\,s\,mm^{-2}$ (SNR 5.1 ± 1.3), HARDI-ZOOMit protocols generated diffusion weighted images with higher SNR level for b-value $550\,s\,mm^{-2}$ (interpolated 6.2 ± 1.2, non-interpolated 5.7 ± 1.1), and with lower SNR for b-value $1000\,s\,mm^{-2}$ (interpolated 4.5 ± 0.9, non-interpolated 4.7 ± 0.9), as anticipated. Full visualization of SNR results is shown in Fig. 1f. NMDCCC leads to a decrease in SNR for all protocols (Fig. 1f). A loss of SNR was also observed in both HARDI-ZOOMit protocols in the lower part of C7 vertebral level (Fig. 1c,e) and may be caused by the increased susceptibility artifact originating from the lungs. The used spherical two-shell HARDI acquisition scheme is shown in Fig. 4a.

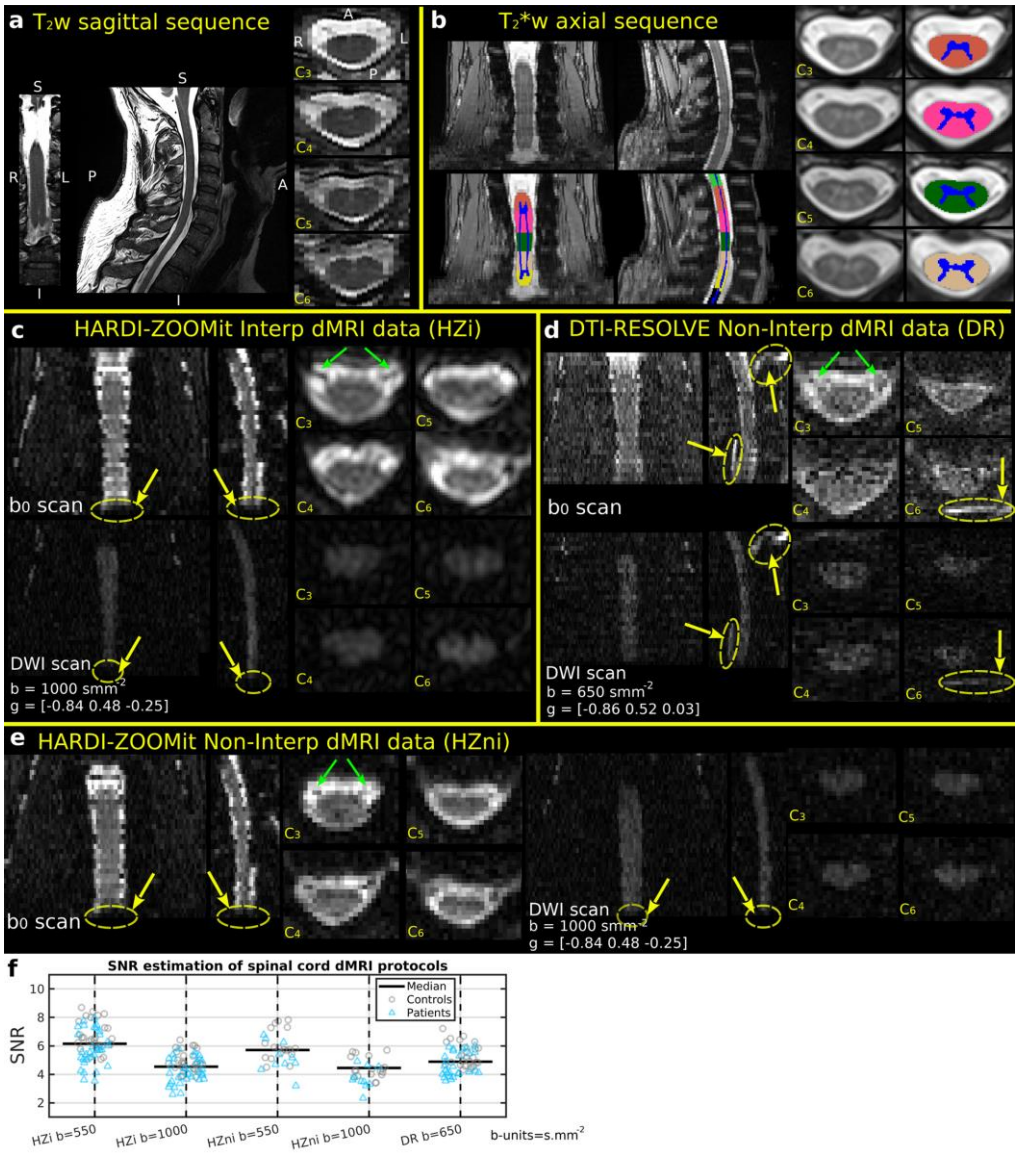

Figure 1. Raw anatomical MRI data, white and gray matter segmentation, and vertebral level labeling in a single-subject (**a**–**e**). Coronal (left), sagittal (middle) and axial (right) images with corresponding cervical (C) vertebral levels are shown; anatomical orientation: *S* superior, *I* inferior, *R* right, *L* left, *A* anterior, *P* posterior, as included in (**a**); anatomical plane order and direction orientation is the same in all other panels. (**a**), T_2w sagittal sequence (**b**), T_2^*w axial sequence with WM/GM segmentation and vertebral level labeling overlay (**c**). Diffusion non-weighted (i.e. b_0 scan in the first row of images) and weighted (i.e. DWI scan in the second row of images) images for the HARDI-ZOOMit protocol with Fourier domain interpolation during image reconstruction. Variable b (i.e. b-value) represents a magnitude of applied gradient waveform in the direction of a gradient vector **g**. Yellow arrows indicate areas of signal loss, green arrows the nerve roots in b_0 scan. (**d**) b_0 and DWI scans for the non-interpolated DTI-RESOLVE protocol. Order of b_0 and DWI scans and diffusion variable description same as in (**c**). Yellow arrows indicate locations of ghost artifacts, green arrows the nerve roots in b_0 scan. (**e**) b_0 (left) and DWI (right) scans for the non-interpolated HARDI-ZOOMit protocol. Diffusion variable description same as in (**c**). Yellow arrow indicate areas of signal loss, green arrows the nerve roots in b_0 scan. (**f**) Estimation of signal-to-noise ratio (SNR) in spinal cord DWI scans of investigated protocols.

Diffusion MRI microstructural metrics. For dMRI analysis, the region of interest (ROI) was reduced to the C3–C6 vertebral levels due to the presence of artifacts at C7 level as described above. Clinical relevance should not be affected much since the expected C7 SC compression in DCM[34] is presented only in 8–11% of cases in the used Caucasian middle-Europe population[21,35]. If the NMDCCC causes more extensive changes even above the affected C7 segment, C3–C6 ROI might still work fine. Diffusion MRI maps characterizing the SC microstructure, warped into T2TRA space, are shown in Fig. 2a–c. As expected, fractional anisotropy (FA) and partial volume of the primary fiber bundle direction (f_1) were lower in GM and higher in the WM corresponding to lateral corticospinal tracts and dorsal columns (i.e. gracile and cuneate fasciculi) for both HARDI-ZOOMit protocols (Fig. 2a,c). In contrast, GM/WM difference was more difficult to identify in the DTI-RESOLVE Non-Interp FA and f_1 maps (Fig. 2b). Single-subject mean/median values of FA and f_1 were higher in the HARDI-ZOOMit protocols than in the DTI-RESOLVE protocol for both WM (Fig. 3, Supplementary Figs. S1, S2) and GM (Supplementary Figs. S1–S3) structures.

Mean diffusivity maps (i.e. MD from the DTI model and d from the Ball and Stick and Stick model) displayed higher values at the edge of SC over all protocols (Fig. 2a–c). The spatial definition of the WM/GM boundary was clearer in HARDI-ZOOMit protocols than DTI-RESOLVE protocol (Fig. 2a,c). Over all dMRI protocols, DTI estimated lower MD values than Ball and Stick and Stick model for d (Figs. 2a–c, 3, Supplementary Figs. S3–S5). HARDI-ZOOMit protocols increased the mutual information (i.e. a usable similarity measure of degree of joint entropy in two multi-modal images with a non-linear contrast transform function, Eq. (7); see more information in Methods) between dMRI metric maps and semi-binarized images (i.e. background = 0, WM = 2 and GM = 1) of WM/GM structures (Fig. 2d).

Most distributions of dMRI parameters estimated from WM revealed narrow confidence intervals for each group of subjects (Fig. 3). These distributions also showed distinct properties between patients and healthy controls in the HARDI-ZOOMit protocol (Fig. 3). DTI-RESOLVE non-interpolated (possibly due to lower angular resolution) has higher inter-subject variance in confidence intervals for f_1 (Fig. 3). Results from GM demonstrated higher between-group overlap (Supplementary Fig. S3), except MD and d estimated from DTI-RESOLVE showing distinct properties between patients and healthy controls (Supplementary Fig. S3).

HARDI acquisition protocols enable to model and visualize multiple fiber bundles within single voxel, i.e., intra-voxel crossing fiber conformations[24,36]. All protocols identified 2nd fiber bundle directions as the 2nd significant fully anisotropic Stick[30] compartment (i.e. $f_2 > 0.05$) especially near to the dorsal horns. HARDI-ZOOMit protocols estimated a higher number of crossing fiber configurations compared to DTI-RESOLVE protocol (Fig. 4b), likely due to the higher angular resolution afforded by HARDI-ZOOMit protocols. Crossing fibers were particularly detected in areas of dorsal horns and anterior white commissure (Fig. 4c). Apart from our own preliminary data[28], this presents one of the first visualizations of crossing fibers from contiguous SC human in-vivo dMRI data (Fig. 4c). However, the amount of detected crossings (Fig. 4b,c) is possibly still underestimated[25–27]. Still, the intra-voxel modelling of crossings yielded better local underlying microstructural decomposition providing maps more close to WM/GM structures (e.g. f_1 vs FA and d vs MD in Fig. 2d) and higher separation of f_1-based dMRI metrics in comparison to complementary FA-based metrics (Table 1). Significant local partial volumes f_2 (i.e. $f_2 > 0.05$) of the 2nd crossing fiber bundles possibly filter out from f_1 maps a variability portion which makes local FA values falsely lower and appearing as flatter tensor of the underlying microstructure for the major fiber bundle than the ground truth is.

Descriptive statistics parameters. For each subject and each dMRI metric, mean, median, standard deviation, skewness and kurtosis of the metric were evaluated within WM and GM, along with differences between means or medians in the WM and GM (e.g. $mean(MD)^{WM} - mean(MD)^{GM}$). Four different dMRI metrics (i.e. FA, f_1, MD and d) were analyzed and yielded 48 descriptive statistics parameters for each dMRI protocol. Findings for all parameters are presented in Supplementary Figs. S1, S2, S4, S5. Nineteen of the 48 parameters demonstrated significant differences ($p_{FWE} < 0.05$) between age-comparable control (C) group and mild (M) or severe (S) compression non-myelopathic patients (Fig. 5; Table 1). Seventeen of the 19 parameters demonstrated significant differences for the HARDI-ZOOMit Interp protocol. The HARDI-ZOOMit Non-Interp protocol showed similar results (Fig. 5, Supplementary Figs. S1, S2, S4, S5), but with fewer significant findings likely due to the lower number of subjects scanned with this protocol. Eight of the 19 parameters were significantly different between controls and patients for the DTI-RESOLVE Non-Interp protocol (Fig. 5, Supplementary Figs. S1, S2, S4, S5). The DTI-RESOLVE only detected differences in the GM of NMDCCC patients and in differences between WM and GM values of the patients. Between-group differences were more robust in the HARDI-ZOOMit Interp protocol, when compared to the DTI-RESOLVE Non-Interp protocol, i.e. more significant observations with lower p values for the HARDI-ZOOMit (Fig. 5; Table 1, Supplementary Figs. S1, S2, S4, S5). We anticipated that the Ball and Stick and Stick model (providing local crossing models with relatively few parameters) might enhance the clinical benefit of the proposed HARDI-ZOOMit protocol. This assumption has been partly validated as the f_1 metric demonstrated lower p values (Wilcoxon rank-sum tests) than FA (Table 1). This is in line with previous observations of improved clinical correlation for generalized fractional anisotropy (GFA)[36] estimated from Q-Ball imaging, in contrast to the DTI FA[7].

Post-hoc ANCOVA test utilizing age as a confounding variable identified 14 of 17 variables to still demonstrate significant differences between age-comparable controls and NMDCCC patients for the HARDI-ZOOMit protocol (Table 2). Skewness of f_1 from WM, median of MD from WM and skewness of d from WM disappeared from the original list. For the DTI-RESOLVE protocol the number of variables increased from 8 to 9 (Table 2), again all are GM related or diffusivity gradient related as in the previous results. ANCOVA observations mostly overlap with the Wilcoxon rank-sum test observations (Fig. 5; Table 1).

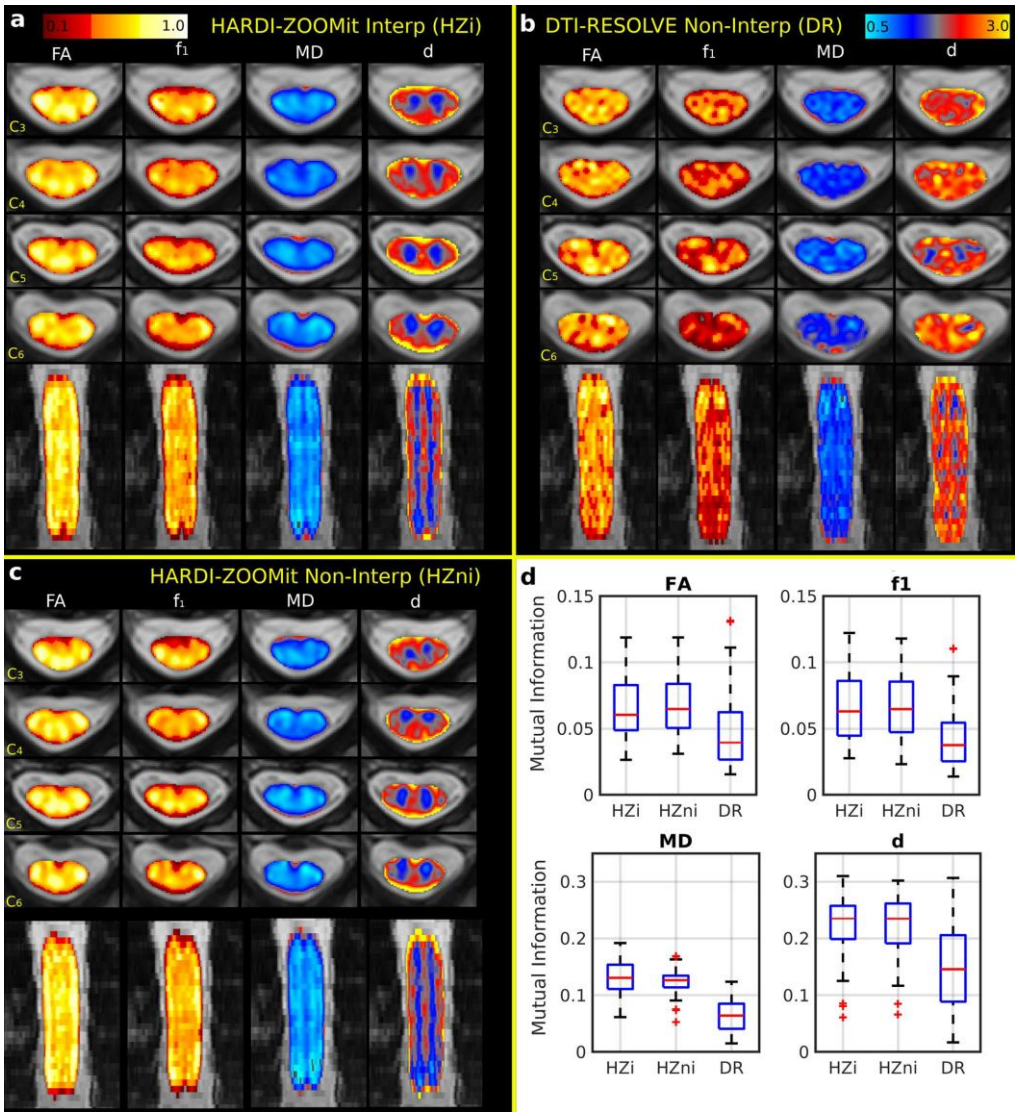

Figure 2. Diffusion MRI metrics and their correspondence to WM/GM structures in a single-subject (**a**–**c**) and across all participants (**d**). FA (DTI model fractional anisotropy), f_1 (Ball and Stick and Stick model partial volume of the 1st principal diffusion direction), MD (DTI model mean diffusivity) and *d* (Ball and Stick and Stick model intra-voxel mean diffusivity) maps are shown for four representative axial slices and one coronal slice for the HARDI-ZOOMit interpolated protocol (**a**), the DTI-RESOLVE non-interpolated protocol (**b**) and the HARDI-ZOOMit non-interpolated protocol (**c**). All FA and f_1 maps use a "hot" colormap (i.e. red–orange–yellow–white colorbar on the top left panel). All MD and *d* maps are a "blue–yellow" colormap (i.e. lightblue–blue–gray–red–orange–yellow colorbar on the top right panel). All direction orientations of the axial (first four rows of images) or coronal slices (last row of slices) are the same as shown for the T_2w sagittal sequence in Fig. 1a. (**d**) Distributions of mutual information between dMRI metrics and semi-threshold (i.e. background = 0, WM = 2 and GM = 1) WM/GM structure images demonstrate (in comparison to the DTI-RESOLVE protocol) increased mutual entropy level for both HARDI-ZOOMit protocols in all dMRI metrics. Ball and Stick and Stick model diffusivity map (*d*) has larger mutual entropy with WM/GM structures than DTI model MD map. Both diffusivity maps have larger mutual entropy with WM/GM structures than FA or f_1 maps. They still contain some information about WM/GM structures, while mutual information coefficients are > 0.

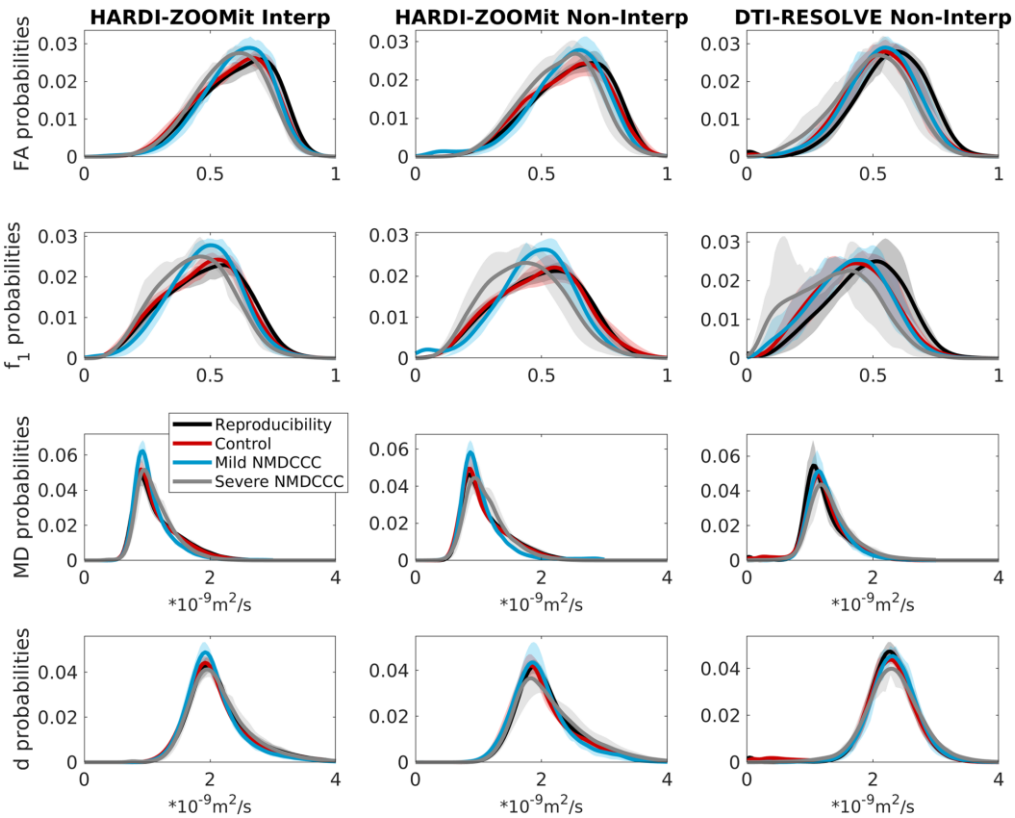

Figure 3. Group-averaged distributions of dMRI microstructural parameters from C3–C6 white matter. The confidence intervals (i.e. corresponding transparent colors) show Q1–Q3 quartiles. The intervals are narrow and distinct for most distributions, except f_1 for non-interpolated HARDI-ZOOMit protocol with lower number of participants, and except f_1 for non-interpolated DTI-RESOLVE protocol where precise f_1 and f_2 volume estimations might fail because of the protocol's lower angular resolution. Trends in distributions are similar for both HARDI-ZOOMit protocols.

For any investigated protocol or variable demonstrating significant differences between age-comparable healthy controls and mild or severe NMDCCC patients, post-hoc Wilcoxon rank-sum tests demonstrated no significant differences (i.e. each $p > 0.05$) in descriptive statistics dMRI parameters of NMDCCC patients with or without radiculopathy.

Novel heuristic parameters. Since the distributions in Fig. 3 demonstrated several dMRI metric intervals with disjunctive probability density functions (g), five heuristic parameters (H) of dMRI metrics (Eqs. 1–5) are proposed:

$$H_{FA} = \int_{0.47}^{0.67} g(FA)dFA \tag{1}$$

$$H_{f_1} = \int_{0.30}^{0.55} g(f_1)df_1 \tag{2}$$

$$H_{MD} = \int_{0.84}^{1.26} g(MD)dMD \tag{3}$$

		HARDI-ZOOMit Interp.							DTI-RESOLVE non-Interp.						
		Control	Mild Comp. patients			Severe Comp. patients			Control	Mild Comp. patients			Severe Comp. patients		
Parameter	Shortcut	Median	Median	diff %	p value	Median	diff %	p value	Median	Median	diff %	p value	Median	diff %	p value
FA_WM_STD	FAwS	0.1422	0.1286	− 9.60	**6.10E−3**	0.1356	− 4.65	5.30E−2	0.1266	0.1239	− 2.11	4.12E−1	0.1325	4.72	1.00E+1
FA_WM_kurtosis	FAwK	2.4934	2.8241	13.26	**5.35E−4**	2.6698	7.07	1.66E−2	2.7666	2.8592	3.35	8.89E−1	2.7658	− 0.03	5.19E−1
f1_WM_STD	f1wS	0.1512	0.1323	− 12.55	**6.10E−3**	0.1397	− 7.61	1.29E−2	0.1398	0.1318	− 5.71	2.54E−1	0.1304	− 6.75	2.49E−1
f1_WM_skewness	f1wSK	− 0.1315	− 0.0805	− 38.82	6.74E−1	0.0313	− 123	**6.57E−3**	− 0.0685	− 0.0078	− 88.68	5.89E−1	0.1390	− 303	1.67E−1
f1_WM_kurtosis	f1wK	2.4683	2.7209	10.23	**1.82E−4**	2.7330	10.72	**3.20E−3**	2.6254	2.6115	− 0.53	6.74E−1	2.7310	4.02	8.90E−1
MD_WM_median	MDwM	1.0509	0.9951	− 5.31	**5.40E−3**	1.0578	0.65	4.61E−1	1.1614	1.1860	2.12	5.62E−1	1.2524	7.83	1.29E−2
MD_WM_mean	MDwm	1.1545	1.0576	− 8.39	**2.51E−3**	1.1005	− 4.68	1.97E−1	1.2414	1.2345	− 0.56	7.64E−1	1.3230	6.58	2.40E−2
MD_WM_STD	MDwS	0.3561	0.2621	− 26.39	**1.10E−3**	0.2863	− 19.60	**2.28E−4**	0.3069	0.2708	− 11.76	3.56E−2	0.3150	2.64	9.63E−1
d_WM_STD	dwS	0.4893	0.4325	− 11.62	**4.77E−3**	0.4545	− 7.11	2.69E−1	0.3727	0.3544	− 4.89	1.93E−1	0.4238	13.72	7.12E−1
d_WM_skewness	dwSK	1.1506	1.1119	− 3.36	9.20E−1	0.9342	− 18.80	**6.57E−3**	0.1457	0.2125	45.86	4.35E−1	0.2112	44.99	3.57E−1
MD_GM_median	MDgm	0.8300	0.8406	1.28	2.38E−1	0.8933	7.64	**4.95E−3**	1.0577	1.1145	5.37	4.75E−2	1.1772	11.29	**4.95E−3**
MD_GM_mean	MDgm	0.8573	0.8633	0.70	4.35E−1	0.9048	5.53	1.46E−2	1.0657	1.1255	5.61	2.63E−2	1.1975	12.37	**2.03E−3**
MD_GM_skewness	MDgSK	1.6110	1.4599	− 9.38	6.17E−1	1.2434	− 22.81	5.89E−2	0.0600	0.5163	760	**7.76E−3**	0.6187	931	**1.07E−3**
d_GM_median	dgM	1.4979	1.5211	1.55	5.22E−2	1.6111	7.56	**6.57E−3**	1.9277	1.9717	2.29	2.63E−2	2.0262	5.11	**1.26E−3**
d_GM_mean	dgm	1.5401	1.5595	1.26	3.92E−2	1.6498	7.13	**2.75E−3**	1.8827	1.9816	5.26	1.54E−2	2.0449	8.62	**5.50E−4**
MD_WM-GM_median	MDwgM	0.2122	0.1470	− 30.71	**8.04E−5**	0.1711	− 19.35	1.88E−2	0.1185	0.0913	− 23.00	9.82E−3	0.1032	− 12.94	2.14E−1
MD_WM-GM_mean	MDwgm	0.2803	0.1906	− 32.00	**6.80E−5**	0.1990	− 29.00	**1.90E−4**	0.1676	0.1172	− 30.09	**1.27E−3**	0.1244	− 25.82	3.41E−2
d_WM-GM_median	dwgM	0.5129	0.4339	− 15.41	**1.32E−4**	0.4122	− 19.63	**1.48E−3**	0.3864	0.3446	− 10.82	4.32E−2	0.2546	− 34.11	**4.29E−3**
d_WG-GM_mean	dwgm	0.5676	0.4580	− 19.31	**2.41E−5**	0.4321	− 23.87	**2.28E−4**	0.3823	0.3340	− 12.64	5.72E−2	0.2373	− 37.92	**3.71E−3**
FA_WM_heuristic	FAwH	0.4729	0.5076	7.36	2.63E−2	0.5349	13.13	**6.52E−4**	0.5467	0.5569	1.87	6.74E−1	0.5412	− 1.00	6.45E−1
f1_WM_heuristic	f1wH	0.5362	0.5819	8.52	**4.21E−3**	0.5897	9.98	**4.29E−3**	0.5789	0.5941	2.64	7.64E−1	0.5505	− 4.90	4.07E−1
MD_WM_heuristic	MDwH	0.5683	0.6706	17.99	**7.18E−4**	0.6403	12.67	**3.20E−3**	0.5432	0.5755	5.94	4.84E−1	0.4757	− 12.42	6.54E−2
d_WM_heuristic	dwH	0.5002	0.5513	10.21	**6.10E−3**	0.5023	0.43	9.27E−1	0.3799	0.3538	− 6.86	4.12E−1	0.3411	− 10.22	3.11E−1
MD_GM_heuristic	MDgH	0.4956	0.5400	8.96	1.05E−1	0.5892	18.90	**1.48E−3**	0.7732	0.7345	− 5.00	4.59E−1	0.6435	− 16.78	**4.95E−3**
d_GM_heuristic	dgH	0.4872	0.4550	− 6.60	9.66E−2	0.3537	− 27.41	**5.71E−3**	0.0774	0.0533	− 31.08	5.22E−2	0.0527	− 31.82	1.53E−1

Table 1. dMRI metrics with significant differences between age-comparable healthy controls and NMDCCC patients with mild or severe compression. List of parameters with their corresponding labels as used in Fig. 6 along with statistics and Wilcoxon rank-sum test p values for HARDI-ZOOMit Interp and DTI-RESOLVE Non-Interp protocols. Significant p values ($p_{FWE} < 0.05 \approx 8.33E{-}3$) are highlighted in bold.

$$H_{d_{WM}} = \int_{1.70}^{2.20} g(d)dd \tag{4}$$

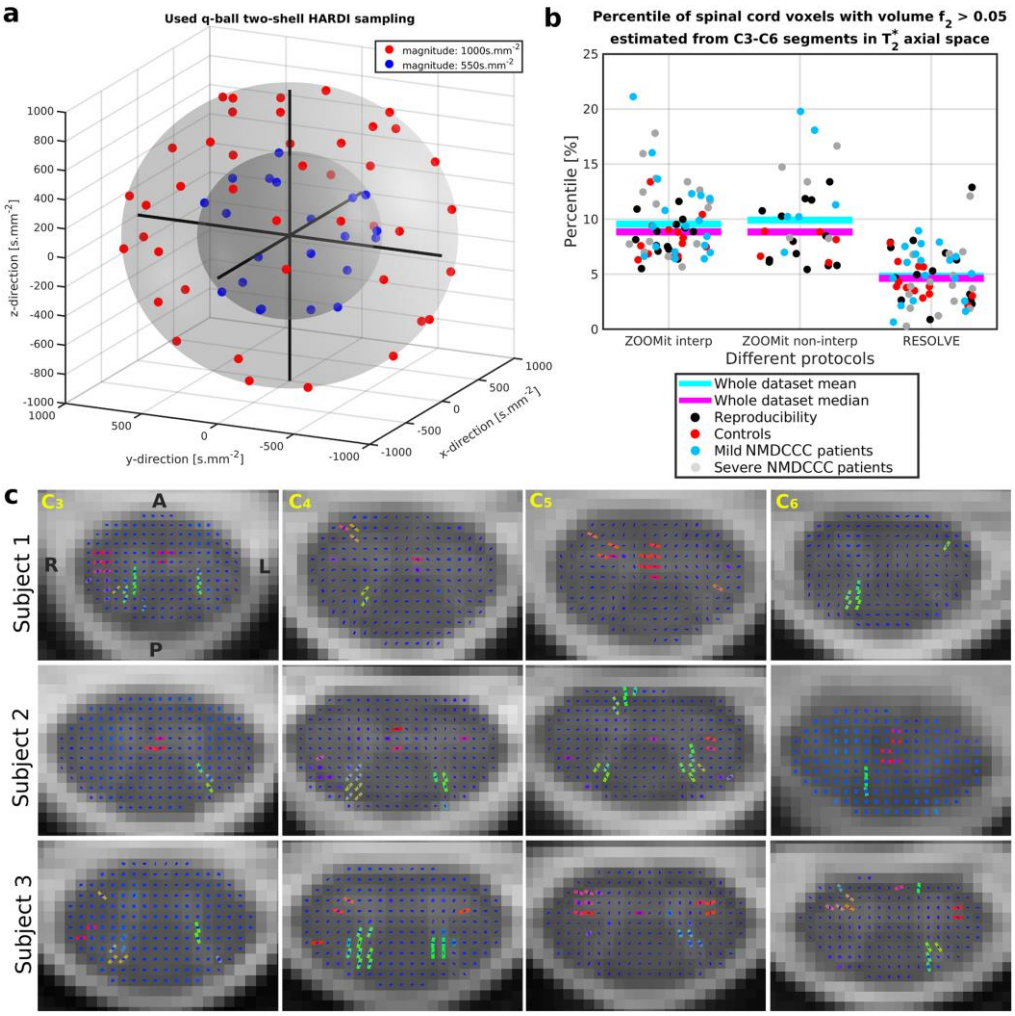

Figure 4. HARDI acquisition scheme and detected crossing fibers. (**a**) The graph visualizes 63 unique MR field gradient directions uniformly sampled over two spherical shells of the q-space. Caruyer et al.[57] sampler was used to design the HARDI acquisition scheme. (**b**) Voxels with significant 2nd fiber orientations (i.e. crossing fibers) were detected for all dMRI protocols. No significant difference in voxel numbers was found between groups. (**c**) As shown for results of HARDI-ZOOMit Interp protocol in native diffusion space, detected crossing fibers are mostly located near the dorsal horns and in the anterior white commissure. Visualizations are shown for three representative participants with four selected C3–C6 axial slices. Orientations are the same over all presented slices with *A* anterior, *P* posterior, *L*left, *R* right directions. The orientation of detected fiber bundles are visualized as RGB (red–green–blue) color-coded lines (i.e. red—right–left direction, green—anterior–posterior direction, blue—superior–inferior direction). The blue dot in the middle of each SC voxel demonstrates an axial projection of the intra-voxel primary fiber bundle with a major superior–inferior direction. In voxels where projections of two lines are present, crossing fibers were detected.

$$H_{d_{GM}} = \int_{1.00}^{1.48} g(d)dd \tag{5}$$

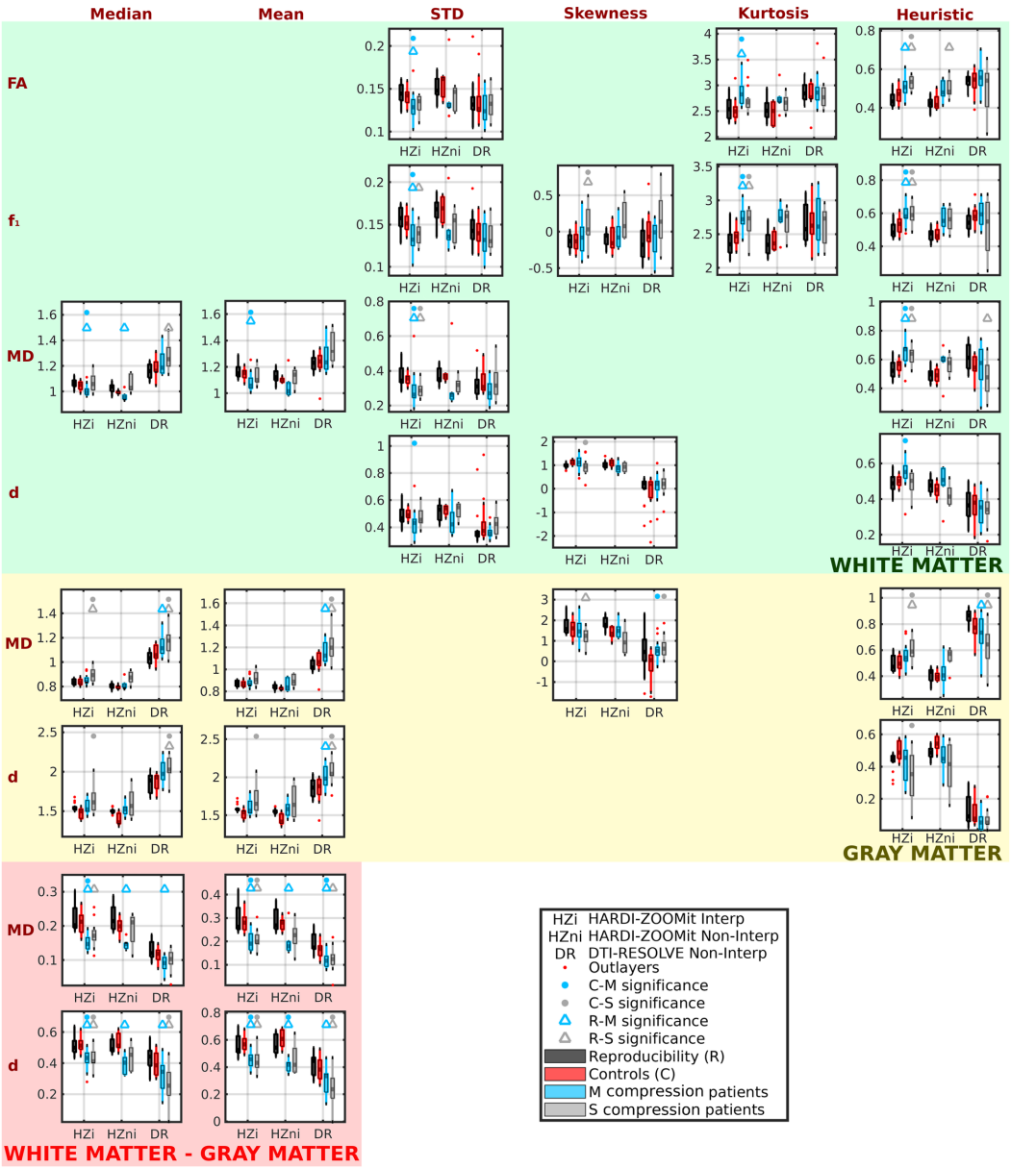

Figure 5. Diffusion MRI metrics with significant between-group differences ($p_{FWE} < 0.05$) for age-comparable controls and mild (M) or severe (S) compression non-myelopathic patient groups. "Reproducibility" refers to a group of young healthy subjects measured twice during separate acquisition sessions. For clarity, graphs are not shown for the diffusion metrics for which control-patient between-group differences were not statistically significant.

All WM-based heuristic parameters (Eqs. 1–4) demonstrated significant clinical differences between control and patient groups (Fig. 5; Table 1) and H_{MD} or H_{dGM} in GM (Eqs. 3, 5; Fig. 5; Table 1) for the HARDI-ZOOMit Interp protocol. H_{MD} measured in GM was significant for the DTI-RESOLVE Non-Interp protocol (Eq. 3; Fig. 5;

Parameters	Shortcut	HARDI-ZOOMit Interp.	DTI-RESOLVE non-Interp.
		C vs M+S	C vs M+S
FA_WM_STD	FAwS	**8.43E−3**	3.27E−1
FA_WM_kurtosis	FAwK	**1.99E−3**	6.32E−1
f1_WM_STD	f1wS	**1.93E−3**	2.21E−1
f1_WM_skewness	f1wSK	7.84E−2	9.62E−1
f1_WM_kurtosis	f1wK	**9.46E−5**	8.46E−1
MD_WM_median	MDwM	6.64E−1	7.65E−2
MD_WM_mean	MDwm	**3.44E−2**	9.25E−2
MD_WM_STD	MDwS	**4.09E−3**	2.53E−1
d_WM_STD	dwS	**3.00E−2**	1.87E−1
d_WM_skewness	dwSK	8.28E−2	2.09E−1
MD_GM_median	MDgM	**3.25E−2**	**1.48E−2**
MD_GM_mean	MDgm	5.60E−2	**5.29E−3**
MD_GM_skewness	MDgSK	2.46E−1	**6.44E−4**
d_GM_median	dgM	**4.79E−3**	**3.66E−4**
d_GM_mean	dgm	**5.94E−3**	**1.49E−4**
MD_WM-GM_median	MDwgM	**2.07E−4**	**2.47E−2**
MD_WM-GM_mean	MDwgm	**3.48E−7**	**1.12E−3**
d_WM-GM_median	dwgM	**2.98E−5**	**2.26E−3**
d_WG-GM_mean	dwgm	**4.11E−7**	**1.64E−3**
FA_WM_heuristic	FAwH	**1.77E−3**	8.87E−1
f1_WM_heuristic	f1wH	**1.35E−3**	8.49E−1
MD_WM_heuristic	MDwH	**1.05E−3**	5.21E−1
d_WM_heuristic	dwH	3.27E−1	1.61E−1
MD_GM_heuristic	MDgH	**7.70E−3**	6.79E−2
d_GM_heuristic	dgH	**3.70E−3**	**2.24E−2**

Table 2. Post-hoc ANCOVA of dMRI metrics with significant differences between age-comparable healthy controls and NMDCCC patients. List of parameters with their corresponding labels as used in Fig. 6 along with ANCOVA test p values for HARDI-ZOOMit Interp and DTI-RESOLVE Non-Interp protocols. Age was the confounding variable. Significant p values ($p < 0.05$) are highlighted in bold. *C* age-comparable healthy controls, *M* mild NMDCCC patients, *S* severe NMDCCC patients.

Table 1). All estimated values of proposed heuristic parameters are shown in Supplementary Fig. S6. Post-hoc ANCOVA with age as a confounding variable rejected the H_{dWM} measured in WM to demonstrate significant differences for the HARDI-ZOOMit protocol (Table 2). For the DTI-RESOLVE protocol, original H_{MD} GM significance disappeared, but H_{dGM} appeared significant (Table 2). Same as for the descriptive statistics parameters, the post-hoc Wilcoxon rank-sum tests demonstrated no significant differences in heuristic dMRI metrics of NMDCCC patients with or without radiculopathy.

Step-wise linear regression and K-means clustering. Descriptive statistics and our heuristic approach identified 25 parameters with significant discrimination power between age-comparable controls and mild or severe NMDCCC patients with Wilcoxon rank-sum tests (Fig. 5; Table 1). Cross-subject cross-correlation matrices demonstrate high similarity between several pairs of dMRI metrics (Fig. 6a). Step-wise linear regression ($\mathbf{Y} = \beta_0 + \mathbf{X}\beta + \epsilon$) identified a minimal linear mixture model maximizing separation between age-comparable healthy controls and all NMDCCC patients for each investigated dMRI protocol. Full visualization of the best model fits is shown in Supplementary Fig. S7 for each protocol. In descending order using Pearson correlation coefficient (r) between class signal ($\mathbf{Y}$) and predicted signal ($\mathbf{Y}_p = \mathbf{X}\beta$):

HARDI-ZOOMit Non-Interp protocol demonstrated four significant variables, i.e. skewness value of d in WM (dwSK), white–gray matter gradient of d median values (dwgM), white–gray matter gradient of d mean values (dwgm) and heuristic parameter of f_1 in WM (f1wH). The model fit efficiency metrics were as follows: $r = 0.892$, $RMSE = 0.252$, model F value $F = 10.74$, model p value $p = 8.56\text{E}^{-4}$, model explained variance of $R^2 = 79.6\%$.

HARDI-ZOOMit Interp protocol demonstrated two significant variables (dwgm; and kurtosis of f_1 in WM—f1wK), with efficiency metrics: $r = 0.733$, $RMSE = 0.317$, $F = 25.01$, $p = 6.23\text{E}^{-8}$, $R^2 = 53.8\%$. There is an overlap with the HARDI-ZOOMit Non-Interp protocol, i.e. the dwgm variable.

DTI-RESOLVE Non-Interp protocol demonstrated three significant variables (skewness of MD in GM—MDgSK; mean value of d in GM—dgm; and white–gray matter gradient of MD mean values—MDwgm), with efficiency metrics: $r = 0.670$, $RMSE = 0.350$, $F = 11.39$, $p = 1.35\text{E}^{-5}$, $R^2 = 44.9\%$.

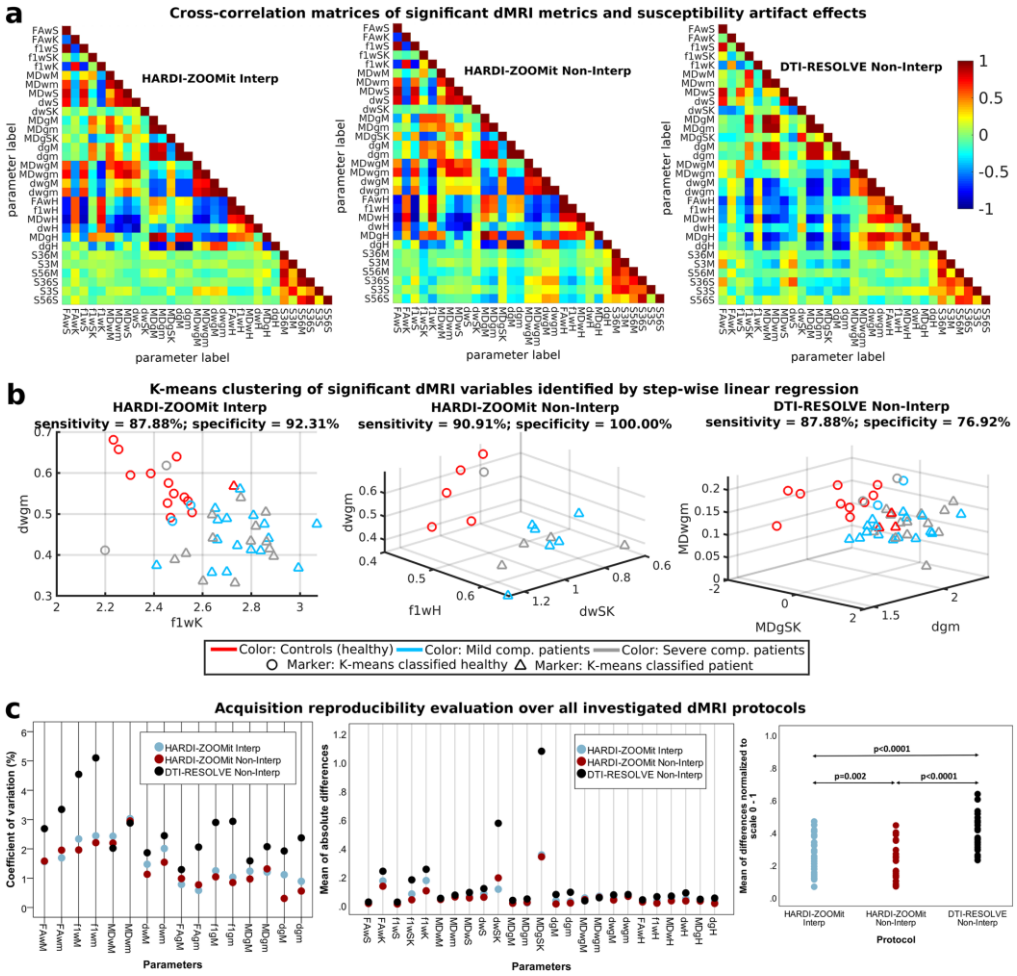

Figure 6. Cross-correlations of clinically significant diffusion MRI metrics and estimated susceptibility distortion parameters (**a**), K-means clustering of diffusion MRI metrics identified using step-wise linear regression (**b**) and reproducibility of diffusion MRI metrics over investigated protocols (**c**). Parameter names consists of 3 parts: (1) FA/f1/MD/d name of the diffusion MRI metric; (2) w/g/wg C3–C6 white matter, gray matter, white matter–gray matter difference respectively; (3) *M* median, *m* mean, *S* standard deviation, *SK* skewness, *K* kurtosis, *H* heuristic parameter. (**a**) The last six variables in matrices starting with letter S (e.g. S36M) represent measures of susceptibility artifact effects from three different ROIs (i.e. 36—C3–C6, 3—C3, 56—C5–C6).

Although significant relationship between age and dMRI metrics was previously observed in a healthy aging population[37] or in patients with degenerative cervical cord compression[16], none of the models identified age variable as the model-significant variable in the present data, suggesting that the age-effect in the dataset is low.

Only regression-identified significant variables were used in the following K-means clustering using two classes (Fig. 6b). In sensitivity (SE) and specificity (SP) descending order, HARDI-ZOOMit Non-Interp protocol demonstrated SE = 90.91%, SP = 100.00%; HARDI-ZOOMit Interp protocol SE = 87.88%, SP = 92.31%; and DTI-RESOLVE Non-Interp protocol SE = 87.88%, SP = 76.92%. K-means approach wrongly classified some outlying NMDCCC patients as healthy controls (Fig. 6b). While the used K-means clustering algorithm estimates and finds a linear hyper-plane separating clusters in the data, more advanced algorithms estimating non-linear hyper-planes[38] may likely improve the sensitivity for each protocol. We have not implemented such methods here, as they require additional datasets for training and the sample sizes of our datasets (46 or 16 data acquisitions) are

rather limited to consider such approach. Using the full dataset for the classifier training (Fig. 6b) might also led to the classifier overfitting in all used protocols.

Level of susceptibility artifacts in dMRI protocols. SC compression can increase local susceptibility off-resonance effects impacting the estimation of dMRI metrics. The level of the effects was evaluated in three different ROIs, i.e. C3–C6 (full FOV), C3 (area without compression) and C5–C6 (area with definite compression). These effects were not significantly different across groups in any ROI (Supplementary Fig. S8). HARDI-ZOOMit protocols were affected by off-resonance effects (group averages of single-subject median effects were 16 ± 8 Hz at C3–C6, 14 ± 7 Hz at C3, and 21 ± 13 Hz at C5–C6 for Interp protocol, 5 ± 3 Hz at C3–C6, 6 ± 4 Hz at C3, and 6 ± 4 Hz at C5–C6 for Non-Interp protocol) although to a lesser degree than the DTI-RESOLVE Non-Interp protocol (20 ± 11 Hz at C3–C6, 23 ± 16 Hz at C3, and 22 ± 15 Hz at C5–C6). Off-resonance effects of HARDI-ZOOMit Interp protocol were not correlated with dMRI derived parameters (Fig. 6a) with $|r| = 0.09 \pm 0.07$, $p_r \approx 0.49$, neither DTI-RESOLVE Non-Interp ($|r| = 0.15 \pm 0.11$, $p_r \approx 0.27$) and neither HARDI-ZOOMit Non-Interp ($|r| = 0.16 \pm 0.12$, $p_r \approx 0.48$). Still, the lowest cross-correlation effects are observed for the HARDI-ZOOMit Interp protocol (Fig. 6a).

Reproducibility in young healthy subjects. Coefficients of variation (CV) for mean/median WM/GM dMRI metrics, and absolute or normalized mean differences in 25 significant dMRI metrics are shown in Fig. 6c. CV revealed a large difference between both HARDI-ZOOMit protocols and DTI-RESOLVE ($p = 0.007$ for both), and no difference between HARDI-ZOOMit protocols, whereas the evaluation of normalized differences proved to be significant between all protocols ($p < 0.0001$ between HARDI-ZOOMit vs. DTI-RESOLVE; $p = 0.002$ between HARDI-ZOOMit protocols). The reproducibility of HARDI-ZOOMit protocols in comparison to the DTI-RESOLVE Non-Interp protocol was either comparable or higher as shown in Fig. 6c.

HARDI-ZOOMit protocol and data analysis innovations. Our proposed HARDI-ZOOMit protocols yielded a larger amount of significant metrics with higher specificity when compared to the DTI-RESOLVE Non-Interp protocol (Figs. 3, 5, 6b; Tables 1, 2). The increased mutual information between microstructural maps and WM/GM structures (Fig. 2d) and better separation ability of primary and secondary fiber bundles (Fig. 4b) can be the improving key aspects.

In comparison to the previously used DTI-RESOLVE Non-Interp protocol, the proposed HARDI-ZOOMit protocol includes several modifications which possibly underlie the higher specificity of the protocol for the targeted clinical application. These include multi-shell gradient waveform sampling (enabling better separation of different microstructural compartments[31]) over spherical q-space, and higher maximal b-value (1000 s mm^{-2} vs 650 s mm^{-2}) increasing the diffusion weighting effects[3] while retaining sufficient SNR (Fig. 1f). The fact that HARDI-ZOOMit protocols yielded higher group mean/median FA and f_1 values than the DTI-RESOLVE Non-Interp protocol (Fig. 3, Supplementary Figs. S1, S2) supports the hypothesis that the data are less noisy, consistent with the fact that the cervical SC largely consists of fiber bundles oriented in the superior–inferior direction with high level of diffusion anisotropy expected.

We proposed the use of skewness, kurtosis and heuristic parameters extracted from subject's cervical dMRI maps as robust statistic parameters in SC injury revealing significant differences between controls and patients (Figs. 5, 6b; Tables 1, 2). Also, while using the subtraction between WM and GM mean/median dMRI metrics, we have demonstrated the most significant inter-group differences (Figs. 5, 6b; Tables 1, 2). The subtraction method is comparable to a simple gradient approximation of dMRI metrics between WM and GM, and is a novel clinically feasible over all tested protocols for MD and d metrics.

Since we used the contiguous C3–C6 ROI space (i.e. data at all spinal levels), the obtained results have higher statistical power than previous studies in NMDCCC typically analyzing dMRI from several separate slices, mostly focused on the maximum compression level and compared to non-compressed levels[20,35]. Our approach addresses the issue of different ROI selection across subjects determined by the presence of SC compression at different segments but also the issue of physiologic dMRI metrics variation in different SC segments[39]. Moreover, the current approach minimizes artifact effects (Fig. 6a) potentially emphasized (Fig. 1f) in areas with the most severe compression.

Limitations and future work. Although C3–C6 WM or GM ROIs are quite large and coarse, it is feasible to proceed to finer analysis of tract-specific dMRI metrics utilizing a template and tract-specific atlas co-registration[37,40]. Tract-specific changes within our studied group of patients might be investigated, as demonstrated in the case of DCM[41–43] or ALS[44] patients.

A HARDI-RESOLVE dMRI protocol with exactly the same gradient waveform samplings, same b-values, and same spatial resolution should be used for the optimal protocol comparison. Such protocol might increase the percentage of observed crossings (Fig. 4b), increase FA and f_1 group medians (Supplementary Figs. S1, S2), and even increase the protocol's sensitivity or specificity to the presymptomatic myelopathy detection. However, the acquisition time of HARDI-RESOLVE protocol would significantly increase in comparison to the original 16 min for the DTI-RESOLVE protocol or 12.5 min for the introduced HARDI-ZOOMit protocols.

Further HARDI-ZOOMit protocol optimization or further increase in the protocol's angular resolution may yield dMRI protocol visualizing SC crossing fibers in-vivo in clinically applicable acquisition time.

Diffusion weighted MR signal loss in areas close to the lungs (i.e. lower part of C7 and T1 acquired here; Fig. 1c,e) crucially limits the usability of the proposed HARDI-ZOOMit protocol for other regions apart from the cervical spine and SC. Suppression of the lung-induced artifacts will be the topic of future research that might extend the usability of the protocol to broader clinical applications imaging beyond cervical SC segments.

We showed that the proposed protocol was able to distinguish age-comparable healthy controls and presymptomatic patients with microstructural myelopathy. Changes in dMRI parameters for DCM patients with advanced clinical symptoms have been already reported[12–18]. Extending the dataset with groups of symptomatic DCM patients spanning from mild to severe cervical SC compressions to delineate the disease progression in all DCM stages will be addressed in upcoming research. Also, step-wise multiple linear regression was used in a relatively simple context, dividing four different groups into two classes (controls or patients). More advanced classification, e.g. patients with mild or severe SC compressions, has not been applied, and should be carried out in the future, along with exploration of the 25 parameters that rendered significant between-group differences (Fig. 5; Table 1). Our results might be influenced by the gender-related difference in the control group (i.e. 9 females and 4 males). However, since the control group results overlapped with the young healthy participant group (i.e. reproducibility group, Fig. 3), we have assumed that gender effect was minimal. Similarly as we assumed it for the age-effect, which we have also confirmed with the ANCOVA test (Table 2). In contrast to the DTI-RESOLVE protocol, the presented HARDI-ZOOMit protocol has not demonstrated so many significant changes for MD or *d* in the GM (Fig. 5; Tables 1, 2). If these findings are confirmed, the clinical DTI-RESOLVE protocol provides additional information about the GM microstructural changes.

Discussion

Using an optimized HARDI-ZOOMit dMRI protocol and a "*high SNR*" DTI-RESOLVE protocol[33], we demonstrated a global difference of diffusion MRI metrics over contiguous C3–C6 levels between healthy controls and NMDCCC patients underlying presymptomatic microstructural myelopathy. The *practical impact* of detecting subclinical microstructural SC injury in NMDCCC using fast, reliable and clinically feasible dMRI protocol is significant. First, in addition to other quantitative MRI methods (i.e. magnetization transfer imaging and T_2^*-weighted imaging), it verifies and quantifies microstructural SC involvement in subjects with compressed spinal cord due to degenerative cervical stenosis[19]. Such knowledge opens the door for more accurate definition of the myelopathy diagnosis which is currently equivocal and often based on clinical symptoms, which appear relatively late. DCM is already symptomatic and clinical deficits may often be irreversible. Second, the time course and reversibility of microstructural dMRI-detected SC changes in the compressed SC and their correlation with similar "*functional*" and possibly "*biochemical*" changes detected in NMDCCC using evoked potentials and magnetic resonance spectroscopycite[45,46] may further describe the DCM pathophysiology and lead to the optimization of the DCM diagnosis. Finally, these changes may help to identify NMDCCC subjects with higher risk of developing DCM (i.e., "*presymptomatic myelopathy*"), in addition to already demonstrated predictors[35,45].

The DTI-RESOLVE Non-Interp scans were occasionally contaminated by insufficient fat suppression or aliasing artifacts (e.g. in the upper parts of the FOV with voxels originating from areas outside the FOV, from subjects' chin or adipose tissue in particular). While the artifacts were mostly present on the outside of the SC ROI, their effect on the dMRI metrics should be minimal. It is also important to note that the performance of HARDI-ZOOMit protocol remains limited for the SC imaging at and below C7 vertebra.

Major fiber tracts in the cervical SC are highly organized along the SC longitudinal axis resulting in relatively high FA or f_1 values. Our finding of higher FA and f_1 mean/median value estimates with HARDI-ZOOMit protocols suggests that the HARDI-ZOOMit data are less noisy than DTI-RESOLVE protocol data. Higher statistical power of between-group differences for f_1 derived statistical parameters (compared to complementary FA parameters) demonstrated the efficiency of the multi-shell data acquisition and additive multi-compartment microstructural models (estimating local fiber crossings) and the potential applicability in the clinical quantitative diagnostic imaging. Further clinical HARDI protocol optimization utilizing other shells with $b > 1000\,s\,mm^{-2}$, sufficient SNR and sufficient acquisition time would permit using other advanced microstructural models such as NODDI (neurite orientation dispersion and density imaging)[47–50], MIX (microstructure imaging of crossing)[51], CHARMED (composite hindered and restricted model of diffusion)[52], AxCaliber[53], ActiveAx[54] or direct multi-shell multi-tissue constrained spherical deconvolution[55], etc. Default implementations of such methods expect high b-values or even variable diffusion δ/Δ times within the same shell. Although low b-value single-shell SC implementation exists for NODDI[56], it remained beyond the focus of our already quite extensive analysis. The current data sets and pipeline codes were made publicly available, so, researchers may investigate and compare other diffusion models.

Methods

Participants. All participants signed an informed consent enabling the experimentation with human subjects and were enrolled in the study that was approved by the *Masaryk University* (*Brno, Czech Republic*) ethics committee and by the *University Hospital Brno* (*Brno, Czech Republic*) ethics committee, both in concordance with the Declaration of Helsinki. NMDCCC patients were identified in an extensive sample of the Caucasian population of the South Moravia region, through an epidemiological study assessing the prevalence of degenerative cervical cord compression[21]. All participants underwent MRI examination of the cervical spine on a 1.5 T MR Philips Achieva scanner with a standard 16-channel head and neck coil. The standardized imaging protocol included conventional pulse sequences in sagittal-T_1, T_2 and short-tau inversion recovery (STIR), and axial planes (gradient-echo T_2) for the purpose of morphological evaluation. The clinical status of patients/healthy controls was blinded to two neuroradiologists who evaluated and agreed on the assessment of the compression in the majority of cases. Where disagreement existed—seldom—the final decision was based on a consensus. The imaging criterion for cervical cord compression, dividing groups at healthy controls and NMDCCC patients, was defined as a change in SC contour or shape at the level of an intervertebral disc on axial or sagittal MRI scan compared to that at midpoint level of neighboring vertebrae. NMDCCC patients were then clinically examined

by two certified neurologists (experienced in degenerative cervical myelopathy diagnosis) who excluded the presence of any clinical myelopathic signs or symptoms[35].

In addition to the assessment of cervical cord compression, the following conventional MRI parameters were also measured to quantify the severity of compression: cross-sectional area (CSA) of the SC and compression ratio (CR) calculated as anteroposterior/laterolateral SC diameter. Severe SC compressions were defined as both CSA $\leq 70\,\mathrm{mm}^2$ and CR ≤ 0.4. These thresholds proved to increase the risk of development of symptomatic DCM in a previous study[35].

Several young healthy volunteers were investigated twice with an inter-scan interval (> 1 day) to evaluate test–retest reliability of used imaging methods, i.e., reproducibility. Young healthy volunteers passed neither radiological nor neurological evaluation. The inter-scan interval ranged from 0 to 29 weeks (mean ± standard deviation 7 ± 11 weeks).

MRI acquisition. High-resolution sagittal T_2-weighted (T_2w) and axial T_2^*-weighted (T_2^*w) anatomical scans were acquired followed by two independent axial dMRI acquisition protocols (i.e. HARDI-ZOOMit Interp and DTI-RESOLVE Non-Interp) in randomized order to disperse the effect of motion artifacts uniformly over sessions. In a subset of study participants, the HARDI-ZOOMit Non-Interp protocol was also acquired. All imaging was performed on a 3T scanner (Magnetom Prisma; *Siemens Healthcare, Erlangen, Germany*) using the standard 64-channel head/neck and the 32-channel spine coils. All axial sequences were pulse triggered increasing the expected data acquisition time (TA) about 10–15% for each sequence.

T_2*-weighted sagittal images* were acquired to cover the whole cervical SC with 30 contiguous slices using a turbo spin-echo sequence with TR = 8640 ms (repetition time), TE = 98 ms (echo time), 4 averages, GRAPPA = 2, field of view (FOV) $250 \times 250\,\mathrm{mm}^2$, matrix size 896×896 voxels, slice thickness 1.3mm, voxel size $0.28 \times 1.30 \times 0.28\,\mathrm{mm}^3$. The acquisition time (TA) was 8min 49s.

T_2^**-weighted axial images* were acquired to cover the C3–C7 levels with 42 contiguous slices using a MEDIC (multi-echo data image combination) sequence with TR = 778 ms, TE = 17 ms (4 echoes), 2 averages, FOV $180 \times 180\,\mathrm{mm}^2$, matrix size 512×512 voxels after interpolation in Fourier domain, slice thickness 2.5 mm, voxel size $0.70 \times 0.70 \times 2.50\,\mathrm{mm}^3$ (re-sampled to $0.35 \times 0.35 \times 2.50\,\mathrm{mm}^3$ within MR scanner image reconstruction), TA would be 7 min 51 s, if pulse trigger was not used.

HARDI-ZOOMit interpolated dMRI protocol was acquired to cover the C3–C7 levels with 35 contiguous axial slices with TR = 6700 ms, TE = 73 ms, FOV = $44 \times 129\,\mathrm{mm}^2$, matrix size 68×200 voxels, slice thickness 3mm, voxel size $1.30 \times 1.30 \times 3.00\,\mathrm{mm}^3$ re-sampled to $0.65 \times 0.65 \times 3.00\,\mathrm{mm}^3$ after interpolation in Fourier domain. Sixty-three diffusion weighted images (42 gradient directions with b-value = $1000\,\mathrm{s\,mm}^{-2}$ and 21 directions with b = $550\,\mathrm{s\,mm}^{-2}$) and 7 images (b_0) with b = $0\,\mathrm{s\,mm}^{-2}$ were collected with anterior-posterior (AP) phase encoding. Five additional b_0 images were acquired using posterior–anterior (PA) phase encoding. A total expected TA without pulse trigger would be 12 min 46 s. The 63 gradient directions were uniformly sampled over two spherical shells (see Fig. 4a) with Caruyer et al.'s[57] sampler.

HARDI-ZOOMit non-interpolated dMRI protocol was acquired with the same protocol without the interpolation in Fourier domain and with the same acquisition time. The matrix size decreased at 34×100 voxels and voxel size stayed $1.30 \times 1.30 \times 3.00\,\mathrm{mm}^3$.

DTI-RESOLVE dMRI protocol consisted of two identical sessions with opposite phase encodings (AP, PA). For each encoding, 30 diffusion weighted images with b = $650\,\mathrm{s\,mm}^{-2}$ and 5 b_0 images were collected. The acquired data cover C3–C7 levels with 30 contiguous axial slices with TR = 4500 ms, TE_1 = 50 ms, TE_2 = 77 ms, FOV = $73 \times 165\,\mathrm{mm}^2$, matrix size 66×118 voxels, slice thickness 3.30 mm, voxel size $1.10 \times 1.10 \times 3.30\,\mathrm{mm}^3$. TA without pulse trigger would be 16 min 16 s.

All MRI acquisition protocol files (i.e. .pdf file with MRI parameters, .exar1 file for an easy upload into the Siemens MR console and .dvs file with HARDI sampling) are stored under the URL link listed in the *Data availability* section.

dMRI protocol's SNR estimation. For each data acquisition and each dMRI protocol separately, DWI and b_0 scans were separated and extracted. *Without any data preprocessing*, mean DWI and mean b_0 images were estimated. SC was segmented with `sct_deepseg_sc`[58] algorithm from the mean DWI image. If the protocol consisted of more than one *q-space* shells, DWI data were separated at each single-shell. The first four and last four slices were excluded from estimation of the mean intensity (I_{SC}) of DWI signal inside SC of each shell. Air area was located in mean b_0 image of each participant with thresholding of the superior half of the FOV. Noise standard deviation (σ_{air}) was estimated from segmented air area. The SNR was estimated with Eq. (6) optimized or estimation from two different ROIs[59]. SNR group medians, means and STDs evaluated the level of the noise of each shell and each protocol.

$$SNR = \frac{I_{SC}}{\sqrt{\frac{2}{4-\pi}}\sigma_{air}} \tag{6}$$

Data processing pipeline. The acquired data were processed with Spinal Cord Toolbox 3.2.3 (SCT)[60], ANTs 2.1.0 (Advanced Normalization Tools)[61] and and FSL 5.0.10 (FMRIB Software Library)[62] software libraries implemented all together within in-house made bash scripts that also include some in-house routines programmed in MATLAB (*MathWorks, Natick, USA*).

Areas outside the body were removed from sagittal and axial anatomical scans with low intensity thresholding and both scans were bias-field corrected[63]. Since the axial T_2^* data were acquired with inter-leaved data collection

process, the data were corrected slice-by-slice with in-house implemented algorithm utilizing affine registeration[64] and additive fusion[64] of even and odd slices. Sagittal scan was re-sampled at voxel size $0.28 \times 0.35 \times 0.28\,mm^3$ resolution and cropped to cover only a cervical area (i.e. T2SAG space). SC was initially segmented from T2SAG scan with a `sct_deepseg_sc`[58] algorithm implemented in SCT[60], z-axis slice number containing C2/C3 disc was manually marked, and `sct_label_vertebrae`[65] library automatically labeled individual vertebral levels. The bias-field corrected T2SAG image was co-registered with fixed axial image (i.e. T2TRA space), using `sct_register_multimodal`[60] script utilizing series of ANTs[61] registration algorithms (initially optimized for brain image registrations)[66]. Segmented SC and its labels were warped from sagittal T2SAG space into co-registered T2TRA space. The 2nd iteration of SC segmentation[58] and labelling[65] was performed in the T2TRA space, following with GM segmentation utilized with `sct_deepseg_gm`[67] library. WM area was obtained by subtraction of the SC and GM masks. All segmented masks and vertebral labelings in T2TRA space were then visually inspected and corrected if necessary.

dMRI data of each protocol were processed separately, utilizing the same pipeline, as follows: Susceptibility, motion and eddy currents artifacts were minimized from the entire FOV with FSL[62] `topup`[68] and `eddy`[69] functions. From the preprocessed dMRI data, DTI[3] and ball and stick[30] models were estimated with `dtifit` and `bedpostx` functions, both implemented in FSL[62]. From DTI estimates, fractional anisotropy (FA)[3] and mean diffusivity (MD)[3] maps were derived for each subject. For the ball and stick models, two crossing fiber bundles with their partial volume fractions (f_1, f_2)[30] were expected as a maximal occurring number (i.e. Ball and Stick and Stick model), and single mean diffusivity values (d)[30] without any variance were estimated per each voxel. Single-subject FA and f_1 maps are complementary, similarly to MD and d maps. From eddy output (4D image), DWIs, b_0 images and their mean versions were extracted and separated by `sct_dmri_separate_b0_and_dwi`[60] function. SC in diffusion space was segmented from the "DWI_mean" image again with the `sct_deepseg_sc`[58] function. Utilizing the `sct_register_multimodal`[60] command, a single-subject "b_0_mean" image was co-registered into T2TRA space with fixed T_2^*-w axial image, while segmented masks of SC from DWI_mean and bias-field corrected T_2^*-w axial images were used to define the regions of interest (ROIs). Estimated warping field was then used for geometrical transformations of all dMRI metrics (i.e. FA, MD, f_1, d, etc.) from diffusion space of each protocol into a T2TRA space. In this space, two different ROIs were defined (using segmented masks and labels), i.e. C3–C6 WM area and C3–C6 GM area. SC at level C3-6 was analyzed as C3–C6 area is the most often affected by SC compression[35]. Diffusion MRI-derived quantitative parameters from the C3–C6 area were compared over 4 different groups of subjects and over three different acquired dMRI protocols, as described in following section.

Mutual information between dMRI metrics and WM/GM structures. Mutual information is a similarity criterion detecting increased magnitude for similar images with both linear or non-linear contrast transform functions[64]. Considering a non-linear transform function between microstructural maps and WM/GM structures, non-normalized mutual information (I, Eq. 7)[64] was estimated between each dMRI metric map (a, i.e. FA, f_1, MD or d) and semi-binarized T_2^*w axial image (b, background = 0; GM = 1; and WM = 2) inside C3–C6 SC area for each subject and protocol. Variable E_a represent the entropy of image a, E_b entropy of image b, and E_{ab} the joint entropy between images a and b[64]. Function $s(a)$ is the histogram of image a with intensity indexes from 1 to q. Function $u(b)$ is the histogram of image b with intensity indexes from 1 to r. Function $v(a, b)$ is the joint histogram[64] between images a and b. Similarity criterion distributions were visualized for each dMRI metric and protocol, and values of distributions' group-averaged quartiles and medians were used for the description and evaluation of the rate of mutual entropy[64] between dMRI metric maps and WM/GM structures over protocols.

$$I = E_a + E_b - E_{ab} = -\sum_{l=1}^{q} s(a_l)\log(s(a_l)) - \sum_{m=1}^{r} u(b_m)\log(u(b_m)) + \sum_{l=1}^{q}\sum_{m=1}^{r} v(a_l, b_m)\log(v(a_l, b_m)) \tag{7}$$

Quantitative measurements from ROIs, group-level and inter-protocol comparisons. ROIs were characterized with several parameters of descriptive statistics usually estimated for random variables (i.e. estimated dMRI metrics: FA, MD, f_1 and d maps). They were the first four moments (i.e. mean, standard deviation - STD, skewness and kurtosis) of Gaussian probability density function (p.d.f.) and median. For each dMRI protocol separately, Wilcoxon rank-sum test was used to investigate whether a group median of some dMRI parameter differed, especially between some group of patients and group of age-comparable controls. Critical p value was set to $p < 0.00833 \approx p_{FWE} < 0.05$, since there are six possible different comparisons over four groups of subjects for one dMRI protocol and $0.05/6 = 8.33E^{-3}$ (FWE—family wise error correction for multiple comparisons).

Because the Gaussian approximation often does not provide a good fit to the measured data especially for random variables with non-symmetric p.d.f.s, we have fitted smooth p.d.f.s directly from a histogram of each ROI with a "normal" kernel (as implemented in MATLAB with `fitdist` function). Mean p.d.f.s with Q1–Q3 confidence intervals (Q—quartile) were derived for each group of subjects and each protocol. Heuristic parameters (H) which may clinically differentiate controls and non-myelopathic patients were proposed as Eq. (8). Values x_1 and x_2 are marginal values of a dMRI metric (x), where confidence intervals are disjunctive for derived smooth p.d.f.s (g).

$$H_x = \int_{x_1}^{x_2} g(x)dx \tag{8}$$

Wilcoxon rank-sum test was used for testing differences between groups of subjects in the same way as for descriptive statistics parameters.

To minimize age-effect in the comparison results, post-hoc ANCOVA (analysis of covariance) was used as an additional between-group difference test where age was used as a confounding variable. One tested group were age-comparable healthy controls, second group were all NMDCCC patients. If test's $p < 0.05$, the between-group difference was considered to be significant.

To evaluate the effect of radiculopathy, post-hoc Wilcoxon rank-sum tests investigated the differences in statistical or heuristic dMRI metrics of NMDCCC patients with or without radiculopathy. Significance level was set at $p < 0.05$.

Diffusion MRI metric redundancy, uniqueness, sensitivity and specificity. Cross-subject Pearson correlation coefficients (r) evaluated level of linear dependence between dMRI metrics demonstrating significant between-group differences. Step-wise linear regression ($\mathbf{Y} = \beta_0 + \boldsymbol{X\beta} + \boldsymbol{\epsilon}$) was used to identify unique dMRI metrics that maximize differences between age-comparable healthy control (C) and NMDCCC patient (M, i.e. mild compression and S, i.e. severe compression) groups. $\mathbf{Y}$ is a vector equal to 0.5 for positions of C subjects and −0.5 to positions of M or S subjects. Significant variables (i.e. dMRI metrics) in model matrix $\mathbf{X}$ were added based on their variable p values (< 0.05) quantifying belonging to the final model fit. Because of an age effect concerns, we have also added the age variable as the tested parameter (i.e. potential significant compartment of the final matrix $\mathbf{X}$). Set of significant variables in model matrix $\mathbf{X}$ was used as an input feature into automatic K-means clustering at 2 classes. Sensitivity (SE) and specificity (SP) of each dMRI protocol was evaluated by comparison of the K-means classification with control-patient classification done by radiologist and neurologist experts.

Level of off-resonance effects in dMRI data. Single-subject mean, median, and STD of absolute off-resonance effects (i.e. field coefficient output of the `topup`[68] function) were estimated for each data acquisition from three different SC ROIs (C3–C6 characterizing our dMRI analysis ROI, C3 characterizing area without probable compression, and C5–C6 characterizing area with possible compression in patients) defined by segmented and labeled SC of T_2^*w axial scan. Differences over subject groups were tested again using Wilcoxon rank-sum test. Cross-subject Pearson correlation coefficients (r) evaluated cross-correlations with dMRI derived parameters observing significant differences between control and patient groups to test whether the observed difference is/is not caused by different level of off-resonance effects.

Test–retest reliability of dMRI protocols. Test–retest reliability (i.e. reproducibility) was tested in a group of seven young healthy volunteers who were scanned twice with time interval between session ranging from 0 to 29 weeks (mean ± standard deviation 7 ± 11 weeks). The minimum distance was 1 day. Mean coefficients of variation (CV, the ratio of standard deviation to the mean of repeated measures) were calculated for parameters expressing single-subject WM/GM dMRI metric mean or median. Absolute differences between consecutive measurements in seven subjects were calculated for all dMRI parameters where significant differences between controls and a patient group were observed. For a comprehensive comparison of protocols, a min–max normalization to range 0–1 was employed on each variable difference through all three protocols. Means of normalized differences were calculated for each variable per protocol. Three different protocols were then compared by CVs and means of normalized differences using series of Wilcoxon signed ranks tests with Bonferroni correction for multiple testing. Statistical testing was performed in SPSS version 23 (*IBM, Armonk, New York*).

Data availability

Acquired MRI data reported in the manuscript, a table with basic participants' demographics, and "*HARDI-ZOOMit.pdf*" and "*HARDI-ZOOMit.exar1*" files with used MRI protocol parameters are available at the URL: https://hdl.handle.net/20.500.12618/0000-5c13d342-4798-41d9-8d2a-bf750ab79fdb.

Code availability

All in-house implemented codes and scripts with the installation manual are available at the URL: https://github.com/renelabounek/sc-dmri-myelopathy.

Received: 19 November 2019; Accepted: 21 July 2020
Published online: 16 October 2020

References

1. Stejskal, E. O. & Tanner, J. E. Spin diffusion measurements: Spin echoes in the presence of a time-dependent field gradient. *J. Chem. Phys.* **42**, 288–292 (1965).
2. Le Bihan, D. *et al.* MR imaging of intravoxel incoherent motions: Application to diffusion and perfusion in neurologic disorders. *Radiology* **161**, 401–407 (1986).
3. Basser, P. J., Mattiello, J. & LeBihan, D. MR diffusion tensor spectroscopy and imaging. *Biophys. J* . **66**, 259–267. https://doi.org/10.1016/S0006-3495(94)80775-1 (1994).
4. Clark, C. A., Werring, D. J. & Miller, D. H. Diffusion imaging of the spinal cord in vivo: Estimation of the principal diffusivities and application to multiple sclerosis. *Magn. Reson. Med.* **43**, 133–138 (2000).

5. Wheeler-Kingshott, C. *et al.* The current state-of-the-art of spinal cord imaging: Applications. *NeuroImage* **84**, 1082–1093. https://doi.org/10.1016/j.neuroimage.2013.04.124 (2014).
6. Martin, A. R. *et al.* Translating state-of-the-art spinal cord MRI techniques to clinical use: A systematic review of clinical studies utilizing DTI, MT, MWF, MRS, and fMRI. *NeuroImage. Clin.* **10**, 192–238. https://doi.org/10.1016/j.nicl.2015.11.019 (2016).
7. Cohen-Adad, J. *et al.* Demyelination and degeneration in the injured human spinal cord detected with diffusion and magnetization transfer MRI. *NeuroImage* **55**, 1024–1033. https://doi.org/10.1016/j.neuroimage.2010.11.089 (2011).
8. Martin, A. R. *et al.* A novel MRI biomarker of spinal cord white matter injury: T2*-weighted white matter to gray matter signal intensity ratio. *Am. J. Neuroradiol.* **38**, 1266–1273 (2017).
9. Bede, P. *et al.* Spinal cord markers in ALS: Diagnostic and biomarker considerations. *Amyotroph. Lateral Scler.* **13**, 407–415. https://doi.org/10.3109/17482968.2011.649760 (2012).
10. Zhang, J. *et al.* Diffusion tensor magnetic resonance imaging of Wallerian degeneration in rat spinal cord after dorsal root axotomy. *J. Neurosci.* **29**, 3160–3171 (2009).
11. Huffnagel, I. C. *et al.* Longitudinal diffusion MRI as surrogate outcome measure for myelopathy in adrenoleukodystrophy. *Neurology* **93**, e2133–e2143. https://doi.org/10.1212/WNL.0000000000008572 (2019).
12. Keřkovský, M. *et al.* Magnetic resonance diffusion tensor imaging in patients with cervical spondylotic spinal cord compression. *Spine* **37**, 48–56. https://doi.org/10.1097/BRS.0b013e31820e6c35 (2012).
13. Jones, J. G. A., Cen, S. Y., Lebel, R. M., Hsieh, P. C. & Law, M. Diffusion tensor imaging correlates with the clinical assessment of disease severity in cervical spondylotic myelopathy and predicts outcome following surgery. *Am. J. Neuroradiol.* **34**, 471–478. https://doi.org/10.3174/ajnr.A3199 (2013).
14. Wen, C.-Y., Cui, J.-L., Mak, K.-C., Luk, K. D. K. & Hu, Y. Diffusion tensor imaging of somatosensory tract in cervical spondylotic myelopathy and its link with electrophysiological evaluation. *Spine J.* **14**, 1493–1500. https://doi.org/10.1016/j.spinee.2013.08.052 (2014).
15. Guan, X. *et al.* Diffusion tensor imaging studies of cervical spondylotic myelopathy: A systemic review and meta-analysis. *PLoS One* **10**, e0117707. https://doi.org/10.1371/journal.pone.0117707 (2015).
16. Keřkovský, M. *et al.* Spinal cord MR diffusion properties in patients with degenerative cervical cord compression. *J. Neuroimaging* **27**, 149–157. https://doi.org/10.1111/jon.12372 (2017).
17. Vedantam, A. *et al.* Diffusion tensor imaging correlates with short-term myelopathy outcome in patients with cervical spondylotic myelopathy. *World Neurosurg.* **97**, 489–494. https://doi.org/10.1016/j.wneu.2016.03.075 (2017).
18. Martin, A. *et al.* Monitoring for myelopathic progression with multiparametric quantitative MRI. *PLoS One* **13**, e0195733. https://doi.org/10.1371/journal.pone.0195733 (2018).
19. Martin, A. R. *et al.* Clinically feasible microstructural MRI to quantify cervical spinal cord tissue injury using DTI, MT, and T2*-weighted imaging: Assessment of normative data and reliability. *Am. J. Neuroradiol.* **38**, 1257–1265. https://doi.org/10.3174/ajnr.A5163 (2017).
20. Martin, A. R. *et al.* Can microstructural MRI detect subclinical tissue injury in subjects with asymptomatic cervical spinal cord compression? A prospective cohort study. *BMJ Open* **8**, e019809. https://doi.org/10.1136/bmjopen-2017-019809 (2018).
21. Kovalova, I. *et al.* Prevalence and imaging characteristics of nonmyelopathic and myelopathic spondylotic cervical cord compression. *Spine* **41**, 1908–1916. https://doi.org/10.1097/BRS.0000000000001842 (2016).
22. Wilson, J. R. *et al.* Frequency, timing, and predictors of neurological dysfunction in the nonmyelopathic patient with cervical spinal cord compression, canal stenosis, and/or ossification of the posterior longitudinal ligament. *Spine* **38**, S37–S54. https://doi.org/10.1097/brs.0b013e3182a7f2e7 (2013).
23. Ellingson, B. M., Salamon, N., Woodworth, D. C., Yokata, H. & Holly, L. T. Reproducibility, temporal stability, and functional correlation of diffusion MR measurements within the spinal cord in patients with asymptomatic cervical stenosis or cervical myelopathy. *J. Neurosurg. Spine* **28**, 472–480. https://doi.org/10.3171/2017.7.SPINE176 (2018).
24. Tuch, D. S. *et al.* High angular resolution diffusion imaging reveals intravoxel white matter fiber heterogeneity. *Magn. Reson. Med.* **48**, 577–582. https://doi.org/10.1002/mrm.10268 (2002).
25. Cohen-Adad, J. *et al.* Detection of multiple pathways in the spinal cord using q-ball imaging. *NeuroImage* **42**, 739–749. https://doi.org/10.1016/j.neuroimage.2013.04.124 (2008).
26. Lundell, H., Nielsen, J. B., Ptito, M. & Dyrby, T. B. Distribution of collateral fibers in the monkey cervical spinal cord detected with diffusion-weighted magnetic resonance imaging. *NeuroImage* **56**, 923–929. https://doi.org/10.1016/j.neuroimage.2013.04.124 (2011).
27. Calabrese, E. *et al.* Postmortem diffusion MRI of the entire human spinal cord at microscopic resolution. *NeuroImage Clin.* **18**, 963–971. https://doi.org/10.1016/j.nicl.2018.03.029 (2018).
28. Labounek, R. *et al.* Fast in vivo high-resolution diffusion MRI of the human cervical spinal cord microstructure. *IFMBE Proceed. World Congress Med. Phys. Biomed. Eng.* **68**, 3–7. https://doi.org/10.1007/978-981-10-9035-6_1 (2019).
29. Samson, R. S. *et al.* ZOOM or non-ZOOM? Assessing spinal cord diffusion tensor imaging protocols for multi-centre studies. *PLoS One* **11**, e0155557. https://doi.org/10.1371/journal.pone.0155557 (2016).
30. Behrens, T. E. J. *et al.* Characterization and propagation of uncertainty in diffusion-weighted MR imaging. *Magn. Reson. Med.* **50**, 1077–1088. https://doi.org/10.1016/j.neuroimage.2013.04.124 (2003).
31. Panagiotaki, E. *et al.* Compartment models of the diffusion MR signal in brain white matter: A taxonomy and comparison. *NeuroImage* **59**, 2241–2254. https://doi.org/10.1016/j.neuroimage.2013.04.124 (2012).
32. Cohen-Adad, J. High-resolution DWI in brain and spinal cord with syngo RESOLVE. *MAGNETOM Flash Mag. MRI* **2**, 16–23 (2012).
33. Zhang, B. T. *et al.* Diffusion tensor imaging of spinal microstructure in healthy adults: Improved resolution with the readout segmentation of long variable echo-trains. *Neural Regener. Res.* **12**, 2067–2070. https://doi.org/10.4103/1673-5374.221166 (2017).
34. Nouri, A. *et al.* MRI analysis of the combined prospectively collected AOSpine North America and international data. *Spine* **42**, 1058–1067. https://doi.org/10.1097/BRS.0000000000001981 (2017).
35. Kadanka, Z. *et al.* Predictors of symptomatic myelopathy in degenerative cervical spinal cord compression. *Brain Behav* **7**, e00797. https://doi.org/10.1002/brb3.797 (2017).
36. Tuch, D. S. Q-ball imaging. *Magn. Reson. Med.* **52**, 1358–1372. https://doi.org/10.1016/j.nicl.2015.11.019 (2004).
37. Taso, M. *et al.* Tract-specific and age-related variations of the spinal cord microstructure: A multi-parametric MRI study using diffusion tensor imaging (DTI) and inhomogeneous magnetization transfer (ihMT). *NMR Biomed.* **29**, 817–832. https://doi.org/10.1016/j.nicl.2015.11.019 (2016).
38. Bishop, C. M. *Pattern Recognition and Machine Learning* (Springer, Berlin, 2006).
39. Massire, A. *et al.* Feasibility of single-shot multi-level multi-angle diffusion tensor imaging of the human cervical spinal cord at 7T. *Magn. Reson. Med.* **80**, 947–957. https://doi.org/10.1016/j.nicl.2015.11.019 (2018).
40. Lévy, S. *et al.* White matter atlas of the human spinal cord with estimation of partial volume effect. *NeuroImage* **119**, 262–271. https://doi.org/10.1016/j.nicl.2015.11.019 (2015).
41. Cui, J. L. *et al.* Quantitative assessment of column-specific degeneration in cervical spondylotic myelopathy based on diffusion tensor tractography. *Eur. Spine J.* **24**, 41–47. https://doi.org/10.1016/j.nicl.2015.11.019 (2015).
42. Grabher, P., Mohammadi, S., David, G. & Freund, P. Neurodegeneration in the spinal ventral horn prior to motor impairment in cervical spondylotic myelopathy. *J. Neurotrauma* **34**, 2329–2334. https://doi.org/10.1089/neu.2017.4980 (2017).

43. Wang, K. Y. *et al.* Tract-specific diffusion tensor imaging in cervical spondylotic myelopathy before and after decompressive spinal surgery: Preliminary results. *Clin. Neuroradiol.* **27**, 61–69. https://doi.org/10.1007/s00062-015-0418-7 (2017).
44. Pisharady, P. *et al.* Tract-specific analysis improves sensitivity of spinal cord diffusion MRI to cross-sectional and longitudinal changes in Amyotrophic Lateral Sclerosis. *Commun. Biol.* **3**, 370. https://doi.org/10.1038/s42003-020-1093-z (2020).
45. Bednarik, J. *et al.* Presymptomatic spondylotic cervical myelopathy: An updated predictive model. *Eur. Spine J.* **17**, 421–431. https://doi.org/10.1007/s00586-008-0585-1 (2008).
46. Ellingson, B. M., Salamon, N., Hardy, A. J. & Holly, L. T. Prediction of neurological impairment in cervical spondylotic myelopathy using a combination of diffusion mri and proton mr spectroscopy. *PLoS One* **10**, e0139451. https://doi.org/10.1371/journal.pone.0139451 (2015).
47. Zhang, H., Schneider, T., Wheeler-Kingshott, C. A. & Alexander, D. C. NODDI: Practical in vivo neurite orientation dispersion and density imaging of the human brain. *NeuroImage* **61**, 1000–1016. https://doi.org/10.1016/j.neuroimage.2012.03.072 (2012).
48. Grussu, F., Schneider, T., Zhang, H., Alexander, D. C. & Wheeler-Kingshott, C. A. M. Neurite orientation dispersion and density imaging of the healthy cervical spinal cord in vivo. *NeuroImage* **111**, 590–601. https://doi.org/10.1016/j.neuroimage.2010.11.089 (2015).
49. By, S., Xu, J., Box, B. A., Bagnato, F. R. & Smith, S. A. Application and evaluation of NODDI in the cervical spinal cord of multiple sclerosis patients. *NeuroImage Clin.* **15**, 333–342. https://doi.org/10.1016/j.nicl.2017.05.010 (2017).
50. Schilling, K. G. *et al.* Diffusion MRI microstructural models in the cervical spinal cord - Application, normative values, and correlations with histological analysis. *NeuroImage* **201**, 116026. https://doi.org/10.1016/j.neuroimage.2010.11.089 (2019).
51. Farooq, H. *et al.* Microstructure imaging of crossing (MIX) white matter Fibers from diffusion MRI. *Sci. Rep.* **6**, 1–9. https://doi.org/10.1038/srep38927 (2016).
52. Assaf, Y. & Basser, P. J. Composite hindered and restricted model of diffusion (CHARMED) MR imaging of the human brain. *NeuroImage* **27**, 48–58. https://doi.org/10.1016/j.neuroimage.2010.11.089 (2005).
53. Duval, T., Smith, V., Stikov, N., Klawiter, E. C. & Cohen-Adad, J. Scan-rescan of axcaliber, macromolecular tissue volume, and g-ratio in the spinal cord. *Magn. Reson. Med.* **79**, 2759–2765. https://doi.org/10.1016/j.neuroimage.2010.11.089 (2018).
54. Alexander, D. C. *et al.* Orientationally invariant indices of axon diameter and density from diffusion MRI. *NeuroImage* **52**, 1374–1389. https://doi.org/10.1016/j.neuroimage.2010.11.089 (2010).
55. Jeurissen, B., Tournier, J. D., Dhollander, T., Connelly, A. & Sijbers, J. Multi-tissue constrained spherical deconvolution for improved analysis of multi-shell diffusion MRI data. *NeuroImage* **103**, 411–426. https://doi.org/10.1016/j.neuroimage.2010.11.089 (2014).
56. Grussu, F., Schneider, T., Zhang, H., Alexander, D. C. & Wheeler-Kingshott, C. A. M. Single-shell diffusion MRI NODDI with in vivo cervical cord data. *Proc. Intl. Soc. Magn. Reson. Med.* **22**, 1716 (2014).
57. Caruyer, E., Lenglet, C., Sapiro, G. & Deriche, R. Design of multishell sampling schemes with uniform coverage in diffusion MRI. *Magn. Reson. Med.* **69**, 1534–1540. https://doi.org/10.1002/mrm.24736 (2013).
58. Gros, C. *et al.* Automatic segmentation of the spinal cord and intramedullary multiple sclerosis lesions with convolutional neural networks. *NeuroImage* **184**, 901–915 (2018).
59. Dietrich, O., Raya, G., Reeder, S. B., Reiser, M. F. & Schoenberg, S. O. Measurement of signal-to-noise ratios in MR images: Influence of multichannel coils, parallel imaging, and reconstruction filters. *J. Magn. Reson. Imaging* **26**, 375–385. https://doi.org/10.1002/jmri.20969 (2007).
60. De Leener, B. *et al.* SCT: Spinal Cord Toolbox, an open-source software for processing spinal cord MRI data. *NeuroImage* **145**, 24–43. https://doi.org/10.3109/17482968.2011.649760 (2017).
61. Avants, B. B., Tustison, N. & Song, G. Advanced normalization tools (ANTs). *Insight J.***2**, 1–35. http://hdl.handle.net/10380/3113 (2009).
62. Jenkinson, M., Beckmann, C. F., Behrens, T. E. J., Woolrich, M. W. & Smith, S. M. Fsl. *NeuroImage* **62**, 782–790. https://doi.org/10.1016/j.neuroimage.2011.09.015 (2012).
63. Tustison, N. J., Cook, P. A. & Gee, J. C. N4ITK: Improved N3 bias correction. *IEEE Trans. Med. Imaging* **29**, 1310–1320. https://doi.org/10.1109/TMI.2010.2046908.N4ITK (2011).
64. Jan, J. *Medical Image Processing, Reconstruction and Restoration: Concepts and Methods* (Taylor, Boca Raton, 2006).
65. De Leener, B., Cohen-Adad, J. & Kadoury, S. Automatic segmentation of the spinal cord and spinal canal coupled with vertebral labeling. *IEEE Trans. Med. Imaging* **34**, 1705–1718. https://doi.org/10.1109/TMI.2015.2437192 (2015).
66. Avants, B. B., Epstein, C. L., Grossman, M. & Gee, J. C. Symmetric diffeomorphic image registration with cross-correlation: Evaluating automated labeling of elderly and neurodegenerative brain. *Med. Image Anal.* **12**, 26–41. https://doi.org/10.3109/17482968.2011.649760 (2008).
67. Perone, C. S., Calabrese, E. & Cohen-Adad, J. Spinal cord gray matter segmentation using deep dilated convolutions. *Sci. Rep.* **8**, 1–13. https://doi.org/10.1038/s41598-018-24304-3 (2018).
68. Andersson, J. L. R., Skare, S. & Ashburner, J. How to correct susceptibility distortions in spin-echo echo-planar images: Application to diffusion tensor imaging. *NeuroImage* **20**, 870–888. https://doi.org/10.3109/17482968.2011.649760 (2003).
69. Andersson, J. L. R. & Sotiropoulos, S. N. An integrated approach to correction for off-resonance effects and subject movement in diffusion MR imaging. *NeuroImage* **125**, 1063–1078. https://doi.org/10.3109/17482968.2011.649760 (2016).

Acknowledgements

The authors thank *Dr. Pavel Hok* from Department of Neurology, Palacký University and University Hospital Olomouc for help with an implementation of dMRI data preprocessing and solving of several co-registration issues, *Ing. Petr Kudlička* and *Ing. Veronika Fabíková* from CEITEC Brno for operating the research scanner, *Dr. Jan Kočica*, *prof. Zdeněk Kadaňka*, *Dr. Zdeněk Kadaňka jr.* and *Ing. Dagmar Kratochvílová* from Department of Neurology, University Hospital Brno for recruitment of healthy controls and patients, *Ing. Jakub Zimolka* and *Ing. Zuzana Piskořová* from Department of Biomedical Engineering, Brno University of Technology for help with implementation of pilot data processing algorithms on pilot experimental and testing dataset, *Dr. Miloš Keřkovský*, *Dr. Tomáš Rohan* and *Dr. Marek Dostál* from Department of Radiology, University Hospital Brno for compression level evaluations by all used participants and for well working discussion about used MRI protocol parameter settings. We acknowledge the core facility MAFIL of CEITEC supported by the Czech-BioImaging large RI project [LM2015062, LM2018129] for their support with obtaining scientific data presented in this paper. This research was supported and funded by the Czech Health Research Council [NV18-04-00159], and by the Ministry of Health of the Czech Republic project for conceptual development in research organizations [65269705-University Hospital, Brno, Czech Republic]. IN was supported by the Million Dollar Bike Ride grant from the Penn Medicine Orphan Disease Center at the University of Pennsylvania [MDBR-17-123-MPS]. CL was partly supported by National Institutes of Health [P41 EB015894, P41 EB027061, P30 NS076408]. JCA was funded by the Canada Research Chair in Quantitative Magnetic Resonance Imaging [950-230815], the Canadian Institute of Health Research [CIHR FDN-143263], the Fonds de Recherche du Québec-Santé [28826], the Fonds

de Recherche du Québec-Nature et Technologies [2015-PR-182754], the Natural Sciences and Engineering Research Council of Canada [RGPIN-2019-07244], the Canada First Research Excellence Fund (IVADO and TransMedTech) and the Quebec BioImaging Network [5886, 35450]. Computational and storage resources were supplied by the project "e-Infrastruktura CZ" (e-INFRA LM2018140) provided within the program Projects of Large Research, Development and Innovations Infrastructures and by the fMRI laboratory, Department of Neurology, Palacky University Olomouc, Czech Republic.

Author contributions

All co-authors read and revised the manuscript draft. R.L. designed the HARDI-ZOOMit protocols, acquired pilot data, implemented and supervised the implementation of the pilot and final algorithms, performed inter-group and inter-protocol inferences and visualizations, designed figures and wrote the manuscript draft. R.L. and I.N. designed skewness and kurtosis evaluations and heuristic parameters. J.V. implemented the final algorithms, analyzed data on single-subject level, performed visual inspection of segmentations and co-registrations, and co-wrote the manuscript draft. T.H. performed visual quality check of the obtained results, managed the data storage and organized the whole team joint collaboration. A.S. and P.B. designed the susceptibility artifact level and reproducibility evaluations. A.S., P.B. and J.B. motivated a clinical application of the protocol. L.V. designed T_2-sagittal and T_2^*-axial protocols of anatomical scans. M.H. processed, evaluated and visualized the reproducibility of acquired protocols. I.N. co-designed several clinically feasible parameters (as written above) and co-wrote the manuscript draft. C.L. helped R.L. to design the HARDI-ZOOMit protocol and supervised the work as a methodological expert. J.C.A. helped R.L. and J.V. with implementation of the SCT into the pipeline, solved several issues and errors which appeared during implementation, and designed the application of step-wise linear regression for identification of set of clinically feasible features from the set of all significant parameters. C.L. and J.C.A. contributed to discussions of novelty and originality of the current Results over the current state of the art. J.B. as the clinical principal investigator defined the clinical research question, the clinical study population, inclusion and exclusion criteria, designed the clinically relevant regions of interest, managed the project, and supervised the clinical interpretation of the obtained results. P.H. as the methodological principal investigator supervised the algorithm implementation and managed the pilot data acquisition for the HARDI-ZOOMit protocol optimization. T.H., A.S., P.B., I.N., J.B. and P.H. approved and co-wrote the clinical interpretation and clinical discussion of results.

Competing interests

The authors declare no competing interests.

Additional information

Supplementary information is available for this paper at https://doi.org/10.1038/s41598-020-70297-3.

Correspondence and requests for materials should be addressed to P.H.

Reprints and permissions information is available at www.nature.com/reprints.

Publisher's note Springer Nature remains neutral with regard to jurisdictional claims in published maps and institutional affiliations.

Open Access This article is licensed under a Creative Commons Attribution 4.0 International License, which permits use, sharing, adaptation, distribution and reproduction in any medium or format, as long as you give appropriate credit to the original author(s) and the source, provide a link to the Creative Commons license, and indicate if changes were made. The images or other third party material in this article are included in the article's Creative Commons license, unless indicated otherwise in a credit line to the material. If material is not included in the article's Creative Commons license and your intended use is not permitted by statutory regulation or exceeds the permitted use, you will need to obtain permission directly from the copyright holder. To view a copy of this license, visit http://creativecommons.org/licenses/by/4.0/.

© The Author(s) 2020

12.2 Annex 2 – Study II (Prospective dMRI study)

Received: 15 June 2021 | Accepted: 16 July 2021

DOI: 10.1111/ene.15027

european journal of neurology
the official journal of the european academy of neurology

ORIGINAL ARTICLE

Diffusion magnetic resonance imaging reveals tract-specific microstructural correlates of electrophysiological impairments in non-myelopathic and myelopathic spinal cord compression

Jan Valošek[1,2] | René Labounek[1,3] | Tomáš Horák[4,5,6] | Magda Horáková[5,6] | Petr Bednařík[4,7] | Miloš Keřkovský[6,8] | Jan Kočica[5,6] | Tomáš Rohan[6,8] | Christophe Lenglet[9] | Julien Cohen-Adad[10,11,12] | Petr Hluštík[1] | Eva Vlčková[5,6] | Zdeněk Kadaňka Jr.[5,6] | Josef Bednařík[4,5,6] | Alena Svatkova[4,13]

[1]Department of Neurology, Faculty of Medicine and Dentistry, Palacký University, Olomouc, Czechia
[2]Department of Biomedical Engineering, University Hospital, Olomouc, Czechia
[3]Division of Clinical Behavioral Neuroscience, Department of Pediatrics, University of Minnesota, Minneapolis, Minnesota, USA
[4]Central European Institute of Technology, Masaryk University, Brno, Czechia
[5]Department of Neurology, University Hospital Brno, Brno, Czechia
[6]Faculty of Medicine, Masaryk University, Brno, Czechia
[7]High Field MR Centre, Department of Biomedical Imaging and Image-guided Therapy, Medical University of Vienna, Vienna, Austria
[8]Department of Radiology and Nuclear Medicine, University Hospital Brno, Brno, Czechia
[9]Center for Magnetic Resonance Research, Department of Radiology, University of Minnesota, Minneapolis, Minnesota, USA
[10]NeuroPoly Lab, Institute of Biomedical Engineering, Polytechnique Montreal, Montreal, Quebec, Canada
[11]Functional Neuroimaging Unit, CRIUGM, University of Montreal, Montreal, Quebec, Canada
[12]Mila - Quebec AI Institute, Montreal, Quebec, Canada
[13]Department of Medicine III, Clinical Division of Endocrinology and Metabolism, Medical University of Vienna, Vienna, Austria

Correspondence
Alena Svatkova, Department of Medicine III, Clinical Division of Endocrinology and Metabolism, Medical University of Vienna, Vienna, Austria.
Email: alena.svatkova@meduniwien.ac.at

Funding information
The core facility Multimodal and Functional Imaging Laboratory, Masaryk University, CEITEC, supported by the MEYS CR (LM2018129 Czech-BioImaging) is acknowledged. This research is funded by the Czech Health Research Council grants NV18-04-00159 and by the Ministry of Health of the Czech Republic project for conceptual development in research organizations, ref. 65269705 (University Hospital, Brno, Czech Republic). JV has received "Aktion Österreich-Tschechien, AÖCZ-Semesterstipendien" scholarship MPC-

Abstract

Background and purpose: Non-myelopathic degenerative cervical spinal cord compression (NMDC) frequently occurs throughout aging and may progress to potentially irreversible degenerative cervical myelopathy (DCM). Whereas standard clinical magnetic resonance imaging (MRI) and electrophysiological measures assess compression severity and neurological dysfunction, respectively, underlying microstructural deficits still have to be established in NMDC and DCM patients. The study aims to establish tract-specific diffusion MRI markers of electrophysiological deficits to predict the progression of asymptomatic NMDC to symptomatic DCM.

Methods: High-resolution 3 T diffusion MRI was acquired for 103 NMDC and 21 DCM patients compared to 60 healthy controls to reveal diffusion alterations and relationships between tract-specific diffusion metrics and corresponding electrophysiological measures and compression severity. Relationship between the degree of DCM disability, assessed by the modified Japanese Orthopaedic Association scale, and tract-specific microstructural changes in DCM patients was also explored.

This is an open access article under the terms of the Creative Commons Attribution-NonCommercial License, which permits use, distribution and reproduction in any medium, provided the original work is properly cited and is not used for commercial purposes.
© 2021 The Authors. *European Journal of Neurology* published by John Wiley & Sons Ltd on behalf of European Academy of Neurology

2020-00013 from Austrian Agency for International Cooperation in Education and Research (OeAD-GmbH), Mobility Programmes, Bilateral and Multilateral Cooperation (MPC) financed by Federal Ministry of Education, Science and Research (BMBWF) of Austria. AS has received funding from the European Union's Horizon 2020 research and innovation programme under the Marie Skłodowska-Curie grant agreement no. 794986. PB was partially supported by a NARSAD Young Investigator Grant from the Brain and Behavior Research Foundation (grant no. 27238) and by the European Union's Horizon 2020 research and innovation programme under the Marie Skłodowska-Curie grant agreement no. 846793. CL is partly supported by NIH grants P41 EB027061 and P30 NS076408. Computational resources were supplied by the project "e-Infrastruktura CZ" (e-INFRA LM2018140) provided within the program Projects of Large Research, Development and Innovations Infrastructures. JCA is funded by the Canada Research Chair in Quantitative Magnetic Resonance Imaging (950-230815), the Canadian Institute of Health Research (CIHR FDN-143263), the Canada Foundation for Innovation (32454, 34824), the Fonds de Recherche du Québec—Santé (28826), the Natural Sciences and Engineering Research Council of Canada (RGPIN-2019-07244), the Canada First Research Excellence Fund (IVADO and TransMedTech), the Courtois NeuroMod project and the Quebec BioImaging Network (5886, 35450).

Results: The study identified diffusion-derived abnormalities in the gray matter, dorsal and lateral tracts congruent with trans-synaptic degeneration and demyelination in chronic degenerative spinal cord compression with more profound alterations in DCM than NMDC. Diffusion metrics were affected in the C3-6 area as well as above the compression level at C3 with more profound rostral deficits in DCM than NMDC. Alterations in lateral motor and dorsal sensory tracts correlated with motor and sensory evoked potentials, respectively, whereas electromyography outcomes corresponded with gray matter microstructure. DCM disability corresponded with microstructure alteration in lateral columns.

Conclusions: Outcomes imply the necessity of high-resolution tract-specific diffusion MRI for monitoring degenerative spinal pathology in longitudinal studies.

KEYWORDS

diffusion magnetic resonance imaging, diffusion tensor imaging, spinal cord compression

INTRODUCTION

The relative resilience of the cervical spinal cord (CSC) to degenerative changes might delay the development of clinically manifest myelopathy and result in non-myelopathic degenerative cervical spinal cord compression (NMDC) [1,2]. The prevalence of NMDC progressively increases throughout aging affecting up to 40% of Caucasian individuals over 60 years of age [3-5]. Over time, a portion of NMDC patients progress into potentially irreversible degenerative cervical myelopathy (DCM) [2,6], which is the most common non-traumatic cause of CSC dysfunction. Delineation of risk factors of NMDC progression to the DCM remains an unsolved challenge [2,6,7]. Whilst radiological measures such as cross-sectional area (CSA), anteroposterior diameter or compression ratio (CR) together with electrophysiological abnormalities might be useful in predicting DCM development [6], standard clinical magnetic resonance imaging (MRI) protocols fail to describe microstructural CSC abnormalities in NMDC and DCM. Hyperintensity on T_2-weighted scans, considered as a radiological correlate of myelopathy, is not inevitably observed even in the most severe DCM patients with clinical myelopathic signs [8]. Yet, it remains a critical factor influencing decision-making in decompressive surgery [9]. Thus, quantitative MRI markers are urgently needed to detect early microstructural NMDC changes and predict progression into symptomatic DCM.

Whereas previous studies demonstrated the ability of diffusion MRI (dMRI) to depict profound microstructural CSC alteration in DCM patients [10-15], NMDC reports provided inconclusive outcomes [6,16-18]. However, all previous studies utilized single-shell dMRI protocols that limited estimation of the high-order diffusion models and exclusively quantified the diffusion tensor imaging (DTI) model [19]. Whereas DTI metrics are sensitive to microstructural integrity (i.e., fractional anisotropy [FA]) and axonal, myelin or membrane density deficits (i.e., axial [AD], radial [RD] and mean diffusivity [MD], respectively), the single tensor per voxel does not account for axonal, glial and extracellular compartments within the tissue and remains nonspecific [20]. To address this issue, optimized multi-shell high angular resolution diffusion imaging (HARDI) sequence with reduced field of view, so-called HARDI-ZOOMit [21], were utilized to estimate critical microstructural information from single-compartment DTI and the more advanced multi-compartment ball-and-sticks model [22]. The ball-and-sticks model indeed better fits dMRI data than DTI [20] and more reliably captures the microstructural tissue property in each voxel.

High-resolution multi-shell diffusion and anatomical sequences were combined with state-of-the-art postprocessing [23-26] to achieve selective tract-specific CSC analyses. Capability of the microstructural dMRI metrics to reliably reflect histopathological studies, which previously demonstrated tract-specific distinctions in CSC integrity in degenerative compression [1,27] was also investigated.

Thus, tract-specific alterations in degenerative spinal cord compression at the compression level and also above the compression were hypothesized with more severe deficits in DCM patients than NMDC patients. Relationships between tract-specific dMRI metrics and corresponding electrophysiology and compression severity, previously confirmed as risk factors of DCM development [6] were further hypothesized. Relationship between the degree of DCM disability assessed by the modified Japanese Orthopaedic Association (mJOA) scale [28] and tract-specific diffusion-informed microstructure was also explored.

MATERIALS AND METHODS

Participants

The ethical committee approved the study, and all participants signed an informed consent form. Healthy controls (HC) between 40 and 80 years of age had to be physically healthy with no history of any neurological or other somatic disorder. DCM and NMDC patients were recruited from the database of a spinal center of a tertiary university hospital. The requirements on subjects are shown in Figure 1a.

All subjects underwent a neurological examination to rule out DCM symptoms/signs in HC and NMDC individuals. The degree of DCM disability was assessed by an mJOA scale [28]. All participants underwent standard clinical MRI on a 1.5 T scanner to evaluate radiological signs of degenerative compression and estimate the maximal compression level (MCL), CSA and CR (see Supplementary Materials and Methods).

Non-myelopathic degenerative cervical spinal cord compression patients and DCM patients underwent electrophysiological examination performed by experienced neurologists to detect abnormalities of dorsal columns and/or dorsal gray matter (GM) horns (i.e., somatosensory evoked potentials, SEP), dysfunction in lateral columns (i.e., motor evoked potentials, MEP) and lesions of ventral GM horns (i.e., electromyography, EMG) as described previously [2,29]. Three DCM and 13 NMDC patients did not agree with electrophysiological examination. A detailed description of electrophysiological measures as well as the definition of MEP, SEP and EMG abnormalities is provided in the Supplementary Materials and Methods.

Magnetic resonance imaging acquisition

All participants were scanned on a 3 T Siemens Prisma scanner (Siemens Healthcare, Erlangen, Germany) using 64-channel head/neck and 32-channel spine coils. Lordosis, which could introduce a partial volume effect from the surrounding cerebrospinal fluid and negatively influence field homogeneity, was minimized by keeping the spinal cord as straight as possible. An optimized multi-shell diffusion protocol with reduced field of view [21] with total acquisition time (TA) of 12 min, 46 s covering C3-6 levels with 21 gradient waveform directions with b_1 = 550 s/mm^2, 42 directions with b_2 = 1000 s/mm^2 and seven b_0 images with anterior–posterior phase encoding, voxel size 0.65 × 0.65 × 3 mm^3 after interpolation in

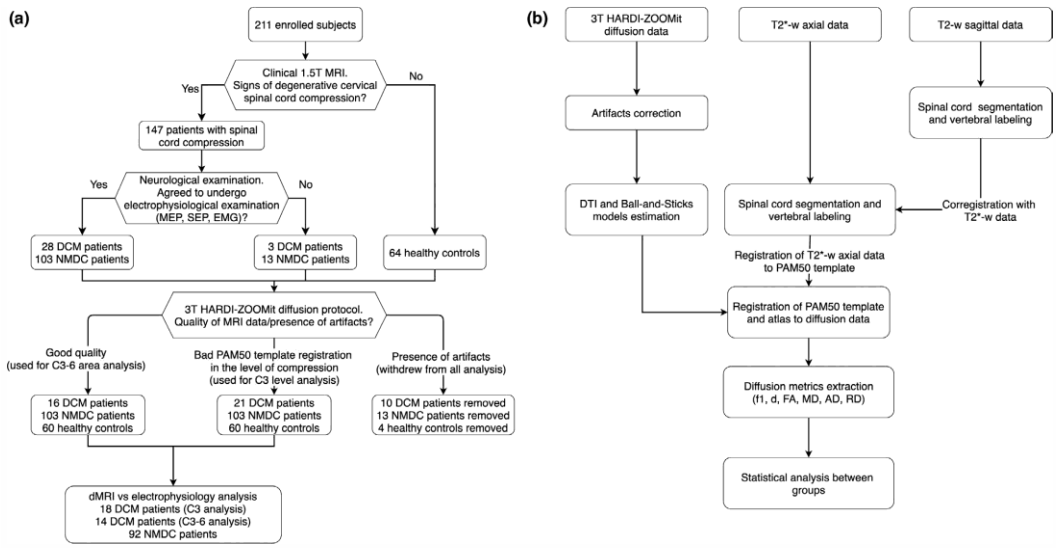

FIGURE 1 Flowcharts of (a) participants' requirements and (b) MRI data analysis

Fourier space, original voxel size 1.30 × 1.30 × 3.00 mm^3 was acquired. An additional five b_0 images with reversed posterior–anterior phase encoding were collected. All gradient waveforms were uniformly sampled over a *q*-space sphere [30]. Axial T_2*-weighted MEDIC images with high grey/white matter contrast using interleaved acquisition (voxel size 0.35 × 0.35 × 2.5 mm^3 after interpolation in Fourier space, original voxel size 0.70 × 0.70 × 2.5 mm^3, TA ≈ 8 min) and T_2-weighted sagittal turbo spin-echo images (voxel size 0.28 × 0.28 × 1.3 mm^3 after interpolation in Fourier space, original voxel size 0.56 × 0.56 × 1.3 mm^3, TA ≈ 9 min) were also collected. Detailed sequence parameters are listed in the Supplementary Materials and Methods.

Image analysis

Images were visually inspected by two independent observers to ensure data quality. Data were analyzed using the Spinal Cord Toolbox [26] v3.2.3 and FMRIB Software Library [31] v5.0.10 (Figure 1b). T_2*-w and T_2-w data were corrected for MR field induced intensity non-uniformities using the N4 bias-field correction tool, and interleaved T_2*-w axial data were additionally slice-by-slice corrected utilizing affine registration between even and odd slices followed by additive image fusion. Spinal cord segmentation and vertebral labeling of T_2-w sagittal data was performed and co-registered with T_2*-w axial data. Then spinal cord segmentation using convolution neural network [23] of T_2*-w axial was performed and vertebral levels were defined [32] using initial information from T_2-w sagittal labeling. Finally, the T_2*-w spinal cord was registered to the PAM50 template [24] using C3 and C6 as labels. Diffusion data were corrected for motion, susceptibility and eddy current artifacts. A conventional DTI [19] model and a multi-compartment ball-and-sticks [22] model were estimated to extract FA, MD, AD and RD as well as f_1 and *d* metrics. The PAM50 template was registered to diffusion data using the initial transformation from the T_2*-w axial image, and the probabilistic spinal cord atlas [25] was warped into diffusion data.

Metric extractions

Diffusion metrics were extracted per subject from all regions of interest (ROIs) utilizing the *sct_extract_metric* function [26] with use of the *maximum a posteriori* optimizing approach [25,26] to eliminate partial volume effect and variability in tract size. ROIs included the GM, ventral, lateral, dorsal columns, fasciculus gracilis, fasciculus cuneatus, lateral corticospinal tracts, spinal lemniscus (i.e., spinothalamic and spinoreticular tracts), dorsal GM horns and ventral GM horns (Figure 2a). Diffusion metrics for individual ROIs were averaged from the whole C3-6 area and from C3 above the compression vertebral level (Figure 2d).

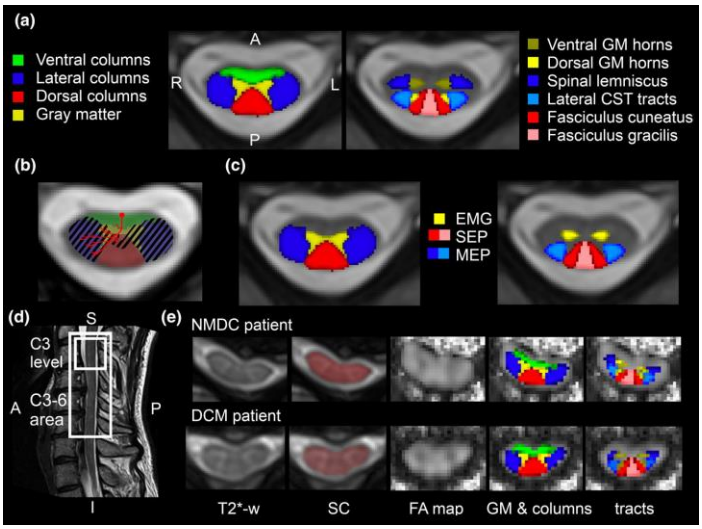

FIGURE 2 (a) Individual ROIs masks from probabilistic PAM50 atlas. (b) Lesion distribution caused by compressed anterior spinal artery. Filled areas are affected by the compression, that is, lateral columns, anterior part of dorsal columns and ventral GM horns. Adapted from Mair and Druckman [27]. (c) Individual ROIs related to electrophysiological measures: EMG, electromyography; SEP, somatosensory evoked potentials; MEP, motor evoked potentials. (d) Two analyzed areas, the C3-6 area and C3 above the compression level. (e) Representative slices from the C4/5 disc from NMDC and DCM patients. From the left: T2*-w axial image, CSC segmentation used for PAM50 registration, fractional anisotropy (FA) map, white matter columns, and gray matter (GM) and individual tracts registered into an FA map

Mean CSA at the C3 level was calculated to quantify atrophy above the compression level from high-resolution T_2*-w data using the *sct_process_segmentation* function [26].

Statistical analysis

Statistical analysis was performed using Matlab R2019b (The Mathworks Inc.), Python 3.7 and SPSS 25 (IBM). Data normality was examined using the Shapiro–Wilk test. Comparison between groups in age, height, weight, body mass index (BMI) and CSA at C3 were tested by the Kruskal–Wallis *H* test, and sex by Fisher's exact test.

Between-group differences in dMRI metrics from the C3-6 area and above the compression (i.e., C3) level were analyzed per individual tract and column using ANCOVA with age and BMI as covariates using Tukey–Kramer post hoc tests. Analyses were corrected using the Holm–Bonferroni correction.

Associations between dMRI metrics from the C3-6 area, age and BMI in 60 controls as well as between CSA and CR at MCL and dMRI metrics from the C3-6 area and C3 above the compression level in DCM and NMDC together with the relationship between the degree of myelopathy (mJOA scale) and dMRI metrics at C3 in DCM were examined using the Spearman correlation. Relationships between electrophysiological abnormalities, reported as categorical and dMRI metrics, were quantified in NMDC and DCM patients by the Mann–Whitney rank tests with Holm–Bonferroni correction. MEPs were related to dMRI from motor tracts, that is, lateral columns and lateral corticospinal tracts. SEPs were correlated with sensory tracts, that is, the dorsal column, fasciculus cuneatus, fasciculus gracilis and dorsal GM horns. Relationships between EMG and dMRI from GM and ventral GM horns (Figure 2c) were examined. Finally, post hoc correlation analysis between quantitative electrophysiological parameters and dMRI metrics was performed (see the Supplementary Materials and Methods).

RESULTS

Participant characteristics

A total of 116 NMDC patients, 31 DCM patients and 64 HC were enrolled in the study. Ten DCM, 13 NMDC patients and four HC were initially excluded due to the presence of motion artifacts, low CSC/cerebrospinal fluid contrast in T2*-w axial images preventing proper CSC segmentation, sub-optimal fat saturation, and dMRI signal dropouts caused by excessive cardiac pulsatile motion.

The final group consisted of 103 NMDC patients, 21 DCM patients and 60 HC. Analyses did not reveal any statistically significant differences in age, height, weight, BMI or sex between groups (Table 1).

None of the 60 HC had MR signs of degenerative CSC compression, whilst all 103 NMDC and 21 DCM patients had MR signs of compression varying from focal impingement to flat compressions with partially preserved or lost subarachnoid space [2,6]. The majority of patients (93.6%) had MCL at the C4/5 level and/or lower. Thus, level C3 was selected as a reference level above the compression to evaluate rostral microstructural changes.

Non-myelopathic degenerative cervical spinal cord compression patients had no radiological signs or neurological symptoms/signs of DCM. Hyperintensities on T_2-w scans were found in one cervical level in 12 DCM patients and two cervical levels in two DCM patients. The mean mJOA scale in the DCM group was 14.5.

Five out of 21 DCM patients were excluded from C3-6 analysis due to imperfect PAM50 atlas registration caused by severe compression, and these subjects were used only in the analysis of the C3 level. The accuracy of CSC segmentation and labeling was verified and corrected if necessary.

Detailed results for the relationship between dMRI metrics and compression measures are described in the Supplementary Results.

Cross-sectional area at the C3 above the compression level

The Kruskal–Wallis *H* test detected a significant between-group difference between groups in CSA above the compression level. Subsequent Dunn's post hoc tests showed significant ($p_{FWEcorr} < 0.05$) CSA reduction between HCs and NMDC patients (−5.0%, $p = 0.007$), HCs and DCM patients (−18.4%, $p < 0.0001$) and NMDC and DCM (−14.1%, $p < 0.0001$) (Table 1, Figure S1).

Correlations between dMRI metrics and demographic characteristics

Analyses revealed significant decreases ($p_{uncorr} < 0.05$) in f_1, FA, *d* and AD in the whole C3-6 area with age, whilst the opposite relationship was found between RD and age in HC (Figure S2). FA, MD, AD and *d* showed significant negative correlations with BMI (Figure S3). Correlation outcomes proved age and BMI as confounding variables, which were thus included as covariates to test between-group differences.

Distinctions between healthy controls and NMDC patients

Analysis of the C3-6 area revealed significantly ($p_{FWEcorr} < 0.05$) lower f_1 and FA in NMDC patients in dorsal and lateral tracts, that is, the fasciculus gracilis, lateral corticospinal tracts, spinal lemniscus and fasciculus cuneatus, compared to HC. Higher *d*, MD, AD and RD in NMDC patients relative to HC were observed in dorsal and lateral tracts and GM horns. Alterations in ventral columns were only revealed by the ball-and-sticks model, and NMDC patients showed higher *d* compared to HC.

TABLE 1 Characteristics of 184 participants

Characteristic	Healthy controls (n = 60)	NMDC patients (n = 103)	DCM patients (n = 21)	p value
Age (years)	53.7 ± 8.7	56.5 ± 9.8	58.2 ± 10.8	0.084
Sex (females/males)	38/22	59/44	12/9	0.711
Height (cm)	172.4 ± 9.8	170.0 ± 8.7	167.0 ± 10.5	0.227
Weight (kg)	78.9 ± 16.5	81.2 ± 16.7	81.7 ± 13.3	0.880
Body mass index (BMI)	26.5 ± 4.8	28.0 ± 4.6	28.8 ± 4.1	0.073
Cross-sectional area (CSA) at C3 level (mm^2)	69.7 ± 7.6	66.0 ± 7.4	56.7 ± 7.1	<0.001*
mJOA	18.0 ± 0.0	18 ± 0.0	14.5 ± 2.6	
Maximally compressed level (MCL)				
C3/4	–	5 (4.8%)	3 (14.3%)	
C4/5	–	28 (27.2%)	4 (19.0%)	
C5/6	–	49 (47.6%)	14 (66.7%)	
C6/7	–	21 (20.4%)	-	
Compression ratio (CR) at MCL	–	0.41 ± 0.07	0.35 ± 0.08	
Cross-sectional area (CSA) at MCL	–	60.71 ± 11.3	52.14 ± 13.84	
Number of stenotic levels				
1 compression	–	39 (37.9%)	6 (28.6%)	
2 compressions	–	33 (32.0%)	8 (38.1%)	
3 compressions	–	25 (24.3%)	4 (19.0%)	
4 compressions	–	6 (5.8%)	3 (14.3%)	
Electrophysiological measurements				
Abnormal MEP	–	11 patients from 87 (12.6%)	12 patients from 18 (66.7%)	
Abnormal SEP	–	28 patients from 87 (32.2%)	13 patients from 18 (72.2%)	
Abnormal EMG	–	24 patients from 92 (26.1%)	11 patients from 17 (64.7%)	

Note: Asterisk (*) indicates significance ($p < 0.05$).

Abbreviations: DCM, degenerative cervical myelopathy; EMG, electromyography; MEP, motor evoked potentials; mJOA, modified Japanese Orthopaedic Association; NMDC, non-myelopathic degenerative cervical spinal cord compression; SEP, somatosensory evoked potentials.

Lower f_1 values at C3 above the compression level were found in lateral columns, specifically in spinal lemniscus, in NMDC patients in comparison to HCs (Figures 3 and 4, Table S1).

Differences between healthy controls and DCM patients

Degenerative cervical myelopathy patients showed significantly lower f_1 and FA ($p_{FWEcorr} < 0.05$) in dorsal and lateral tracts, that is, fasciculus cuneatus, fasciculus, lateral corticospinal tracts and spinal lemniscus, in the C3-6 area compared to HC. The ball-and-sticks model demonstrated lower f_1 values in DCM patients relative to HC in ventral columns and ventral and dorsal GM horns. Higher MD and RD values in DCM patients in comparison to HC were detected in dorsal and lateral tracts, whilst higher RD in DCM patients was also observed in ventral columns. In contrast, higher d and AD in DCM patients were solely revealed in dorsal tracts. Ventral and dorsal GM horns exhibited higher d, MD, AD and RD in DCM patients compared to HC.

Lower f_1 in DCM patients relative to HC above the compression level was detected in dorsal and lateral tracts, that is, the fasciculus cuneatus, fasciculus, lateral corticospinal tracts, spinal lemniscus and dorsal GM horns, whilst lower FA affected identical areas but spared the dorsal GM. Higher MD and RD were found in dorsal and lateral columns and GM, higher d and AD were observed only in ventral GM horns and the GM of DCM patients compared to HCs. No changes were detected in dMRI metrics at the C3 level in ventral columns (Figures 3 and 4 and Table S1).

Comparisons between NMDC and DCM patients

Degenerative cervical myelopathy patients exhibited significantly lower f_1 and FA compared to NMDC patients in dorsal and lateral tracts, that is, the fasciculus cuneatus, fasciculus, lateral corticospinal

tracts and spinal lemniscus, with lower f_1 values also in the dorsal GM horns of DCM patients at the C3-6 level. Higher MD and RD were detected in the dorsal and lateral tracts as well as ventral and dorsal GM horns with higher *d* and AD in GM horns in DCM patients relative to NMDC patients.

Above the compression level, lower f_1 and FA and higher MD and RD were detected in the fasciculus cuneatus, fasciculus, lateral corticospinal tracts and spinal lemniscus, and the dorsal GM horns in DCM relative to NMDC. Higher *d* and AD were observed in GM, specifically in ventral GM horns in DCM compared to NMDC (Figures 3 and 4 and Table S1).

Relationship between dMRI and electrophysiological measures

Patients with abnormal MEP findings exhibited significantly lower f_1 and FA in lateral columns and lateral corticospinal tracts ($p_{FWEcorr} < 0.05$) and lower AD in lateral columns compared to patients with normal MEP findings in the C3-6 area. Similarly, patients with altered SEPs demonstrated significantly lower FA in the dorsal columns, fasciculus gracilis, fasciculus cuneatus and dorsal GM horns compared to unaffected patients. Abnormal EMG was also reflected by higher RD in GM and ventral GM horns comparing patients with abnormal and normal EMG (Figure 5 and Table S2).

A comparison of dMRI metrics at the C3 above the compression level revealed significantly lower f_1 and FA and higher RD in the lateral columns and lateral corticospinal tracts ($p_{FWEcorr} < 0.05$) in patients with abnormal versus normal MEP. Also, lower *d* and AD were detected in the lateral columns in patients with abnormal MEP. Altered SEP measurements were associated with lower f_1 and FA in dorsal columns, fasciculus gracilis and fasciculus cuneatus, as well as lower FA and *d* in dorsal GM horns compared to patients with normal SEP. Lower f_1, FA and RD were detected in the GM in patients with abnormal EMG compared to individuals with unaffected EMG (Figure 5 and Table S2).

Overall, patients with abnormal electrophysiological measurements showed significantly lower f_1, FA, *d* and AD values, and higher RD values, in corresponding anatomical areas in comparison to patients with normal electrophysiological findings at the compression level but also above at C3 (Figure 5 and Table S2).

Results of post hoc correlation analysis between quantitative electrophysiological parameters and dMRI metrics are shown in the Supplementary Results.

Relationship between dMRI and clinical mJOA scale at the C3 level in DCM

Exploratory correlation analysis revealed significant positive correlations between mJOA and f_1, FA, *d* and AD from the C3 level in lateral columns in DCM patients. FA, AD and *d* in the spinal lemniscus and FA in ventral columns showed significant positive correlations with the mJOA scale. A negative relationship was identified between the mJOA scale and RD in lateral columns (Figures 6 and S6).

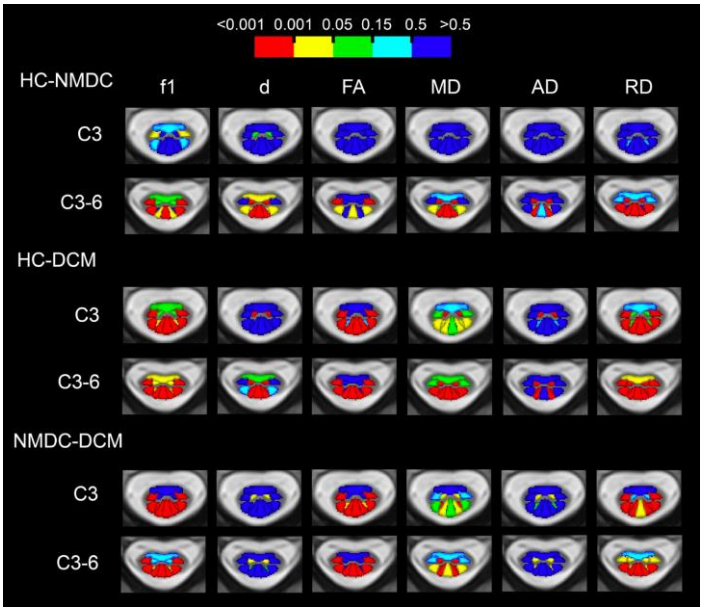

FIGURE 3 Between-group differences in diffusion metrics for tract-specific ROIs from C3 above the compression level and C3-6 area color coded by their *p* values ($p_{FWEcor} < 0.05$)

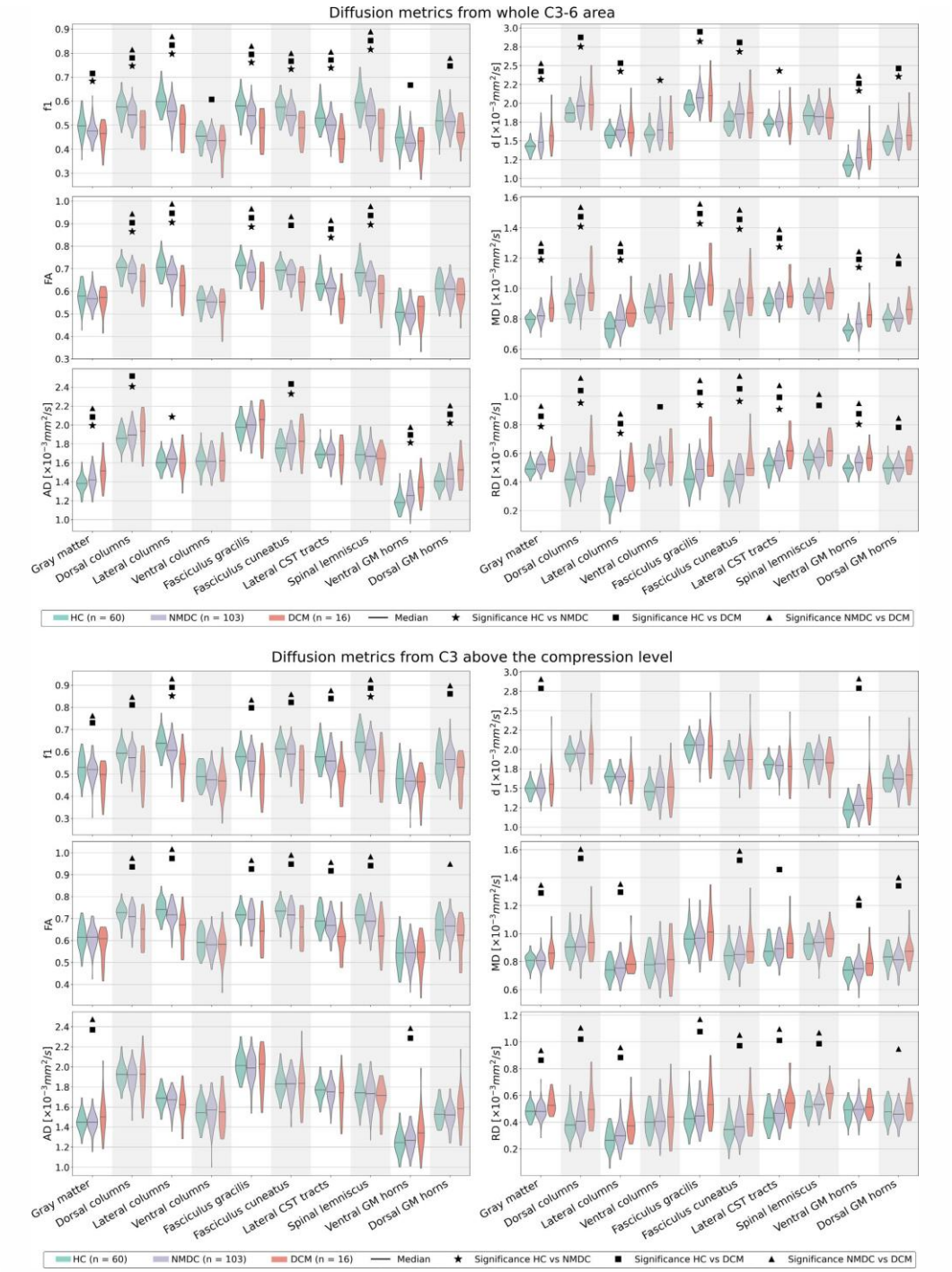

FIGURE 4 Violin plots showing between-group differences from the C3-6 area and C3 above the compression level. Markers indicate $p_{FWEcorr} < 0.05$

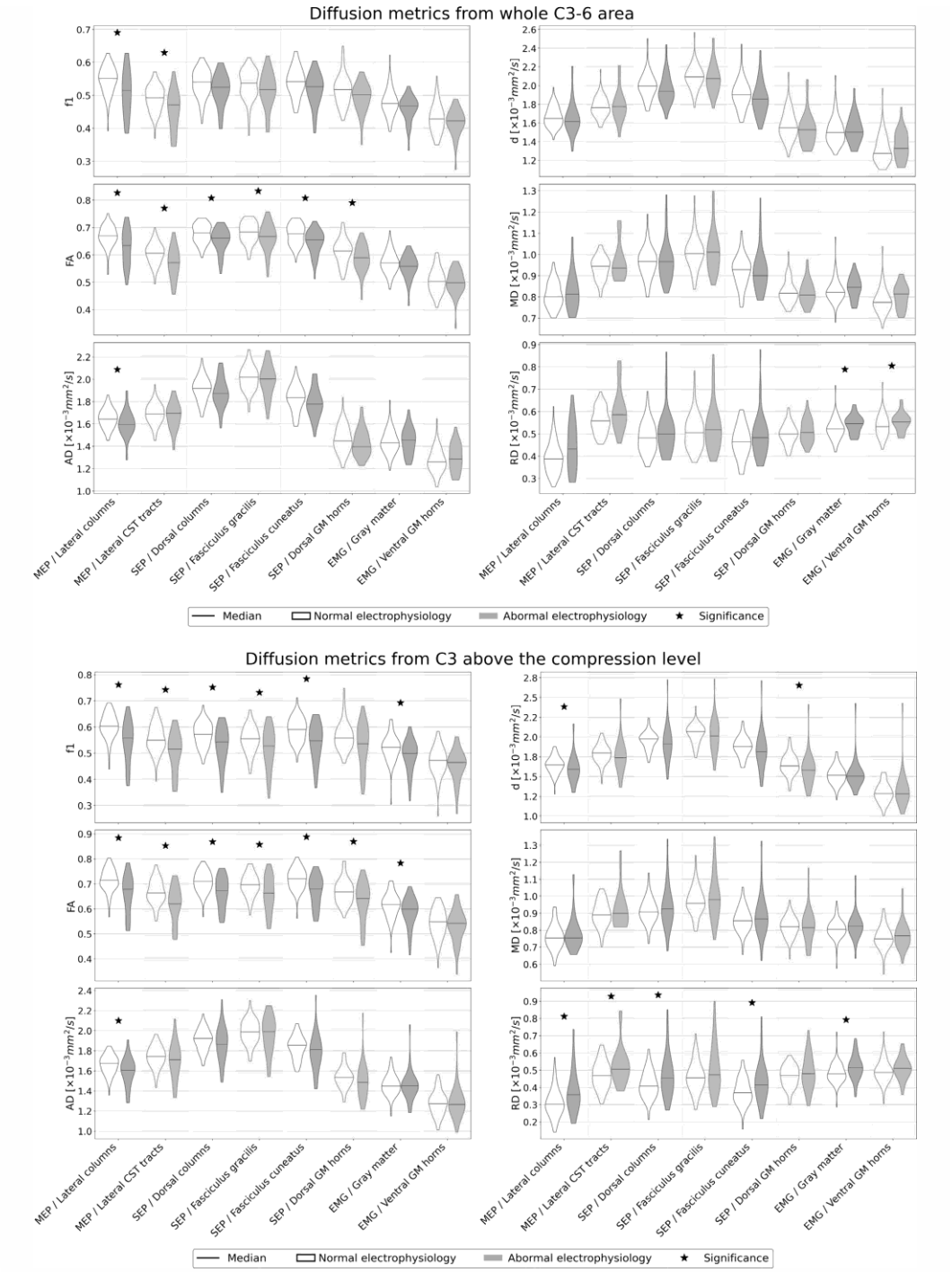

FIGURE 5 Violin plots showing relationship between electrophysiological finding and diffusion metrics extracted from the C3-6 area and C3 above the compression level. Asterisks (*) indicate $p_{FWEcorr} < 0.05$

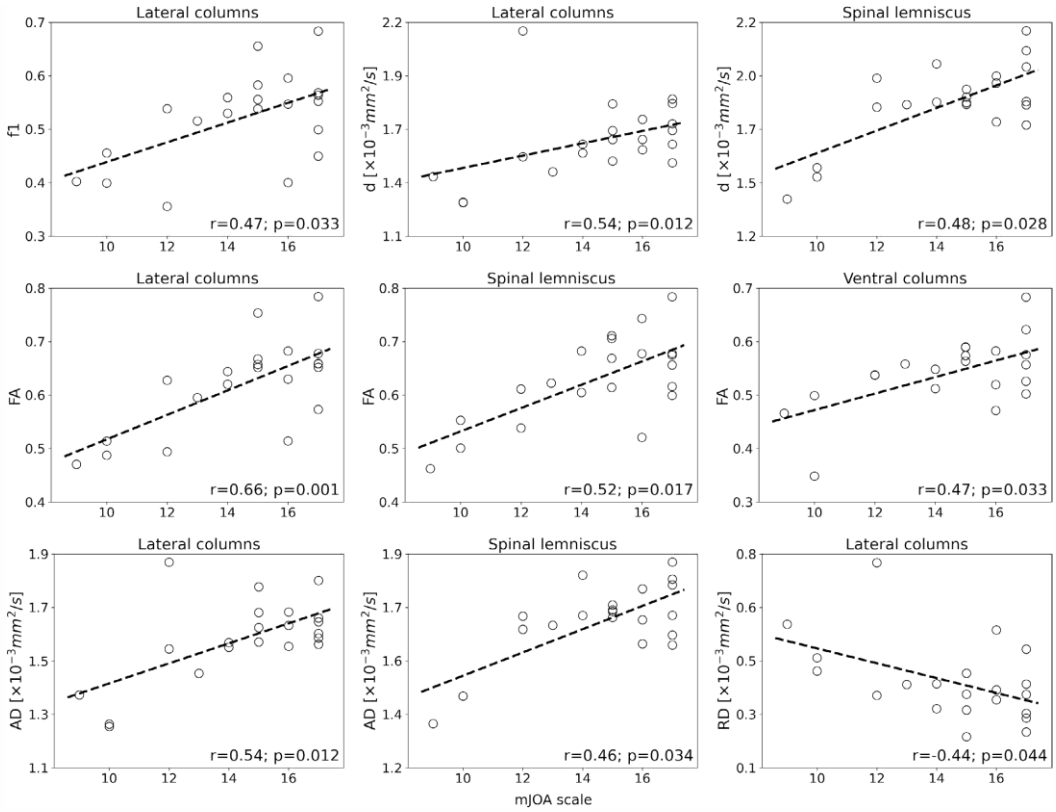

FIGURE 6 Correlations between dMRI metrics from C3 above the compression level and the modified Japanese Orthopaedic Association (mJOA) scale in DCM patients

DISCUSSION

Our study detected tract-specific distinctions in diffusion metrics between NMDC and symptomatic DCM patients compared to HC in the GM and dorsal columns, that is, fasciculus gracilis, fasciculus cuneatus, and in the lateral columns composed of lateral corticospinal tracts and spinal lemniscus. DCM patients also showed additional alterations in the ventral columns compared to HC. Diffusion changes were found in the C3-6 area as well as above the compression level at C3, and were accompanied by reduced cord cross-sectional area at the C3 level in both NMDC and DCM relative to HC. Importantly, diffusion metrics in the GM and motor and sensory tracts correlated with relevant electrophysiological abnormalities and clinical mJOA scale, implying the critical importance of tract-specific measures for future longitudinal studies.

Differences in dMRI metrics in the C3-6 area in NMDC patients compared to HC confirmed incipient CSC damage in the early stages of degenerative compression in the dorsal and lateral tracts. The findings align with post-mortem histopathological studies, in which chronic CSC compression led to damage of the lateral pial plexus resulting in limited blood flow and axonal degeneration of lateral corticospinal tracts and dorsal areas [1]. Malperfusion through the compressed anterior spinal artery initially affects GM, lateral columns and the anterior part of the dorsal columns and can ultimately result in progressive demyelination [1,27]. Indeed, lower f_1 and FA and higher diffusivity metrics in the lateral and dorsal tracts and GM observed in our study in NMDC and DCM patients compared to HC suggest ongoing demyelination [13]. Differences in f_1 in the lateral and dorsal tracts separated DCM from NMDC with more profound deficits found in DCM than NMDC patients. Thus, dMRI alterations corroborate post-mortem studies, which reported lesions of the anterior GM horns, the lateral tracts and the anterior part of the dorsal tracts but showed no changes in the ventral columns in the early stages of degenerative compression [13,33]. Additional f_1 and RD deficits occur in ventral columns as the compression progresses from NMDC to symptomatic DCM. Our findings thus align with histopathological samples when revealing alterations in diffusion metrics in ventral columns in DCM but not in NMDC. Direct comparison between NMDC and DCM groups showed profound changes in dorsal and lateral columns as well as GM that further confirmed the influence of gradual alteration

of arterial flow on the compression-related deficits and myelopathy [34,35]. Whilst lower FA corroborates previous DTI studies in DCM patients [10,14,36-38], asymptomatic patients with CSC compression [16] and patients with slowly progressing CSC compression [39], to date no study showed tract-specific changes in a large sample of both NMDC and DCM patients. Spatial distinctions in alterations between DCM and NMDC further emphasize the necessity of tract-specific analysis in CSC studies.

Our findings also demonstrate malicious effects of the compression on microstructural CSC integrity above the compression level at the C3 level. Deficits at C3 in NMDC were limited to the spinal lemniscus and were depicted solely using the ball-and-sticks f_1 metric pointing to incipient remote degeneration in NMDC patients in the early stages of degenerative CSC compression. As the compression progressed to DCM, additional f_1, FA and RD alterations in dorsal and lateral columns occurred. The ball-and-sticks f_1 demonstrated higher discrimination when showing changes in the spinal lemniscus that were not detected using the DTI model. Significantly lower f_1 and FA above the compression level in DCM patients compared to HC point to progressive anterograde and retrograde axonal degeneration of dorsal sensory pathways such as fasciculus gracilis, cuneatus and spinal lemniscus as well as lateral motor corticospinal tracts, respectively [1,13,14]. Alterations of FA at the C3 level are in agreement with a recent study from Seif et al. [14] which demonstrated a remote FA decrease in the lateral corticospinal and spinothalamic tracts at the C2/3 level in DCM patients and patients with traumatic spinal cord injury compared to HC. Changes in GM along with spinal cord CSA reduction above the compression level in DCM patients compared to NMDC patients and HC point to trans-synaptic degeneration and GM atrophy above the stenosis level in patients with myelopathy [13]. Direct comparison between symptomatic DCM and NMDC patients demonstrated more severe deficits in DCM patients in the dorsal and lateral columns, as well as in the ventral and dorsal GM horns. Whereas remote degeneration in DCM patients compared to HC corroborates previous reports [13,14,38,40,41], tract-based approaches also delineated gradual changes between NMDC and symptomatic DCM patients. Alterations above the compression level further endorse brain studies [42-44] that reported changes in motor and somatosensory cortex in symptomatic DCM patients with degenerative CSC compression. A decrease of CSA at the C3 level in DCM compared to HC corresponds with previous studies [10,13,14,40] and further points to remote degeneration rostrally to MCL. A smaller yet significant CSA deficit was also found in the NMDC group, suggesting more profound changes in DCM than in NMDC compared to HC.

Tract-specific analysis also revealed a relationship between the degree of disability (i.e., mJOA scale) and diffusion metrics in lateral columns and spinal lemniscus comprising motor and sensory pathways in DCM patients. DCM patients with lower mJOA scale (worse DCM disability) exhibited a decrease of f_1, FA and AD and an increase of RD compared to NMDC patients and HC. These findings correspond to more severe demyelination and axonal damage in DCM patients with profound motor and sensory disability.

Most importantly, significant dMRI changes in individual tracts between patients with and without electrophysiological deficits point to a crucial relationship between functional impairments and microstructural dMRI degeneration. Patients with abnormal electrophysiology findings showed lower values of f_1, FA, d and AD metrics and higher values of RD and MD compared to those with normal electrophysiological findings. Microstructural changes in sensory and motor tracts were related to SEP and MEP, respectively, with altered GM found in patients with EMG changes. Whilst previous studies also examined the relationship between dMRI and electrophysiology, they failed to detect dMRI distinctions between patients with and without electrophysiological deficits [18], or detected FA alterations in DCM patients with normal SEP [38]. Whereas electrophysiological measures serve as essential predictors of DCM development [2,6], optimized spatially selective tract-based measures of the CSC overcome previous unselective dMRI analyses of the whole axial spinal cord volumes. Thus, the proven significant relationship between electrophysiology and tract-based dMRI metrics suggest that tract-specific analysis might provide an objective tool to examine the relationship between diffusion-informed microstructural changes and functional electrophysiological impairments. Tract-specific dMRI should be explored as a potential predictor in future longitudinal studies utilizing current high-resolution methods. Also, dMRI is a non-invasive tool that is easier to perform than electrophysiological measures.

Our outcomes imply the importance of novel dMRI models in CSC analysis. The multi-compartment ball-and-sticks model, which incorporates intra-axonal restriction and better explains the data than DTI [20], has not been utilized in a large sample of NMDC or DCM patients yet. The ball-and-sticks f_1 metric indeed revealed additional between-group alterations at the C3-6 area in GM as well as ventral columns and fasciculus cuneatus, which were not revealed by FA. Lemniscal alterations between NMDC patients and HCs at C3 above the compression level were also exclusively revealed by the ball-and-sticks f_1 metric.

Our study was limited by spatial coverage of dMRI data (i.e., the C3-6 area). Caudal vertebral levels were not explored due to scanning time constraints and possible signal loss at the C7 level caused by the character of the HARDI-ZOOMit protocol [21]. Semi-automatic analyses also required time-consuming manual adjustment of segmentations, mainly in patients with severe CSC compression. Severe compression further limited proper white matter atlas registration in five DCM patients. Although the atlas-based approach provides higher accuracy and less propensity to susceptibility distortions than tractography-based methods [45], future studies may benefit from subject-specific tractography approaches, which are not yet fully developed.

In conclusion, the combination of conventional DTI and the multi-compartment ball-and-sticks model allowed to reveal tract-specific dMRI changes congruent with previous histopathological studies. Compression-caused demyelination, atrophy and axonal degeneration in white matter tracts and GM progressed from less severe NMDC to symptomatic DCM. Tract-specific diffusion abnormalities

correlated with clinical deficits and abnormal electrophysiology in relevant anatomical tracts. Thus, our study demonstrated that high-resolution tract-specific dMRI is a sensitive microstructural marker of CSC alterations for longitudinal trials aiming to provide early predictors of progression into symptomatic myelopathy and potentially can be translated also for patients with traumatic spinal cord injury.

ACKNOWLEDGEMENTS

The authors would like to thank to Pavel Hok for help with data processing, Petr Kudlička and Veronika Fábíková for MRI data acquisition and Dagmar Kratochvílová for subject recruitment.

CONFLICT OF INTEREST

No authors disclosed any relevant relationships.

AUTHOR CONTRIBUTIONS

Jan Valošek: Conceptualization (equal); data curation (equal); formal analysis (equal); funding acquisition (supporting); investigation (equal); methodology (equal); resources (supporting); software (equal); validation (equal); visualization (lead); writing—original draft (lead); writing—review and editing (lead). René Labounek: Conceptualization (equal); data curation (equal); formal analysis (equal); funding acquisition (equal); investigation (equal); methodology (equal); resources (equal); software (equal); supervision (equal); validation (equal); visualization (equal); writing—original draft (equal); writing—review and editing (equal). Tomáš Horák: Data curation (equal); formal analysis (equal); investigation (equal); methodology (equal); software (equal); validation (equal); visualization (equal); writing—original draft (equal); writing—review and editing (equal). Magda Horakova: Data curation (equal); investigation (equal); methodology (equal); project administration (equal); software (equal); validation (equal); visualization (equal); writing—original draft (equal); writing—review and editing (equal). Petr Bednařík: Conceptualization (equal); data curation (equal); formal analysis (equal); funding acquisition (equal); investigation (equal); methodology (equal); resources (equal); software (equal); supervision (equal); validation (equal); visualization (equal); writing—original draft (equal); writing—review and editing (equal). Miloš Keřkovský: Conceptualization (equal); data curation (equal); formal analysis (equal); funding acquisition (equal); investigation (equal); methodology (equal); project administration (equal); resources (equal); software (equal); supervision (equal); validation (equal); writing—original draft (equal); writing—review and editing (equal). Jan Kočica: Data curation (equal); investigation (equal); validation (equal); visualization (equal); writing—original draft (equal); writing—review and editing (equal). Tomáš Rohan: Data curation (equal); investigation (equal); validation (equal); visualization (equal); writing—original draft (equal); writing—review and editing (equal). Christophe Lenglet: Conceptualization (equal); investigation (equal); methodology (equal); supervision (equal); visualization (equal); writing—original draft (equal); writing—review and editing (equal). Julien Cohen-Adad: Data curation (equal); investigation (equal); methodology (equal); supervision (equal); validation (equal); visualization (equal); writing—original draft (equal); writing—review and editing (equal). Petr Hlustik: Conceptualization (equal); data curation (equal); formal analysis (equal); funding acquisition (equal); investigation (equal); methodology (equal); project administration (equal); resources (equal); software (equal); supervision (lead); validation (equal); visualization (equal); writing—original draft (equal); writing—review and editing (equal). Eva Vlckova: Conceptualization (equal); data curation (equal); formal analysis (equal); funding acquisition (equal); investigation (equal); methodology (equal); project administration (equal); validation (equal); visualization (equal); writing—original draft (equal); writing—review and editing (equal). Zdeněk Kadaňka Jr: Conceptualization (equal); investigation (equal); methodology (equal); validation (equal); visualization (equal); writing—original draft (equal); writing—review and editing (equal). Josef Bednarik: Conceptualization (lead); data curation (equal); formal analysis (equal); funding acquisition (lead); investigation (equal); methodology (equal); project administration (lead); resources (lead); software (equal); supervision (lead); validation (equal); visualization (equal); writing—original draft (equal); writing—review and editing (equal). Alena Svatkova: Conceptualization (equal); data curation (equal); formal analysis (equal); funding acquisition (equal); investigation (equal); methodology (equal); resources (equal); software (equal); supervision (lead); validation (equal); visualization (equal); writing—original draft (equal); writing—review and editing (equal).

DATA AVAILABILITY STATEMENT

The data that support the findings of this study are available from the corresponding author upon reasonable request.

ORCID

Jan Valošek https://orcid.org/0000-0002-7398-4990
René Labounek https://orcid.org/0000-0003-0439-1304
Tomáš Horák https://orcid.org/0000-0003-1743-1133
Magda Horáková https://orcid.org/0000-0003-3317-2661
Petr Bednařík https://orcid.org/0000-0002-8828-7661
Miloš Keřkovský https://orcid.org/0000-0003-0587-9897
Jan Kočica https://orcid.org/0000-0002-2937-6373
Tomáš Rohan https://orcid.org/0000-0002-7105-583X
Christophe Lenglet https://orcid.org/0000-0003-4646-3185
Julien Cohen-Adad https://orcid.org/0000-0003-3662-9532
Petr Hluštík https://orcid.org/0000-0002-1951-0671
Eva Vlčková https://orcid.org/0000-0003-2322-5539
Zdeněk Kadaňka Jr. https://orcid.org/0000-0001-5146-2457
Josef Bednařík https://orcid.org/0000-0001-7420-2383
Alena Svatkova https://orcid.org/0000-0002-9188-4280

REFERENCES

1. Badhiwala JH, Ahuja CS, Akbar MA, et al. Degenerative cervical myelopathy—update and future directions. *Nat Rev Neurol*. 2020;16:108-124.
2. Bednarik J, Kadanka Z, Dusek L, et al. Presymptomatic spondylotic cervical myelopathy: an updated predictive model. *Eur Spine J*. 2008;17:421-431.
3. Smith SS, Stewart ME, Davies BM, et al. The prevalence of asymptomatic and symptomatic spinal cord compression on magnetic

resonance imaging: a systematic review and meta-analysis. *Global Spine Journal*. 2021;11(4):597-607.
4. Kovalova I, Kerkovsky M, Kadanka Z, et al. Prevalence and imaging characteristics of nonmyelopathic and myelopathic spondylotic cervical cord compression. *Spine (Phila Pa 1976)*. 2016;41(24):1908-1916.
5. Adamova B, Bednarik J, Andrasinova T, et al. Does lumbar spinal stenosis increase the risk of spondylotic cervical spinal cord compression? *Eur Spine J*. 2015;24:2946-2953.
6. Kadanka Z, Adamova B, Kerkovsky M, et al. Predictors of symptomatic myelopathy in degenerative cervical spinal cord compression. *Brain Behav*. 2017;7:e00797.
7. Bednarik J, Kadanka Z, Dusek L, et al. Presymptomatic spondylotic cervical cord compression. *Spine (Phila Pa 1976)*. 2004;29(20):2260-2269.
8. Witiw CD, Mathieu F, Nouri A, et al. Clinico-radiographic discordance: an evidence-based commentary on the management of degenerative cervical spinal cord compression in the absence of symptoms or with only mild symptoms of myelopathy. *Glob Spine J*. 2018;8:527-534.
9. Wilson JR, Barry S, Fischer DJ, et al. Frequency, timing, and predictors of neurological dysfunction in the nonmyelopathic patient with cervical spinal cord compression, canal stenosis, and/or ossification of the posterior longitudinal ligament. *Spine (Phila Pa 1976)*. 2013;38:S37-S54.
10. Martin AR, De Leener B, Cohen-Adad J, et al. A novel MRI biomarker of spinal cord white matter injury: T2*-weighted white matter to gray matter signal intensity ratio. *Am J Neuroradiol*. 2017;38:1266-1273.
11. Dong F, Wu Y, Song P, et al. A preliminary study of 3.0-T magnetic resonance diffusion tensor imaging in cervical spondylotic myelopathy. *Eur Spine J*. 2018;27:1839-1845.
12. Shabani S, Kaushal M, Budde MD, et al. Diffusion tensor imaging in cervical spondylotic myelopathy: a review. *J Neurosurg Spine*. 2020;33:65-72.
13. David G, Mohammadi S, Martin AR, et al. Traumatic and nontraumatic spinal cord injury: pathological insights from neuroimaging. *Nat Rev Neurol*. 2019;15:718-731.
14. Seif M, David G, Huber E, et al. Cervical cord neurodegeneration in traumatic and non-traumatic spinal cord injury. *J Neurotrauma*. 2020;37:860-867.
15. Martin AR, De Leener B, Cohen-Adad J, et al. Monitoring for myelopathic progression with multiparametric quantitative MRI. *PLoS One*. 2018;13(4):e0195733.
16. Martin AR, De Leener B, Cohen-Adad J, et al. Can microstructural MRI detect subclinical tissue injury in subjects with asymptomatic cervical spinal cord compression? A prospective cohort study. *BMJ Open*. 2018;8:e019809.
17. Keřkovský M, Bednařík J, Jurová B, et al. Spinal cord MR diffusion properties in patients with degenerative cervical cord compression. *J Neuroimaging*. 2017;27:149-157.
18. Kerkovský M, Bednarík J, Dušek L, et al. Magnetic resonance diffusion tensor imaging in patients with cervical spondylotic spinal cord compression: correlations between clinical and electrophysiological findings. *Spine (Phila Pa 1976)*. 2012;37(1):48-56.
19. Basser PJ, Mattiello J, LeBihan D. MR diffusion tensor spectroscopy and imaging. *Biophys J*. 1994;66:259-267.
20. Panagiotaki E, Schneider T, Siow B, et al. Compartment models of the diffusion MR signal in brain white matter: a taxonomy and comparison. *NeuroImage*. 2012;59:2241-2254.
21. Labounek R, Valošek J, Horák T, et al. HARDI-ZOOMit protocol improves specificity to microstructural changes in presymptomatic myelopathy. *Sci Rep*. 2020;10:17529.
22. Behrens TEJ, Woolrich MW, Jenkinson M, et al. Characterization and propagation of uncertainty in diffusion-weighted MR imaging. *Magn Reson Med*. 2003;50:1077-1088.
23. Gros C, De Leener B, Badji A, et al. Automatic segmentation of the spinal cord and intramedullary multiple sclerosis lesions with convolutional neural networks. *NeuroImage*. 2019;184:901-915.
24. De Leener B, Fonov VS, Collins DL, Callot V, Stikov N, Cohen-Adad J. PAM50: unbiased multimodal template of the brainstem and spinal cord aligned with the ICBM152 space. *NeuroImage*. 2018;165:170-179.
25. Lévy S, Benhamou M, Naaman C, et al. White matter atlas of the human spinal cord with estimation of partial volume effect. *NeuroImage*. 2015;119:262-271.
26. De Leener B, Lévy S, Dupont SM, et al. SCT: Spinal Cord Toolbox, an open-source software for processing spinal cord MRI data. *NeuroImage*. 2017;145:24-43.
27. Mair WGP, Druckman R. The pathology of spinal cord lesions and their relation to the clinical features in protrusion of cervical intervertebral discs (a report of four cases). *Brain*. 1953;76:70-91.
28. Tetreault L, Kopjar B, Nouri A, et al. The modified Japanese Orthopaedic Association scale: establishing criteria for mild, moderate and severe impairment in patients with degenerative cervical myelopathy. *Eur Spine J*. 2017;26:78-84.
29. Bednařík J, Kadaňka Z, Voháňka S, et al. The value of somatosensory and motor evoked potentials in pre-clinical spondylotic cervical cord compression. *Eur Spine J*. 1998;7:493-500.
30. Caruyer E, Lenglet C, Sapiro G, et al. Design of multishell sampling schemes with uniform coverage in diffusion MRI. *Magn Reson Med*. 2013;69:1534-1540.
31. Jenkinson M, Beckmann CF, Behrens TEJ, et al. FSL. *NeuroImage*. 2012;62:782-790.
32. Ullmann E, Pelletier Paquette JF, Thong WE, et al. Automatic labeling of vertebral levels using a robust template-based approach. *Int J Biomed Imaging*. 2014;2014:719520.
33. Cohen-Adad J. Microstructural imaging in the spinal cord and validation strategies. *NeuroImage*. 2018;182:169-183.
34. Badhiwala JH, Ahuja CS, Akbar MA, et al. Degenerative cervical myelopathy - update and future directions. *Nat Rev Neurol*. 2020;16(2):108-124.
35. Baptiste DC, Fehlings MG. Pathophysiology of cervical myelopathy. *Spine J*. 2006;6(6 Suppl):190S-197S.
36. Lee JW, Kim JH, Park JB, et al. Diffusion tensor imaging and fiber tractography in cervical compressive myelopathy: preliminary results. *Skeletal Radiol*. 2011;40:1543-1551.
37. Lindberg PG, Sanchez K, Ozcan F, et al. Correlation of force control with regional spinal DTI in patients with cervical spondylosis without signs of spinal cord injury on conventional MRI. *Eur Radiol*. 2016;26:733-742.
38. Wen CY, Cui JL, Liu HS, et al. Is diffusion anisotropy a biomarker for disease severity and surgical prognosis of cervical spondylotic myelopathy. *Radiology*. 2014;270:197-204.
39. Facon D, Ozanne A, Fillard P, et al. MR diffusion tensor imaging and fiber tracking in spinal cord compression. *AJNR Am J Neuroradiol*. 2005;26:1587-1594.
40. Grabher P, Mohammadi S, Trachsler A, et al. Voxel-based analysis of grey and white matter degeneration in cervical spondylotic myelopathy. *Sci Rep*. 2016;6:24636.
41. Budzik J-F, Balbi V, Le Thuc V, Duhamel A, Assaker R, Cotten A. Diffusion tensor imaging and fibre tracking in cervical spondylotic myelopathy. *Eur Radiol*. 2011;21:426-433.
42. Kowalczyk I, Duggal N, Bartha R. Proton magnetic resonance spectroscopy of the motor cortex in cervical myelopathy. *Brain*. 2012;135:461-468.
43. Bernabéu-Sanz Á, Mollá-Torró JV, López-Celada S, et al. MRI evidence of brain atrophy, white matter damage, and functional adaptive changes in patients with cervical spondylosis and prolonged spinal cord compression. *Eur Radiol*. 2020;30:357-369.
44. Zhou FQ, Tan YM, Wu L, Zhuang Y, He LC, Gong HH. Intrinsic functional plasticity of the sensory-motor network in patients with cervical spondylotic myelopathy. *Sci Rep*. 2015;5(1):9975.

45. Cohen-Adad J, Wheeler-Kingshott C. *Quantitative MRI of the Spinal Cord*. San Diego, CA: Academic Press (Elsevier); 2014.

SUPPORTING INFORMATION

Additional supporting information may be found online in the Supporting Information section.

Supplementary Material

How to cite this article: Valošek J, Labounek R, Horák T, et al. Diffusion magnetic resonance imaging reveals tract-specific microstructural correlates of electrophysiological impairments in non-myelopathic and myelopathic spinal cord compression. *Eur J Neurol*. 2021;28:3784–3797. https://doi.org/10.1111/ene.15027

12.3 Annex 3 – Narrative Review

Journal of
Clinical Medicine

MDPI

Review

Quantitative MR Markers in Non-Myelopathic Spinal Cord Compression: A Narrative Review

Jan Valošek [1,2,3], Petr Bednařík [4,5], Miloš Keřkovský [6,7], Petr Hluštík [1,8], Josef Bednařík [6,9,10] and Alena Svátková [4,5,11,*]

1 Department of Neurology, Faculty of Medicine and Dentistry, Palacký University Olomouc, 779 00 Olomouc, Czech Republic; jan.valosek@upol.cz (J.V.); phlustik@upol.cz (P.H.)
2 Department of Radiology, Faculty of Medicine and Dentistry, Palacký University Olomouc, 779 00 Olomouc, Czech Republic
3 Department of Biomedical Engineering, University Hospital Olomouc, 779 00 Olomouc, Czech Republic
4 Danish Research Centre for Magnetic Resonance, Centre for Functional and Diagnostic Imaging and Research, Copenhagen University Hospital Amager and Hvidovre, 2650 Hvidovre, Denmark; petrb@drcmr.dk
5 Department of Radiology, Centre for Functional and Diagnostic Imaging and Research, Copenhagen University Hospital Amager and Hvidovre, 2650 Hvidovre, Denmark
6 Faculty of Medicine, Masaryk University, 625 00 Brno, Czech Republic; kerkovsky.milos@fnbrno.cz (M.K.); bednarik.josef@fnbrno.cz (J.B.)
7 Department of Radiology and Nuclear Medicine, University Hospital Brno, 625 00 Brno, Czech Republic
8 Department of Neurology, University Hospital Olomouc, 779 00 Olomouc, Czech Republic
9 Department of Neurology, University Hospital Brno, 625 00 Brno, Czech Republic
10 Central European Institute of Technology, Masaryk University, 625 00 Brno, Czech Republic
11 Department of Medicine III, Clinical Division of Endocrinology and Metabolism, Medical University of Vienna, 1090 Vienna, Austria
* Correspondence: alenas@drcmr.dk

Abstract: Degenerative spinal cord compression is a frequent pathological condition with increasing prevalence throughout aging. Initial non-myelopathic cervical spinal cord compression (NMDC) might progress over time into potentially irreversible degenerative cervical myelopathy (DCM). While quantitative MRI (qMRI) techniques demonstrated the ability to depict intrinsic tissue properties, longitudinal in-vivo biomarkers to identify NMDC patients who will eventually develop DCM are still missing. Thus, we aim to review the ability of qMRI techniques (such as diffusion MRI, diffusion tensor imaging (DTI), magnetization transfer (MT) imaging, and magnetic resonance spectroscopy (^{1}H-MRS)) to serve as prognostic markers in NMDC. While DTI in NMDC patients consistently detected lower fractional anisotropy and higher mean diffusivity at compressed levels, caused by demyelination and axonal injury, MT and ^{1}H-MRS, along with advanced and tract-specific diffusion MRI, recently revealed microstructural alterations, also rostrally pointing to Wallerian degeneration. Recent studies also disclosed a significant relationship between microstructural damage and functional deficits, as assessed by qMRI and electrophysiology, respectively. Thus, tract-specific qMRI, in combination with electrophysiology, critically extends our understanding of the underlying pathophysiology of degenerative spinal cord compression and may provide predictive markers of DCM development for accurate patient management. However, the prognostic value must be validated in longitudinal studies.

Keywords: non-myelopathic cervical spinal cord compression; degenerative cervical myelopathy; diffusion magnetic resonance imaging; quantitative magnetic resonance imaging

Citation: Valošek, J.; Bednařík, P.; Keřkovský, M.; Hluštík, P.; Bednařík, J.; Svátková, A. Quantitative MR Markers in Non-Myelopathic Spinal Cord Compression: A Narrative Review. *J. Clin. Med.* **2022**, *11*, x. https://doi.org/10.3390/xxxxx

Academic Editor: Anna Caroli

Received: 25 February 2022
Accepted: 12 April 2022
Published: date

Publisher's Note: MDPI stays neutral with regard to jurisdictional claims in published maps and institutional affiliations.

Copyright: © 2022 by the authors. Submitted for possible open access publication under the terms and conditions of the Creative Commons Attribution (CC BY) license (https://creativecommons.org/licenses/by/4.0/).

1. Introduction

The resilience of the cervical spinal cord (SC) to incipient compressive changes, such as intervertebral disc bulging, herniation, or osteophyte formation, often leads to non-myelopathic degenerative cervical spinal cord compression (NMDC), a condition that precedes clinically manifested degenerative cervical myelopathy (DCM) [1–4]. Although

the degenerative spinal cord compression (DSCC) occurs predominantly between the C4/5 and C6/7 cervical levels [5,6], secondary degenerative changes, such as axonal degeneration and demyelination, propagate remotely in both the superior and inferior directions, affecting levels above and below the compression and even leading to alterations in the brain [7–9]. The recent systematic review [10] showed that the prevalence of NMDC in the Caucasian population over 60 years is up to 39.7% and further increases with age [6,10,11]. Even though NMDC patients may only exhibit cervical axial pain and/or signs or symptoms of radiculopathy, without any signs or symptoms of clinical manifest myelopathy (Table 1), up to 23% of NMDC patients progress into symptomatic DCM during a follow-up of 44 months [3,12]. The current clinical guidelines [4,13] imply conservative clinical treatment in NMDC patients without symptoms of radiculopathy, whereas guidelines recommend the consideration of surgical intervention in NMDC patients with clinical and/or electrophysiological evidence of radiculopathy. Given the undeniable risks of decompressive surgery in 7–11% of patients [1], aging of the population worldwide, and substantially reduced quality of life in DCM patients [1,14], there is an urgent need to reliably identify NMDC patients with a higher risk of progression to irreversible DCM [13].

While previous reviews [1,7,15–18] focused on the epidemiology, pathophysiology, and assessment of DCM using structural MRI, diffusion tensor imaging (DTI) [19,20], and magnetic resonance spectroscopy (MRS) [20], so far, limited attention has been paid to NMDC patients. To date, a single systematic review by Smith et al. [10] covered the NMDC prevalence in structural MRI but did not discuss the benefits and pitfalls of quantitative MRI (qMRI) techniques, which provide crucial in-vivo insight into the pathophysiology of degenerative compression. Thus, our review aims to identify and discuss the potential of qMRI techniques to quantify NMDC alterations in vivo and determine the likeliness of progression to DCM. Due to the relatively limited number of qMRI studies in NMDC patients, DCM studies were also included to elaborate on their prospects in NMDC.

Table 1. Nomenclature and definitions of non-myelopathic spinal cord compression across studies.

Study	Nomenclature	Definition
	Original Articles	
Bednarik et al. 2004 [2], 2008 [3]	Pre-symptomatic spondylotic cervical cord compression (P-SCCC)	MR signs of DSCC (spondylotic or discogenic) and axial cervical pain or clinical signs and/or symptoms of radiculopathy, but no clinical signs of myelopathy (mJOA ≥ 16; note—mJOA decreased, due to radiculopathy)
Keřkovský et al. 2012 [21]	Asymptomatic spondylotic cervical cord encroachment (SCCE)	MR signs of DSCC and cervical pain and/or symptoms/signs of cervical radiculopathy, but without symptoms/signs of cervical spondylotic myelopathy (mJOA = 18)
Adamova et al. 2015 [22]	Asymptomatic spondylotic cervical cord compression (ASCCC)	No detailed description (study focused on prevalence of ASCCC in patients with clinically symptomatic lumbar spinal stenosis) (mJOA not reported)
Kovalova et al. 2016 [6]	Non-myelopathic spondylotic cervical cord compression (NMSCCC)	MR signs of DSCC and possible presence of radiculopathy, but no myelopathic signs (mJOA not reported)
Keřkovský et al. 2017 [23]	Asymptomatic degenerative cervical cord compression (ADCCC)	MR finding of DSCC and various clinical signs of cervical spine degenerative disease (cervical pain and radiculopathy), but no signs or symptoms of DCM (mJOA = 18)
Ellingson et al. 2018 [24]	Asymptomatic cervical stenosis	No neurological symptomatology (mJOA = 18), but complaints of neck pain

Martin et al. 2018 [25]	Asymptomatic spinal cord compression (ASCC)	MR finding of DSCC, but an absence of any neurological symptoms and signs; neck pain was not considered a neurological symptom (mJOA = 18)
Kadanka Jr. et al. 2017 [26], Labounek et al. 2020 [27]	Non-myelopathic degenerative cervical cord compression (NMDCCC)	MR signs of DSCC, but an absence of any myelopathic signs, possible presence of axial pain, symptoms or signs of upper extremity monoradiculopathy, or completely asymptomatic individuals (mJOA not reported)
Kadanka Jr. et al. 2021 [28]	Non-myelopathic degenerative cervical cord compression (NMDCC)	MR signs of DSCC and presence of maximally one clinical myelopathic symptom, but no clinical myelopathic signs (mJOA ≥ 17)
Valošek et al. 2021 [5], Horak et al. 2021 [29], Horakova et al. 2022 [30]	Non-myelopathic degenerative cervical spinal cord compression (NMDC)	MR signs of DSCC with or without radiculopathy and electrophysiological changes, but without myelopathic symptoms/signs (mJOA = 18)
	Reviews	
Wilson et al. 2013 [12]	Non-myelopathic patients with cervical stenosis	Review—no single definition
Witiw et al. 2018 [11]	Asymptomatic cervical spinal cord compression (CSCC)	Review—no single definition
Smith et al. 2020 [10]	Asymptomatic spinal cord compression (ASCC)	Review—no single definition
Badhiwala et al. 2020 [1]	Cervical spinal cord compression without myelopathy	Review—MR signs of DSCC, absence of any myelopathic signs, and clinical radiculopathy with or without electrophysiological changes or no signs of symptoms of radiculopathy (mJOA = 18)

DSCC, degenerative spinal cord compression; mJOA, modified Japanese Orthopaedic Association scale; MR, magnetic resonance.

2. MRI in the Non-Myelopathic and Myelopathic Spinal Cord Compression

2.1. Structural MRI

Conventional clinical MRI is primarily acquired in the sagittal orientation to evaluate SC signal abnormalities, such as the presence of T2-w hyperintensities and T1-w hypointensities [31]. Subjectively-evaluated T2-w hyperintensities are still considered an important factor influencing decision-making for decompressive surgery [12], although their presence does not necessarily correspond with the clinical DCM signs and symptoms [32]. Intramedullary T2-w hyperintensities have, indeed, been reported in 58–85% of patients with clinically manifest DCM [33], whereas in NMDC inconsistently ranged between 2.3–24.6% [3,6,26,34]. T1-w hypointensities are associated with permanent SC injury [31], and they are relatively rare, occurring in 19–30% of DCM patients [32]; thus, their predictive value in NMDC patients is limited.

In addition to the conventional clinical description of signal changes, sequences with a sufficient axial in-plane resolution below 1 mm and good contrast between white/gray matter (WM/GM) and cerebrospinal fluid (CSF) (typically 3D isotropic T1-w and 2D axial multi-echo gradient echo T2*-w sequences) allow for assessing morphometric metrics, in order to further validate the severity of compression. The cross-sectional area (i.e., area of the SC in the axial plane) of ≤ 70.1 mm^2, and the compression ratio (i.e., the ratio between the anteroposterior diameter and the transverse diameter) of ≤ 0.4 distinguished NMDC patients who developed symptomatic DCM with sensitivities of 66.7 and 82.5, respectively, as well as specificities of 60.0 and 89.7, respectively [26]. Recently proposed morphometric metrics, reflecting SC flattening, indentation, and torsion (Figure 1A) [30,35], semi-automatically detected DSCC with the area under the curve of 0.947 (compared to expert raters); however, no morphometric metric distinguished between NMDC and DCM patients [30]. NMDC patients also showed an increased T2*-w WM/GM intensity

ratio relative to healthy controls (HC) in a maximally compressed level (MCL) as well as rostrally and caudally [25].

SC volumetry adds to the compression metrics at MCL when assessing changes above and below the compression levels. So far, studies demonstrated a gradual reduction of SC, WM, and GM volumes at C2/3 above the compression level in DCM and NMDC, relative to HC (Figure 2) [5,29,36–40]. Exacerbation of alterations in DCM then NMDC points to more progressive Wallerian neurodegeneration and atrophy in DSCC [5,38]. A recent study also reported atrophy of SC, WM, and GM below MCL at the T11-L1 level in DCM patients, relative to HC, due to the trans-synaptic degeneration [40].

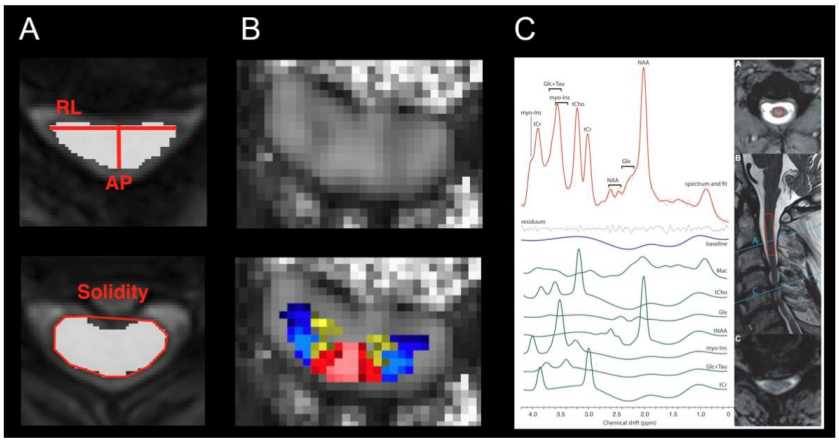

Figure 1. Quantitative MRI (qMRI) markers, derived using various qMRI methods. (**A**) Morphometric metrics measuring the degree of spinal cord compression, based on structural MRI. Upper panel shows compression ratio calculated as a ratio between the anteroposterior (AP) and transverse (RL) diameters, and lower panel shows solidity calculated as a ratio of cross-sectional area to the area of the smallest convex polygon surrounding all positive pixels in the image. Image courtesy of Magda Horáková. (**B**) Map of fractional anisotropy (FA), estimated using diffusion tensor imaging model from diffusion-weighted imaging data. Upper panel shows the FA map, and lower panel shows the FA map overlayed with probabilistic PAM50 atlas of white and gray matter, allowing for tissue-specific analysis. Adapted with permission from Ref. [5] under creative common license; (**C**) single-voxel magnetic resonance spectroscopy (^{1}H-MRS) measuring metabolic concentrations from above the compression level C2/3 (red box). Adapted with permission from Ref. [29] under creative common license.

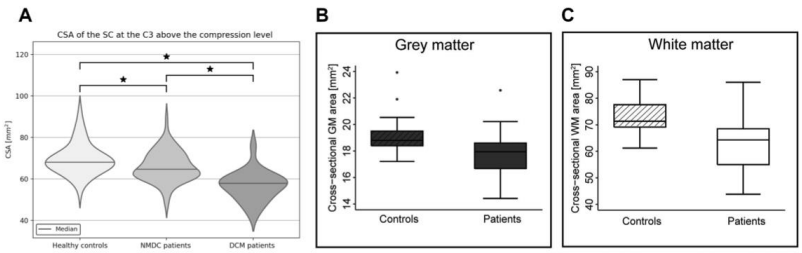

Figure 2. Significant reduction of the cross-sectional area (CSA) above the stenosis level. (**A**) Spinal cord (SC) CSA reduction at the C3 level, between NMDC and DCM patients, relative to healthy controls. Asterisk symbols (*) indicate significant difference between groups. Adapted with permission from Ref. [5] under creative common license; (**B**) Grey and (**C**) white CSA reduction at C2/3 level, between DCM patients and HC. Adapted with permission from Ref. [37] under creative common license.

2.2. Microstructural Quantitative MRI

2.2.1. Diffusion MRI

Diffusion magnetic resonance imaging (dMRI, or diffusion-weighted imaging, DWI) is sensitive to random water molecule movement within the tissue, which is restricted/hindered by myelination and axonal configuration [42]. Clinical dMRI has been used for the quantification of diffusion restriction or apparent diffusion coefficient caused, for example, by vasogenic edema due to acute ischemia [42]. The research applications rely on the fitting of diffusion models, which provide quantitative microstructural markers that are sensitive to different pathologies, such as axonal damage and demyelination [42]. The most commonly used diffusion model in the SC research is diffusion tensor imaging (DTI) [7,43,44]. DTI provides fractional anisotropy (FA) (Figure 1B), referring to the directional preference of diffusion, affected by the degree of myelination, axonal packing, axon size, coherence and co-linearity of fiber organization, mean diffusivity (MD) measuring the overall molecular diffusion rate, and axial (AD) and radial diffusivity (RD), referring to the degree of tissue edema, axonal damage, and demyelination, respectively [42,45]. However, DTI, as a single-compartment model, allows us to reconstruct only a primary diffusion direction and fails to estimate more complex WM fiber configurations [44]. Higher-order diffusion models, such as neurite orientation dispersion and density imaging (NODDI) [46–51], ball-and-sticks [5,27], and diffusion kurtosis imaging (DKI) [52,53], which overcome DTI's limitation by modeling several tissue compartments, were recently translated from the brain to SC imaging, in order to provide more precise depiction of its complex microstructure.

Diffusion Tensor Imaging

Multiple studies [19,21,23,27,33,35,39,51,54–70] and reviews [19,20] covered DTI in symptomatic DCM patients, whereas only a few works are available in NMDC patients [5,21,23–27] (Table 2). One of the first 1.5T studies in NMDC patients compared the DTI metrics of 13 HC with 20 DCM and 32 NMDC patients and detected lower FA and higher MD at MCL in DCM, compared to NMDC patients, with lower FA and no significant MD deficits between NMDC patients and HC [21]. Outcomes were corroborated by the second study [23] on 37 DCM patients, 93 NMDC patients, and 71 HC with the same inclusion/exclusion criteria, although no comparison between NMDC patients and HC was provided. However, both studies employed a single ROI that covered the entire axial SC, and it is, thus, unclear whether the decreased FA was caused by a higher proportion of GM with naturally lower FA, compared to WM, or by actual WM damage. The first 3T NMDC DTI study [25] detected lower FA in the entire axial ROI at MCL in 20 NMDC patients, relative to 20 HC, and corroborated the previous 1.5T study [21], although it utilized a slightly distinct inclusion criteria, compared to the Czech studies [5,21,23] (Table 1). The additional column-specific analysis showed decreased FA in the ventral columns of NMDC patients [25]. A recent 3T tract-specific study detected lower FA and higher MD and RD at MCL in dorsal and lateral tracts in a large cohort of 103 NMDC and 21 DCM patients, compared to 60 HC with more profound alterations in DCM than NMDC [5]. In agreement with histopathology [1,71], which demonstrated malperfusion throughout the territory of compressed anterior spinal artery with restrained blood supplies in the lateral columns, anterior part of dorsal columns, and ventral GM horns, GM also showed a significant alteration, with higher MD, AD, and RD in both NMDC and DCM patients, relative to HC [5]. Another 1.5T study found lower FA and higher RD at MCL in the lateral corticospinal tracts in 16 DCM patients with clinical DCM symptoms, without evidence of SC damage on T2-w images, compared to 20 HC [72]; no changes were demonstrated in the remaining medial parts, further confirming demyelination in dorsal and lateral WM tracts [5,72].

Table 2. List of studies comprising of patients with non-myelopathic/asymptomatic spinal cord compression utilizing qMRI techniques. Studies are ordered chronologically.

Study	Cohort	Field Strength, Voxel Size, qMRI Technique, ROI	Key Results	Conclusion/Interpretation
Keřkovský et al., 2012 [21]	32 NMDC patients (mJOA = 18)	1.5T	Lower FA and higher MD at MCL in DCM, compared to NMDC	DTI showed potential to discriminate between NMDC and symptomatic DCM patients
	20 DCM patients (mJOA < 18)	1.25 × 1.25 × 4 mm^3	Lower FA, no MD change at MCL in NMDC, relative to HC	Differences between NMDC and HC could be caused by demyelination, but potentially also by WM/GM mixing
	13 HC	DTI (FA, MD), entire axial SC		There was no difference in any of the DTI parameters for subsets of patients with and without electrophysiological abnormality
Keřkovský et al., 2017 [23]	93 NMDC patients (mJOA = 18)	1.5T	Lower FA and increased MD at MCL in DCM, compared to NMDC	DTI showed differences in FA and MD between NMDC and symptomatic DCM patients
	37 DCM patients (mJOA < 18)	1.25 × 1.25 × 4 mm^3		No differences between NMDC and HC reported
	71 HC	DTI (FA, MD), entire axial SC		
Kadanka et al., 2017 [26]	40 NMDC patients (mJOA not reported)	1.5T	DTI parameters showed no significant predictive power in longitudinal follow-up	The development of DCM was associated with several parameters, such as radiculopathy or electrophysiological measures
	72 subjects with cervical radiculopathy or cervical pain (mJOA not reported)	1.25 × 1.25 × 4 mm^3		DTI parameters showed no significant predictive power
		DTI (FA, MD), entire axial SC		
Martin et al., 2018 [25]	20 NMDC patients (mJOA = 18)	3T	Lower FA at MCL in entire axial ROI and ventral columns in NMDC, compared to HC	Changes in FA, MTR, and T2*WI WM/GM intensity point to demyelination and axonal injury as predominant pathogenic mechanisms in NMDC patients
	20 HC	1.25 × 1.25 × 5 mm^3 (DWI); 1 × 1 × 5 mm^3 (MT)	Lower MTR in the rostral region (C1-C3) and ventral columns in NMDC, compared to HC	Changes were observed at MCL, but also rostrally and caudally
		DTI (FA), MT (MTR) and T2*WI WM/GM, entire axial ROI and WM columns and GM	Higher T2*WI WM/GM at MCL and in rostral and caudal regions in NMDC compared to controls	
Ellingson et al., 2018 [24]	18 NMDC patients (mJOA = 18)	3T	Most patients (47 from 66) showed stationary longitudinal DTI measurements	DTI metrics correlated with neurological impairments, assessed by the mJOA scale, and may be valuable predictors of neurological status
	48 patients with clinical symptoms (mJOA < 18)	1.1 × 1.1 × 4–5 mm^3	Pooled FA and MD at MCL from all patients and all time points showed correlation with mJOA scale	
		DTI (FA, MD), entire axial SC		
Labounek et al., 2020 [27]	33 NMDC patients (divided into two groups—mild and severe compression)	3T	Lower MD in WM in NMDC with mild compression, compared to HC	DTI and ball-and-sticks models demonstrated differences between HC and NMDC patients in both WM and GM
	13 HC	0.65 × 0.65 × 3.00 mm^3 (interpolated)	Higher MD and d in GM in NMDC with severe compression, relative to HC	Optimized multi-shell dMRI protocol, with reduced field-of-view, outperformed clinically used single-shell protocol
		DTI (FA, MD) and ball-and-sticks model (f1, d), WM–GM difference, and "heuristic" parameters derived from these metrics, WM, and GM	Lower WM–GM difference for MD and d in NMDC with mild and severe compression, compared to HC	
			Difference in several "heuristic" parameters derived from FA, MD, f1, and d between groups, see the study [27] for details	

Valošek et al., 2021 [5]	103 NMDC patients (mJOA = 18)	3T	Lower FA and f1 and higher MD, AD, RD, and d in NMDC and DCM, compared to HC, with more severe changes in DCM, compared to NMDC	Compression primary affected lateral and dorsal white matter tracts and gray matter, pointing to demyelination and trans-synaptic degeneration
	21 DCM patients (mJOA < 18)	0.65 × 0.65 × 3.00 mm^3 (interpolated)	Changes were detected predominantly in dorsal and lateral tracts and GM at MCL and rostrally at the C3 level	Above the compression changes suggest Wallerian degeneration
	60 HC	DTI (FA, MD, AD, RD) and ball-and-sticks models (f1, d), WM columns and tracts, and GM regions	DCM patients showed changes also in the ventral columns, compared to HC	Changes were more profound in DCM, compared to NMDC and HC, suggesting progressive changes in patients with compression over time
			dMRI changes correlated with the mJOA scale and reflected electrophysiological findings	Ball-and-sticks model showed changes not detected by DTI model
Horak et al., 2021 [29]	60 NMDC patients (mJOA = 18)	3T	Increased total creatin/tNAA ratio in NMDC and DCM, relative to HC	^{1}H-MRS revealed neurochemical changes at the above the compression level C2/3 in both DCM and NMDC, compared to HC
	13 DCM patients (mJOA < 18)	8 × 9 × 45 mm^3 (single MRS voxel)	Changed myo-inositol/tNAA and glutamate + glutamine/tNAA ratios in DCM, compared to HC	Neurochemical changes suggest demyelination and Wallerian degeneration
	47 HC	^{1}H-MRS	myo-inositol/tNAA ratio in DCM patients correlated with the mJOA scale	
Horakova et al., 2022 [30]	102 NMDC (mJOA = 18)	1.5T and 3T	Logistic model combining compression ratio, cross-sectional area, solidity, and torsion detected compression with AUC = 0.947 (compared to expert raters)	The semi-automated method demonstrated outstanding compression detection, with better inter-trial variability, compared to manual raters
	16 DCM (mJOA < 18)	0.60 × 0.60 × 4.0 mm^3 (1.5T) 0.35 × 0.35 × 2.5 mm^3 (3T – interpolated)	The inter-trial variability (1.5 and 3 T) was better for the semi-automated method (intraclass correlation coefficient 0.858 for CR and 0.735 for CSA), compared to expert raters (mean coefficient for three expert raters 0.722 for CR and 0.486 for CSA)	
	66 HC	Morphometric parameters (cross-sectional area (CSA), compression ratio (CR), solidity, and torsion)	No morphometric metric showed the discriminative power to distinguish between NMDC and DCM	

AUC, area under the curve; CR, compression ratio; CSA, cross-sectional area; FA, fractional anisotropy; MD, mean diffusivity; AD, axial diffusivity; RD, radial diffusivity; f1, primary partial volume fraction (anisotropic compartment of ball-and-sticks model); d, ball-and-sticks model diffusivity; MTR, magnetic transfer ratio; ^{1}H-MRS, single-voxel magnetic resonance spectroscopy; WM, white matter; GM, gray matter; mJOA, modified Japanese Orthopaedic Association scale; tNAA, total N-acetylaspartate.

Besides the direct changes at the stenosis level, studies have also focused on remote neurodegeneration above the compression level. DCM studies [5,36,37,39,40,65] consistently detected decreased FA and increased diffusivity measures at the C2/C3 level in the dorsal and lateral WM tracts, compared to HC, whereas only two DCM studies showed changes in rostral GM [5,37]. The recent NMDC study then detected similar changes at the C3 level, i.e., decreased FA and increased MD and RD in the dorsal and lateral tracts and increased diffusivity measures in GM between DCM and NMDC patients [5]. Thus, outcomes congruently demonstrated the remote rostral neurodegeneration of long lateral and dorsal WM tracts, as well as trans-synaptic degeneration of GM in symptomatic DCM patients, relative to HC. Incipient remote changes in NMDC patients, relative to HC, were not detectable by DTI [25] and were, so far, observed only using the multi-compartment ball-and-sticks model, emphasizing the need for further research and utilization of multi-compartment dMRI models [5].

Importantly, to date, only two DTI studies [24,26] examined NMDC patients longitudinally to monitor progression from NMDC to DCM, and both utilized entire axial ROI (i.e., tissue non-specific). The first study [26] monitored DCM development in 112 NMDC patients, in 3 years median follow-ups, using a 1.5T scanner, and found no predictive power of DTI. The second 3T study [24] followed-up 66 nonoperatively treated patients with DSCC, for an average follow-up of 1.4 years, and reported that 47 out of 66 patients showed stationary FA and MD.

High-Order Diffusion Models

While higher-order diffusion models have been frequently utilized in DCM studies [5,46,47,51–53,68], only a limited number of works also included NMDC patients [5,27].

Recently, a multi-shell diffusion protocol, with reduced field-of-view, allowed for the estimation of more complex diffusion models, such as the ball-and-sticks model [73], in addition to the DTI model [27]. The multi-compartment ball-and-sticks model describes diffusion by a single isotropic and several anisotropic compartments and better characterizes diffusion data than the single-compartment DTI model [74]. The ball-and-sticks model initially demonstrated sensitivity to subtle microstructural changes in both WM and GM in 33 NMDC patients, relative to 13 HC [27], and was thereafter used in a large cohort of 103 NMDC, 21 DCM patients, and 60 HC to delineate changes in dorsal and lateral tracts and GM between NMDC and HC at MCL, as well as rostrally (Figure 3A) [5]. Results suggest superior discriminant power of the multi-compartment ball-and-sticks model over DTI, when abnormalities were depicted in the f1 metric (i.e., the primary anisotropic volume fraction), which were not detectable by DTI [5].

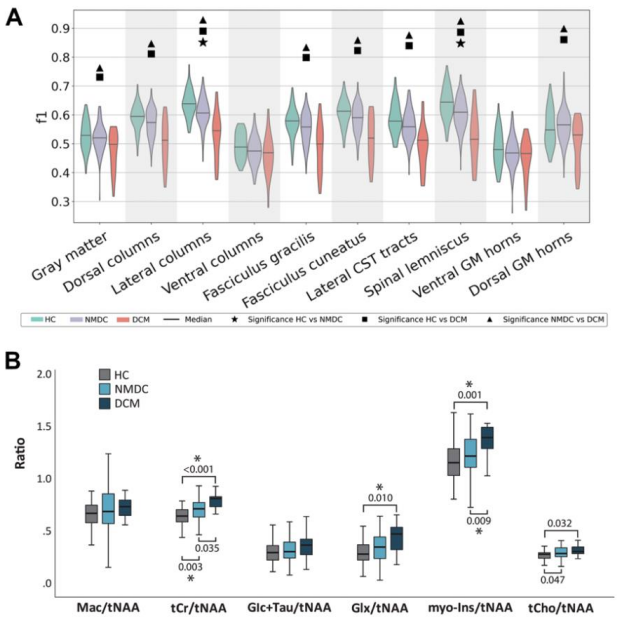

Figure 3. Group differences between NMDC and DCM patients, relative to healthy controls (HC). (**A**) Between-group differences in the f1 diffusion metric (i.e., primary partial volume fraction of the ball-and-sticks model) at C3, above the compression level. Adapted with permission from Ref. [5] under creative common license. (**B**) Between-group difference in neurometabolies ratios, gained from single-voxel magnetic resonance spectroscopy (^{1}H-MRS) from above the compression level

C2/3. Asterisk symbols (*) indicate significant difference between groups. Adapted with permission from Ref. [29] under creative common license.

Two retrospective studies [47,51], utilizing the three-compartment NODDI model [75], alongside DTI, to monitor surgical outcome in DCM patients, showed increased FA at MCL two weeks after surgery and increased intracellular volume fraction at MCL six months after surgery [47,51]. Conclusions indicate that neurite density damage in DCM patients might not be irreversible [47]. A concurrent DTI, NODDI, and DKI study demonstrated lower FA and DKI-FA and a higher DKI-MD, isotropic CSF volume fraction, and orientation dispersion index from the entire axial ROI at MCL in 48 DCM patients, relative to 36 HC [68]. The isotropic CSF volume fraction, FA, and DKI-FA also correlated with the recovery rate, calculated based on preoperative and three-month follow-up mJOA scales, indicating possible usage of these metrics as predictors in surgically-treated DCM patients [68].

So far, all published NODDI [47,51,68], DKI [52,53,68], and QSI [53] studies comprised solely of DCM patients, establishing a further need for the application of innovative dMRI techniques in NMDC patients.

Intravoxel Incoherent Motion Imaging

Intravoxel incoherent motion (IVIM) imaging measures the microscopic movement of water molecules caused by capillary perfusion, using a dMRI sequence with low b-values (≤300 mm^2/s) to assess flowing blood fraction and pseudo-diffusion coefficient [76]. Pilot IVIM studies in the human SC at 7T in 6 HC [77] and at 3T in 2 DCM patients, along with 11 HC [78], depicted higher perfusion in GM, compared to WM in HC, and impaired perfusion in DCM patients at compression levels. However, interpretation is limited, due to the small sample size and possible influence of CSF pulsation [78]. IVIM imaging is a promising technique for future DCM and NMDC studies, as post-mortem studies showed that degenerative compression results in hypoperfusion and ischemia in specific WM/GM regions [1,71].

2.2.2. Magnetization Transfer

Magnetization transfer (MT) imaging is based on the exchange of magnetization between the protons associated with free water and those linked with immobile macromolecules, such as proteins and lipids, and provides MT ratio (MTR) and MT saturation markers, which indirectly measure the myelination [79,80]. Martin et al. [25] reported decreased MTR extracted from the entire axial ROI in 20 NMDC subjects, compared to 20 HC above the compression (C1-C3), but not at MCL. Column-specific MTR analysis corroborated DTI when it demonstrated decreased MTR in ventral columns of NMDC subjects, relative to HC [25]. The same group also reported MTR, together with FA, cross-sectional area, and T2* WM/GM ratio, as useful measures within a composite score for monitoring 26 DCM patients in a 13.5 (mean) month follow-up and identified worsening in 11 DCM patients [35]. Another work then showed the predictive value of a combination of the preoperative MTR and shape analysis for surgery response and recovery in DCM patients [81]. Finally, a combination of MT imaging and dMRI was used to calculate myelin water fraction and axon volume fraction in 24 DCM patients, compared to 5 HC, and the results reported changes in axon volume fraction between groups in the fasciculus gracilis, fasciculus cuneatus, and lateral corticospinal tract [46].

2.2.3. Magnetic Resonance Spectroscopy

Proton magnetic resonance spectroscopy (^{1}H-MRS) quantifies the neurochemical profile within the spectroscopic volume of interest (i.e., spectroscopic voxel) and provides unique information about microstructural or metabolic pathophysiological processes that are inaccessible with conventional imaging methods (Figure 1C) [82,83]. SC ^{1}H-MRS is challenged by its small transversal area, which is further diminished at the compression level. Therefore, ^{1}H-MRS studies in DCM patients assessed the neurochemical profile only

above the stenosis level and observed neurochemical changes rostrally to the compression, likely due to the Wallerian degeneration, which manifested as increased levels of total creatine (tCr)/total NAA (tNAA) [84–87] and total choline (tCho)/tNAA [85,86,88]. A recent ^{1}H-MRS study in 47 HC, 60 NMDC, and 13 DCM patients showed, for the first time, increased tCr/tNAA and myo-Ins/tNAA ratios above the stenosis level in NMDC, relative to HC, pointing to neurochemical changes detectable in clinically silent subjects (Figure 3B) [29]. The high sensitivity of this study arises from superior accuracy in semi-LASER voxel localization [89], improved signal-to-noise ratio at high-field 3T scanner, and cardiac triggering, minimizing bias from surrounding tissue and cardiac pulsations [29].

Despite the degeneration of afferent tracts, which propagated the changes in DCM patients, up to the sensorimotor regions in the brain [8,9], the SC might display earlier alteration of the neurochemical profile and can be a more appropriate target to detect early markers in non-myelopathic compression. Several studies, indeed, suggested a potential predictive value of neurochemical markers when they showed a correlation between the severity of myelopathy symptoms (i.e., mJOA scale) and metabolite ratios [29,85,90].

2.2.4. T1 and T2 Relaxometry

To date, T1 relaxometry, sensitive to myelination [45], provided contradictory outcomes, when it detected lower T1 times in 31 DCM patients at 1.5T at compression levels, compared to non-stenotic counterparts [91], but higher T1 times at 3T at compression levels in 22 DCM patients, compared to 10 HC [92]. Such opposite trends call for further harmonization of field strengths, imaging protocols, and inclusion criteria.

Thus far, 3T myelin water imaging, based on T2 relaxometry, demonstrated myelin content reduction in dorsal columns of 14 DCM patients with pathological somatosensory-evoked potentials [93], and the multicomponent-driven equilibrium steady-state estimation of myelin water fraction, as well as T1 and T2 times, provided a myelin imaging atlas of HC and setup framework for future studies [94].

2.2.5. Functional MRI

Functional MRI (fMRI) measures the oscillations in neuronal activity by either a T2*-w sequence, sensitive to local magnetic field inhomogeneities related to blood oxygenation level-dependent effect, or arterial spin labeling sequences that utilize arterial blood as an endogenous tracer to measure cerebral blood flow [95]. Brain fMRI studies, indeed, revealed: remote changes in the activations of motor areas during finger-tapping tasks between DCM patients and HC [9,96], alterations of the sensorimotor network in resting-state fMRI in DCM patients [97], the relationship between severity of compression in DCM patients and activation volume in the motor cortex [98], and differences in brain activations in DCM patients with abnormal motor evoked potentials [99], suggesting that DSCC causes secondary brain changes. A single SC resting-state fMRI study showed neuronal activity changes in the GM horns of 18 DCM patients, relative to 25 HC, as well as an association of severity of myelopathy with neuronal activity response [100]. To date, no SC fMRI study has been performed in NMDC patients [101], further emphasizing the need to overcome the anatomy-related image distortions, low signal-to-noise ratio, and physiological movement artifacts [102], which limited fMRI use in patients with DSCC.

2.2.6. Perfusion Weighted Imaging

Chronic DSCC reduces blood flow in spinal arteries and results in chronic SC ischemia in histological and animal models [1,71], which is a vital factor in DCM pathogenesis. While perfusion imaging methods, including dynamic susceptibility contrast (DSC), dynamic contrast-enhanced (DCE), and arterial spin labeling perfusion imaging, are commonly used in brain studies, there have been sparse applications in the SC [103–105]. A recent 3T study, in 22 DSCC patients with or without myelopathy, identified a significant relationship ($p < 0.05$) of DSC markers with the anteroposterior diameter and mJOA scale

and suggested that the degree of ischemia and hypoxia correlates with compression severity and clinical status, respectively [103]. Another 1.5T DSC study, in 14 DCM patients, then showed improvement in the spinal perfusion after surgical decompression [104] and pseudo-continuous arterial spin labeling, which, unlike DSC and DCE, does not require an intravenous contrast agent, revealed secondary alteration of cerebral blood flow perfusion in DCM patients [105].

2.3. Spinal Cord MRI Data Acquisition and Processing

The SC is a small structure with anteroposterior and transverse diameters at the C2 level of 8.8 and 12.4 mm, respectively [106], which is placed in a bony spinal canal, surrounded by CSF, with variability in the magnetic susceptibilities. Thus, optimized acquisition protocols and dedicated analysis tools are required for accurate and reliable processing [79]. This need is further highlighted in patients with DSCC with altered anatomy.

2.3.1. Data Acquisition

Sequences with sufficient in-plane resolution, signal-to-noise ratio, and clinically acceptable acquisition times of complete examination (under 30–40 min) are crucial for tissue-specific analysis. Generally, anisotropic resolution, on the order of $1 \times 1 \times 5$ mm^3, is recommended for dMRI and MT sequences, since the SC is a relatively homogenous structure in the superior-inferior direction, and higher slice thickness allows us to increase the signal-to-noise ratio and in-plane resolution [79,107]. Recently, the SC community released a prospectively harmonized *spine generic* acquisition protocol for 3T and 1.5T [107], allowing for multi-center studies [108]. Although higher field strength provides superior spatial resolution and signal-to-noise ratio, it introduces larger susceptibility artifacts and geometrical distortions, especially for dMRI sequences. Generally, dMRI sequences with reduced field-of-view are recommended over sequences with outer volume suppression to mitigate these artifacts [27,107,109]. Cardiac triggering might reduce pulsatile CSF flow and partial volume effect in dMRI [107,110] as well as ^{1}H-MRS [29]. The acquisition of two dMRI sequences, with opposite phase-coding and usage of dedicated post-processing tools for correction of motion artifacts and geometrical distortions [111,112], were used across SC studies, even though these tools were primarily designed for the brain, and their usage for the SC is the subject of ongoing debate (https://forum.spinalcordmri.org/t/how-to-correct-for-distortions-in-spinal-cord-diffusion-mri-data/326, accessed January 15, 2022). An increased signal-to-noise ratio of the 3T dMRI sequences also allows for acquiring multi-shell diffusion data with higher b-values, which is crucial for the fitting of multi-compartment diffusion models, such as NODDI, ball-and-sticks, or DKI [107]. Usually, high angular resolution diffusion imaging [113] sequences are employed, utilizing diffusion gradient sampling on several whole q-space spheres (i.e., multi-shell diffusion protocols) [114] and allowing for reliable estimation of the higher-order models.

The ^{1}H-MRS sensitivity benefits from ultra-high fields [115,116], implementation of advanced shimming approaches minimizing anatomically determined pronounced B_0-inhomogenety in the spinal canal [117], and prospective motion correction methods alleviating motion artifacts pronounced during longer acquisitions [118]. In addition, the automatization of ^{1}H-MRS data acquisition, including automatic voxel placement, allows for shortening the scan and obtaining operator-independent data with the methodology previously implemented for the brain [119].

2.3.2. Spinal Cord Data Processing

Analyses of the entire axial ROI in older NMDC works [21,23,24,26], which lack spatial resolution and did not allow for tracing the spatial origin of the observed microstructural changes, were overcome, thanks to probabilistic PAM50 atlas [41,120] and methods for minimizing of partial volume effect [41,121]. Atlas-based analysis was successfully used in several recent studies and revealed tissue-specific changes in both DCM and NMDC

patients, as well as in patients with traumatic SC injury [5,25,65]. Alternative approaches for tract delineation are tractography [63,64,122], manually drawn ROIs [61,62,66], or the usage of tract-based spatial statistics (TBSS) approach [123]. However, tractography can suffer from inaccuracies caused by severe compression, and manually-defined ROIs are prone to user bias and take time to draw; thus, atlas-based approach is currently preferred [45,79].

The advent of the Spinal Cord Toolbox (SCT) [121] now allows for robust automatic segmentation of the SC and GM [124,125] and the processing of structural and qMRI images, as well as utilizing the probabilistic template and PAM50 atlas [41,120]. Alternative packages, such as FMRIB Software Library (FSL) [126], Statistical Parametric Mapping (SPM) software package [127], or JIM (http://www.xinapse.com, accessed January 15, 2022), designed for brain analysis or dedicated libraries, such as Dipy [128] or LCmodel [129], for dMRI and MRS analysis, respectively, can also be used for SC data processing. Usually, a combination of tools is used to facilitate multimodal qMRI analysis; for example, SCT is utilized for automatic SC and GM segmentations, morphometric metrics extraction, and registration of PAM50 atlas, and it is supplemented by FSL or Dipy, which provide tools for fMRI analysis and the estimation of higher-order diffusion models. Note that anatomy altered by compression can negatively influence image acquisition and data processing, and it is, thus, necessary to perform quality checks, potential manual correction of segmentation, and adjustment of processing parameters (e.g., type of registration). Typical dMRI workflow is summarized in Figure 4.

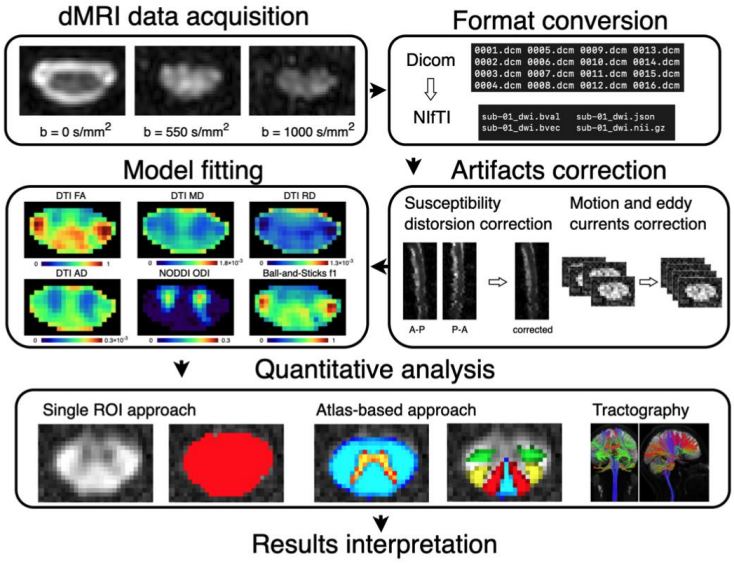

Figure 4. Typical dMRI workflow. dMRI data acquisition is followed by format conversion, usually from DICOM format, provided by the scanner, to NIfTI format [130], which is supported by many of neuroimaging tools. The subsequent processing pipeline typically includes correction of susceptibility-induced geometrical distortions, motion and eddy currents artifacts, and estimation of diffusion model(s). Final quantitative analysis can be done in various ways using a single region-of-interest (ROI) approach, atlas-based approach, or tractography. DTI, diffusion tensor imaging; FA, fractional anisotropy; MD, mean diffusivity; RD, radial diffusivity; AD, axial diffusivity; NODDI, neurite orientation dispersion and density imaging; ODI, orientation dispersion index; f1, primary partial volume fraction (anisotropic compartment of the ball-and-sticks model). The illustration of the tractography is reprinted with permission from Ref. [79]. Copyright, 2014, Elsevier.

2.4. Quantitative MRI in the Spinal Cord Compression and Correlations with Clinical Outcomes

A proper estimation of the relationship between qMRI markers and clinical status, assessed by mJOA scale [131] or electrophysiological measurements, is needed to gain insight into the clinical relevance of qMRI markers, prior to multicentric longitudinal trials. dMRI studies in DCM patients consistently reported significant correlations between the mJOA scale and FA ($r > 0.45$) [5,24] and MD ($r = -0.32$) [24], while MRS studies disclosed significant correlations between the mJOA scale and myo-Ins/tNAA ($r = -0.67$) [29], Cho/NAA ($r > -0.44$) [85,88], and NAA/Cr ($r = 0.50$) [85]. Nevertheless, the usage of the mJOA scale in NMDC patients is limited, since these patients are usually asymptomatic and, thus, without clinical deficits. T2-w signal intensity changes, electrophysiological abnormalities, and signs of radiculopathy were reported as predictors of progression from NMDC into DCM [3]; however, the subsequent studies did not find any association with DTI extracted from the entire axial SC ROI [21,26]. While Kadanka et al. [21], indeed, did not detect any significant difference in DTI markers from the entire axial SC in NMDC patients with and without electrophysiological abnormality, recent tissue-specific reports demonstrated a relationship between altered electrophysiology and DTI and ball-and-sticks metrics in both NMDC and DCM patients [5,60]. Diffusion metrics in the lateral motor and dorsal sensory tracts corresponded to alterations in motor and somatosensory-evoked potentials, and electromyography corresponded to diffusion metrics in GM [5,60]. Finally, Liu et al. [93] found a correlation between the decrease of myelin content in dorsal columns assessed by myelin water imaging and prolonged cortical somatosensory-evoked potential latencies in DCM patients.

3. Conclusions and Future Directions

While previous studies confirmed the SC microstructure alterations detected by qMRI in both NMDC and DCM patients, relative to HC, the results showed inconsistencies, due to distinctions in scanners' field strength, acquisition protocols, and data post-processing. Additionally, unification of the inclusion criteria is particularly needed for NMDC individuals, as some studies include only those without radiculopathy [25], while others also incorporated NMDC subjects with radiculopathy [5,21,23].

To date, DTI studies at 1.5T and 3T consistently detected lower FA and higher MD at MCL in NMDC and DCM patients, relative to HC, with more progressive changes in DCM, compared to NMDC. These changes are likely caused by edema, deficits in the degree of myelination, axonal packing, and axon size. Some also found RD and MTR abnormalities pointing to demyelination [5,25,72] and AD alteration, due to axonal injury, as the primary alteration at MCL [5]. Rostral secondary changes in DCM patients presented as lower FA and higher diffusivity measures in dorsal columns and lateral corticospinal tracts, and alterations in ^{1}H-MRS ratios at the C2/3 level point to remote Wallerian degeneration above the compression level [5,29,36,37,39,40,65,88,132], accompanied by the SC, WM, and GM volumes reduction [5,29,36–40]. Subtle remote changes at the C2/3 level between NMDC and HC were unraveled by the multi-compartment ball-and-sticks diffusion model, ^{1}H-MRS, and MTR [5,25,29]. Moreover, brain fMRI and ^{1}H-MRS studies in DCM patients showed secondary changes, even in the brain, suggesting alterations in neuronal activations and brain plasticity caused by DSCC [8,9]. Existing studies also showed the relationship between clinical impairments, assessed by clinical scales and microstructural degeneration, measured using qMRI [5,24,29,62,85,88]. Several works also provided evidence of the relationship between functional impairments, measured using electrophysiology and tract-specific qMRI metrics [5,60,93].

The widespread availability of 3T scanners in the clinical practice also further emphasizes the need to harmonize protocols across scanners and vendors, in order to estimate normative values, which was, so far, limited by the usage of different sequences and acquisition parameters. Indeed, the release of the *spine generic* acquisition protocol [107] provided a critical step forward for the upcoming longitudinal multicentric studies, with the promise of normative quantitative values. The 3T protocols, which minimize image artifacts, while benefitting from increased signal-to-noise ratio, compared to lower fields,

are essential for methods such as dMRI and ^{1}H-MRS [79]. High in-plane resolution of recent dMRI and MT sequences [5,25,40,110] allowed for tissue- and tract-specific analysis. Lastly, pilot studies at 7T showed promising results for future research that might further increase our understanding of metabolic and microstructural damage, yet the utilization will require further sequence development and usage of dedicated coils.

In conclusion, while high-resolution 3T qMRI, with tissue- and tract-specific analysis, supplemented by electrophysiological measures and clinical scales, indeed showed ongoing microstructure alterations, even in NMDC patients, longitudinal and multicentric studies with optimized protocols are critical for future NMDC research. The application of qMRI, as a potential predictor of progression from NMDC to clinically manifested DCM, must be further verified by an estimation of the normative values for clinical practice; however, such a goal requires the harmonization of SC protocols across scanners and vendors.

Author Contributions: Conceptualization, J.V., P.B., J.B., and A.S.; writing—original draft preparation, J.V. and A.S.; writing—review and editing, J.V., P.B., M.K., P.H., J.B., and A.S.; visualization, J.V., P.B., and A.S.; supervision, P.B., M.K., P.H., J.B., and A.S.; funding acquisition, P.H. and J.B. All authors have read and agreed to the published version of the manuscript.

Funding: This research was funded by the Czech Health Research Council (grants NV18-04-00159 and NU22-04-00024) and Palacký University Olomouc (grant IGA_LF_2022_015). Supported by Ministry of Health, Czech Republic – conceptual development of research organizations (FNOl, 00098892) and (FNBr, 65269705). The core facility Multimodal and Functional Imaging Laboratory, Masaryk University, CEITEC, supported by the MEYS CR (LM2018129 Czech-BioImaging), is acknowledged. JV has received the "Aktion Österreich-Tschechien, AÖCZ-Semesterstipendien" scholarship (MPC-2020-00013) from the Austrian Agency for International Cooperation in Education and Research (OeAD-GmbH), Mobility Programmes, Bilateral and Multilateral Cooperation (MPC), financed by the Federal Ministry of Education, Science and Research (BMBWF) of Austria. AS has received funding from the European Union's Horizon 2020 research and innovation programme, under the Marie Skłodowska-Curie grant (agreement no. 794986).

Institutional Review Board Statement: Not applicable.

Informed Consent Statement: Not applicable.

Data Availability Statement: Not applicable.

Acknowledgements: We thank Eva Vlčková, from University Hospital Brno, for her rigorous revisions of the text and for providing valuable advice.

Conflicts of Interest: The authors declare no conflict of interest.

References

1. Badhiwala, J.H.; Ahuja, C.S.; Akbar, M.A.; Witiw, C.D.; Nassiri, F.; Furlan, J.C.; Curt, A.; Wilson, J.R.; Fehlings, M.G. Degenerative cervical myelopathy—Update and future directions. *Nat. Rev. Neurol.* **2020**, *16*, 108–124. https://doi.org/10.1038/s41582-019-0303-0.
2. Bednarik, J.; Kadanka, Z.; Dusek, L.; Novotny, O.; Surelova, D.; Urbanek, I.; Prokes, B. Presymptomatic spondylotic cervical cord compression. *Spine* **2004**, *29*, 2260–2269. https://doi.org/10.1097/01.brs.0000142434.02579.84.
3. Bednarik, J.; Kadanka, Z.; Dusek, L.; Kerkovsky, M.; Vohanka, S.; Novotny, O.; Urbanek, I.; Kratochvilova, D. Presymptomatic spondylotic cervical myelopathy: An updated predictive model. *Eur. Spine J.* **2008**, *17*, 421–431. https://doi.org/10.1007/s00586-008-0585-1.
4. Fehlings, M.G.; Tetreault, L.A.; Riew, K.D.; Middleton, J.W.; Aarabi, B.; Arnold, P.M.; Brodke, D.S.; Burns, A.S.; Carette, S.; Chen, R.; et al. A Clinical Practice Guideline for the Management of Patients with Degenerative Cervical Myelopathy: Recommendations for Patients with Mild, Moderate, and Severe Disease and Nonmyelopathic Patients with Evidence of Cord Compression. *Glob. Spine J.* **2017**, *7*, 70S–83S. https://doi.org/10.1177/2192568217701914.
5. Valošek, J.; Labounek, R.; Horák, T.; Horáková, M.; Bednařík, P.; Keřkovský, M.; Kočica, J.; Rohan, T.; Lenglet, C.; Cohen-Adad, J.; et al. Diffusion magnetic resonance imaging reveals tract-specific microstructural correlates of electrophysiological impairments in non-myelopathic and myelopathic spinal cord compression. *Eur. J. Neurol.* **2021**, *28*, 3784–3797. https://doi.org/10.1111/ene.15027.
6. Kovalova, I.; Kerkovsky, M.; Kadanka, Z.; Kadanka, Z.; Nemec, M.; Jurova, B.; Dusek, L.; Jarkovsky, J.; Bednarik, J. Prevalence and imaging characteristics of nonmyelopathic and myelopathic spondylotic cervical cord compression. *Spine* **2016**, *41*, 1908–1916. https://doi.org/10.1097/BRS.0000000000001842.
7. David, G.; Mohammadi, S.; Martin, A.R.; Cohen-Adad, J.; Weiskopf, N.; Thompson, A.; Freund, P. Traumatic and nontraumatic spinal cord injury: Pathological insights from neuroimaging. *Nat. Rev. Neurol.* **2019**, *15*, 718–731. https://doi.org/10.1038/s41582-

019-0270-5.
8. Kowalczyk, I.; Duggal, N.; Bartha, R. Proton magnetic resonance spectroscopy of the motor cortex in cervical myelopathy. *Brain* **2012**, *135*, 461–468. https://doi.org/10.1093/brain/awr328.
9. Bernabéu-Sanz, Á.; Mollá-Torró, J.V.; López-Celada, S.; Moreno López, P.; Fernández-Jover, E. MRI evidence of brain atrophy, white matter damage, and functional adaptive changes in patients with cervical spondylosis and prolonged spinal cord compression. *Eur. Radiol.* **2020**, *30*, 357–369. https://doi.org/10.1007/s00330-019-06352-z.
10. Smith, S.S.; Stewart, M.E.; Davies, B.M.; Kotter, M.R.N. The Prevalence of Asymptomatic and Symptomatic Spinal Cord Compression on Magnetic Resonance Imaging: A Systematic Review and Meta-analysis. *Glob. Spine J.* **2021**, *11*, 597–607. https://doi.org/10.1177/2192568220934496.
11. Witiw, C.D.; Mathieu, F.; Nouri, A.; Fehlings, M.G. Clinico-Radiographic Discordance: An Evidence-Based Commentary on the Management of Degenerative Cervical Spinal Cord Compression in the Absence of Symptoms or With Only Mild Symptoms of Myelopathy. *Glob. Spine J.* **2018**, *8*, 527–534. https://doi.org/10.1177/2192568217745519.
12. Wilson, J.R.; Barry, S.; Fischer, D.J.; Skelly, A.C.; Arnold, P.M.; Riew, K.D.; Shaffrey, C.I.; Traynelis, V.C.; Fehlings, M.G. Frequency, Timing, and Predictors of Neurological Dysfunction in the Nonmyelopathic Patient with Cervical Spinal Cord Compression, Canal Stenosis, and/or Ossification of the Posterior Longitudinal Ligament. *Spine* **2013**, *38*, S37–S54. https://doi.org/10.1097/BRS.0b013e3182a7f2e7.
13. WFNS Cervical Spondylotic Myelopathy. Available online: http://wfns-spine.org/recom-cervical-spondylotic-myelopathy-1 (accessed on January 15, 2022).
14. Oh, T.; Lafage, R.; Lafage, V.; Protopsaltis, T.; Challier, V.; Shaffrey, C.; Kim, H.J.; Arnold, P.; Chapman, J.; Schwab, F.; et al. Comparing Quality of Life in Cervical Spondylotic Myelopathy with Other Chronic Debilitating Diseases Using the Short Form Survey 36-Health Survey. *World Neurosurg.* **2017**, *106*, 699–706. https://doi.org/10.1016/j.wneu.2016.12.124.
15. Baptiste, D.C.; Fehlings, M.G. Pathophysiology of cervical myelopathy. *Spine J.* **2006**, *6*, 190–197. https://doi.org/10.1016/j.spinee.2006.04.024.
16. Akter, F.; Yu, X.; Qin, X.; Yao, S.; Nikrouz, P.; Syed, Y.A.; Kotter, M. The Pathophysiology of Degenerative Cervical Myelopathy and the Physiology of Recovery Following Decompression. *Front. Neurosci.* **2020**, *14*, 138. https://doi.org/10.3389/fnins.2020.00138.
17. Akter, F.; Kotter, M. Pathobiology of Degenerative Cervical Myelopathy. *Neurosurg. Clin. N. Am.* **2018**, *29*, 13–19. https://doi.org/10.1016/j.nec.2017.09.015.
18. Tu, J.; Vargas Castillo, J.; Das, A.; Diwan, A.D. Degenerative Cervical Myelopathy: Insights into Its Pathobiology and Molecular Mechanisms. *J. Clin. Med.* **2021**, *10*, 1214. https://doi.org/10.3390/jcm10061214.
19. Guan, X.; Fan, G.; Wu, X.; Gu, G.; Gu, X.; Zhang, H.; He, S. Diffusion Tensor Imaging Studies of Cervical Spondylotic Myelopathy: A Systemic Review and Meta-Analysis. *PLoS ONE* **2015**, *10*, e0117707. https://doi.org/10.1371/journal.pone.0117707.
20. Ellingson, B.M.; Salamon, N.; Holly, L.T. Advances in MR imaging for cervical spondylotic myelopathy. *Eur. Spine J.* **2015**, *24*, 197–208. https://doi.org/10.1007/s00586-013-2915-1.
21. Kerkovský, M.; Bednaník, J.; Dušek, L.; Šprláková-Puková, A.; Urbánek, I.; Mechl, M.; Válek, V.; Kadanka, Z. Magnetic Resonance Diffusion Tensor Imaging in Patients with Cervical Spondylotic Spinal Cord Compression. *Spine* **2012**, *37*, 48–56. https://doi.org/10.1097/BRS.0b013e31820e6c35.
22. Adamova, B.; Bednarik, J.; Andrasinova, T.; Kovalova, I.; Kopacik, R.; Jabornik, M.; Kerkovsky, M.; Jakubcova, B.; Jarkovsky, J. Does lumbar spinal stenosis increase the risk of spondylotic cervical spinal cord compression? *Eur. Spine J.* **2015**, *24*, 2946–2953. https://doi.org/10.1007/s00586-015-4049-0.
23. Keřkovský, M.; Bednařík, J.; Jurová, B.; Dušek, L.; Kadaňka, Z.; Kadaňka, Z.; Němec, M.; Kovaľová, I.; Šprláková-Puková, A.; Mechl, M. Spinal Cord MR Diffusion Properties in Patients with Degenerative Cervical Cord Compression. *J. Neuroimaging* **2017**, *27*, 149–157. https://doi.org/10.1111/jon.12372.
24. Ellingson, B.M.; Salamon, N.; Woodworth, D.C.; Yokota, H.; Holly, L.T. Reproducibility, temporal stability, and functional correlation of diffusion MR measurements within the spinal cord in patients with asymptomatic cervical stenosis or cervical myelopathy. *J. Neurosurg. Spine* **2018**, *28*, 472–480. https://doi.org/10.3171/2017.7.SPINE176.
25. Martin, A.R.; De Leener, B.; Cohen-Adad, J.; Cadotte, D.W.; Nouri, A.; Wilson, J.R.; Tetreault, L.; Crawley, A.P.; Mikulis, D.J.; Ginsberg, H.; et al. Can microstructural MRI detect subclinical tissue injury in subjects with asymptomatic cervical spinal cord compression? A prospective cohort study. *BMJ Open* **2018**, *8*, e019809. https://doi.org/10.1136/bmjopen-2017-019809.
26. Kadanka, Z.; Adamova, B.; Kerkovsky, M.; Kadanka, Z.; Dusek, L.; Jurova, B.; Vlckova, E.; Bednarik, J. Predictors of symptomatic myelopathy in degenerative cervical spinal cord compression. *Brain Behav.* **2017**, *7*, e00797. https://doi.org/10.1002/brb3.797.
27. Labounek, R.; Valošek, J.; Horák, T.; Svátková, A.; Bednařík, P.; Vojtíšek, L.; Horáková, M.; Nestrašil, I.; Lenglet, C.; Cohen-Adad, J.; et al. HARDI-ZOOMit protocol improves specificity to microstructural changes in presymptomatic myelopathy. *Sci. Rep.* **2020**, *10*, 17529. https://doi.org/10.1038/s41598-020-70297-3.
28. Kadanka, Z.; Kadanka, Z.; Skutil, T.; Vlckova, E.; Bednarik, J. Walk and Run Test in Patients with Degenerative Compression of the Cervical Spinal Cord. *J. Clin. Med.* **2021**, *10*, 927. https://doi.org/10.3390/jcm10050927.
29. Horak, T.; Horakova, M.; Svatkova, A.; Kadanka, Z.; Kudlicka, P.; Valosek, J.; Rohan, T.; Kerkovsky, M.; Vlckova, E.; Kadanka, Z.; et al. In vivo Molecular Signatures of Cervical Spinal Cord Pathology in Degenerative Compression. *J. Neurotrauma* **2021**, *38*, 2999–3010. https://doi.org/10.1089/neu.2021.0151.

30. Horáková, M.; Horák, T.; Valoš̌ek, J.; Rohan, T.; Koriťáková, E.; Dostál, M.; Koč̌ica, J.; Skutil, T.; Keřkovský, M.; Kadaňka Jr, Z.; et al. Semi-automated detection of cervical spinal cord compression with the Spinal Cord Toolbox. *Quant. Imaging Med. Surg.* **2022**, *12*, 2261–2279. https://doi.org/10.21037/qims-21-782.
31. Nouri, A.; Martin, A.R.; Kato, S.; Reihani-Kermani, H.; Riehm, L.E.; Fehlings, M.G. The Relationship between MRI Signal Intensity Changes, Clinical Presentation, and Surgical Outcome in Degenerative Cervical Myelopathy. *Spine* **2017**, *42*, 1851–1858. https://doi.org/10.1097/BRS.0000000000002234.
32. Martin, A.R.; Tetreault, L.; Nouri, A.; Curt, A.; Freund, P.; Rahimi-Movaghar, V.; Wilson, J.R.; Fehlings, M.G.; Kwon, B.K.; Harrop, J.S.; et al. Imaging and Electrophysiology for Degenerative Cervical Myelopathy [AO Spine RECODE-DCM Research Priority Number 9]. *Glob. Spine J.* **2022**, *12*, 130S–146S. https://doi.org/10.1177/21925682211057484.
33. Nouri, A.; Martin, A.R.; Mikulis, D.; Fehlings, M.G. Magnetic resonance imaging assessment of degenerative cervical myelopathy: A review of structural changes and measurement techniques. *Neurosurg. Focus* **2016**, *40*, E5. https://doi.org/10.3171/2016.3.FOCUS1667.
34. Kato, F.; Yukawa, Y.; Suda, K.; Yamagata, M.; Ueta, T. Normal morphology, age-related changes and abnormal findings of the cervical spine. Part II: Magnetic resonance imaging of over 1200 asymptomatic subjects. *Eur. Spine J.* **2012**, *21*, 1499–1507. https://doi.org/10.1007/s00586-012-2176-4.
35. Martin, A.R.; De Leener, B.; Cohen-Adad, J.; Kalsi-Ryan, S.; Cadotte, D.W.; Wilson, J.R.; Tetreault, L.; Nouri, A.; Crawley, A.; Mikulis, D.J.; et al. Monitoring for myelopathic progression with multiparametric quantitative MRI. *PLoS ONE* **2018**, *13*, e0195733. https://doi.org/10.1371/journal.pone.0195733.
36. Grabher, P.; Mohammadi, S.; David, G.; Freund, P. Neurodegeneration in the Spinal Ventral Horn Prior to Motor Impairment in Cervical Spondylotic Myelopathy. *J. Neurotrauma* **2017**, *34*, 2329–2334. https://doi.org/10.1089/neu.2017.4980.
37. Grabher, P.; Mohammadi, S.; Trachsler, A.; Friedl, S.; David, G.; Sutter, R.; Weiskopf, N.; Thompson, A.J.; Curt, A.; Freund, P. Voxel-based analysis of grey and white matter degeneration in cervical spondylotic myelopathy. *Sci. Rep.* **2016**, *6*, 24636. https://doi.org/10.1038/srep24636.
38. Valošek, J.; Bednařík, P.; Horák, T.; Horáková, M.; Svátková, A.; Labounek, R.; Hluštík, P.; Bednařík, J. Cervical Spinal Cord Atrophy Above Level of Asymptomatic Degenerative Cervical Cord Compression. In Proceedings of the 26th Annual Meeting of the Organization for Human Brain Mapping; Virtual, 2020; p. 3136.
39. Vallotton, K.; David, G.; Hupp, M.; Pfender, N.; Cohen-Adad, J.; Fehlings, M.G.; Samson, R.S.; Wheeler-Kingshott, C.A.M.G.; Curt, A.; Freund, P.; et al. Tracking White and Gray Matter Degeneration along the Spinal Cord Axis in Degenerative Cervical Myelopathy. *J. Neurotrauma* **2021**, *38*, 2978–2987. https://doi.org/10.1089/neu.2021.0148.
40. David, G.; Vallotton, K.; Hupp, M.; Curt, A.; Freund, P.; Seif, M. Extent of Cord Pathology in the Lumbosacral Enlargement in Non-Traumatic versus Traumatic Spinal Cord Injury. *J. Neurotrauma* **2022**. https://doi.org/10.1089/neu.2021.0389.
41. Lévy, S.; Benhamou, M.; Naaman, C.; Rainville, P.; Callot, V.; Cohen-Adad, J. White matter atlas of the human spinal cord with estimation of partial volume effect. *Neuroimage* **2015**, *119*, 262–271. https://doi.org/10.1016/j.neuroimage.2015.06.040.
42. Johansen-Berg, H.; Behrens, T.E.J. *Diffusion MRI: From Quantitative Measurement to In Vivo Neuroanatomy*, 2nd ed.; Elsevier Science: Amsterdam, The Netherlands, 2013; ISBN 9780123964601.
43. Martin, A.R.; Aleksanderek, I.; Cohen-Adad, J.; Tarmohamed, Z.; Tetreault, L.; Smith, N.; Cadotte, D.W.; Crawley, A.; Ginsberg, H.; Mikulis, D.J.; et al. Translating state-of-the-art spinal cord MRI techniques to clinical use: A systematic review of clinical studies utilizing DTI, MT, MWF, MRS, and fMRI. *NeuroImage Clin.* **2016**, *10*, 192–238. https://doi.org/10.1016/j.nicl.2015.11.019.
44. Mori, S.; Tournier, J.-D. *Introduction to Diffusion Tensor Imaging: And Higher Order Models*, 2nd ed.; Academic Press: Amsterdam, The Netherlands, 2014; ISBN 978-0123983985.
45. Cohen-Adad, J. Microstructural imaging in the spinal cord and validation strategies. *Neuroimage* **2018**, *182*, 169–183. https://doi.org/10.1016/j.neuroimage.2018.04.009.
46. Hori, M.; Hagiwara, A.; Fukunaga, I.; Ueda, R.; Kamiya, K.; Suzuki, Y.; Liu, W.; Murata, K.; Takamura, T.; Hamasaki, N.; et al. Application of Quantitative Microstructural MR Imaging with Atlas-based Analysis for the Spinal Cord in Cervical Spondylotic Myelopathy. *Sci. Rep.* **2018**, *8*, 5213. https://doi.org/10.1038/s41598-018-23527-8.
47. Iwama, T.; Ohba, T.; Okita, G.; Ebata, S.; Ueda, R.; Motosugi, U.; Onishi, H.; Haro, H.; Hori, M. Utility and validity of neurite orientation dispersion and density imaging with diffusion tensor imaging to quantify the severity of cervical spondylotic myelopathy and assess postoperative neurological recovery. *Spine J.* **2020**, *20*, 417–425. https://doi.org/10.1016/j.spinee.2019.10.019.
48. Grussu, F.; Schneider, T.; Zhang, H.; Alexander, D.C.; Wheeler-Kingshott, C.A.M. Single-shell diffusion MRI NODDI with in vivo cervical cord data. In Proceedings of the ISMRM, Milan, Italy, 10–16 May 2014; Volume 1716.
49. Grussu, F.; Schneider, T.; Zhang, H.; Alexander, D.C.; Wheeler-Kingshott, C.A.M. Neurite orientation dispersion and density imaging of the healthy cervical spinal cord in vivo. *Neuroimage* **2015**, *111*, 590–601. https://doi.org/10.1016/j.neuroimage.2015.01.045.
50. Grussu, F.; Schneider, T.; Tur, C.; Yates, R.L.; Tachrount, M.; Ianus ß, A.; Yiannakas, M.C.; Newcombe, J.; Zhang, H.; Alexander, D.C.; et al. Neurite dispersion: A new marker of multiple sclerosis spinal cord pathology? *Ann. Clin. Transl. Neurol.* **2017**, *4*, 663–679. https://doi.org/10.1002/acn3.445.
51. Okita, G.; Ohba, T.; Takamura, T.; Ebata, S.; Ueda, R.; Onishi, H.; Haro, H.; Hori, M. Application of neurite orientation dispersion and density imaging or diffusion tensor imaging to quantify the severity of cervical spondylotic myelopathy and to assess postoperative neurologic recovery. *Spine J.* **2018**, *18*, 268–275. https://doi.org/10.1016/j.spinee.2017.07.007.
52. Hori, M.; Tsutsumi, S.; Yasumoto, Y.; Ito, M.; Suzuki, M.; Tanaka, F.S.; Kyogoku, S.; Nakamura, M.; Tabuchi, T.; Fukunaga, I.;

et al. Cervical spondylosis: Evaluation of microstructural changes in spinal cord white matter and gray matter by diffusional kurtosis imaging. *Magn. Reson. Imaging* **2014**, *32*, 428–432. https://doi.org/10.1016/j.mri.2014.01.018.
53. Hori, M.; Fukunaga, I.; Masutani, Y.; Nakanishi, A.; Shimoji, K.; Kamagata, K.; Asahi, K.; Hamasaki, N.; Suzuki, Y.; Aoki, S. New diffusion metrics for spondylotic myelopathy at an early clinical stage. *Eur. Radiol.* **2012**, *22*, 1797–1802. https://doi.org/10.1007/s00330-012-2410-9.
54. Lee, J.W.; Kim, J.H.; Park, J.B.; Park, K.W.; Yeom, J.S.; Lee, G.Y.; Kang, H.S. Diffusion tensor imaging and fiber tractography in cervical compressive myelopathy: Preliminary results. *Skeletal Radiol.* **2011**, *40*, 1543–1551. https://doi.org/10.1007/s00256-011-1161-z.
55. Ellingson, B.M.; Salamon, N.; Grinstead, J.W.; Holly, L.T. Diffusion tensor imaging predicts functional impairment in mild-to-moderate cervical spondylotic myelopathy. *Spine J.* **2014**, *14*, 2589–2597. https://doi.org/10.1016/j.spinee.2014.02.027.
56. Wen, C.Y.; Cui, J.L.; Liu, H.S.; Mak, K.C.; Cheung, W.Y.; Luk, K.D.K.; Hu, Y. Is diffusion anisotropy a biomarker for disease severity and surgical prognosis of cervical spondylotic myelopathy. *Radiology* **2014**, *270*, 197–204. https://doi.org/10.1148/radiol.13121885.
57. Jones, J.G.A.; Cen, S.Y.; Lebel, R.M.; Hsieh, P.C.; Law, M. Diffusion tensor imaging correlates with the clinical assessment of disease severity in cervical spondylotic myelopathy and predicts outcome following surgery. *Am. J. Neuroradiol.* **2013**, *34*, 471–478. https://doi.org/10.3174/ajnr.A3199.
58. Uda, T.; Takami, T.; Tsuyuguchi, N.; Sakamoto, S.; Yamagata, T.; Ikeda, H.; Nagata, T.; Ohata, K. Assessment of cervical spondylotic myelopathy using diffusion tensor magnetic resonance imaging parameter at 3.0 tesla. *Spine* **2013**, *38*, 407–414. https://doi.org/10.1097/BRS.0b013e31826f25a3.
59. Banaszek, A.; Bladowska, J.; Szewczyk, P.; Podgórski, P.; Sąsiadek, M. Usefulness of diffusion tensor MR imaging in the assessment of intramedullary changes of the cervical spinal cord in different stages of degenerative spine disease. *Eur. Spine J.* **2014**, *23*, 1523–1530. https://doi.org/10.1007/s00586-014-3323-x.
60. Wen, C.Y.; Cui, J.L.; Mak, K.C.; Luk, K.D.K.; Hu, Y. Diffusion tensor imaging of somatosensory tract in cervical spondylotic myelopathy and its link with electrophysiological evaluation. *Spine J.* **2014**, *14*, 1493–1500. https://doi.org/10.1016/j.spinee.2013.08.052.
61. Maki, S.; Koda, M.; Ota, M.; Oikawa, Y.; Kamiya, K.; Inada, T.; Furuya, T.; Takahashi, K.; Masuda, Y.; Matsumoto, K.; et al. Reduced Field-of-View Diffusion Tensor Imaging of the Spinal Cord Shows Motor Dysfunction of the Lower Extremities in Patients with Cervical Compression Myelopathy. *Spine* **2018**, *43*, 89–96. https://doi.org/10.1097/BRS.0000000000001123.
62. Maki, S.; Koda, M.; Saito, J.; Takahashi, S.; Inada, T.; Kamiya, K.; Ota, M.; Iijima, Y.; Masuda, Y.; Matsumoto, K.; et al. Tract-Specific Diffusion Tensor Imaging Reveals Laterality of Neurological Symptoms in Patients with Cervical Compression Myelopathy. *World Neurosurg.* **2016**, *96*, 184–190. https://doi.org/10.1016/j.wneu.2016.08.129.
63. Cui, J.L.; Li, X.; Chan, T.Y.; Mak, K.C.; Luk, K.D.K.; Hu, Y. Quantitative assessment of column-specific degeneration in cervical spondylotic myelopathy based on diffusion tensor tractography. *Eur. Spine J.* **2015**, *24*, 41–47. https://doi.org/10.1007/s00586-014-3522-5.
64. Budzik, J.F.; Balbi, V.; Le Thuc, V.; Duhamel, A.; Assaker, R.; Cotten, A. Diffusion tensor imaging and fibre tracking in cervical spondylotic myelopathy. *Eur. Radiol.* **2011**, *21*, 426–433. https://doi.org/10.1007/s00330-010-1927-z.
65. Seif, M.; David, G.; Huber, E.; Vallotton, K.; Curt, A.; Freund, P. Cervical Cord Neurodegeneration in Traumatic and Non-Traumatic Spinal Cord Injury. *J. Neurotrauma* **2020**, *37*, 860–867. https://doi.org/10.1089/neu.2019.6694.
66. Wang, K.Y.; Idowu, O.; Thompson, C.B.; Orman, G.; Myers, C.; Riley, L.H.; Carrino, J.A.; Flammang, A.; Gilson, W.; Sadowsky, C.L.; et al. Tract-Specific Diffusion Tensor Imaging in Cervical Spondylotic Myelopathy Before and After Decompressive Spinal Surgery: Preliminary Results. *Clin. Neuroradiol.* **2017**, *27*, 61–69. https://doi.org/10.1007/s00062-015-0418-7.
67. Rajasekaran, S.; Yerramshetty, J.S.; Chittode, V.S.; Kanna, R.M.; Balamurali, G.; Shetty, A.P. The Assessment of Neuronal Status in Normal and Cervical Spondylotic Myelopathy Using Diffusion Tensor Imaging. *Spine* **2014**, *39*, 1183–1189. https://doi.org/10.1097/BRS.0000000000000369.
68. Zhang, M.; Ou-Yang, H.; Liu, J.; Jin, D.; Wang, C.; Zhang, X.; Zhao, Q.; Liu, X.; Liu, Z.; Lang, N.; et al. Utility of Advanced DWI in the Detection of Spinal Cord Microstructural Alterations and Assessment of Neurologic Function in Cervical Spondylotic Myelopathy Patients. *J. Magn. Reson. Imaging* **2022**, *55*, 930–940. https://doi.org/10.1002/jmri.27894.
69. Mamata, H.; Jolesz, F.A.; Maier, S.E. Apparent diffusion coefficient and fractional anisotropy in spinal cord: Age and cervical spondylosis-related changes. *J. Magn. Reson. Imaging* **2005**, *22*, 38–43. https://doi.org/10.1002/jmri.20357.
70. Rao, A.; Soliman, H.; Kaushal, M.; Motovylyak, O.; Vedantam, A.; Budde, M.D.; Schmit, B.; Wang, M.; Kurpad, S.N. Diffusion Tensor Imaging in a Large Longitudinal Series of Patients with Cervical Spondylotic Myelopathy Correlated with Long-Term Functional Outcome. *Neurosurgery* **2018**, *83*, 753–760. https://doi.org/10.1093/neuros/nyx558.
71. Mair, W.G.P.; Druckman, R. The pathology of spinal cord lesions and their relation to the clinical features in protrusion of cervical intervertebral discs (a report of four cases). *Brain* **1953**, *76*, 70–91. https://doi.org/10.1093/brain/76.1.70.
72. Lindberg, P.G.; Sanchez, K.; Ozcan, F.; Rannou, F.; Poiraudeau, S.; Feydy, A.; Maier, M.A. Correlation of force control with regional spinal DTI in patients with cervical spondylosis without signs of spinal cord injury on conventional MRI. *Eur. Radiol.* **2016**, *26*, 733–742. https://doi.org/10.1007/s00330-015-3876-z.
73. Behrens, T.E.J.; Woolrich, M.W.; Jenkinson, M.; Johansen-Berg, H.; Nunes, R.G.; Clare, S.; Matthews, P.M.; Brady, J.M.; Smith, S.M. Characterization and Propagation of Uncertainty in Diffusion-Weighted MR Imaging. *Magn. Reson. Med.* **2003**, *50*, 1077–1088. https://doi.org/10.1002/mrm.10609.
74. Panagiotaki, E.; Schneider, T.; Siow, B.; Hall, M.G.; Lythgoe, M.F.; Alexander, D.C. Compartment models of the diffusion MR signal in brain white matter: A taxonomy and comparison. *Neuroimage* **2012**, *59*, 2241–2254.

https://doi.org/10.1016/j.neuroimage.2011.09.081.
75. Zhang, H.; Schneider, T.; Wheeler-Kingshott, C.A.; Alexander, D.C. NODDI: Practical in vivo neurite orientation dispersion and density imaging of the human brain. *Neuroimage* **2012**, *61*, 1000–1016. https://doi.org/10.1016/j.neuroimage.2012.03.072.
76. Le Bihan, D. What can we see with IVIM MRI? *Neuroimage* **2019**, *187*, 56–67. https://doi.org/10.1016/j.neuroimage.2017.12.062.
77. Lévy, S.; Rapacchi, S.; Massire, A.; Troalen, T.; Feiweier, T.; Guye, M.; Callot, V. Intravoxel Incoherent Motion at 7 Tesla to quantify human spinal cord perfusion: Limitations and promises. *Magn. Reson. Med.* **2020**, *84*, 1198–1217. https://doi.org/10.1002/mrm.28195.
78. Lévy, S.; Freund, P.; Callot, V.; Seif, M. Spinal cord perfusion mapping using Intra-Voxel Incoherent Motion at 3T in healthy individuals and Degenerative Cervical Myelopathy patients. In Proceedings of the 29th Annual Meeting ISMRM; Virtual 15–20 May 2021; p. 3462.
79. Cohen-Adad, J.; Wheeler-Kingshott, C. *Quantitative MRI of the Spinal Cord*; Elsevier: Amsterdam, The Netherlands, 2014; ISBN 9780123969736.
80. Schmierer, K.; Scaravilli, F.; Altmann, D.R.; Barker, G.J.; Miller, D.H. Magnetization transfer ratio and myelin in postmortem multiple sclerosis brain. *Ann. Neurol.* **2004**, *56*, 407–415. https://doi.org/10.1002/ana.20202.
81. Paliwal, M.; Weber, K.A.; Hopkins, B.S.; Cantrell, D.R.; Hoggarth, M.A.; Elliott, J.M.; Dahdaleh, N.S.; Mackey, S.; Parrish, T.D.; Dhaher, Y.; et al. Magnetization Transfer Ratio and Morphometrics of the Spinal Cord Associates with Surgical Recovery in Patients with Degenerative Cervical Myelopathy. *World Neurosurg.* **2020**, *144*, e939–e947. https://doi.org/10.1016/j.wneu.2020.09.148.
82. Öz, G.; Alger, J.R.; Barker, P.B.; Bartha, R.; Bizzi, A.; Boesch, C.; Bolan, P.J.; Brindle, K.M.; Cudalbu, C.; Dinçer, A.; et al. Clinical Proton MR Spectroscopy in Central Nervous System Disorders. *Radiology* **2014**, *270*, 658–679. https://doi.org/10.1148/radiol.13130531.
83. Öz, G. Imaging Neurodegeneration: What Can Magnetic Resonance Spectroscopy Contribute? In *Contemporary Clinical Neuroscience*; Springer: Cham, Switzerland, 2016; pp. 1–11.
84. Aleksanderek, I.; McGregor, S.M.K.; Stevens, T.K.; Goncalves, S.; Bartha, R.; Duggal, N. Cervical spondylotic myelopathy: Metabolite changes in the primary motor cortex after surgery. *Radiology* **2017**, *282*, 817–825. https://doi.org/10.1148/radiol.2016152083.
85. Holly, L.T.; Ellingson, B.M.; Salamon, N. Metabolic imaging using proton magnetic spectroscopy as a predictor of outcome after surgery for cervical spondylotic myelopathy. *Clin. Spine Surg.* **2017**, *30*, E615–E619. https://doi.org/10.1097/BSD.0000000000000248.
86. Ellingson, B.M.; Salamon, N.; Hardy, A.J.; Holly, L.T. Prediction of neurological impairment in cervical spondylotic myelopathy using a combination of diffusion mri and proton mr spectroscopy. *PLoS ONE* **2015**, *10*, e0139451. https://doi.org/10.1371/journal.pone.0139451.
87. Aleksanderek, I.; Stevens, T.K.; Goncalves, S.; Bartha, R.; Duggal, N. Metabolite and functional profile of patients with cervical spondylotic myelopathy. *J. Neurosurg. Spine* **2017**, *26*, 547–553. https://doi.org/10.3171/2016.9.SPINE151507.
88. Salamon, N.; Ellingson, B.M.; Nagarajan, R.; Gebara, N.; Thomas, A.; Holly, L.T. Proton magnetic resonance spectroscopy of human cervical spondylosis at 3T. *Spinal Cord* **2013**, *51*, 558–563. https://doi.org/10.1038/sc.2013.31.
89. Wilson, M.; Andronesi, O.; Barker, P.B.; Bartha, R.; Bizzi, A.; Bolan, P.J.; Brindle, K.M.; Choi, I.; Cudalbu, C.; Dydak, U.; et al. Methodological consensus on clinical proton MRS of the brain: Review and recommendations. *Magn. Reson. Med.* **2019**, *82*, 527–550. https://doi.org/10.1002/mrm.27742.
90. Wyss, P.O.; Huber, E.; Curt, A.; Kollias, S.; Freund, P.; Henning, A. MR spectroscopy of the cervical spinal cord in chronic spinal cord injury. *Radiology* **2019**, *291*, 131–138. https://doi.org/10.1148/radiol.2018181037.
91. Maier, I.L.; Hofer, S.; Eggert, E.; Schregel, K.; Psychogios, M.-N.; Frahm, J.; Bähr, M.; Liman, J. T1 Mapping Quantifies Spinal Cord Compression in Patients with Various Degrees of Cervical Spinal Canal Stenosis. *Front. Neurol.* **2020**, *11*, 1427. https://doi.org/10.3389/fneur.2020.574604.
92. Baucher, G.; Rasoanandrianina, H.; Levy, S.; Pini, L.; Troude, L.; Roche, P.-H.; Callot, V. T1 Mapping for Microstructural Assessment of the Cervical Spinal Cord in the Evaluation of Patients with Degenerative Cervical Myelopathy. *Am. J. Neuroradiol.* **2021**, *42*, 1348–1357. https://doi.org/10.3174/ajnr.A7157.
93. Liu, H.; MacMillian, E.L.; Jutzeler, C.R.; Ljungberg, E.; MacKay, A.L.; Kolind, S.H.; Mädler, B.; Li, D.K.B.; Dvorak, M.F.; Curt, A.; et al. Assessing structure and function of myelin in cervical spondylotic myelopathy. *Neurology* **2017**, *89*, 602–610. https://doi.org/10.1212/WNL.0000000000004197.
94. Dvorak, A.V.; Ljungberg, E.; Vavasour, I.M.; Lee, L.E.; Abel, S.; Li, D.K.B.; Traboulsee, A.; MacKay, A.L.; Kolind, S.H. Comparison of multi echo T2 relaxation and steady state approaches for myelin imaging in the central nervous system. *Sci. Rep.* **2021**, *11*, 1369. https://doi.org/10.1038/s41598-020-80585-7.
95. Glover, G.H. Overview of Functional Magnetic Resonance Imaging. *Neurosurg. Clin. N. Am.* **2011**, *22*, 133–139. https://doi.org/10.1016/j.nec.2010.11.001.
96. Duggal, N.; Rabin, D.; Bartha, R.; Barry, R.L.; Gati, J.S.; Kowalczyk, I.; Fink, M. Brain reorganization in patients with spinal cord compression evaluated using fMRI. *Neurology* **2010**, *74*, 1048–1054. https://doi.org/10.1212/WNL.0b013e3181d6b0ea.
97. Tan, Y.; Zhou, F.; Wu, L.; Liu, Z.; Zeng, X.; Gong, H.; He, L. Alteration of Regional Homogeneity within the Sensorimotor Network after Spinal Cord Decompression in Cervical Spondylotic Myelopathy: A Resting-State fMRI Study. *Biomed Res. Int.* **2015**, *2015*, 1–6. https://doi.org/10.1155/2015/647958.
98. Cronin, A.E.; Detombe, S.A.; Duggal, C.A.; Duggal, N.; Bartha, R. Spinal cord compression is associated with brain plasticity in

degenerative cervical myelopathy. *Brain Commun.* **2021**, *3*, fcab131. https://doi.org/10.1093/braincomms/fcab131.
99. Hrabálek, L.; Hok, P.; Hluštík, P.; Čecháková, E.; Wanek, T.; Otruba, P.; Vaverka, M.; Kaňovský, P. Longitudinal brain activation changes related to electrophysiological findings in patients with cervical spondylotic myelopathy before and after spinal cord decompression: An fMRI study. *Acta Neurochir.* **2018**, *160*, 923–932. https://doi.org/10.1007/s00701-018-3520-1.
100. Liu, X.; Qian, W.; Jin, R.; Li, X.; Luk, K.D.; Wu, E.X.; Hu, Y. Amplitude of Low Frequency Fluctuation (ALFF) in the Cervical Spinal Cord with Stenosis: A Resting State fMRI Study. *PLoS ONE* **2016**, *11*, e0167279. https://doi.org/10.1371/journal.pone.0167279.
101. Powers, J.; Ioachim, G.; Stroman, P. Ten Key Insights into the Use of Spinal Cord fMRI. *Brain Sci.* **2018**, *8*, 173. https://doi.org/10.3390/brainsci8090173.
102. Eippert, F.; Kong, Y.; Jenkinson, M.; Tracey, I.; Brooks, J.C.W. Denoising spinal cord fMRI data: Approaches to acquisition and analysis. *Neuroimage* **2017**, *154*, 255–266. https://doi.org/10.1016/j.neuroimage.2016.09.065.
103. Ellingson, B.M.; Woodworth, D.C.; Leu, K.; Salamon, N.; Holly, L.T. Spinal Cord Perfusion MR Imaging Implicates Both Ischemia and Hypoxia in the Pathogenesis of Cervical Spondylosis. *World Neurosurg.* **2019**, *128*, e773–e781. https://doi.org/10.1016/j.wneu.2019.04.253.
104. Uemura, K.; Matsumura, A.; Isobe, T.; Anno, I.; Kawamura, H.; Minami, M.; Tsukada, A. Perfusion-Weighted Magnetic Resonance Imaging of the Spinal Cord in Cervical Spondylotic Myelopathy. *Neurol. Med. Chir.* **2006**, *46*, 581–588. https://doi.org/10.2176/nmc.46.581.
105. Zhou, F.; Huang, M.; Wu, L.; Tan, Y.; Guo, J.; Zhang, Y.; He, L.; Gong, H. Altered perfusion of the sensorimotor cortex in patients with cervical spondylotic myelopathy: An arterial spin labeling study. *J. Pain Res.* **2018**, *11*, 181–190. https://doi.org/10.2147/JPR.S148076.
106. Sherman, J.L.; Nassaux, P.Y.; Citrin, C.M. Measurements of the normal cervical spinal cord on MR imaging. *Am. J. Neuroradiol.* **1990**, *11*, 369–372.
107. Cohen-Adad, J.; Alonso-Ortiz, E.; Abramovic, M.; Arneitz, C.; Atcheson, N.; Barlow, L.; Barry, R.L.; Barth, M.; Battiston, M.; Büchel, C.; et al. Generic acquisition protocol for quantitative MRI of the spinal cord. *Nat. Protoc.* **2021**, *16*, 4611–4632. https://doi.org/10.1038/s41596-021-00588-0.
108. Cohen-Adad, J.; Alonso-Ortiz, E.; Abramovic, M.; Arneitz, C.; Atcheson, N.; Barlow, L.; Barry, R.L.; Barth, M.; Battiston, M.; Büchel, C.; et al. Open-access quantitative MRI data of the spinal cord and reproducibility across participants, sites and manufacturers. *Sci. Data* **2021**, *8*, 219. https://doi.org/10.1038/s41597-021-00941-8.
109. Samson, R.S.; Lévy, S.; Schneider, T.; Smith, A.K.; Smith, S.A.; Cohen-Adad, J.; Gandini Wheeler-Kingshott, C.A.M. ZOOM or Non-ZOOM? Assessing Spinal Cord Diffusion Tensor Imaging Protocols for Multi-Centre Studies. *PLoS ONE* **2016**, *11*, e0155557. https://doi.org/10.1371/journal.pone.0155557.
110. Martin, A.R.; De Leener, B.; Cohen-Adad, J.; Cadotte, D.W.; Kalsi-Ryan, S.; Lange, S.F.; Tetreault, L.; Nouri, A.; Crawley, A.; Mikulis, D.J.; et al. Clinically Feasible Microstructural MRI to Quantify Cervical Spinal Cord Tissue Injury Using DTI, MT, and T2*-Weighted Imaging: Assessment of Normative Data and Reliability. *AJNR Am. J. Neuroradiol.* **2017**, *38*, 1257–1265. https://doi.org/10.3174/ajnr.A5163.
111. Andersson, J.L.R.; Skare, S.; Ashburner, J. How to correct susceptibility distortions in spin-echo echo-planar images: Application to diffusion tensor imaging. *Neuroimage* **2003**, *20*, 870–888. https://doi.org/10.1016/S1053-8119(03)00336-7.
112. Andersson, J.L.R.; Sotiropoulos, S.N. An integrated approach to correction for off-resonance effects and subject movement in diffusion MR imaging. *Neuroimage* **2016**, *125*, 1063–1078. https://doi.org/10.1016/j.neuroimage.2015.10.019.
113. Tuch, D.S.; Reese, T.G.; Wiegell, M.R.; Makris, N.; Belliveau, J.W.; Van Wedeen, J. High angular resolution diffusion imaging reveals intravoxel white matter fiber heterogeneity. *Magn. Reson. Med.* **2002**, *48*, 577–582. https://doi.org/10.1002/mrm.10268.
114. Caruyer, E.; Lenglet, C.; Sapiro, G.; Deriche, R. Design of multishell sampling schemes with uniform coverage in diffusion MRI. *Magn. Reson. Med.* **2013**, *69*, 1534–1540. https://doi.org/10.1002/mrm.24736.
115. Deelchand, D.K.; Ho, M.-L.; Nestrasil, I. Ultra-High-Field Imaging of the Pediatric Brain and Spinal Cord. *Magn. Reson. Imaging Clin. N. Am.* **2021**, *29*, 643–653. https://doi.org/10.1016/j.mric.2021.06.013.
116. Roussel, T.; Le Fur, Y.; Guye, M.; Viout, P.; Ranjeva, J.; Callot, V. Respiratory-triggered quantitative MR spectroscopy of the human cervical spinal cord at 7 T. *Magn. Reson. Med.* **2022**, *87*, 2600–2612. https://doi.org/10.1002/mrm.29182.
117. Juchem, C.; Cudalbu, C.; Graaf, R.A.; Gruetter, R.; Henning, A.; Hetherington, H.P.; Boer, V.O. B 0 shimming for in vivo magnetic resonance spectroscopy: Experts' consensus recommendations. *NMR Biomed.* **2021**, *34*, e4350. https://doi.org/10.1002/nbm.4350
118. Andronesi, O.C.; Bhattacharyya, P.K.; Bogner, W.; Choi, I.; Hess, A.T.; Lee, P.; Meintjes, E.M.; Tisdall, M.D.; Zaitsev, M.; Kouwe, A. Motion correction methods for MRS: experts' consensus recommendations. *NMR Biomed.* **2021**, *34*, e4364. https://doi.org/10.1002/nbm.4364.
119. Deelchand, D.K.; Henry, P.; Joers, J.M.; Auerbach, E.J.; Park, Y.W.; Kara, F.; Ratai, E.; Kantarci, K.; Öz, G. Plug-and-play advanced magnetic resonance spectroscopy. *Magn. Reson. Med.* **2022**, *87*, 2613–2620. https://doi.org/10.1002/mrm.29164.
120. De Leener, B.; Fonov, V.S.; Collins, D.L.; Callot, V.; Stikov, N.; Cohen-Adad, J. PAM50: Unbiased multimodal template of the brainstem and spinal cord aligned with the ICBM152 space. *Neuroimage* **2018**, *165*, 170–179. https://doi.org/10.1016/j.neuroimage.2017.10.041.
121. De Leener, B.; Lévy, S.; Dupont, S.M.; Fonov, V.S.; Stikov, N.; Louis Collins, D.; Callot, V.; Cohen-Adad, J. SCT: Spinal Cord Toolbox, an open-source software for processing spinal cord MRI data. *Neuroimage* **2017**, *145*, 24–43. https://doi.org/10.1016/j.neuroimage.2016.10.009.
122. McLachlin, S.; Leung, J.; Sivan, V.; Quirion, P.; Wilkie, P.; Cohen-Adad, J.; Whyne, C.M.; Hardisty, M.R. Spatial correspondence

of spinal cord white matter tracts using diffusion tensor imaging, fibre tractography, and atlas-based segmentation. *Neuroradiology* **2021**, *63*, 373–380. https://doi.org/10.1007/s00234-021-02635-9.
123. Dostál, M.; Keřkovský, M.; Staffa, E.; Bednařík, J.; Šprláková-Puková, A.; Mechl, M. Voxelwise analysis of diffusion MRI of cervical spinal cord using tract-based spatial statistics. *Magn. Reson. Imaging* **2020**, *73*, 23–30. https://doi.org/10.1016/j.mri.2020.07.008.
124. Gros, C.; De Leener, B.; Badji, A.; Maranzano, J.; Eden, D.; Dupont, S.M.; Talbott, J.; Zhuoquiong, R.; Liu, Y.; Granberg, T.; et al. Automatic segmentation of the spinal cord and intramedullary multiple sclerosis lesions with convolutional neural networks. *Neuroimage* **2019**, *184*, 901–915. https://doi.org/10.1016/j.neuroimage.2018.09.081.
125. Perone, C.S.; Calabrese, E.; Cohen-Adad, J. Spinal cord gray matter segmentation using deep dilated convolutions. *Sci. Rep.* **2018**, *8*, 5966. https://doi.org/10.1038/s41598-018-24304-3.
126. Jenkinson, M.; Beckmann, C.F.; Behrens, T.E.J.; Woolrich, M.W.; Smith, S.M. FSL. *Neuroimage* **2012**, *62*, 782–790. https://doi.org/10.1016/j.neuroimage.2011.09.015.
127. Penny, W.; Friston, K.; Ashburner, J.; Kiebel, S.; Nichols, T. *Statistical Parametric Mapping*; Elsevier: Amsterdam, The Netherlands, 2007; ISBN 9780123725608.
128. Garyfallidis, E.; Brett, M.; Amirbekian, B.; Rokem, A.; van der Walt, S.; Descoteaux, M.; Nimmo-Smith, I. Dipy, a library for the analysis of diffusion MRI data. *Front. Neuroinform.* **2014**, *8*, 8. https://doi.org/10.3389/fninf.2014.00008.
129. Provencher, S.W. Estimation of metabolite concentrations from localized in vivo proton NMR spectra. *Magn. Reson. Med.* **1993**, *30*, 672–679. https://doi.org/10.1002/MRM.1910300604.
130. Li, X.; Morgan, P.S.; Ashburner, J.; Smith, J.; Rorden, C. The first step for neuroimaging data analysis: DICOM to NIfTI conversion. *J. Neurosci. Methods* **2016**, *264*, 47–56. https://doi.org/10.1016/j.jneumeth.2016.03.001.
131. Tetreault, L.; Kopjar, B.; Nouri, A.; Arnold, P.; Barbagallo, G.; Bartels, R.; Qiang, Z.; Singh, A.; Zileli, M.; Vaccaro, A.; et al. The modified Japanese Orthopaedic Association scale: Establishing criteria for mild, moderate and severe impairment in patients with degenerative cervical myelopathy. *Eur. Spine J.* **2017**, *26*, 78–84. https://doi.org/10.1007/s00586-016-4660-8.
132. Holly, L.T.; Freitas, B.; McArthur, D.D.L.; Salamon, N. Proton magnetic resonance spectroscopy to evaluate spinal cord axonal injury in cervical spondylotic myelopathy: Laboratory investigation. *J. Neurosurg. Spine* **2009**, *10*, 194–200. https://doi.org/10.3171/2008.12.SPINE08367.